UNIVERSITE A.BAKR BELKAID DE TLEMCEN   **UNIVERSITE PAUL VERLAINE DE METZ**

THESE ——

Présentée à

L'UNIVERSITE A.BAKR BELKAID de TLEMCEN et L'UNIVERSITE PAUL VERLAINE DE METZ

Par

Sara CHENTOUF

Pour l'obtention de grade de:

Docteur de l'Université A.Bakr Belkaid de Tlemcen et l'Université Paul-Verlaine de Metz

---

Etude du comportement de Fe_3Al et son joint de grains $\sum 5(310)[001]$ en présence de Ti et Zr par méthodes ab initio avec prise en compte de l'effet de la température.

Soutenance prévue 18 Janvier 2011 à Metz, devant le jury compose de:

Mr. Jacques LACAZE	Directeur de Recherche, CIRIMAT, ENSIACET, Toulouse, France	Président
Mme. Anna FRACZKIEWICZ	Directrice de Recherche, PECM, St-Etienne, France.	Examinateur
Mr. Martin FRIAK	Directeur de Recherche, Max-Plank-Institut fur Eisenforschung, Allemagne.	Examinateur
Mr. Abdelhafid KELLOU	Professeur, LPT, USTHB, Alger Algérie.	Examinateur
Mr. Ghouti MERAD	Professeur, LEPM, Université A.Bakr Belkaid, Tlemcen, Algérie.	Examinateur
Mr. Hafid AOURAG	Professeur, LEPM, Université A.Bakr Belkaid, Tlemcen, Algérie.	Directeur de thèse
Mr. Thierry GROSDIDIER	Professeur, LEM3, Université Paul-Verlaine, Metz, France	Co-directeur de thèse
Mr. Jean-Marc RAULOT	Maître de conférences, LEM3, Université Paul-Verlaine, Metz, France	Co-directeur de thèse

---

Laboratoire d'**E**tude et **P**rédiction des **M**atériaux (**LEPM-URMER**)

To my parents

Acknowledgment

I would like to express my gratitude to the many people who have supported me as I completed my graduate studies and dissertation.

First, I would like to sincerely thank my advisor, Pr. Thierry GROSDIDIER, for providing continuous support and instructive guidance throughout my doctoral studies. I feel lucky to have an adviser like him with great patience and understanding to the difficult conditions that I had during this thesis. His effort, encouragement and advices are greatly appreciated.

I gratefully acknowledge Pr. Hafid AOURAG who introduced me to research and I will always be highly grateful to him for his commitment to my academic success.

I also would like to thank my co-director Dr. Jean-Marc RAULOT for the many interesting discussions we had, and for his ability to inspire thoughts and suggestions on a large variety of topics, ranging from fundamentals of theoretical condensed matter physics to applications and computational issues.

I wish to thank the reviewers, Dr Anna FRACZKIEWICZ, Pr. Abdelhafid KELLOU and Dr. Martin FRIAK, to have the patience to read this dissertation and to give me valuable and detailed comments on my thesis. Thanks also to the members of the jury, Pr. Ghouti MERAD and Dr. Jacques LACAZE, as it is a great honor for me to have them to evaluate my work.

This thesis has been carried out in the Framework of the French/Algerien CMEP PHC *Tassili project* N° 12053TL and the *Eiffel Excellence Scholarship* N° 690532C. I would like to acknowledge EGIDE (Centre Français pour l'Accueil et les Échanges Internationaux) for the Financial support. I present also my sincere thanks to Pr. Ghouti MERAD for giving me the opportunity to work with his team in the LEPM laboratory and providing the support to do my research.

Finally, I could not forget to thank my parents, without whom all this would never have taken place, at least not for me.

Contents

Introduction

Fe$_3$Al-based intermetallic compounds are promising materials for structural applications at high temperature. Their advantageous properties originate from their low density and their high corrosion resistance in oxidizing and sulfidizing environments. At ambient and intermediate temperatures, Fe$_3$Al shows higher strength than other single-phase iron alloys due to its ordered D0$_3$ superlattice structure. However, at about 550 °C, disordering of the D0$_3$ structure as well as a sharp drop in the flow stresses occur in the binary stoichiometric Fe$_3$Al compound, causing detrimental effects to this material with regard to structural applications. An interesting aspect of these alloys is their behavior towards transition metal impurities. Some elements like Ti increase the stability of the D0$_3$ by increasing the D0$_3$/B2 transition towards higher temperature. The situation is less clear for Zr addition, indeed, despite the beneficial effect of small Zr addition on the grain boundary cohesion and ductility; there is no experimental data available concerning its effects on the stability of the D0$_3$-Fe$_3$Al compounds.

In this thesis the effect of the Ti and Zr transition metals on the D0$_3$-Fe$_3$Al inntermetallic compounds has been investigated by means ab initio PseudoPotentials numerical simulations based on Density Functional Theory. Two main issues will be addressed *(i)* the understanding of the role of the these two transition metals in terms of stability of the bulk at the light of their site preference in the D0$_3$-Fe$_3$Al structure *(ii)* knowing that the ductility of iron aluminides is affected by grain boundary brittleness and that experimental information on segregation at grain boundary (G.B.) is hardly available because of the resolution of the measuring tools, the behaviour of Ti and Z transition metals in the $\sum 5$ (310) [001] grain boundary will then be studied

to point out their effect on the structural stability of this interface. The particular $\sum$5 (310) [001] grain boundary has been selected because of its short period and the presence of a single type of (310) planes in the $D0_3$ structures. These two factors make it much easier a numerical simulation by keeping the calculation time within reasonable limit. It is also reasonable to consider however that, due to its high degree of coincidence, this specific grain boundary can be representative of a wide range of boundaries in Fe_3Al alloys. Thus, the behavior depicted here for Ti and Zr atoms with respect to their neighbor atoms should not change drastically with the nature of the grain boundary.

In principle, and this is the approach emphasized in this thesis, a theory attempting to realistically describe of the structural properties (stability of the $D0_3$ structure and grain boundary relaxation) needs to take into account the effect of temperature. This requires a molecular dynamics treatment of the atoms in the supercell. The technique known as *ab initio* molecular dynamics (AIMD) solves these problems by combining 'on the fly' electronic structure calculations with finite temperature dynamics. Thus, our study was conducted both using the conventional static ab initio calculations (0K) as well as by taken into account the effect of temperature (Ab Initio Molecular Dynamics).

The most important element in an AIMD calculation is the representation of the electronic structure. The calculation of the exact ground-state electronic wave-function is intractable, and approximations must be used. In the present study, we choose to use pseudopotentials methods implemented in the Vienna Ab Initio Simulation Package (VASP). It is one of the most powerful ab initio DFT pseudopotential-based packages available at present. It has been already applied to a wide range of problems and materials, including bulk systems, surfaces and interfaces.

This thesis is organized as follows. In Chapter I we provide a literature review concerning the effect of alloying elements on the properties of FeAl based inntemetallics compounds.

In Chapter II an outline of the theoretical background that serves as a foundation of our calculations is given. The implementation of Ab Initio Molecular Dynamics within the framework of plane wave pseudopotential density functional theory is given in detail. A short introduction to density functional and pseudopotential theory will be given in the second part of this chapter.

Chapter III and IV are devoted to the application of these methods and the use of tools described in the previous section. In Chapter III, the results of the static ab initio calculations of the substitutions of the Ti and Zr transition metals in the bulk as well as the $\sum$5 grain boundary are

presented. Chapter IV gives the results of Ab Initio Molecular Dynamic calculations that was set up to investigate the effect of temperature on the structural stabilities of the two transition metals impurities in the bulk and $\sum 5$ (310) [001] grain boundary of the $D0_3$-Fe_3Al compounds.

Finally, we conclude the document and summarize the basic insights.

Introduction

Fe$_3$Al-based intermetallic compounds are promising materials for structural applications at high temperature. Their advantageous properties originate from their low density and their high corrosion resistance in oxidizing and sulfidizing environments. At ambient and intermediate temperatures, Fe$_3$Al shows higher strength than other single-phase iron alloys due to its ordered D0$_3$ superlattice structure. However, at about 550 °C, disordering of the D0$_3$ structure as well as a sharp drop in the flow stresses occur in the binary stoichiometric Fe$_3$Al compound, causing detrimental effects to this material with regard to structural applications. An interesting aspect of these alloys is their behavior towards transition metal impurities. Some elements like Ti increase the stability of the D0$_3$ by increasing the D0$_3$/B2 transition towards higher temperature. The situation is less clear for Zr addition, indeed, despite the beneficial effect of small Zr addition on the grain boundary cohesion and ductility; there is no experimental data available concerning its effects on the stability of the D0$_3$-Fe$_3$Al compounds.

In this thesis the effect of the Ti and Zr transition metals on the D0$_3$-Fe$_3$Al intermetallic compounds has been investigated by means of ab initio PseudoPotentials numerical simulations based on Density Functional Theory. Two main issues will be addressed *(i)* the understanding of the role of the these two transition metals in terms of stability of the bulk at the light of their site preference in the D0$_3$-Fe$_3$Al structure *(ii)* knowing that the ductility of iron aluminides is affected by grain boundary brittleness and that experimental information on segregation at grain boundary (G.B.) is hardly available because of the resolution of the measuring tools, the behaviour of Ti and Zr transition metals in the $\sum$5 (310) [001] grain boundary will then be studied to point out their effect on the structural stability of this interface. The particular $\sum$5

(310) [001] grain boundary has been selected because of its short period and the presence of a single type of (310) planes in the D0$_3$ structures. These two factors make it much easier a numerical simulation by keeping the calculation time within reasonable limit. It is also reasonable to consider however that, due to its high degree of coincidence, this specific grain boundary can be representative of a wide range of boundaries in Fe$_3$Al alloys. Thus, the behavior depicted here for Ti and Zr atoms with respect to their neighbor atoms should not change drastically with the nature of the grain boundary.

In principle, and this is the approach emphasized in this thesis, a theory attempting to realistically describe of the structural properties (stability of the D0$_3$ structure and grain boundary relaxation) needs to take into account the effect of temperature. This requires a molecular dynamics treatment of the atoms in the supercell. The technique known as *ab initio* molecular dynamics (AIMD) solves these problems by combining 'on the fly' electronic structure calculations with finite temperature dynamics. Thus, our study was conducted both using the conventional static ab initio calculations (0K) as well as by taken into account the effect of temperature (Ab Initio Molecular Dynamics).

The most important element in an AIMD calculation is the representation of the electronic structure. The calculation of the exact ground-state electronic wave-function is intractable, and approximations must be used. In the present study, we choose to use pseudopotentials methods implemented in the Vienna Ab Initio Simulation Package (VASP). It is one of the most powerful ab initio DFT pseudopotential-based packages available at present. It has been already applied to a wide range of problems and materials, including bulk systems, surfaces and interfaces.

This thesis is organized as follows. In Chapter I we provide a literature review concerning the effect of alloying elements on the properties of FeAl based intermetallics compounds.

In Chapter II an outline of the theoretical background that serves as a foundation of our calculations is given. The implementation of Ab Initio Molecular Dynamics within the framework of plane wave pseudopotential density functional theory is given in detail. A short introduction to density functional and pseudopotential theory will be given in the second part of this chapter.

Chapter III and IV are devoted to the application of these methods and the use of tools described in the previous section. In Chapter III, the results of the static ab initio calculations of the substitutions of the Ti and Zr transition metals in the bulk as well as the $\sum 5$ grain boundary are presented. Chapter IV gives the results of Ab Initio Molecular Dynamic calculations that was set

up to investigate the effect of temperature on the structural stabilities of the two transition metals impurities in the bulk and $\sum 5$ (310) [001] grain boundary of the $D0_3$-Fe_3Al compounds.

Finally, we conclude the document and summarize the basic insights

Chapter I

Background for the iron aluminides based intermetallics analysis

In this chapter, we give survey of the literature concerning the effect of the alloying elements on the properties of FeAl based intermetallics compounds. After a brief introduction to the properties of the intermetallics and the more especially the intermetallic compounds based on the FeAl system, in Section I and II, the different strengthening mechanisms of the alloying elements in the bulk are presented in Section III. In Section IV the effect of additions at the grain boundaries are also discussed with a description of the different tools for the characterization of the grain boundaries.

I. Intermetallic compounds

Intermetallic compounds can be simply defined as ordered alloy phases formed between two or more metallic elements. These materials have different crystal structures from those of their based metallic constituents metallic components and exhibits long-range ordered superlattices. In comparison with conventional metallic materials, intermetallic compounds have the advantages of high melting point and high specific strength, which make them promising high temperature structural materials for automotive, aircraft, and aerospace applications.

The ordered nature of intermetallic compounds generates high temperature properties due to the presence of long-range-ordered superlattice, which reduce dislocation mobility and diffusion processes at elevated temperatures [1, 2]. Aluminides based intermetallics are low density materials which are distinctly different from conventional solid-solution alloys. For example,

Ni$_3$Al exhibits an increase in yield strength with increasing temperature, whereas conventional alloys exhibit a general decrease in strength with temperature [3, 4]. Nickel and iron aluminides also possess sufficiently high concentration of aluminium, thus formation of a continuous and adherent alumina scale on the external surface of the material could always be achieved. In contrast, most of the alloys and capable of operating above 700 °C in oxygen-containing environments contain less than 2 wt. % aluminium, and invariably contain high concentration of chromium for oxidation protection with chromia. Nickel and iron aluminides therefore could provide excellent oxidation resistance at temperatures ranging from 1100 to 1400 °C owing to their high aluminium contents and high melting points [4].

II. Iron aluminides

Among the big family of intermetallic compounds, the Fe-Al, Ni-Al and Ti-Al systems are attracting most of the attention. The FeAl system is attractive because of specific features. Due to their excellent oxidation resistance _first noted in the 1930s_ iron aluminides have been the subjected to extensive studies with respect to structural and functional applications [6]. In addition to their superior oxidation and sulfidation resistance, iron aluminides also offer the advantages of low material cost, Consisting of non-strategic elements, their density is also lower in comparison with stainless steels. Therefore they have long been considered for applications in the automotive and petrochemical industries as well as conventional power plants and coal conversion plants, fot components such as, shofts, pipes as well as coatings for heat exchangers and molten soft applications [7]. However, their poor ductility at room temperature and significant drop in strength above 600 °C together with inadequate high temperature creep resistance has limited their potential for structural applications.

The phase diagram of the binary Fe–Al system, according to Kubaschewski [8], is shown in Fig. I-1. The solid solubility of Al in f.c.c. γ-Fe is limited to 1.3 at.% at 1180 °C. In contrast, in the disordered b.c.c. α-Fe (A2) up to 45 at.% Al can be dissolved at high temperature (1310 °C). Between 0 and 54 at.% Al two ordered compounds exist. The D0$_3$-ordered Fe$_3$Al is stable at compositions around 27 at.% Al and from room temperature to 550°C (830K). Above 550°C the ordered Fe$_3$Al with D0$_3$ structure transforms to an imperfectly ordered B2 (α_2') structure, which ultimately changes to a disordered solid solution, A2 (α). On the other hand, FeAl exists with B2 structure and is stable from about 36-48 at% Al, and the transition from B2 (α_2(I)) to A2 occurs well above 1100°C. In contrast to the newer diagrams by Massalski [9] the ordered α_2 phase field has been subdivided into three separate modifications, α_2' and α_2(I) region at lower and

α_2(h) one at higher temperatures. The subdivision is a result of measurements by Köster and Gödecke [10] who recorded energy evolution as well as expansion coefficients and elastic moduli as function of composition and temperature.

In the present work, we are studying the Fe3Al stochiometric alloy with the D03 structure. According to the phase diagram in Fig. I-1, it is expected that, at this composition, the structure encounters the change at about 550°C (850K). Following by the change at 790°C (1063K)
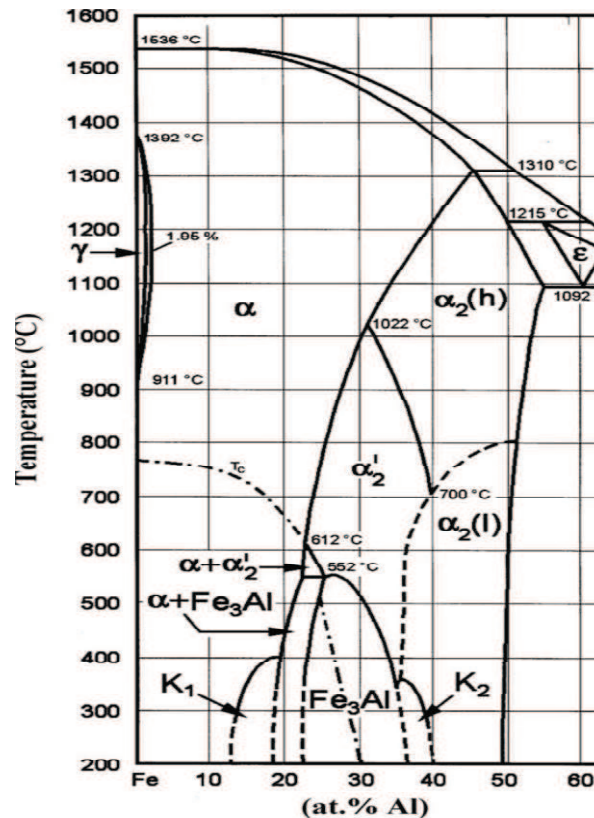
Figure.I- 1 Fe-rich part of the Fe–Al system according to Kubaschewski [8]. In addition to the phase boundaries for γ (disordered A1), α (disordered A2), Fe$_3$Al (ordered D0$_3$) and FeAl (α$_2$; ordered B2) additional lines are shown for the Curie temperature (T$_c$), for different variants of α$_2$ and the area in which the so-called '*k*-state' is observed.

During the last decade, efforts have been made to enhance room-temperature ductility, high-temperature strength, and high-temperature creep resistance by alloying of iron aluminides. Two approaches, namely, solid-solution strengthening and precipitation strengthening, were considered for strengthening of iron aluminides. Elements such as Nb, Cu, Ta, Zr, B and C were considered for precipitation strengthening; while Cr, Ti, Mn, Si, Mo, V and Ni were added into iron aluminides for solid solution strengthening. In general, the addition of elements either for precipitation strengthening or solid solution strengthening to improve high temperature tensile strength and creep resistance resulted in low room temperature tensile elongations [11].

It is well established that the fracture of iron-based intermetallics is often brittle in nature occurring by cleavage and/or intergranular (i.e occurring along grain boundaries) fracture. In this context, it is important to determine the effect of ternary element additions both on *(i)* bulk strengthening as well as *(ii)* grain boundary "softening".

III. Bulk strengthening

III.1 Strengthening by solid-solution hardening

The Fe–Al–Cr system is an example where, within a large area of compositions only, solid-solution hardening is possible. In Fig. I-2 the isothermal section at 1000 °C is shown [12]. At this temperature the phase boundary between α-(Fe,Al) and FeAl has not been determined and the term α-(Fe,Al)/FeAl is used here and also otherwise in this chapter when no distinction between the two phases is made. Complete solid solubility between α-(Fe,Al)/FeAl and α-Cr exists and according to the 1000 °C isotherm solid-solution hardening is the only strengthening mechanism available from the phase diagram for compositions up to 50 at.% Al. Only at higher Al contents the possibility of precipitating a second phase, e.g. hexagonal Al_8Cr_5, exists. There are a number of Fe–Al–X systems, e.g. with X=Si, V, Mn, Co, Ni, Cu, Zn, where an extended solid solubility for X in α-(Fe,Al)/FeAl exists.
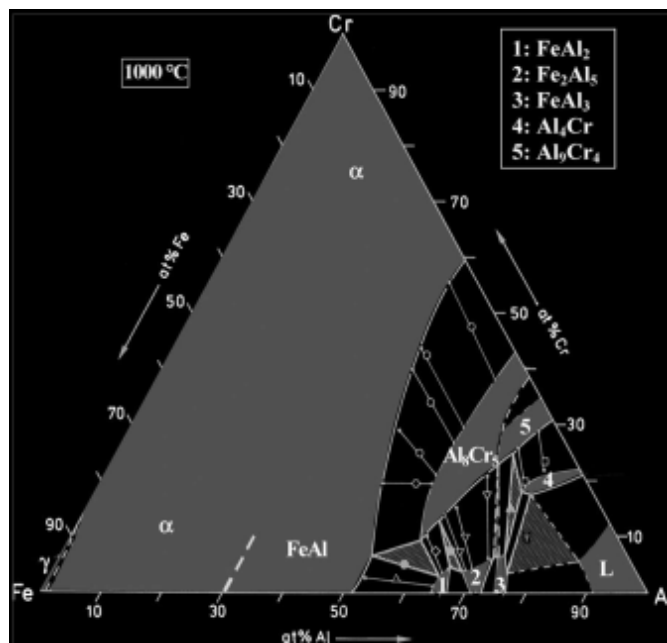
Figure.I- 2 Isothermal section of the Fe–Al–Cr system at 1000 °C [12]. The phase boundary between α-(Fe,Al) and FeAl has not been determined and is therefore given by a broken line.

It has been reported that the addition of Cr, which is beneficial for increasing the room temperature ductility [13, 14], does not show any effect on yield stress at 600 °C for alloys with 25 at.% Al [15]. This is not corroborated by the results of Stein et al. [16] who investigated the effect of solid-solution hardening for various alloying additions for alloys containing 26 at.% Al (Fig. I-3). At 600 °C an increase of the yield stress is observed by adding 2 at.% of Ti, V, Cr, or Mo. If higher amounts are added a further increase of the yield stress is only observed for Mo while for V and Cr even a decrease of the yield stress is reported [16]. At 700 °C the yield stress increases continuously with the amount of alloying addition for Ti, V and Mo while for Cr only an addition of 2 at.% increases the yield stress. At 800 °C again a continuous increase of the yield stress with the amount of alloying addition is observed for Ti, V and Mo within the investigated composition range while the addition of Cr has no marked effect on the yield stress at this temperature (Fig. I-3).
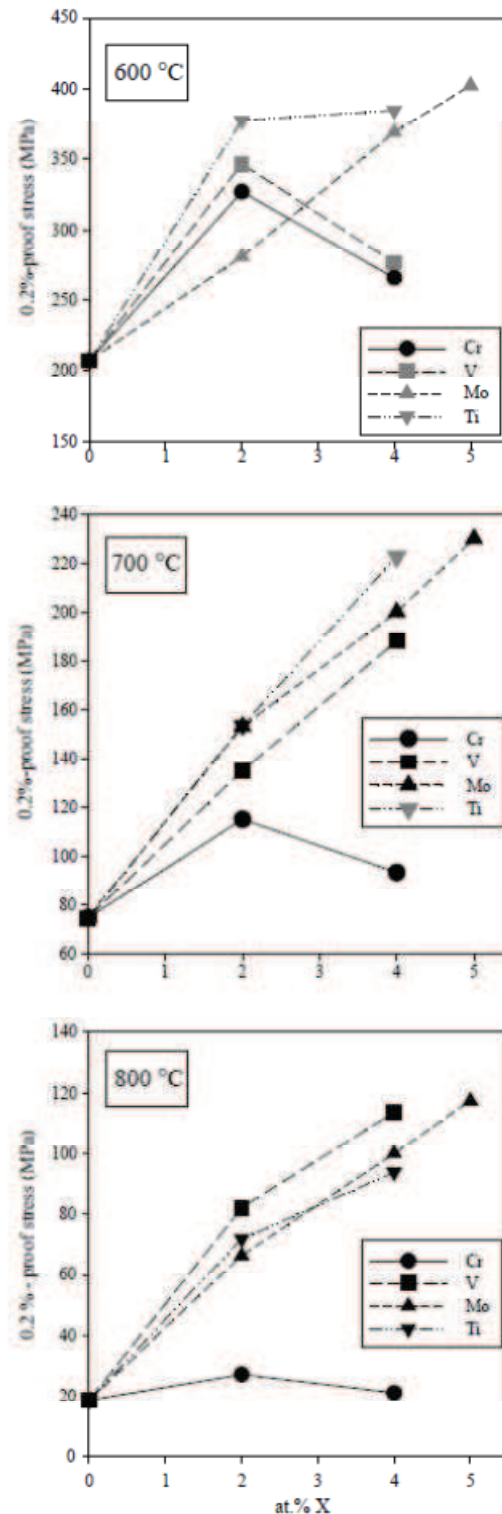
Figure.I- 3 0.2%-yield stress (in compression; 10^{-4} s^{-1} deformation rate) at 600, 700 and 800 °C for Fe–26Al with additions of 2 and 4 at.% X (X = Cr, V, Mo, Ti) [16] and Fe–28Al–5Mo [17]. Black symbols denote B2-type ordering while grey symbols denote D0$_3$/L2$_1$-type ordering at the respective temperature.

Several experimental and theoretical studies have focused on the structural and magnetic properties of Fe-Cr-Al with the D0$_3$-type structure. X-ray, neutron, magnetization and

Mossbauer effect [18] studies which have been carried out on $Fe_{3-x}Cr_xAl$ alloys with $x < 0.6$ showed that chromium atoms occupy preferentially FeI-sites and enter also Al-positions. Their magnetic moments are small, if any, and they diminish the value of the neighbouring iron atoms by roughly 0.1 u_B per chromium atom. Ready et al.[20] have found that Cr couple antiferromagneticaly with the Fe atoms and occupy the FeI site. More recently the self-consistent TB-LMTO calculations [19] confirm the result of Ready and al. indicating that a strong exists preference of the FeI-site occupation by chromium in Fe_3Al. The TB-LMTO calculations [19] show also the effect of the surroundings on the magnetic moment. They confirm negative magnetic moment of chromium found experimentally in [18].

III.2. Strengthening by incoherent precipitates

III.2.1. Precipitation of intermetallic phases

In many Fe–Al–X systems the solid solubility for the third element within the Fe–Al phases is limited and the possibility of strengthening Fe–Al-based alloys by precipitation of another intermetallic compound exists. In several systems this intermetallic phase is a Laves phase, e.g. in the Fe–Al–X systems with X=Ti, Zr, Nb and Ta. In order to study the effect of precipitates on strengthening, the Fe–Al–Zr system may be considered as a prototype system as only limited solid solubility for Zr in the Fe–Al phases has been found, which is independent from temperature, at least between 800 and 1150 °C [21]. Fig. I-4 presents the partial isothermal section of the Fe-corner at 1000 °C, which is shown by means of example, for the phase equilibria in the temperature range 800–1150 °C. The isothermal section reveals that for α-(Fe,Al)-based alloys strengthening by a Laves phase is possible in this temperature range while FeAl-based alloys may be strengthened by precipitates of the tetragonal phase $(Fe,Al)_{12}Zr$ (τ_1). As the solubility for Zr in α-(Fe,Al)/FeAl does not increase with temperature, no possibility exists for generating fine and evenly distributed precipitates from a solid solution.
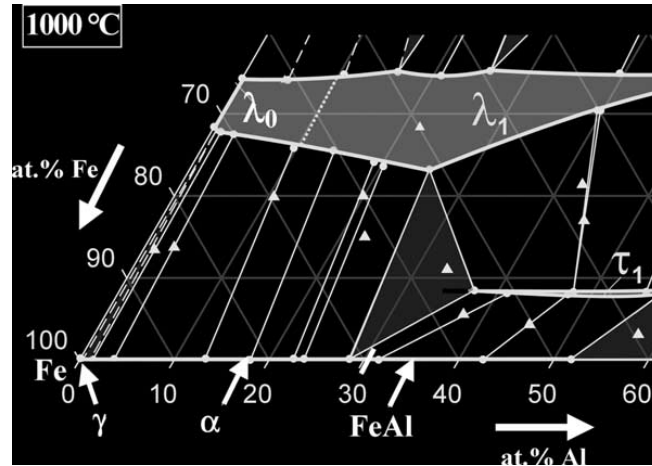
Figure.I- 4 Partial isothermal section of the Fe–Al–Zr system at 1000 °C [21]. The two ternary compounds, which are in equilibrium with the Fe–Al phases, are either a Laves phase (λ, with λ_0 denoting the cubic C15 structure and λ_1 denoting the hexagonal C14 structure) or the tetragonal ThMn$_{12}$- type phase (Fe,Al)$_{12}$Zr (τ_1).

A set of experiments with the laves phases in the Fe-Al system have been done. However, the dependence of their mechanical properties on the chemical composition is not yet understood. Thus a deeper understanding of the structure stability and mechanical properties of the laves phases is essential to control the material properties of the iron aluminides. Recently, experimental investigations of the pure lave phases Fe$_2$Nb [22] and (FeAl)$_2$Nb [23] have been performed and the phase equilibria in the respective ternary systems has been studied.

In addition to experiments, the structural properties of the Fe$_2$Nb laves phase (C14 Hexagonal structure) has been investigated by quantum-mechanical ab initio calculations [24]. Fig. I-5 shows the results of the calculated single crystalline elastic constants tensor C$_{ij}$, which gives direct insight into the directional dependence of the Young modulus. It indicats a rather strong elastic anisotropy, i.e. deviations from an ideal sphere. The derived Young's modulus at T=0K by using selfconsistent crystal homogenization method is about 250 ± 22 GPa. The authors have determined also the site preference of Al between the Fe sublattices of the C14 structure using a combined experimental and theoretical approach.
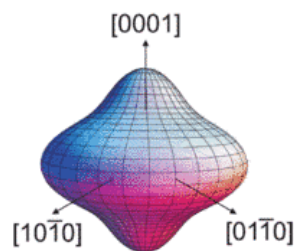
Figure.I- 5 Quantum-mechanically calculated directional dependence of single-crystalline Young's modulus of Fe$_2$Nb with the hexagonal C14 structure. Shape deviations from an ideal sphere identify elastic anisotropy of the studied Laves phase compound.

In the ab *initio* investigation, the site preference has been investigated at both low and elevated temperatures, making use of CALPHAD-like statistical sublattice models to determine the configurational entropy. The resulting free energies are shown for $(Fe_{0.75}Al_{0.25})_2Nb$ in Fig. I-6 (considering a double-layer antiferromagnetic structure). The *x* axis at the bottom/top indicates the fraction of 2a/6h sites occupied by Al. The authors show that the 2a site has the lowest solution free enthalpy already at T = 0 K (see Fig.I-6). With increasing temperature, the larger number of sites and thus configurations in the 6h sublattice and the corresponding gain in configurational entropy make the occupation of this sublattice more and more attractive. However, even for temperatures up to 1500 K the minimum of the free enthalpy curve is above x = 0.25 (the value corresponding to the statistical distribution), yielding a net-preference to the 2a sites.
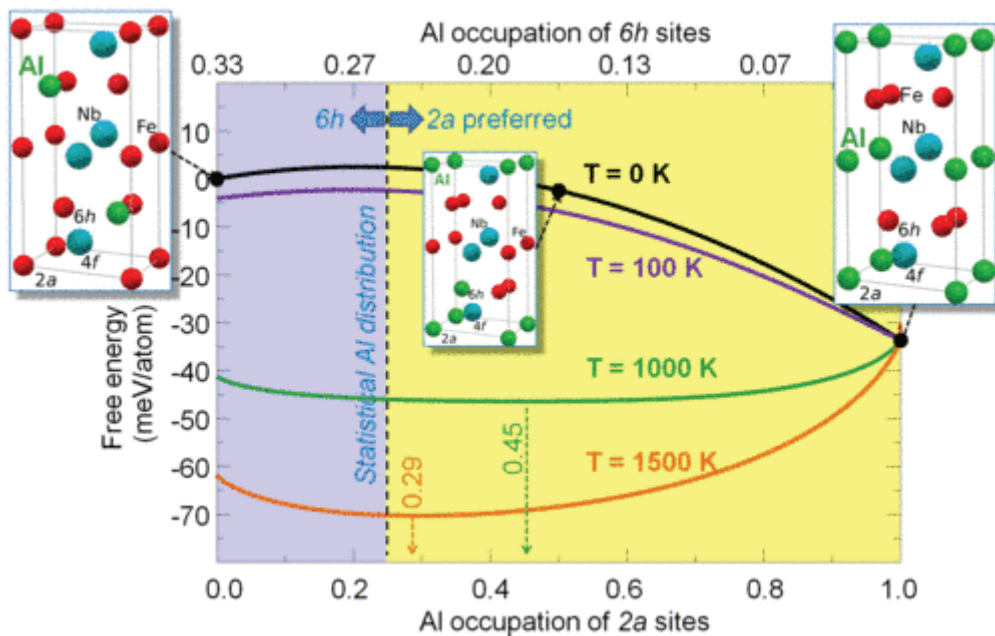
Figure.I- 6 The ab initio calculated solution free enthalpies for $(Fe_{0.75}Al_{0.25})_2Nb$ at different temperatures. The black dots indicate results of ab intitio calculations, solid lines combine these results with a sublattice regular solution model [24].

III.2.2. Precipitation of carbides

Besides hardening by precipitation of intermetallic phases, carbides could also act as strengthening phases. Fig. I-7 shows two partial isothermal sections at 800 and 1000 °C of the Fe corner of the Fe–Al–C system [25]. At both temperatures α-(Fe,Al) and FeAl are in equilibrium with the cubic K-phase Fe_3AlC. The solid solubility for carbon in α-(Fe,Al)/FeAl changes only slightly between 800 and 1200 °C but is considerably lower at lower temperatures, e.g. drops from about 1 at.% C at 1000 °C to about 50 ppm at 320 °C [26]. This leads to the precipitation of

fine needle shaped precipitates of the *k* phase at the grain boundaries during cooling. As the carbon diffusivity is even high at ambient temperatures, these precipitates at the grain boundaries are found at room temperature in all alloys of appropriate compositions even after quenching and they do strongly affect mechanical properties at low temperatures [26]. The effect of *k* phase precipitates on the mechanical behaviour of Fe–Al-based alloys with Al contents between 25 and 30 at.% has been studied in detail by Schneider et al. [27].
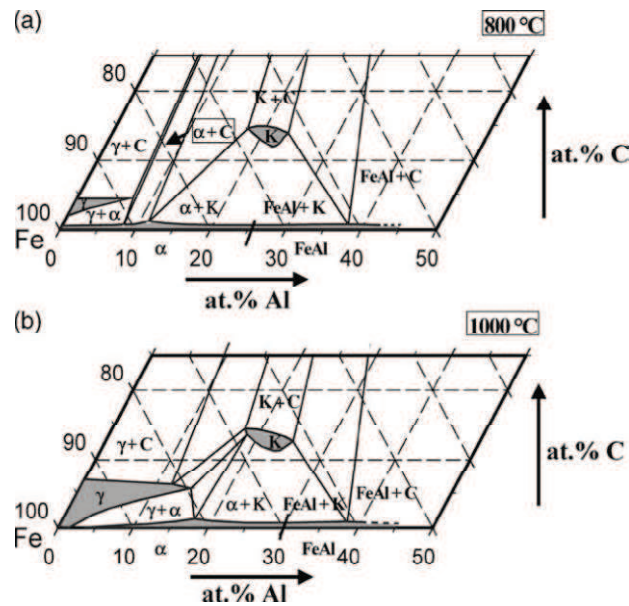
Figure.I- 7 Partial isothermal sections of the Fe–Al–C system at (a) 800 (b) and 1000 °C [15]. The exact course of the α-(Fe,Al)/FeAl phase boundary has not been determined within the ternary system and therefore only its position in the binary Fe–Al system is indicated by a bar on the Fe–Al axis.

To control the precipitation end microstructures for the carburizing process of the Fe-Al alloys, it is necessary to rely on the thermodynamical properties of the iron riche phases Fe-Al-C system, and to know the fundamental properties of these phases. Several experimental and theoretical informations are present in the literature about the *k* carbide. The *k* phase is associated to the Fe_3AlC structure, with the *Strukturbericht Designation* $E2_1$ (a perovskite-type structure). This carbide is based on the fcc ordered structure Fe_3Al-L1_2 where the iron atoms are located in the center of each face, and the aluminium atoms sit on the corners of the cube (see Fig. I-8). The carbon atom occupies the central octahedral interstitial position formed by the six iron atoms as first nearest neighbours.
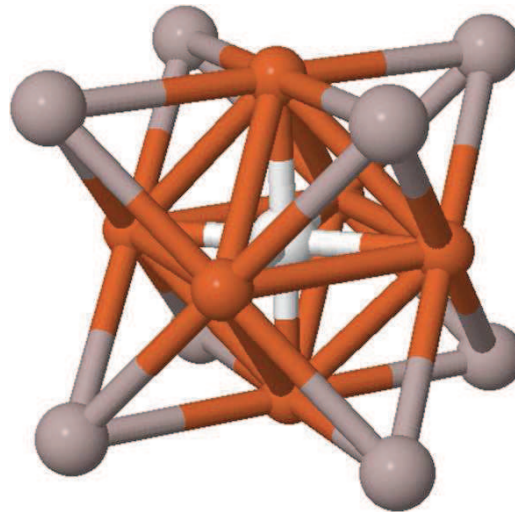
Figure.I- 8 Conventional cell of the *k*-Fe$_3$AlC carbide. The carbon atom is represented in white in octahedral position, the aluminium atoms in grey and the iron atoms in dark-grey.

The stoichiometric Fe$_3$AlC has, in fact, never been observed. Experimentally, the stoichiometry proposed for *k* is Fe$_{4-y}$Al$_y$C$_x$ where 0.8<*y*<1.2 and 0<*x*<1 [28]. Other results indicate that the composition of the different synthesized compounds is probably close to Fe$_3$AlC$_{x=1/2}$ [29, 30]. In addition, the experimental magnetic nature of the compound (ferro- or nonmagnetic) is not yet well established. Since the investigations of Morral (1934) [31], it has been stated several times that the Kappa phase is ferromagnetic. The given Curie temperature values would lie between 125 [32] and 290 °C [33]. However, the investigations of Parker et al. [34] indicate that the *k* phase might not be magnetic. Later, the investigations of Andryushchenko et al. [28] seem to have confirmed these observations. These authors have observed that the distribution of aluminium on the corners of the cube and of iron on the faces of the cube is apparently not perfect. Antisites' defects (aluminium atoms on iron sites and reciprocally iron on aluminium sites) seem to be at the origin of the reduced magnetic moment.

Ohtani et al. [35] have published a Fe-Al-C phase diagram based on ab initio calculations within an all electron approach, and Maugis et al. [36] have discussed the relative stability of various phases in aluminium- containing steels, through ab initio calculations using the VASP package. More recently, Connétable et al. [37] have investigated the influence of the carbon on different properties of the Fe$_3$Al system using ab intio calculations. The authors have found that the insertion of the carbon atom decreases the magnetism of the iron atoms and modifies strongly the heat capacity and the elastic constant in k-phase compared to the Fe$_3$Al-L1$_2$ structure. The interactions between the Fe and the C are is the main origin of these modifications. Kellou et al. have also investigated the structural and thermal properties of Fe$_3$AlC *k*-carbide [78]. The

authors show that The C addition has the highest effect in strengthening the cohesion of the Fe_3Al base between several additions. These authors have found that the bulk modulus (166GPa) and cohesive energy (5.7eV/ atom) of the Fe_3AlC (*k*-carbide) phase has been found to the highest from all the investigated Fe_3AlX compounds (X=. H, B, C, N, O) [78].

III.3. Strengthening by coherent precipitates

In the Fe–Al–Ni system a miscibility gap between disordered α-(Fe,Al) (A2) and ordered NiAl (B2) exists at temperatures below about 1200 °C [38]. The lattice mismatch of both phases is sufficiently small so that it is possible to produce very fine-scale coherent two-phase microstructures of disordered α-(Fe,Al) (A2) + ordered (Ni,Fe)Al (B2). Except for the Fe–Al–Ni system, the mechanical properties of the coherent two-phase microstructures have not been studied in detail. The coherent precipitates have a strong strengthening effect and microstructures can be varied such that the hard (Ni,Fe)Al phase is either the matrix or the precipitate and in both cases a strengthening effect has been achieved. The deformation behaviour of ternary Fe–Al–Ni alloys at high temperatures has been studied [39]. These studies have been extended to quaternary Fe–Al–Ni–Cr alloys and first results, especially on the creep behaviour of these alloys, are reported by Stallybrass et al. [40].

III.4. Strengthening by order

An additional possibility for strengthening of Fe–Al based alloys is to stabilise the $D0_3$ structure with respect to the B2 structure to higher temperatures. Nishino et al. [41, 42] have determined the $D0_3$- B_2 transformation temperatures in $(Fe_{1-x}M_x)_3Al$ with M= Ti, V, Cr, Mn and Mo. In particular, the transformation temperatures T_0 for M= Ti and V increase rapidly with increasing x, reaching T_0 values as high as 1300 K for x=0.15 (approx. 11 at.% Ti) and x=0.25 (approx. 19 at.% V). Anthony and Fultz [43] have reviewed the solute effects on T_0 in Fe_3Al and also measured the changes in T_0 for a large number of solutes only in the dilute limit (see Fig. I-9).
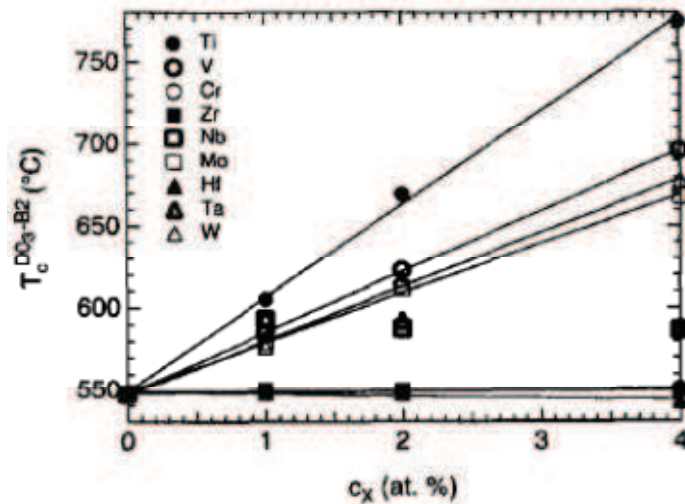
Figure.I- 9 Effect of ternary concentrations on $\Delta T_0^{D0_3-B_2}$ [43].

Among the transition elements, the addition of Ti gives rise to the sharpest increase in T_0 at the rate of 55 K/at.% Ti [43, 41]. Likewise, the additions of V and Mo increase T_0 but only at the rates of 35 K/at.% V [43, 41], and 25 [44, 42] or 30 [43] K/at.% Mo. An initial rise in T_0 for M=Ti, V and Mo tends to moderate at a higher composition. An approximately linear dependence of T^{D03-B2} on ternary concentration is observed for all except for two elements of the transition metals. The two exceptions, Nb and Ta, have a limited solubility in Fe$_3$Al, and the increase in T^{D03-B2} saturates at a 1% concentration [43] (as seen from Fig. I-9). In contrast, the Cr, Hf and the Zr additions have been reported to have no significant effect on T_0 [43], except for a slight increase in T_0 reported by Mendiratta and Lipsitt [45]. It is worthwhile mentioning here that an increase in the D0$_3$-B2 transformation temperature T_0 can lead to an improvement in the high-temperature strength of Fe$_3$Al-based alloys [2, 46]. Nishino et al. [42] have indeed demonstrated that a peak in hardness extends to higher temperatures in parallel with the increase in T_0 for M= Ti, V and Mo. At present, there is no clear understanding of why these solutes have their characteristic effects on the transformation temperature. The effect of solute atom on T_0 D0$_3$-B$_2$ is expected to be related to its c istallographic site preference in the D0$_3$ structure.

III.4.1. Site preference

Fe$_3$Al crystallizes in a D0$_3$-type structure shown in Fig. I-10. In this structure, there are two inequivalent Fe sites with specific neighbor configurations, which are named FeI and FeII sites. The former has eight Fe nearest neighbors in an octahedral configuration, and the latter has four Fe and four Al nearest neighbors in a tetrahedral configuration. It is known in Fe$_3$Si, which is isomorphous with Fe$_3$Al, that transition-metal impurities occupy the FeI or the FeII site

selectively [47]. The elements to the left of Fe in the periodic table, i.e. Ti, V, Cr and Mn, substitute for the FeI site, while those to the right, i.e. Ni and Co, substitute for the FeII site. Such a selective site substitution has also been found for Fe_3Ga based alloys [48, 49], where the $D0_3$ phase is always stabilized although Fe_3Ga forms an $L1_2$ phase, unlike Fe_3Si and Fe_3Al, in the low-temperature equilibrium state.
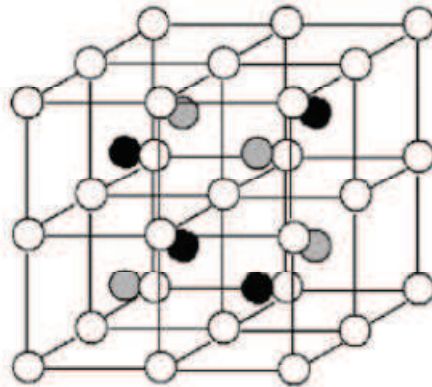
Figure.I- 10 The unit cell of $D0_3$ ordered Fe_3Al.

The site preference of transition elements in Fe_3Al may to follow that of Fe_3Si and Fe_3Ga, as supported by the band calculations [50]. Nevertheless, the site preference data on Fe_3Al are still incomplete. While Ti, Mo [44, 43, 51] and probably Mn [51] occupy the FeI site, Mossbauer experiments for the substitution of V [52] and Cr [53] provided tentative exceptions to the above trend. Other results of Mossbauer experiments have reported that Cr occupies preferentially the FeI site and also enters the Al site [54]. More recently, Reddy et al. [20], by using the ab initio calculations found, that the Cr can occupy the FeI and FeII sites with nearly equal energies. However, the authors [20] confirmed that the Cr couple anti-ferromagnticaly with Fe atoms and prefer to occupy the FeI site. The results of Reedy et al. [20] also show that the V occupies the FeI site (see Fig. I-11). Comparatively, the Co and Ni, though the difference is small between the FeI and FeII occupation, it has been found that these two impurities prefer the FeII site [20]. Furthermore, X-ray analysis [41] and ab initio calculations [55] have indeed demonstrated the FeI site selection of V atoms. The situation is less clear concerning an element such as Zr for which there is no data on site preference in $D0_3$-Fe_3Al.
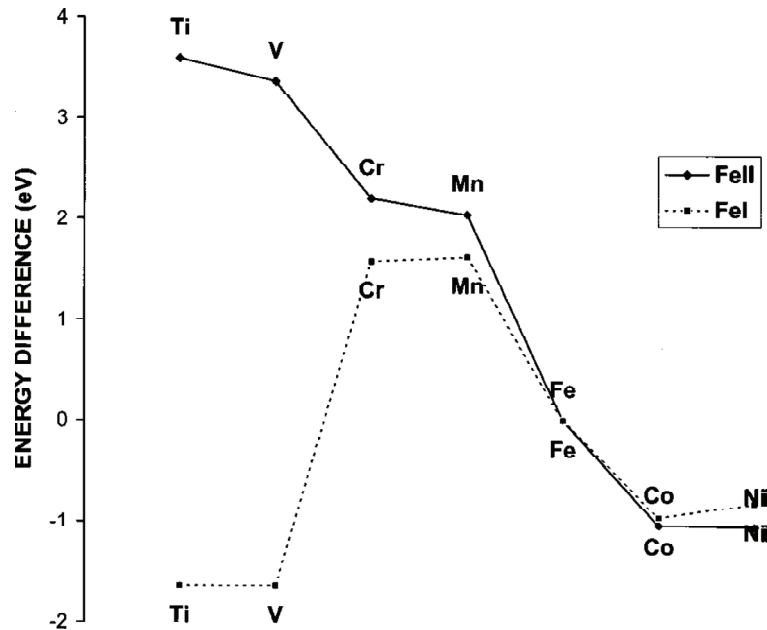
Figure.I- 11 The energy gain/loss when the FeI /FeII sites are replaced by various 3*d* transition-metal atoms. The negative energies correspond to the gain in energy while the positive energy corresponds to a lowering of the overall binding energy with respect to pure clusters [20].

After all, we believe that the site preference plays an important role in stabilizing the $D0_3$ phase of Fe_3Al-based alloys. Therefore, it is of the utmost interest to determine the site preference and ab-initio calculations coupled with temperature effect analysis are a good tool for this.

III.4.2. Solute effects on $D0_3$ ordering

Although pseudopotential calculations [56] predicted some of the solute effects on the transformation temperature T_0, further questions should be addressed as to why certain transition elements cause their own characteristic increases in T_0. Fortnum and Mikkola [44] suggested that the difference between solutes in raising T_0 is most probably caused by the difference between their electronic structures and/or atomic sizes. Anthony and Fultz [43] have shown that the solute effect on T_0 is related to the difference between the metallic radii of a solute atom and an Al atom: the closer the metallic radius of a ternary solute to that of Al, the greater its effectiveness in raising T_0, as shown in Fig. I-12. A qualitative support for this atomic size argument is provided by their lattice parameter results: additions of Mo, W and Ta are effective both in raising T_0 as well as in increasing the lattice parameter.
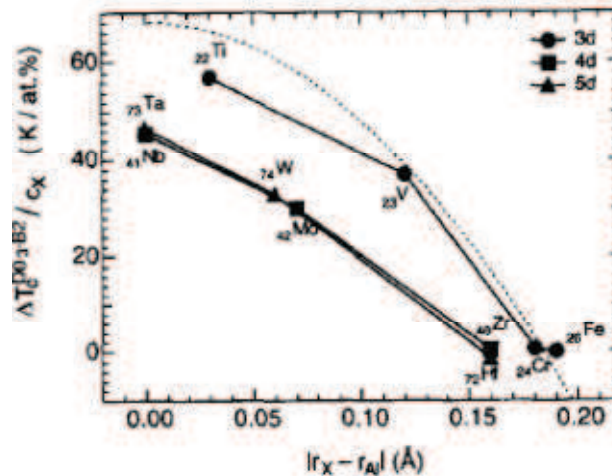
Figure.I- 12 The showing the relationship between the efficiency of a ternary additive in raising $\Delta T_0^{D0_3-B_2}$, and the absolute value of the difference in metallic radii between that ternary element and Al [43].

However, the atomic size effect inevitably assumes the FeI site occupation of any solute atom, regardless of the site preference rule, and is also in conflict with the lattice contraction for M=V, as shown in Fig. I-13. In this respect, the atomic size mismatch may not be a major factor controlling the phase stability. The large increase in T_0 is rather related to an increase in the ordering energy of the $D0_3$ superlattice caused by the site preference as demonstrated by Fortnum and Mikkola [44]
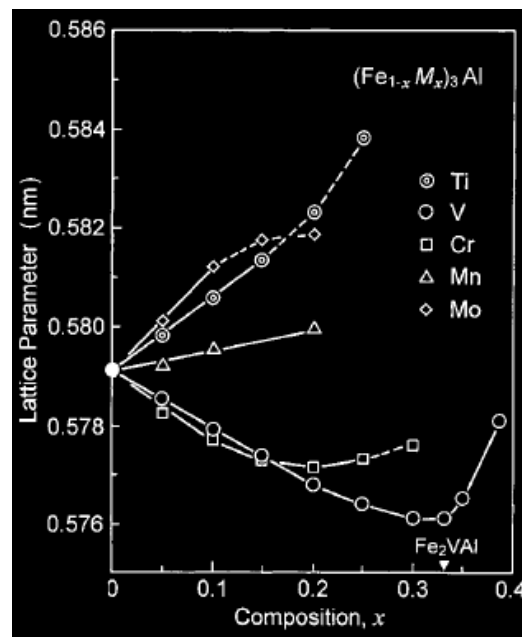
Figure.I- 13 Lattice parameters of the $D0_3$ phase in $(Fe_{1-x}M_x)_3Al$ as a function of composition x for M= Ti, V, Cr, Mn and Mo. The $D0_3$ single-phase state is obtained in the range shown by the solid lines [41].

Taking the site preference into consideration, an attention is directed to the variation of electron concentration, as proposed by Nishino et al. [41, 49]. Fig. I-14 shows the $D0_3$-B_2 transformation temperatures T_0 in $(Fe_{1-x}M_x)_3Al$ with M=Ti, V, Cr, Mn and Mo as a function of the average electron concentration e/a. The $D0_3$-B_2 transformation temperature always increases at the values of e/a lower than 6.75 for Fe_3Al since, the Fe atoms are substituted by the transition elements with less than half-filled *d states*. As mentioned in Section III-4.2, the increasing rate of T_0 for the addition of Mo is lower than that of V. In contrast, as shown in Fig. I-14, the curve of the Mo addition almost coincides with that of the V addition in the range of the $D0_3$ single-phase state when plotted as a function of *e/a*. The electron concentration effect further demonstrates that the curves for *M=* V and Mo are rather close to that for *M=* Ti, despite the sharpest increase in T_0 for the Ti addition. Consequently, the variation of the electron concentration plays a dominant role in determining the values of T_0. The situation is less clear for *M=* Cr, since the site preference of Cr is not as clear as in *M=* Ti, V and Mo. Finally, it was also suggested that the electron concentration effect could predict the increase in T_0 even for the additions of two or more kinds of transition elements, if these complex alloys have a $D0_3$ single phase structure.
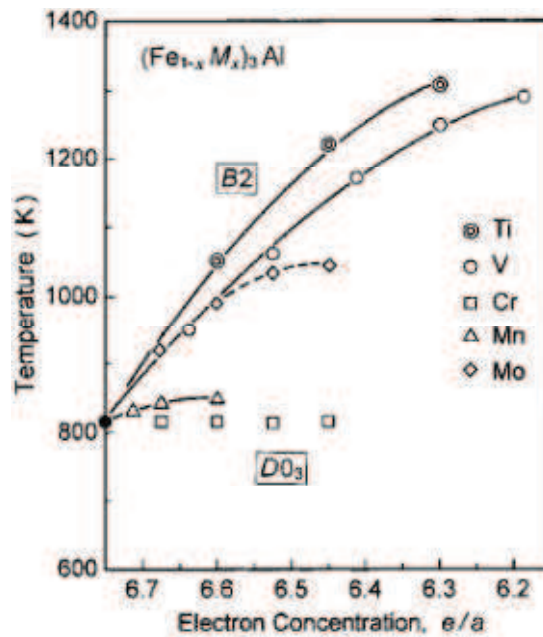
Figure.I- 14 $D0_3$-B2 transformation temperatures in $(Fe_{1-x}M_x)_3Al$ as a function of average electron concentration (e/a) for M=Ti, V, Cr, Mn and Mo [49].

The results of Reddy et al. [20] suggest that it is the sign of magnetic coupling that determines the preferential location of the impurity atoms. Impurities to the left of Fe couple antiferromagnetically to Fe and prefer FeI sites while the impurities to the right (Co and Ni) couple ferromagnetically and prefer FeII sites. For the case of Cr, whereas the small difference

between energies when substituted in FeI/FeII sites, it is found to couple antiferromagnetically to Fe and ocuppy the FeI site (Table. I-1). However, these calculations have been carried out at 0 Kelvin, and the nature of coupling changes with increasing the temperature has not been investigated.

Table.I- 1 The bond length (BL), binding energy (BE), and the nature of coupling in various 21immers. The corresponding bond lengths in the relaxed 35-atom clusters are also given [20].

System	Dimer			Relaxed Cluster
	BL (a.u.)	BE (eV)	coupling	BL (a.u.)
TiAl	4.80	1.94	FM	4.73
TiFe	3.23	4.22	AFM	4.36
CrAl	5.07	1.33	AFM	4.55
CrFe	4.41	1.38	AFM	4.20
NiAl	4.19	2.75	AFM	4.38
NiFe	3.91	2.79	FM	4.30

III. 5 Objective of our work for bulk analysis

The above analysis of the effect of the transition metals in raising the temperature of transition $D0_3 \rightarrow B_2$ (T_c) and consequently the strength of the Fe_3Al intermetallic shows that the increases in T_c is related to the increases in the ordering of the $D0_3$ superlattice caused by specific site substitutions by the solutes. The most effective solutes in raising T_c, (Ti , V and Mo) have been found to occupy the FeI site in the $D0_3$ structure. The situation is different and in contradictions for Cr additions. Whereas for the case of Zr, there is no experimental data about it site preference in the $D0_3$ Fe_3Al. Additionally, the majority of the calculations for the intermetallic compounds are performed at zero tempreture. The effect of temperature rarely used because of the time consuming calculations.

In this framework, the purpose of the present work is to compare the behviours of Ti and Zr in the bulk of Fe_3Al. In particular we aim at determining:

- ✓ The temperature dependence of the site preference of Ti and Zr.
- ✓ The effect of temperature on the stability of the $D0_3$ phase of the pure as well as Ti and Zr doped Fe_3Al.
- ✓ The effect of temperature on the structural properties of the pure Fe_3Al as well as the Ti and Zr doped compounds.

IV. Effect of alloying elements on ductility

IV. 1 Boron addition and grain boundary strength

In the case of many intermetallic alloys, small boron additions modify their ambient temperature properties. In fact, these alloys, which present an intrinsic intergranular brittleness in their 'pure' state, change their fracture mode, when boron-doped. In some cases – like in the B-doped Ni_3Al alloys – the fracture becomes ductile. In other cases, like in FeAl-B2 alloys, even in the B-doped alloys a brittle fracture is observed, it takes place cleavage in a transgranular manner. If the first (intergranular) type of room temperature brittleness of intermetallic alloys is commonly considered as an *intrinsic* one, the second one (transgranular) seems in fact to be due to an *extrinsic* embrittling action of atomic hydrogen, created during the oxidation reaction on the sample surface.

$$2Al+3H_2O \rightarrow Al_2O_3+6H \qquad \text{(Eq. I-1)}$$

This phenomenon, first identified by Liu et al. [60], is known as the 'environmental effect'.

The boron effect in intermetallic alloys is typically attributed to its intergranular segregation. This hypothesis is a simple conclusion of experimental measurements of some intergranular boron enrichment, mainly in Ni_3Al alloys, by the Auger Electrons Spectrometry (AES) method [61, 62]. This hypothesis was confirmed by the experimental results of Fraczkiewicz et al. [63].
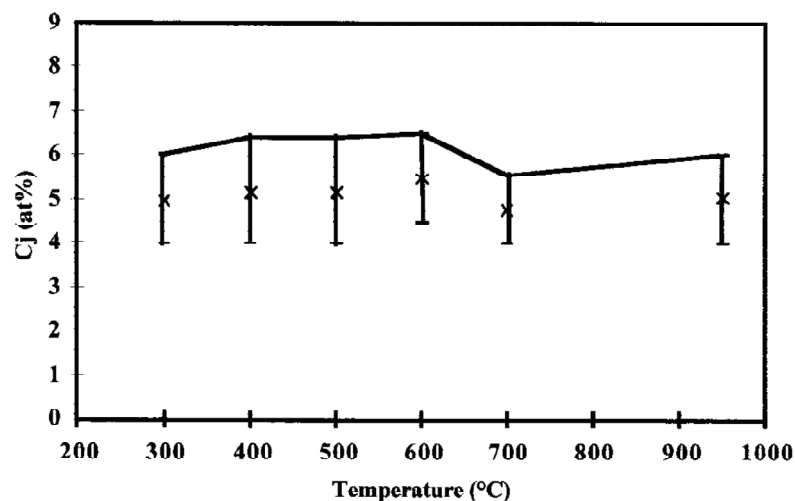

Figure.I- 15 Effect of temperature on the intergranular concentration of boron. Fe-45Al+400 appm B alloy; annealing during 24 h [63].

The authors [63] have used AES to measure the concentration dependence of boron segregation at grain boundaries of polycrystalline Fe-40 at.% Al base intermetallics. In a series of alloys

containing different (80–2000 at. ppm) contents of boron, a maximum grain boundary concentration of about 13 at.% boron was measured for the bulk concentrations above 800 at. ppm boron, i.e. close to its solid solubility limit under these conditions. The Fowler approach [64] was used to fit the experimental results providing them with the values of the Gibbs free energy of segregation, $\Delta G_B^0=-41$ kJ/mol, and the Fowler interaction parameter $zw=+96$ kJ/mol [63]. The numerical values of thermodynamic parameters describing this system were corrected later by the same authors [65]. In fact, a strong non-equilibrium segregation was still present in the studied materials under the applied conditions of the heat treatment. After a prolonged annealing, however, all boron remaining at the grain boundaries can be considered to be in segregation equilibrium. The true equilibrium grain boundary fractions of boron, $^E X_B^{GB}$, are shown in Table. I-2. Based on this correction, the values of ΔG_B^0 ranging from -30 to -34 kJ/mol, and zw ranging from $+220$ to 320 kJ/mol were obtained. More recently, by means of ab initio pseudopotential calculations [66], the comparison between the formation energies of boron insertions in the bulk and at a $\sum 5$ grain boundary shows that the boron atoms prefer to segregate at the grain boundary of the FeAl intemetallic compound.

Table.I- 2 Measured dependence of grain boundary atomic fraction of boron, $^M X_B^{GB}$, in polycrystalline Fe–40 at.% Al alloy at 673 K on bulk boron concentration, c_B [63] and corresponding equilibrium values of grain boundary atomic fraction, $^E X_B^{GB}$ [65].

c_B (at.ppm)	$^M X_B^{GB}$	$^E X_B^{GB}$	$^F X_B^{GB}$	$^{(3)} X_B^{GB}$	$^{(2)} X_B^{GB}$	$^{(1)} X_B^{GB}$	$^{(1)} X_B^{GB,opt}$
80	0.05	0.018	0.018	0.011	0.013	0.020	0.017
200	0.08	0.028	0.028	0.025	0.026	0.031	0.030
400	0.11	0.040	0.038	0.043	0.041	0.037	0.039
800	0.12	0.047	0.049	0.065	0.057	(0.041)	0.047
2000	0.13	0.051					
ΔG_B^0(673K) (kJ/mol)			-34	-39 ± 2.1	-43 ± 1.6	-51 ± 1.9	-48 ± 0.4
zw (kJ/mol)	$+228$						
X^*_{tot}				0.139	0.093	0.046	0.058

IV. 2. Transition metal additions

The room temperature ductility of Fe_3Al can also be significantly improved with Cr alloying [13, 14] together with increasing the Al-content from the stochiometric 25 towards 28 at.% [65, 66]. A small addition of Zr (up to about 1 at.%) are also beneficial for the ductility by increasing the grain boundary strength and by trapping of hydrogen by zirconium rich precipitates [67]. Furthermore, the results of a combined experimental and finite element modeling simulations of intergranular fracture indicates that the 0.5% of Zr to the ternary Fe-28%Al-5%Cr alloy increases the intrinsic fracture resistance at room temperature [68].

Stein et al. have measured the flexural fracture strains of as-cast samples as a function of temperature in four-point bending tests, in order to test their Britle-Ductile Temperature Transition BDTT. The results show that the BDT temperatures of the ternary alloys strongly increase with increasing volume fraction of second phase τ1. The effect of the Al content on the BDT of the investigated ternary Fe–Al–Zr alloys is qualitatively very similar to that of binary Fe–Al alloys even in the presence of 50 vol% of second phase τ1. At Al contents below 40at.% there is only a very weak dependence of the temperature range of the BDT on Al content, whereas the alloy series with 40at.% Al shows a strong increase of the BDT temperatures.
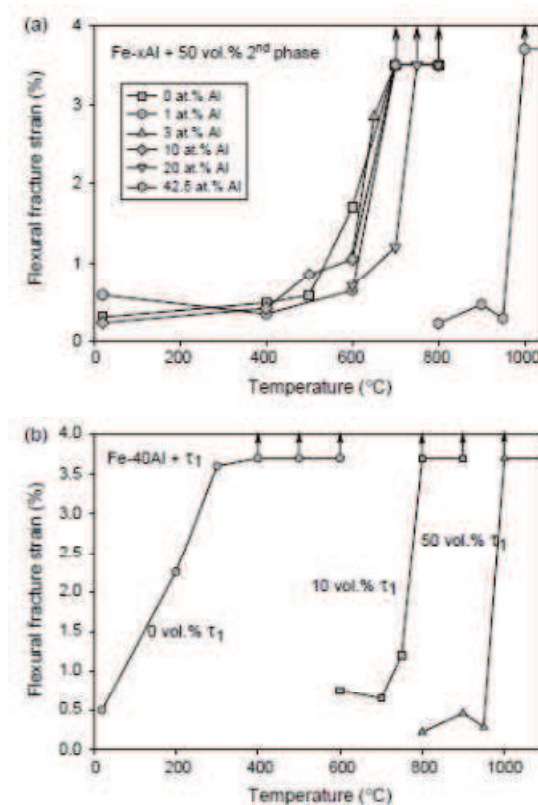
Figure.I- 16 Flexural fracture strains as a function of temperature for two series of Fe–Al–Zr alloys (a) with varying Al content in Fe–Al+50 vol% Laves phase alloys and (b) with varying volume fraction of the second phase in Fe–40AlCx vol% t1 phase (the arrows indicate fracture strains above 3%).

IV. 3 Modelling approach and objectives of our G.B. simulations

After all, we believe that the grain boundaries are the key parameters determining the macroscopic mechanical properties of iron aluminides, and must therefore be characterized as regards of their intrinsic structural properties or the influence of the alloying elements.

To this purpose, experimental techniques _High-Resolution Transmission Electron Microscopy (HRTEM) and Auger Electron Spectroscopy, among others_ are particularly well adapted to

yield structural information. However, Fe-Al samples (high-purity bicrystals prepared in well-controlled conditions, for instance), because of their extreme sensitivity to impurities, are very difficult to obtain and manipulate, which certainly contributes to limit experiments. In complementary manner, atomic-scale simulations can offer a valuable way of investigating both the structure and thermodynamics of model interfaces. This must yield matter for comparison with available or future experimental results and/or provide with new insights for understanding of the related mechanisms.

In performing atomic-scale simulations, special care has to be taken of the choice of the potential-energy model. *Ab initio* methods provide the reputedly most accurate state-of-the-art potentials but require a high computational power compared to other semi-emperical (e.g. tight-binding) or empirical (e.g., embedded atom method, EAM) models. In spite of the continuous enhancement of the available computer power, the high computational cost of the *ab initio* calculations limits the size of tractable systems to about 50 transition-metal atoms, hindering comprehensive grain boundary studies that have to include point defect thermodynamics, chemical and segregation effects, in addition to more common studies generally limited to a few specific grain boundary variants. In particular, in order to determine the ground state properties of a given grain boundary, the configurational atomic phase space that has to be investigated must include in-plane rigid-body translations (RBT's) and local composition that can be different from the bulk one (if segregation occurs). Owing to the difficulty of this task, there is no example of *ab initio* study embracing the full problem, including both the chemical and translational degrees of freedom, a deficiency that still makes relevant the use of the empirical potentials.

Although alloy interfacial segregation is a well-known phenomenon, deeper insight into it was recently gained from the ab initio, explaining in particular the effect the grain boundary segregation of boron and sulphur on grain boundary cohesion [69] and co-segregation of boron, titanium and oxygen at the grain boundaries of α-iron [70]. Segregated gallium was found to draw charge from the surrounding aluminium atoms, thus, to reduce the cohesion of aluminium [71]. On the basis of the local density functional equations, several phenomena were also determined: the structure and electronic properties of boron and sulphur at the coherent twin boundary in ferritic iron [72], the embrittlement of the same boundary induced by phosphorus segregation [73], hydrogen segregation [74] or the effect of boron [75] on the cohesion of iron. The first-principles quantum mechanical calculations showed that large bismuth atoms weaken the interatomic bonding by pushing apart the copper atoms at the interface [76]

The density-functional theory was further applied to study the geometric and magnetic structures of fully relaxed symmetrical tilt {013} grain boundary in iron and {012} grain boundary in nickel. In both cases, enhancements of the local magnetic moments of the atoms in the grain boundary plane were found. Calculated values of the segregation enthalpy of silicon and tin at these grain boundaries were in good agreement with experiment [77].

Concerning more specifically the atomic simulation of the grain boundary segregation in intermetallics, except for some studies by Besson et al. [79] and Raulot et al. [64], they were done Ni-Al. Concerning the modeling works carried out on Fe-Al based alloys, the majority of these calculations were always carried out without taking into account the vibrational effect related to the effect of temperature.

In this context the goals of the present modeling work on the $\sum 5$ (310)[001] in $D0_3$-Fe_3Al are done to determine:

- ✓ The site preference of the two transition metals (Ti and Zr) between different configurations on the grain boundary interface.
- ✓ The effect of the transition metals on the stability of the grain boundary.
- ✓ The effect of the relaxation on the structural deformations of the grain boundary interface.
- ✓ The effect of temperature on structural relaxation of the grain boundary.
- ✓ The temperature dependence of the site preference of the two transition metals Ti and Zr.

References

[1] N. S. Stoloff and R. Cl. Davies, Prog. Mater. Sci. **13**, 1 (1966).

[2] J. H. Westbrook (Ed.), Intermetallic Compounds. John Wiley and Sons, Inc., New York (1967).

[3] S. M. Kopley and B. H. Kear, Trans. Metall. Sot. **239**, 977 (1967).

[4] P. H. Thornton, R. G. Davies and T. L. Johnston, Metall. Trans. **1**, 207 (1970).

[5] S. C. Deevi and V. K. Sikka, lntermetallics **5**, 17 (1997).

[6] C.G. McKamey, J.H. De Van, P.F. Tortorelli and V.K. Sikka, J Mater Res **6**, 1779 (1991).

[7] N.S. Stoloff, Mater Sci Eng A **258**, 1 (1998).

[8] O. Kubaschewski. Iron—binary phase diagrams. Berlin: Springer; 1982. p. 5.

[9] T.B. Massalski. Binary alloy phase diagrams. 2nd edition. Materials Park:ASM, 1990.

[10] W. Koster and T. Godecke, Z Metallk **71**, 765 (1980).

[11] C. G McKamey, J. H DeVan, P. F. Tortorelli, & V. K. Sikka, J. Muter. Res. **6 (8)**, 1779 (1991).

[12] M. Palm. J Alloys Comd **252**, 192 (1997).

[13] C. G. McKamey, J. A. Horton and C. T. Liu, Ser. Metall. **22**, 1679 (1988).

[14] D.G Morris, M.M Dadras and M.A. Morris **41**, 97 (1993).

[15] C G. McKamey, J.A. Horton and C.T. Liu. J Mater Res **4**, 1156 (1989).

[16] F. Stein, A. Schneider, G. Frommeyer . Unpublished data presented at: Discussion meeting on the development of innovative aluminium alloys. Dusseldorf; 9.3.2004.

[17] M. Eumann, M. Palm, G. Sauthoff. Intermetallics **12**, 625 (2004).

[18] D.Satuła, L. Dobrzyński, J. Waliszewski, K. Szymańsk, K. Rećk, A. Malinowski, Th. Brückel, O. Schärpf , K. Blinowski, J of Magn. and Magn. Mater **169**, 240 (1997).

[19] A. Go, M. Pugaczowa-Michalska, L. Dobrzynski, Physica status solidi. B. **243** 1241 (2006).

[20] B.V. Reddy, D.H. Satry, S.C. Deevi, S.N. Khanna, Physical Review B **64** (2001) 224419.

[21] F. Stein, G. Sauthoff, M. Palm. Z. Metallkde **96**, 469 (2004).

[22] S. Voß, F. Stein, M. Palm and D. Raabe, Mater. Science and Engineering: A **527** 7848 (2010).

[23] O. Prymak, F. Stein, intermetallics **18** 1322 (2010).

[24] S. Voß, F. Stein, M. Palm, D. Raabe , F. Liot, M. Friák, T. Hickel, J. Neugebauer, Fe-based Laves Phase Precipitates in High-Temperature Steels, http://www.mpie.de/index.php?id=3457

[25] M. Palm, G. Inden. Intermetallics **3**, 443 (1995).

[26] J. Herrmann, G. Inden, G. Sauthoff. Steel Res Int **75**, 343 (2004).

[27] A. Schneider, L. Falat, G. Sauthoff, G. Frommeyer. Intermetallics **13**, 1286 (2005).

[28] V.A. Andryushchenko, V.G. Gavrilyuk, V.M. Nadutov, The Physics of Metals and Metallography **60**, 50 (1985).

[29] M. Palm, G. Inden, Intermetallics **3**, 443 (1995).

[30] J. Yang, P. Laa, W. Liu, Y. Hao, Materials Science and Engineering A **8**, 382 (2004).

[31] F.R. Morral, Journal of the Iron and Steel Institute **130**, 419 (1934).

[32] L. Meyer, H-E Bühler. Aluminium **43**, 733 (1967).

[33] G.S. Krivonogov, M.F. Alekseyenko, G.G. Solovyeva, The Physics of Metals and Metallography **39** 86 (1976).

[34] S. F. H. Parker, P. J. Grundy, G. A. Jones, I. Briggs, A. G. Clegg. Journal of Materials Science **23** 217 (1988).

[35] H. Ohtani, M. Yamano, M. Hasebe. ISIJ International **44** 1738 (2004).

[36] P. Maugis, J. Lacaze , R. Besson, J. Morillo, Metallurgical and Materials Transactions A **37** 3397 (2006).

[37] D. Connétable, P. Maugis. Intermetallics **16** 345 (2008).

[38] S.M. Hao, T. Takayama, K. Ishida, T. Nishizawa. Metall Trans A **15**, 1819 (1984).

[39] I. Jung, G. Sauthoff. Z Metallkde **80**, 484 (1989).

[40] C. Stallybrass, A. Schneider, G. Sauthoff. Intermetallics **13**, 1286 (2005).

[41] Y. Nishino, C. Kumada, S. Asano, Scr. Mater. **36**, 461 (1997).

[42] Y. Nishino, S. Asano, T. Ogawa, Mater. Sci. Eng. **A234-236**, 271 (1997).

[43] L. Anthony, B. Fultz, Acta Metall. Mater. **43**, 3885 (1995).

[44] R.T. Fortnum, D.E. Mikkola, Mater. Sci. Eng. **91**, 223 (1987).

[45] M.G. Mendiratta, H.A. Lipsitt, in: C.C. Koch, C.T. Liu, N.S. Stoloff (Eds.), High-Temperature Ordered Intermetallic Alloys, Mater. Res. Soc. Symp. Proc. Vol. 39, MRS, Pittsburgh, 1985, p. 155.

[46] R.S. Diehm, D.E. Mikkola, in: N.S. Stoloff, C.C. Koch, C.T. Liu, O. Izumi (Eds), High-Temperature Ordered Intermetallic Alloys II, Mater. Res. Soc. Symp. Proc. Vol. 81, MRS, Pittsburgh, 1987, p. 329.

[47] V.A. Niculescu, T.J. Burch, J.I. Budnick, J. Magn. & Magn. Mater. **39**, 223 (1983).

[48] N. Kawamiya, K. Adachi, J. Magn. & Magn. Mater. **145** 31 (1983).

[49] Y. Nishino, M. Matsuo, S. Asano, N. Kawamiya, Scr. Metall. Mater. **25**, 2291 (1991).

[50] S. Ishida, J. Ishida, S. Asano, J. Yamashita, J. Phys. Soc. Jpn. **41**, 1570 (1976).

[51] G. Athanassiadis, G. Le Caer, J. Foct, L. Rimlinger, Phys. Stat. Sol. (a) **40**, 425 (1977).

[52] E. Popiel, M. Tuszyński, W. Zarek, T. Rendecki, J. Less-Common Metals **146**, 127 (1989).

[53] N. Lakshmi, K. Venugopalan, J. Varma, Phys. Rev. B **47**, 14054 (1993).

[54] D. Satula, L. Dobrzyński, J. Waliszewski, et al., J. Magn. & Magn. Mater. **169**, 240 (1997).

[55] M. Friák, J. Deges, R. Krein, G. Frommeyer and J. Neugebauer, Intermetallics 18, 1310 (2010).

[56] A.O. Mekhrabov, A. Ressamoğlu, T. Őztőrk, J. Alloys Compd. **205**, 147 (1994).

[57] Y. Nishino. Mater science and engineering **A258**, 50 (1998).

[58]. C.T. Liu, E.H. Lee and C.G. McKamey, Scr. Metall **23**, 875 (1989).

[59] A. Choudhury, C.L. White and C.R. Brooks, Acta Metall **33**, 213 (1985).

[60] T.H. Chuang, Mater. Sci. Eng **A141**, 169 (1991).

[61] A. Fraczkiewicz, A-S Gay and M. Biscondi. Materials Science and Engineering: **A 258**, 108 (1998).

[62] E.D. Hondros, M.P. Seah, S. Hofmann, P. Lejček . In: R.W. Cahn, P. Haasen, editors. Physical metallurgy, 4th ed. Amsterdam: North-Holland; 1996. p. 1201

[63] A.S. Gay, A. Fraczkiewicz and M. Biscondi, J. Phys. **IV9** 75 (1999).

[64] J.M. Raulot, A. Fraczkiewicz, T. Cordonnier, H. Aourag and T. Grosdidier, Journal of Materials Science **43**, 3867 (2008).

[65] C.G. Mckamey In: Stoloff NS, Sikka VK, editors. Physical metallurgy and processing of intermetallic compounds, New York: Chapman and Hall; 1996. p. 351.

[66] C.G. Mckamey, J.A.Horton, C.T. Liu, Mater Res Soc Symp Proc **81**, 321 (1986).

[67] D.A. Alven, N.S. Stoloff, Materials Science and Engineering **A239-240**, 362 (1997).

[68] B.S.J. Kang and R. Cisloiu, Theoritical and Applied Fracture Mechanics **45**, 25 (2006).

[69] G.S. Painter, F.W. Averill, Phys. Rev. Lett. **58**, 234 (1987).

[70] S.P. Chen, A.F. Voter, R.C. Albers, D.J. Srolovitz, Scripta Metall. **20**, 1389 (1986).

[71] Y. Zhang, G.H. Lu, T. Wang, S. Deng, M. Kohyama, R. Yamamoto, Mater. Trans. **47**, 2678 (2006).

[72] S. Tang, A.J. Freeman, G.B. Olson, Phys. Rev. B **50**, 1 (1994).

[73] R. Wu, A.J. Freeman, G.B. Olson, Phys. Rev. B **50**, 75 (1994).

[74] L. Zhong, R. Wu, A.J. Freeman, G.B. Olson, Phys. Rev. B **62**, 13938 (2000).

[75] R. Wu, A.J. Freeman, G.B. Olson, Science **265**, 376 (1994).

[76] R. Schweinfest, A.T. Paxton, M.W. Finnis, Nature **432**, 1008 (2004).

[77] M. Cak, M. Sob, J. Hafner, Phys. Rev. B **78**, 054418 (2008).

[78] A. Kellou, J-M. Raulot, T. Grosdidier, Intermetallics **18**, 1293 (2010).

[79] R. Besson, A. Legris and J. Morillo, Phys. Rev. B **64**, 174105 (2001).

Chapter II

Theoretical tools

In this Chapter we review the theoretical models that were used in our simulations. Two major theories will be described, the Ab Initio Molecular Dynamics and the Density Functional Theory. In the first part, the focus is on the temporal evolution of a molecular system. In particular, the methods considering the nuclei as classical particles are described. However, the goal is not to list in an exhaustive manner the different methods of molecular dynamics but to clarify the context within which the ab initio molecular dynamics takes place. In the second part, the Density Functional Theory 'DFT' used in the context of our simulations is described. Finally we detail the computational techniques that were used to carry out our pseudopotential calculations through the VASP (Vienna Ab initio Simulation Package) code.

Part A: Ab Initio Molecular Dynamics

I.1. Introduction

Modern theoretical methodology, aided by the advent of high speed and massively parallel computing, has advanced to a level that the microscopic details of chemical processes in condensed phases can now be treated on a relatively routine basis. One of the most commonly used theoretical approaches for such studies is the Molecular Dynamics (MD) method, in which the classical Newtonian equations of motion for a system are solved numerically starting from a specified initial state and subject to a set of boundary conditions appropriate to the problem. MD methodology allows both equilibrium thermodynamic and dynamical properties of a system at finite temperature to be computed. The quality of a MD calculation rests largely on the method by which the forces are specified. In many applications, these forces are computed from an empirical model or "force field", an approach that has enjoyed tremendous success in the treatment of systems ranging from simple liquids and solids to polymers and biological systems including proteins, membranes, and nucleic acids. Since most force fields do not include electronic polarization effects [1] and can treat chemical reactivity only through specialized techniques [2], it is often necessary to turn to the methodology of *ab initio* MD (AIMD).

AIMD is a rapidly evolving and growing technique that constitutes one of the most important theoretical tools developed in the last decades. In an AIMD calculation, finite-temperature dynamical trajectories are generated by using forces obtained directly from electronic structure calculations performed "on the fly" as the simulation proceeds. Thus, AIMD permits chemical bond breaking and forming events to occur and accounts for electronic polarization effects [3, 4]. AIMD has been successfully applied to a wide variety of important problems in physics and chemistry and is now beginning to influence biology as well. In numerous studies, new physical phenomena have been revealed and microscopic mechanisms elucidated that could not have been uncovered by using empirical methods, often leading to new interpretations of experimental data and even suggesting new experiments to be perform.
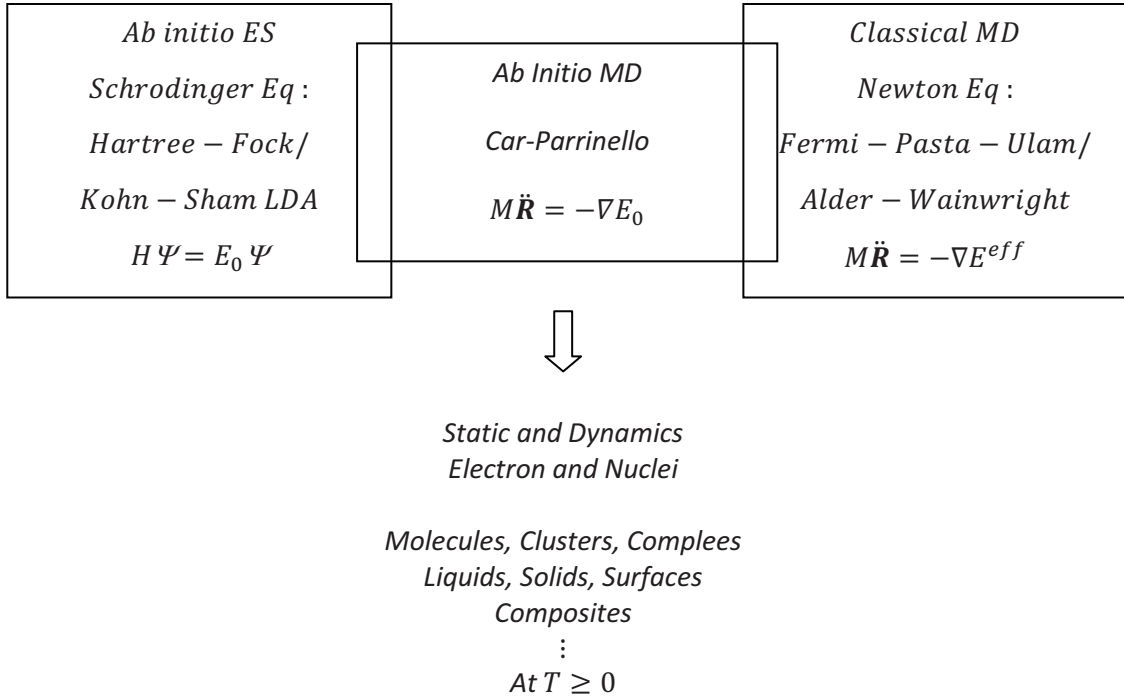
Ab initio ES		
Schrodinger Eq :	Ab Initio MD	Classical MD
Hartree − Fock/	Car-Parrinello	Newton Eq :
Kohn − Sham LDA	$M\ddot{\boldsymbol{R}} = -\nabla E_0$	Fermi − Pasta − Ulam/
$H\Psi = E_0\Psi$		Alder − Wainwright
		$M\ddot{\boldsymbol{R}} = -\nabla E^{eff}$

⇩

Static and Dynamics
Electron and Nuclei

Molecules, Clusters, Complees
Liquids, Solids, Surfaces
Composites
⋮
At $T \geq 0$

Figure. II- 1 Ab initio molecular dynamics unifies approximate ab initio electronic structure theory (i.e solving Schrodinger's wave equation numerically using, for instance, Hartree-Fock theory or the Local Density Approximation (LDA) within Kohn-Sham theory) and classical molecular dynamics (i.e solving Newton's equation of motion numerically for given interaction potential as reported by Fermi, Pasta, Ulam, and Tsingou for one-dimensional anharmonic chain model of solids and published by Alder and Wainwright for the three-dimensional hard-sphere model of fluids [5]).

I.2. Quantum Molecular Dynamic

I.2.1. Deriving Classical Molecular Dynamics

The starting point of the following discussion is non-relativistic quantum mechanics as formalized via the time-dependent Schrödinger equation

$$i\hbar\frac{\partial}{\partial t}\phi(\{\boldsymbol{r}_i\}, \{\boldsymbol{R}_I\}; t) = H\phi(\{\boldsymbol{r}_i\}, \{\boldsymbol{R}_I\}; t) \qquad \text{(Eq. A-1)}$$

in its position representation in conjunction with the standard Hamiltonian

$$H = -\sum_I \frac{\hbar^2}{2M_I}\nabla_I^2 - \sum_i \frac{\hbar^2}{2m_e}\nabla_i^2 + \sum_{i<j}\frac{e^2}{|\boldsymbol{r}_i - \boldsymbol{r}_j|} - \sum_{I,i}\frac{e^2}{|\boldsymbol{R}_I - \boldsymbol{r}_i|} + \sum_{I<J}\frac{e^2 Z_I Z_J}{|\boldsymbol{R}_I - \boldsymbol{R}_J|}$$

$$= -\sum_I \frac{\hbar^2}{2M_I}\nabla_I^2 - \sum_i \frac{\hbar^2}{2m_e}\nabla_i^2 + V_{n-e}(\{\boldsymbol{r}_i\}, \{\boldsymbol{R}_I\})$$

$$= -\sum_I \frac{\hbar^2}{2M_I}\nabla_I^2 + H_e(\{\boldsymbol{r}_i\}, \{\boldsymbol{R}_I\}) \qquad \text{(Eq. A-2)}$$

for the electronic $\{r_i\}$ and nuclear $\{R_I\}$ degrees of freedom.

The goal of this section is to derive classical molecular dynamics [7-8, 9] starting from Schrodinger's wave equation and following the elegant route of Tully [10, 11]. To this end, the nuclear and electronic contributions to the total wave function $\phi(\{r_i\}, \{R_I\}; t)$, which depends on both the nuclear and electronic coordinates, have to be separated. The simplest possible form is a product ansatz

$$\phi(\{r_i\}, \{R_I\}; t) \approx \psi(\{r_i\}; t)\chi(\{R_I\}; t)\, exp\left[\frac{i}{\hbar}\int_{t_0}^{t} dt' E_e(t')\right] \qquad \text{(Eq. A-3)}$$

Where the nuclear and electronic wave functions are separately normalized to unity at every instant of time, i.e $\langle \chi; t | \chi; t \rangle = 1$ and $\langle \psi; t | \psi; t \rangle = 1$, respectively. In addition, a convenient phase factor

$$E = \int dr dR\; \psi^*(\{r_i\}; t)\, \chi^*(\{R_I\}; t) H_e\, \psi(\{r_i\}; t)\chi(\{R_I\}; t) \qquad \text{(Eq. A-4)}$$

was introduced at this stage such that the final equations will look nice; $\int dr dR$ refers to the integration over all i=1,... and I=1,... variables $\{r_i\}$ and $\{R_I\}$, respectively. It is mentioned in passing that this approximation is called a one-determinant or single-configuration ansatz for the total wavefunction, which at the end must lead to a mean-field description of the coupled dynamics. Note also that this product ansatz (excluding the phase factor) differs from the Born-Oppenheimer ansatz [12, 13] for separating the fast and slow variables

$$\phi_{BO}(\{r_i\}, \{R_I\}; t) = \sum_{k=0}^{\infty} \widetilde{\psi}_k(\{r_i\}, \{R_I\})\widetilde{\chi}_k(\{R_I\}; t) \qquad \text{(Eq. A-5)}$$

even in its one-determinant limit, where only a single electronic state k (evaluated for the nuclear configuration$\{R_I\}$) in included in the expansion.

Inserting the separation ansatz Eq. (A-3) into Eqs. (A-1)-(A-2) yields (after multiplying from the left by $\langle \psi |$ and $\langle \chi |$ and imposing energy conservation $d\langle H \rangle / dt \equiv 0$) the following relations

$$i\hbar\frac{\partial \psi}{\partial t} = \sum_i \frac{\hbar^2}{2m_e}\nabla_i^2 + \{\int dR\chi^*(\{R_I\}; t)V_{n-e}(\{r_i\}, \{R_I\})\chi(\{R_I\}; t)\}\psi \qquad \text{(Eq. A-6)}$$

$$i\hbar\frac{\partial \chi}{\partial t} = -\sum_I \frac{\hbar^2}{2M_I}\nabla_I^2\, \chi + \{\int dr\psi^*(\{r_i\}; t)H_e(\{r_i\}, \{R_I\})\, \psi(\{r_i\}; t)\}\chi \qquad \text{(Eq. A-7)}$$

This set of coupled equations defines the basis of the Time-Dependent Self-Consistent Field (TDSCF) method introduced as early as 1930 by Dirac [14]. Both electrons and nuclei move quantum-mechanically in a time-dependent effective potential (or self-consistently obtained

average fields) obtained from appropriate averages (quantum mechanical equation values $\langle ... \rangle$) over other class of degree of freedom (by using the nuclear and electronic wavefunctions, respectively). Thus, the single-determinant ansatz Eq. (A-3) produces, as already anticipated, a mean-field description of the coupled nuclear-electronic quantum dynamics. This is the price to pay for the simplest possible separation of electronic and nuclear variables.

The next step in the derivation of classical molecular dynamics is the task to approximate the nuclei as classical point particles. How can this be achieved in the framework of the TDSCF approach, given one quantum-mechanical wave equation describing all nuclei. A well-known route to extract classical mechanics from quantum mechanics in general starts with rewriting the corresponding wavefunction

$$\chi(\{R_I\}; t) = A(\{R_I\}; t) \exp[iS(\{R_I\}; t)/\hbar] \tag{Eq. A-8}$$

In terms of an amplitude factor A and a phase S which are both considered to be real and A>0 in this polar representation [15]. After transforming the nuclear wave function in Eq. (A-7) accordingly and after separating the real and imaginary parts, the TDSCF equation for the nuclei

$$\frac{\partial S}{\partial t} + \sum_I \frac{1}{2M_I} (\nabla_I S)^2 + \int dr \ \psi^* H_e \psi = \hbar^2 \sum_I \frac{1}{2M_I} \frac{\nabla_I^2 A}{A} \tag{Eq. A-9}$$

$$\frac{\partial A}{\partial t} + \sum_I \frac{1}{M_I} (\nabla_I A)(\nabla_I S) + \sum_I \frac{1}{2M_I} A(\nabla_I S)^2 = 0 \tag{Eq. A-10}$$

is (exactly) re-expressed in terms of the new variables A and S. This so-called "quantum fluid dynamical representation" Eqs. (A-9),(A-10) can actually be used to solve the time-dependent Schrodinger equation [16]. The relation for A, Eq. (A-10), can be rewritten as continuity equation [15] with the help of identification of the nuclear density $|\chi|^2 \equiv A^2$ as directly obtained from the definition Eq. (A-8). This continuity equation is independent of $\hbar$ and ensures locally the conservation of the particle probability $|\chi|^2$ associated to the nuclei in the presence of a flux.

More important for the present purpose is a more detailed discussion of the relation for S, Eq. (A-9). This equation contains one term that depends on $\hbar$, a contribution that vanishes if the classical limit

$$\frac{\partial S}{\partial t} + \sum_I \frac{1}{2M_I} (\nabla_I S)^2 + \int dr \ \psi^* H_e \psi = 0 \tag{Eq. A-11}$$

Is taken as $\hbar \rightarrow 0$; an expansion in terms of $\hbar$ would lead to a hierarchy of semi-classical methods. The resulting equation is now isomorphic to equations of motion in the Hamilton-Jacobi formulation [17]

$$\frac{\partial S}{\partial t} + H(\{\boldsymbol{R}_I\}, \{\nabla_I S\}) = 0 \tag{Eq. A-12}$$

of classical mechanics with the classical Hamilton function

$$H(\{\boldsymbol{R}_I\}, \{\boldsymbol{P}_I\}) = T(\{\boldsymbol{P}_I\}) + V(\{\boldsymbol{R}_I\}) \tag{Eq. A-13}$$

Defined in terms of (generalized) coordinates $\{\boldsymbol{R}_I\}$ and their conjugate momenta $\{\boldsymbol{P}_I\}$. With the help of the connecting transformation

$$\boldsymbol{P}_I \equiv \nabla_I S \tag{Eq. A-14}$$

the Newtonian equation of motion $\dot{\boldsymbol{P}}_I = -\nabla_I V(\{\boldsymbol{R}_I\})$ corresponding to Eq. (A-11)

$$\frac{d\boldsymbol{P}_I}{dt} = -\nabla_I \int d\boldsymbol{r} \; \psi^* H_e \quad \text{or}$$

$$M_I \ddot{\boldsymbol{R}}_I(t) = -\nabla_I \int d\boldsymbol{r} \; \psi^* H_e \psi \tag{Eq. A-15}$$

$$= -\nabla_I V_e^E(\{\boldsymbol{R}_I(t)\}) \tag{Eq. A-16}$$

can be read off. Thus, the nuclei move according to classical mechanics in an effective potential V_e^E due to the electrons. This potential is a function of only the nuclear positions at time t as a result of averaging H_e over the electronic degrees of freedom, i.e. computing its quantum expectation value $\langle \psi | H_e | \psi \rangle$, while keeping the nuclear positions fixed at their instantaneous values $\{\boldsymbol{R}_I(t)\}$.

However, the nuclear wave function still occurs in the TDSCF equation for the electronic degrees of freedom and has to be replaced by the positions of the nuclei for consistency. In this case the classical reduction can be achieved simply by replacing the nuclear density $|\chi(\{\boldsymbol{R}_I\}; t)|^2$ in equation Eq. (A-6) in limit $\hbar \rightarrow 0$ by a product of delta functions $\Pi_I \delta(\boldsymbol{R}_I - \boldsymbol{R}/t$ centered at the instantaneous positions $\boldsymbol{R}/t$ of the classical nuclei as given by Eq. (A-15). This yields e.g. for the position operator

$$\int d\boldsymbol{R} \; \chi^*(\{\boldsymbol{R}_I\}; t) \boldsymbol{R}_I \chi(\{\boldsymbol{R}_I\}; t) \xrightarrow{\hbar \rightarrow 0} \boldsymbol{R}_I(t) \tag{Eq. A-17}$$

the required expectation value. This classical limit leads to a time-dependent wave equation for the electrons

$$i\hbar \frac{\partial \psi}{\partial t} = -\sum_i \frac{h^2}{2m_e} \nabla_i^2 \psi + V_{n-e}(\{r_i\}, \{R_I(t)\}) \psi$$

$$= H_e(\{r_i\}, \{R_I(t)\}) \psi(\{r_i\}, \{R_I\}; t) \qquad \text{(Eq. A-18)}$$

Which evolve self-consistently as the classical nuclei are propagated via Eq. (A-15). Note that now H_e and thus ψ depend parametrically on the classical nuclear position $\{R_I(t)\}$ at the time t through $V_{n-e}(\{r_i\}, \{R_I(t)\})$.

The approach relying on solving Eq. (A-15) together with Eq. (A-18) is sometimes called "Ehrenfest molecular dynamics" in honor of Ehrenfest who was the first to address the question of how Newtonian classical dynamics can be derived from Schrodinger's wave equation [18]. In the present case this leads to a hybrid or mixed approach because only the nuclei are forced to behave like classical particles, whereas the electrons are still treated as quantum objects.

I.2.2. « Ehrenfest » Molecular Dynamics

Although the TDSCF approach underlying Ehrenfest molecular dynamics clearly is a mean-field theory, transitions between electronic states are included in this scheme. This can be made evident by expanding the electronic wavefunction Ψ (as opposed to the total wave function ϕ according to Eq. (A-5)) in terms of many electronic states or determinants Ψ_k

$$\Psi(\{r_i\}, \{R_I\}; t) = \sum_{k=0}^{\infty} c_k(t) \Psi_k(\{r_i\}, \{R_I\}) \qquad \text{(Eq. A-19)}$$

with complex coefficients $\{c_k(t)\}$. In this case, the coefficients $\{|c_k(t)|^2\}$ (with $\sum_k |c_k(t)|^2 \equiv 1$) describe explicitly the time evolution of the populations (occupations) of the different states $\{k\}$ whereas interferences are included via the $\{c_k^* c_l \neq k\}$ contributions. One possible choice for the basis functions $\{\Psi_k\}$ is the adiabatic basis obtained from solving the time-independent electronic Schrodinger equation

$$H_e(\{r_i\}; \{R_I\} \Psi_k = E_k(\{R_I\}) \Psi_k(\{r_i\}; \{R_I\}) \qquad \text{(Eq. A-20)}$$

where $\{R_I\}$ are the instantaneous nuclear positions at time t according to Eq. (A-15).

Thereby, the *a priori* construction of any type of potential energy surface is avoided from the outset by solving the time-dependent electronic Schrodinger equation "on the fly". This allows

one to compute the force from $\nabla_I \langle H_e \rangle$ for each configuration $\{\boldsymbol{R}_I(t)\}$ generated by molecular dynamics. The corresponding equations of motion in terms of the adiabatic basis Eq. (A-20) and the time-dependent expansion coefficients Eq. (A-19)

$$M_I \ddot{\boldsymbol{R}}_I(t) = -\sum_k |c_k(t)|^2 \nabla_I E_k - \sum_{k,l} c_k^* c_l (E_k - E_l) d_I^{kl} \qquad \text{(Eq. A-21)}$$

$$i\hbar \dot{c}_k(t) = c_k(t) E_k - i\hbar \sum_{I,l} c_l(t) \dot{\boldsymbol{R}}_I d_I^{kl} \qquad \text{(Eq. A-22)}$$

Where the coupling terms are given by

$$d_l^{kl}(\{\boldsymbol{R}_I(t)\}) = \int d\boldsymbol{r} \; \Psi_k^* \nabla_I \Psi_I \qquad \text{(Eq. A-23)}$$

with the property $d_I^{kk} \equiv 0$. The Ehrenfest approach is thus seen to include rigorously non-adiabatic transitions between different electronic states Ψ_k and Ψ_l within the framework of classical nuclear motion and the mean-field (TDSCF) approximation to the electronic structure.

The restriction to one electronic state in the expansion Eq. (A-19), which is in most cases the ground state Ψ_0, leads to

$$M_I \ddot{\boldsymbol{R}}_I(t) = -\nabla_I \langle \Psi_0 | H_e | \Psi_0 \rangle \qquad \text{(Eq. A-24)}$$

$$i\hbar \frac{\partial \Psi_0}{\partial t} = H_e \Psi_0 \qquad \text{(Eq. A-25)}$$

note that H_e is time-dependent via the nuclear coordinates $\{\boldsymbol{R}_I(t)\}$. A point worth mentioning here is that the propagation of the wavefunction is unitary, i.e. the wavefunction preserves its norm and the set of orbitals used to build up the wavefunction will stay orthonormal.

Ehrenfest molecular dynamics is certainly the oldest approach to "on the fly" molecular dynamics and is typically used for collision- and scattering-type problems. However, it was never in widespread use for systems with many active degrees of freedom typical for condensed matter problems (although a few exceptions exist [19, 20] but here the number of explicitly treated electrons is fairly limited with the exception of [21]).

I.2.3. « Born-Oppenheimer » Molecular Dynamics

An alternative approach to include the electronic structure in molecular dynamics simulations consists in straightforwardly solving the static electronic structure problem in each molecular dynamics step given the set of fixed nuclear positions at that instance of time. Thus, the electronic structure part is reduced to solving a time-independent quantum problem, e.g. by

solving the time-independent Schrodinger equation, concurrently to propagating the nuclei via classical molecular dynamics.

Thus, the time-dependence of the electronic structure is a consequence of nuclear motion, and not intrinsic as in Ehrenfest molecular dynamics. The resulting Born-Oppenheimer molecular dynamics method is defined by

$$M_I \ddot{R}_I(t) = -\nabla_I \, min\{\langle \psi_0 | H_e | \psi_0 \rangle\} \qquad \text{(Eq. A-26)}$$

$$E_0 \psi_0 = H_e \, \Psi_0 \qquad \text{(Eq. A-27)}$$

for the electronic ground state. A deep difference with respect to Ehrenfest dynamics concerning the nuclear equation of motion is that the minimum of $\langle H_e \rangle$ has to be reached in each Born-Oppenheimer molecular dynamics step according to Eq. (A-26). In Ehrenfest dynamics, on the other hand, a wavefunction that minimized $\langle H_e \rangle$ initially will also stay in its respective minimum as the nuclei move according to Eq. (A-24).

A natural and straightforward extension [22] of ground-state Born-Oppenheimer dynamics is to apply the same scheme to any excited electronic state ψ_k without considering any interferences. In particular, this means that also the "diagonal correction terms" [23]

$$D_l^{kk}(\{R_I(t)\}) = - \int d\mathbf{r} \; \psi_k^* \nabla_I^2 \; \psi_k \qquad \text{(Eq. A-28)}$$

are always neglected; the inclusion of such terms is discussed for instance in (Refs. [10, 11]). These terms renormalize the Born-Oppenheimer or "clamped nuclei" potential energy surface E_k of a given state Ψ_k (which might also be the ground state Ψ_0) and lead to the so-called "adiabatic potential energy surface" of that state [23]. Whence, Born-Oppenheimer molecular dynamics should not be called "adiabatic molecular dynamics", as is sometime done.

It is useful for the sake of later reference to formulate the Born-Oppenheimer equations of motion for the special case of effective one-particle Hamiltonians. This might be the Hartree-Fock approximation defined to be the variational minimum of the energy expectation value $\langle \psi_0 | H_e | \psi_0 \rangle$ given a single Slater determinant $\psi_0 = det\{\psi_i\}$ subject to the constraint that the one-particle orbitals ψ_i are orthonormal $\langle \psi_i | \psi_j \rangle = \delta_{ij}$. The corresponding constraint minimization of the total energy with respect to the orbitals

$$min\{\langle \psi_0 | H_e | \psi_0 \rangle\}\big|_{\{\langle \psi_i | \psi_j \rangle = \delta_{ij}\}} \qquad \text{(Eq. A-29)}$$

can be cast into Lagrange's formalism

$$L = -\langle \psi_0 | H_e | \psi_0 \rangle + \sum_{i,j} \Lambda_{ij} (\langle \psi_i | \psi_j \rangle - \delta_{ij}) \qquad \text{(Eq. A-30)}$$

where Λ_{ij} are the associated Lagrangian multipliers. Unconstrained variation of this Lagrangian with respect to the orbitals

$$\frac{\delta L}{\delta \psi_i^*} = 0 \qquad \text{(Eq. A-31)}$$

leads to the well-known Hartree-Fock equations

$$H_e^{HF} \psi_i = \sum_j \Lambda_{ij} \psi_j \qquad \text{(Eq. A-32)}$$

The diagonal canonical form $H_e^{HF} \psi_i = \epsilon_i \psi_i$ is obtained after a unitary transformation and H_e^{HF} denotes the effective one-particle Hamiltonian. The equations of motion corresponding to Eqs.(A-26)-(A-27) read

$$M_I \ddot{\boldsymbol{R}}_I(t) = -\nabla_i \min\{ \langle \psi_0 | H_e^{HF} | \psi_0 \rangle \} \qquad \text{(Eq. A-33)}$$

$$0 = -H_e^{HF} \psi_i + \sum_j \Lambda_{ij} \psi_j \qquad \text{(Eq. A-34)}$$

for the Hartree-Fock case. A similar set of equations is obtained if Hohenberg-Kohn-Sham density functional theory [24, 25] is used, where H_e^{HF} has to be replaced by the Kohn-Sham effective one-particle Hamiltonian H_e^{HF}. Instead of diagonalizing the one-particle Hamiltonian an alternative but equivalent approach consists in directly performing the constraint minimization according to Eq. (A-29) via nonlinear optimization techniques.

Early applications of Born-Oppenheimer molecular dynamics were performed in the framework of a semi empirical approximation to the electronic structure problem [26, 27]. But only a few years later an *ab initio* approach was implemented within the Hartree-Fock approximation [28]. Born-Oppenheimer dynamics started to become popular in the early nineties with the availability of more efficient electronic structure codes in conjunction with sufficient computer power to solve "interesting problems".

Undoubtedly, the breakthrough of Hohenberg-Kohn-Sham density functional theory in the realm of chemistry - which took place around the same time - also helped a lot by greatly improving the "price/performance ratio" of the electronic structure part [29, 30]. A third and possibly the crucial reason that boosted the field of *ab initio* molecular dynamics was the pioneering

introduction of the Car-Parrinello approach [31]. This technique opened novel avenues to treat large-scale problems via *ab initio* molecular dynamics and catalyzed the entire field by making "interesting calculations" possible, see also the closing section on applications.

I.2.4. « Car-Parrinello » Molecular Dynamics

A non-obvious approach to cut down the computational expenses of molecular dynamics which includes the electrons in a single state was proposed by Car and Parrinello in 1985 [31]. In retrospect it can be considered to combine the advantages of both Ehrenfest and Born-Oppenheimer molecular dynamics. In Ehrenfest dynamics the time scale and thus the time step to integrate Eqs.(A-24) and(A-25) simultaneously is dictated by the intrinsic dynamics of the electrons. Since electronic motion is much faster than nuclear motion, the largest possible time step is that which allows to integrate the electronic equations of motion. Contrary to that, there is no electron dynamics whatsoever involved in solving the Born-Oppenheimer Eqs.(A-26)-(A-27), i.e. they can be integrated on the time scale given by nuclear motion. However, this means that the electronic structure problem has to be solved self-consistently at each molecular dynamics step, whereas this is avoided in Ehrenfest dynamics due to the possibility to propagate the wavefunction by applying the Hamiltonian to an initial wavefunction (obtained e.g. by one self-consistent diagonalization).

The basic idea of the Car-Parrinello approach can be viewed to exploit the quantum-mechanical adiabatic time-scale separation of fast electronic and slow nuclear motion by transforming that into classical-mechanical adiabatic energy-scale separation in the framework of dynamical systems theory. In order to achieve this goal the two-component quantum/classical problem is mapped onto a two-component purely classical problem with two separate energy scales at the expense of losing the explicit time-dependence of the quantum subsystem dynamics. Furthermore, the central quantity, the energy of the electronic subsystem $\langle \psi_0 | H_e | \psi_0 \rangle$ evaluated with some wavefunction ψ_0, is certainly a function of the nuclear positions $\{ R_I \}$. But at the same time it can be considered to be a functional of the wavefunction ψ_0 and thus of a set of one-particle orbitals $\{ \psi_i \}$.

Now, in classical mechanics the force on the nuclei is obtained from the derivative of a Lagrangian with respect to the nuclear positions. This suggests that a functional derivative with respect to the orbitals, which are interpreted as classical fields, might yield the force on the orbitals, given a suitable Lagrangian. In addition, possible constraints within the set of orbitals have to be imposed, such as e.g. orthonormality.

Car and Parrinello postulated the following class of Lagrangians [31]

$$L_{CP} = \sum_I \frac{1}{2} M_I \dot{R}_I^2 + \sum_i \frac{1}{2} \mu_i \langle \dot{\psi}_i | \dot{\psi}_i \rangle - \langle \psi_0 | H_e | \psi_0 \rangle + constraints \quad \text{(Eq. A-35)}$$

to serve this purpose. The corresponding Newtonian equations of motion are obtained from the associated Euler-Lagrange equations

$$\frac{d}{dt} \frac{\partial L}{\partial \dot{R}_I} = \frac{\partial L}{\partial R_I} \quad \text{(Eq. A-36)}$$

$$\frac{d}{dt} \frac{\delta L}{\delta \dot{\psi}_i^*} = \frac{\delta L}{\delta \psi_i^*} \quad \text{(Eq. A-37)}$$

like in classical mechanics, but here for both the nuclear positions and orbitals; note $\psi_i^* = \langle \psi_i |$ and that the constraints are holonomic [32]. Following this route of ideas, generic Car-Parrinello equations of motion are found to be of the form

$$M_I \ddot{R}_I(t) = -\frac{\partial}{\partial R_I} \langle \psi_0 | H_e | \psi_0 \rangle + \frac{\partial}{\partial R_I} \{constraints\} \quad \text{(Eq. A-38)}$$

$$\mu_i \ddot{\psi}_i(t) = -\frac{\delta}{\delta \psi_i^*} \langle \psi_0 | H_e | \psi_0 \rangle + \frac{\delta}{\delta \psi_i^*} \{constraints\} \quad \text{(Eq. A-39)}$$

where $\mu_i (= \mu)$ are the "fictitious masses" or inertia parameters assigned to the orbital degrees of freedom; the units of the mass parameter μ are energy times a squared time for reasons of dimensionality.

$$constraints = constraints \left(\{\psi_i\}, \{R_I\} \right) \quad \text{(Eq. A-40)}$$

might be a function of both the set of orbitals $\{\psi_i\}$ and the nuclear positions $\{R_I\}$. These dependencies have to be taken into account properly in deriving the Car-Parrinello equations following from Eq. (A-35) using Eqs.(A-36)-(A-37).

According to the Car-Parrinello equations of motion, the nuclei evolve in time at a certain (instantaneous) physical temperature $\propto \sum_I M_I \dot{R}_I^2$, whereas a "fictitious temperature" $\propto \sum_i \mu_i \langle \dot{\psi}_i | \dot{\psi}_i \rangle$ is associated to the electronic degrees of freedom. In this terminology, "low electronic temperature" or "cold electrons" means that the electronic subsystem is close to its instantaneous minimum energy $min_{\{\psi_i\}} \langle \psi_0 | H_e | \psi_0 \rangle$, i.e. close to the exact Born-Oppenheimer surface. Thus, a ground-state wave function optimized for the initial configuration of the nuclei will stay close to its ground state also during time evolution if it is kept at a sufficiently low temperature.

I.3. Integration of the equations of motion

In the classical MD [9, 7, 33], the trajectory for the various components of the system is generated by integrating the Newton equations of motion, which, for each particle i, write:

$$\begin{cases} M_I \frac{d^2 R_I(t)}{dt^2} = f_I(t) \\ f_I(t) = -\frac{\partial U(R_I)}{\partial R_I(t)} \end{cases}$$

(Eq. A-41)

V(x) is the potential energy function of the N–particle system, which only depends upon the Cartesian coordinates $\{\vec{R}_I\}$. Eqs.(A-41) are integrated numerically using an infinitesimal time–step, δt, to guarantee the conservation of the total energy of the system.

Hoping to generate exact trajectories over long times is, however, illusory, considering that the Newton equations of motion are solved numerically, with a finite time–step. The exactness of the solution of Eqs.(A-41) is, nevertheless, not as crucial as it would seem. What really matters in reality is the correct statistical behavior of the trajectory to ensure that the thermodynamic and dynamic properties of the system be reproduced with a sufficient accuracy. This pivotal condition is fulfilled only if the integrator employed to propagate the motion possesses the property of symplecticity [34–35]. A so-called symplectic propagator conserves the invariant metric of the phase space, Γ. As a result, the error associated with this propagator is bound:

$$\lim_{n_{step} \to \infty} \left(\frac{1}{n}\right) \sum_{k=1}^{n} \left| \frac{\epsilon(k\delta t) - \epsilon(0)}{\epsilon(0)} \right| \le \varepsilon_{MD}$$

(Eq. A-42)

Here, n_{step} denotes the number of steps of the simulation, $\epsilon(0) \equiv H(R_I, p_x; 0)$, the initial total energy of the equilibrated system, and ε_{MD}, the upper bound for energy conservation—viz. 10^{-4} constitutes an acceptable value. Assuming that the time–step is limited, integration of the equations of motion does not lead to an erratic growth of the error associated with the conservation of the total energy, which may affect significantly the statistical behavior of MD over long times. In order to clarify the statistical equivalence between the numerical solution and the exact solution of the equations of motion, it is useful to recall some points of hamilton's approach and relationship with statistical mechanics.

I.3.1. Hamiltion's point of view and statistical mechanics

The Hamiltonian of a system with N particles moving under the influence of a potential function *U* is defined as

$$H(\mathbf{R}^N, \mathbf{P}^N) = \sum_{I=1}^{N} \frac{P_I^2}{2M_I} + U(\mathbf{R}^N) \qquad \text{(Eq. A-43)}$$

Were $\{\mathbf{P}_I\}$ are the momenta of particles defined as $\vec{P}_I = M\vec{V}_I$. $\mathbf{R}^N(\mathbf{P}^N)$ is the union of all positions (or momenta) $\{\mathbf{R}_1, \mathbf{R}_2, \dots, \mathbf{R}_N\}$.

The forces on the particle are derived from the potential

$$F_I(\mathbf{R}^N) = -\frac{\partial U(\mathbf{R}^N)}{\partial R_I} \qquad \text{(Eq. A-44)}$$

The equations of motion are according to Hamilton's equation

$$\dot{\mathbf{R}}_I = \frac{\partial H}{\partial P_I} = \frac{P_I}{M_I} \qquad \text{(Eq. A-45)}$$

$$\dot{\mathbf{P}}_I = -\frac{\partial H}{\partial R_I} = -\frac{\partial U}{\partial R_I} = F_I(\mathbf{R}^N) \qquad \text{(Eq. A-46)}$$

From which we get Newton's second law using $\mathbf{P}_I = M_I \dot{\mathbf{R}}_I$

$$M_I \ddot{\mathbf{R}}_I = F_I(\mathbf{R}^N) \qquad \text{(Eq. A-47)}$$

The equations of motion can also be derived using the Lagrange formalism. The Lagrange function is

$$L(\mathbf{R}^N, \dot{\mathbf{R}}^N) = \sum_{I=1}^{N} \frac{1}{2} M_I \dot{R}_I^2 - U(\mathbf{R}^N) \qquad \text{(Eq. A-48)}$$

And the associated Euler-Lagrange equation

$$\frac{d}{dt} \frac{\partial L}{\partial \dot{R}_i} = \frac{\partial L}{\partial R_i} \qquad \text{(Eq. A-49)}$$

leads to the same final results. The two formulations are equivalent, but the ab initio molecular dynamics literature almost exclusively uses the Lagrangian techniques.

I.3.2. Microcanonical Ensemble

The equations of motion are time reversible (invariant to the transformation t → -t) and the total energy is a constant of motion

$$\frac{\partial E}{\partial t} = \frac{\partial H(\mathbf{R}^N, \dot{\mathbf{R}}^N)}{\partial t} = 0 \qquad \text{(Eq. A-50)}$$

These properties are important to establish a link between molecular dynamics and statistical mechanics. The latter connects the microscopic details of a system the physical observables such

as equilibrium thermodynamic properties, transport coefficients, and spectra. Statistical mechanics is based on the Gibbs' ensemble concept. That is, many individual microscopic configurations of a very large system lead to the same macroscopic properties, implying that it is not necessary to know the precise detailed motion of every particle in a system in order to predict its properties. It is sufficient to simply average over a large number of identical systems, each in a different configuration; i.e. the macroscopic observables of a system are formulated in term of ensemble averages. Statistical ensembles are usually characterized by fixed values of thermodynamic variables such as energy, E; temperature, T; pressure, P; volume, V; particle number, N; or chemical potential μ. One fundamental ensemble is called the microcanonical ensemble and is characterized by constant particle number, N; constant volume, V ; and constant total energy, E, and is denoted the *NVE* ensemble. Other examples include the canonical or *NVT* ensemble, the isothermal–isobaric or *NPT* ensemble, and the grand canonical or μV T ensemble. The thermodynamic variables that characterize an ensemble can be regarded as experimental control parameters that specify the conditions under which an experiment is performed. Now consider a system of N particles occupying a container of volume V and evolving under Hamilton's equation of motion. The Hamiltonian will be constant and equal to the total energy E of the system. In addition, the number of particles and the volume are assumed to be fixed. Therefore, a dynamical trajectory (i.e. the positions and momenta of all particles over time) will generate a series of classical states having constant N, V, and E, corresponding to a microcanonical ensemble. If the dynamics generates all possible states then an average over this trajectory will yield the same result as an average in a microcanonical ensemble. The energy conservation condition, $H\left(\boldsymbol{R}^N, \dot{\boldsymbol{R}}^N\right)$ which imposes a restriction on the classical microscopic states accessible to the system, defines a hypersurface in the phase space called a constant energy surface. A system evolving according to Hamilton's equation of motion will remain on this surface. The assumption that a system, given an infinite amount of time, will cover the entire constant energy hypersurface is known as the ergodic hypothesis. Thus, under the ergodic hypothesis, averages over a trajectory of a system obeying Hamilton's equation are equivalent to averages over the microcanonical ensemble. In addition to equilibrium quantities also dynamical properties are defined through ensemble averages. Time correlation functions are important because of their relation to transport coefficients and spectra via linear response theory [36, 37].

The important points are: by integration Hamilton's equation of motion for a number of particles in a fixed volume, we can create a trajectory; time averages and time correlation functions of the trajectory are directly related to ensemble averages of the microcanonical ensemble.

I.3.3. The molecular dynamics propagators

Several approaches for integrating numerically the Newton equations of motion (Eq. A-41) are currently available. Among them, three will be detailed here. Unquestionably the simplest, the Verlet algorithm relies upon the knowledge of the triplet $\{R_I(t), R_I(t - \delta t), a_I(t)\}$, where $a_I(t) = \ddot{R}_I(t)$ denotes the acceleration of particles I [38]. Modifying the positions of the particles is achieved through a Taylor expansion of the position $t - \delta t$ and at $t + \delta t$, leading to:

$$R_I(t + \delta t) = 2R_I(t) - R_I(t - \delta t) + a_I(t)\,\delta t^2 \qquad \text{(Eq. A-51)}$$

Which implies possible errors in (δt^4). It is worth noting that the velocities, $v_I(t) = \dot{R}_I(t) = dR_I(t)/dt$, do not appear explicitly in this scheme. They cancel out in the Taylor expansion of $x_I(t + \delta t)$ and $x_I(t - \delta t)$. Though unnecessary for describing the trajectory, their evaluation is an obligatory step for computing the kinetic energy, (p), which depends upon the sole momentum variables, **p**, and, consequently, the total energy of the system, according to:

$$V_I(t) = \frac{R_I(t+\delta t) - R_I(t-\delta t)}{2\,\delta t} \qquad \text{(Eq. A-52)}$$

At each time-step, the associated error is in (δt^2).

The so-called *leap-frog* algorithm, derived from the preceding one, makes use the $\{R_I(t), V_I(t - \delta t2), a_I(t)$ triplet. The origin of its name appears clearly in the writing of the algorithm:

$$\begin{cases} R_I(t + \delta t) = R_I(t) + V_I\left(t + \frac{\delta t}{2}\right)\delta t \\ V_I\left(t + \frac{\delta t}{2}\right) = V_I\left(t - \frac{\delta t}{2}\right) + a_I(t)\delta t \end{cases} \qquad \text{(Eq. A-53)}$$

In practice, the first step is the computation of $V_I(t + \delta t/2)$, from which $V_I(t)$ is deduced, which is a requisite for evaluating the term, , following:

$$\begin{cases} R_I(t + \delta t) = R_I(t) + V_I(t)\delta t + \frac{1}{2}a_I(t)\delta t^2 \\ V_I(t + \delta t) = V_I(t) + \frac{a_I(t)+a_I(a+\delta t)}{2}\delta t \end{cases} \qquad \text{(Eq. A-54)}$$

This scheme involves the two following steps:

$$V_I\left(t + \frac{\delta t}{2}\right) = V_I(t) + \frac{1}{2}a_I(t)\delta t \qquad \text{(Eq. A-55)}$$

From which the thermodynamic forces, f_I, and accelerations, a_I, at time $t + \delta t$ can be evaluated. It ensures that:

$$V_I(t + \delta t) = V_I \left(t + \frac{\delta t}{2} \right) + \frac{1}{2} a_I(t + \delta t)\delta t \qquad \text{(Eq. A-56)}$$

The kinetic energy may then be deduced at time $t + \delta t$, while the potential energy, , is computed in the force loops.

I.3.4. Extended System Approach

In the framework of statistical mechanics all ensembles can be formally obtained from the microcanonical *NVE* ensemble – where particle number, volume and energy are the external thermodynamic control variables – by suitable Laplace transforms of its partition function. Thermodynamically this corresponds to Legendre transforms of the associated thermodynamic potentials where intensive and extensive conjugate variables are interchanged. In thermodynamics, this task is achieved by a "sufficiently weak" coupling of the original system to an appropriate infinitely large bath or reservoir via a link that establishes thermodynamic equilibrium. The same basic idea is instrumental in generating distribution functions of such ensembles by computer simulation. Additional degrees of freedom that control the quantity under consideration are added to the system. The simulation is then performed in the extended microcanonical ensemble with a modified total energy as a constant of motion. This system has the property that after the correct integration over the additional degrees of freedom has been performed the distribution function of the targeted ensemble is recovered. Two important special cases are: thermostats and barostats, which are used to impose temperature instead of energy and / or pressure instead of volume as external control parameters [7, 9, 39, 40, 41, 42, 43].

I.3.4.1. Barostats

Keeping the pressure constant is a desirable feature for many applications of molecular dynamics. The concept of barostats and thus constant–pressure molecular dynamics was introduced in the framework of extended system dynamics by Andersen [42]. His method was devised to allow for isotropic fluctuations in the volume of the supercell. An extension of Andersen's method consists in allowing for changes of the shape of the computational cell to occur as a result of applying external pressure [41], including the possibility of non–isotropic external stress; the additional fictitious degrees of freedom in the Parrinello–Rahman approach [41] are the lattice vectors of the supercell. These variable–cell approaches make it possible to study dynamically structural phase transitions in solids at finite temperatures. The basic idea to allow for changes in the cell shape consists in constructing an extended Lagrangian where the lattice vectors $\mathbf{a}_1$, $\mathbf{a}_2$ and $\mathbf{a}_3$ of the simulation cell are additional dynamical variables. Using the 3

$\times$ 3 matrix h = [$\mathbf{a}_1$, $\mathbf{a}_2$, $\mathbf{a}_3$] (which fully defines the cell with volume *det h*) the real–space position R_I of a particle in this original cell can be expressed as

$$R_I = h\,S_I \qquad \text{(Eq. A-57)}$$

where S_I is a scaled coordinate with components $S_{i,u} \in [0,1]$ that defines the position of the *i*th particle in a unit cube (i.e. $\Omega_{unit} = 1$) which is the scaled cell [41]. The resulting metric tensor $G = h^t h$ converts distances measured in scaled coordinates to distances as given by the original coordinates. The variable-cell extended Lagrangian can be postulated

$$L = \sum_I^N \frac{1}{2} M_I \left(\dot{S}_I^t G \dot{S}_I \right) - U(h, S^N) + \frac{1}{2} W\, Tr\, \dot{h}^t \dot{h} - p\Omega \qquad \text{(Eq. A-58)}$$

with additional nine dynamical degrees of freedom that are associated to the lattice vectors of the supercell *h*. Here, *p* defines the externally applied hydrostatic pressure, *W* defines the fictitious mass or inertia parameter that controls the time–scale of the motion of the cell h. In particular, this Lagrangian allows for symmetry–breaking fluctuations – which might be necessary to drive a solid–state phase transformation – to take place spontaneously. The resulting equations of motion read

$$M_I \ddot{S}_{I,u} = -\sum_{v=1}^{3} \frac{\partial U(h, S^N)}{\partial R_{I,v}} (h^t)^{-1}_{vu} - M_I \sum_{v=1}^{3} \sum_{s=1}^{3} G^{-1}_{uv} \dot{G}_{vs} \dot{S}_{I,s} \qquad \text{(Eq. A-59)}$$

$$W \ddot{h}_{uv} = \Omega \sum_{s=1}^{3} (\Pi^{tot}_{us} - p\delta_{us})(h^t)^{-1}_{sv} \qquad \text{(Eq. A-60)}$$

Where the total internal stress tensor

$$\Pi^{tot}_{us} = \frac{1}{\Omega} \sum_I M_I \left(\dot{S}_I^t G \dot{S}_I \right)_{us} + \Pi_{us} \qquad \text{(Eq. A-61)}$$

Is the sum of the thermal contribution due to the nuclear motion at finite temperature and the internal stress tensor Π derived from the interaction potential. A modern formulation of barostats that combines the equation of motion also with thermostats (see next section) was given by Martyna et al. [43].

I.3.4.2. Thermostats

Standard molecular dynamics generates the microcanonical or *NVE* ensemble where in addition the total momentum is conserved [9]. The temperature is not a control variable and cannot be preselected and fixed. But it is evident that also within molecular dynamics the possibility to control the average temperature (as obtained from the average kinetic energy of the nuclei and

the energy equipartition theorem) is welcome for physical reasons. A deterministic algorithm of achieving temperature control in the spirit of extended system dynamics [42] by a sort of dynamical friction mechanism was devised by Nosé and Hoover [40, 44]. Thereby, the canonical or *NVT* ensemble is generated in the case of ergodic dynamics. It is well–known that the standard Nosé–Hoover thermostat method suffers from non– ergodicity problems for certain classes of Hamiltonians, such as the harmonic oscillator [44]. A closely related technique, the so–called Nosé–Hoover–chain thermostat [45], cures that problem and assures ergodic sampling of phase space even for the pathological harmonic oscillator. This is achieved by thermostatting the original thermostat by another thermostat, which in turn is thermostatted and so on. In addition to restoring ergodicity even with only a few thermostats in the chain, this technique is found to be much more efficient in imposing the desired temperature. The underlying equations of motion read

$$M_I \ddot{R}_I = -\nabla_I E^{KS} - M_I \dot{\xi}_1 \dot{R}_I \qquad \text{(Eq. A-62)}$$

$$Q_1^n \ddot{\xi}_1 = \left[\sum_I M_I \dot{R}_I^2 - g k_B T \right] - Q_1^n \dot{\xi}_1 \dot{\xi}_2 \qquad \text{(Eq. A-63)}$$

$$Q_k^n \ddot{\xi}_k = \left[Q_{k-1}^n \dot{\xi}_{k-1}^2 - k_B T \right] - Q_k^n \dot{\xi}_k \dot{\xi}_{k+1} (1 - \delta_{kK}) \quad where \ k = 2, \dots, K \qquad \text{(Eq. A-64)}$$

By inspection of (Eq. A-22) it becomes intuitively clear how the thermostat works: $\dot{\xi}_1$ can be considered as a dynamical friction coefficient. The resulting "dissipative dynamics" leads to non–Hamiltonian flow, but the friction term can acquire positive or negative sign according to its equation of motion. This leads to damping or acceleration of the nuclei and thus to cooling or heating if the instantaneous kinetic energy of the nuclei is higher or lower than $k_B T$ which is preset. As a result, this extended system dynamics can be shown to produce a canonical ensemble in the subspace of the nuclear coordinates and momenta. In spite of being non–Hamiltonian, Nosé–Hoover (–chain) dynamics is also distinguished by conserving an energy quantity of the extended system; see (Eq. A-67).

The desired average physical temperature is given by T and g denotes the number of dynamical degrees of freedom to which the nuclear thermostat chain is coupled (i.e. constraints imposed on the nuclei have to be subtracted). It is found that this choice requires a very accurate integration of the resulting equations of motion (for instance by using a high–order Suzuki–Yoshida integrator [46]). The integration of these equations of motion is discussed in detail in Ref. [46] using the velocity Verlet algorithm. One of the advantages of the velocity Verlet integrator is that it can be easily used together with higher order schemes for the thermostats.

The choice of the "mass parameters" assigned to the thermostat degrees of freedom should be made such that the overlap of their power spectra and the ones of the thermostatted subsystems is maximal [46]. The relations

$$Q_1^n = \frac{g k_B T}{\omega_n^2} \qquad \text{(Eq. A-65)}$$

$$Q_k^n = \frac{k_B T}{\omega_n^2} \qquad \text{(Eq. A-66)}$$

Assures this if ω_n is a typical phonon or vibrational frequency of the nuclear subsystem (say of the order of 2000 to 4000 cm^{-1}). There is a conserved energy quantity in the case of thermostatted molecular dynamics. This constant of motion reads

$$E_{cons}^{NVT} = \sum_I \frac{1}{2} M_i \dot{\boldsymbol{R}}_i^2 + U(\boldsymbol{R}^N) + \sum_{k=1}^{K} \frac{1}{2} Q_k^n \dot{\xi}_k^2 + \sum_{k=2}^{K} k_B T \xi_k + g k_B T \xi_1 \qquad \text{(Eq. A-67)}$$

For Nosé-Hoover-chain thermostatted molecular dynamics.

References:

[1] S.W. Rick and S.J. Stuart, Rev. Comp. Chem. **18**, 89 (2002).

[2] A. Warshel and R.M. Weiss, J. Am. Chem. Soc. **102**, 6218 (1980).

[3] D. Marx and J. Hutter in Modern Methods and Algorithms of Quantum Chemistry, ed. Grotendorst, J. (Forschun-gszentrun, Julich, germany) John von Neumann_Institut fur Computing, Vol. 1, pp. 301-449 (2000).

[4] M.E. Tuckernman, J. Phys. B Condens. Matter 14, (2002) R1297-R1355.

[6] D. Marx and J. Hutter in Ab Initio Molecular Dynamics: Basic theory and advanced methods, Cambridge University Press (2009).

[7] M. P. Allen and D. J. Tildesley, Computer Simulation of Liquids (Clarendon Press, Oxford, 1987; reprinted 1990).

[8] R. Haberlandt, S. Fritzsche, G. Peinel, and K. Heinzinger, Molekulardynamik - Grundlagen und Anwendungen (Vieweg Verlag, Braunschweig, 1995).

[9] D. Frenkel and B. Smit, Understanding Molecular Simulation - From Algorithms to Applications (Academic Press, San Diego, 1996).

[10] J. C. Tully, in Modern Methods for Multidimensional Dynamics Computations in Chemistry, ed. D. L. Thompson (World Scientific, Singapore, 1998).

[11] J. C. Tully, in Classical and Quantum Dynamics in Condensed Phase Simulations, Chapt. 21, p. 489, eds. B. J. Berne, G. Ciccotti, and D. F. Coker (World Scientific, Singapore, 1998).

[12] W. Ko los, Adv. Quant. Chem. **5**, 99 (1970).

[13] W. Kutzelnigg, Mol. Phys. **90**, 909 (1997).

[14] P. A. M. Dirac, Proc. Cambridge Phil. Soc. **26**, 376 (1930).

[15] P. A. M. Dirac, The Principles of Quantum Mechanics (Oxford University Press, Oxford, 1947; third edition).

[16] B. K. Dey, A. Askar, and H. Rabitz, J. Chem. Phys. **109**, 8770 (1998).

[17] H. Goldstein, Klassische Mechanik (Aula-Verlag, Wiesbaden, 1987).

[18] P. Ehrenfest, Z. Phys. **45,** 455 (1927).

[19] A. Selloni, P. Carnevali, R. Car, and M. Parrinello, Phys. Rev. Lett. **59**, 823 (1987).

[20] R. N. Barnett, U. Landman, and A. Nitzan, J. Chem. Phys. **89**, 2242 (1988).

[21] J. Theilhaber, Phys. Rev. B **46**, 12 990 (1992).

[22] B. Hartke and E. A. Carter, Chem. Phys. Lett. **189**, 358 (1992).

[23] W. Ko los, Adv. Quant. Chem. **5**, 99 (1970).

[24] R. M. Dreizler and E. K. U. Gross, Density-Functional Theory (Springer, Berlin, 1990).

[25] R. G. Parr and W. Yang, Density-Functional Theory of Atoms and Molecules (Oxford University Press, Oxford, 1989).

[26] I. S. Y. Wang and M. Karplus, J. Amer. Chem. Soc. **95**, 8160 (1973).

[27] A. Warshel and M. Karplus, Chem. Phys. Lett. **32**, 11 (1975).

[28] C. Leforestier, J. Chem. Phys. **68**, 4406 (1978).

[29] E. Wimmer, Science **269**, 1397 (1995).

[30] M. Springborg (Ed.), Density-Functional Methods in Chemistry and Materials Science, (John Wiley & Sons, New York, 1997).

[31] R. Car and M. Parrinello, Phys. Rev. Lett. **55**, 2471 (1985).

[32] G. Galli and A. Pasquarello, in Computer Simulation in Chemical Physics, eds. M. P. Allen and D. J. Tildesley (Kluwer, Dordrecht, 1993).

[33] W.F. Van Gunsteren, H.J.C. Berendsen, Computer simulation of molecular dynamics: Methodology, applications, and perspectives in chemistry, Angew. Chem. Int. Ed. Engl. 1990, 29, 992–1023.

[34] M.E. Tuckerman, G.J. Martyna, Understanding modern molecular dynamics: Techniques and applications, J. Phys. Chem. B 2000, 104, 159–178.

[35] E. Hairer, C. Lubich, G. Wanner, Geometric numerical integration. Structure–preserving algorithms for ordinary differential equations. in Springer series in computational mathematics, vol. 31. Springer–Verlag, Berlin (2002).

[36] R. Kubo, M. Toda, N. Hashitsume, Statistical Physics II, Springer–Verlag, Berlin 1978.

[37] B.J. Berne and G.D. Harp, Adv. Chem. Phys. **17** 63 (1970).

[38] L. Verlet, Computer "experiments" on classical fluids. I. Thermodynamical properties of Lennard–Jones molecules, Phys. Rev. **159**, 98 (1967).

[39] D. Marx, in Classical and Quantum Dynamics in Condensed Phase Simulations Chapt. 15, eds. B. J. Berne, G. Ciccotti, and D. F. Coker (World Scientific, Singapore, 1998).

[40] S. Nosé and M. L. Klein, Mol. Phys. **50**, 1055 (1983).

[41] M. Parrinello and A. Rahman, Phys. Rev. Lett. **45**, 1196 (1980).

[42] H. C. Andersen, J. Chem. Phys. **72**, 2384 (1980).

[43] G. J. Martyna, D. J. Tobias, and M. L. Klein, J. Chem. Phys. **101**, 4177 (1994).

[44] W. G. Hoover, Phys. Rev. A **31**, 1695 (1985).

[45] G. J. Martyna, M. L. Klein, and M. Tuckerman, J. Chem. Phys. **97**, 2635 (1992).

[46] M. E. Tuckerman and M. Parrinello, J. Chem. Phys. **101**, 1302 (1994).

Part B: The Electronic Structure Methods

II. 1. Introduction

Up to this point, the electronic structure method to calculate the *ab initio* forces $\nabla_I \langle \Psi_0 | H_e | \Psi_0 \rangle$ was not specified in detail. It is immediately clear that ab initio molecular dynamics is not tied to any particular approach, although very accurate techniques are of course prohibitively expensive. It is also evident that the strength or weakness of a particular ab initio molecular dynamics scheme is intimately connected to the strength or weakness of the chosen electronic structure method. Over the years a variety of different approaches were combined with molecular dynamics. The focus of the present review *is classical* molecular dynamics in conjunction with Hohenberg-Kohn-Sham density functional theory [1, 2]. In the following, only those parts of density functional theory are presented that impact directly on our static *ab initio* and molecular dynamics calculations.

II. 2. Density Functional Theory

The total ground-state energy of the interacting system of electrons with classical nuclei fixed at positions $\{R_I\}$ can be obtained

$$\min_{\Psi_0} \{ \langle \Psi_0 | H_e | \Psi_0 \rangle \} = \min_{\{\phi_i\}} E^{KS} \left[\{\phi_i\} \right] \tag{Eq. B-1}$$

as the minimum of the Kohn-Sham energy [1, 2]

$$E^{KS}\left[\{\phi_i\}\right] = T_s\left[\{\phi_i\}\right] + \int d\boldsymbol{r}\, V_{ext}(\boldsymbol{r})\, n(\boldsymbol{r}) + \frac{1}{2}\int d\boldsymbol{r} V_H(\boldsymbol{r}) n(\boldsymbol{r}) + E_{xc}[n] \tag{Eq. B-2}$$

which is an explicit functional of the set of auxiliary functions $\{\phi_i(\boldsymbol{r})\}$ that satisfy the orthonormality relation $\langle \phi_i | \phi_i \rangle = \delta_{ij}$. This is a dramatic simplification since the minimization with respect to all possible *many-body* wavefunctions $\{\Psi\}$ is replaced by a minimization with respect to a set of orthonormal one-particle functions, the Kohn-Sham orbitals $\{\phi_i\}$. The associated electronic one body density or charge density

$$n(\boldsymbol{r}) = \sum_i^{occ} f_i |\phi_i(\boldsymbol{r})|^2 \tag{Eq. B-3}$$

is obtained from a single Slater determinant built from the occupied orbitals, where $\{f_i\}$ are integer occupation numbers. The first term in the Kohn-Sham functional (Eq. B-1) is the kinetic energy of a non-interacting reference system

$$T_s[\{\phi_i\}] = \sum_i^{occ} f_i \left\langle \phi_i \left| -\frac{1}{2}\nabla^2 \right| \phi_i \right\rangle \qquad \text{(Eq. B-4)}$$

consisting of the same number of electrons exposed to the same external potential as in the fully interacting system. The second term comes from the fixed external potential

$$V_{ext}(\boldsymbol{r}) = -\sum_I \frac{Z_I}{|\boldsymbol{R}_I - \boldsymbol{r}|} + \sum_{I<J} \frac{Z_I Z_J}{|\boldsymbol{R}_I - \boldsymbol{R}_J|} \qquad \text{(Eq. B-5)}$$

in which the electrons move, which comprises the Coulomb interactions between electrons and nuclei and in the definition used here also the internuclear Coulomb interactions; this term changes in the first place if core electrons are replaced by pseudopotentials. The third term is the Hartree energy, i.e. the classical electrostatic energy of two charge clouds which stem from the electronic density and is obtained from the Hartree potential

$$V_H(\boldsymbol{r}) = \int d\boldsymbol{r}' \frac{n(\boldsymbol{r}')}{|\boldsymbol{r} - \boldsymbol{r}'|} \qquad \text{(Eq. B-6)}$$

which in turn is related to the density via

$$\nabla^2 V_H(\boldsymbol{r}) = -4\pi n(\boldsymbol{r}) \qquad \text{(Eq. B-7)}$$

Poisson's equation. The last contribution in the Kohn-Sham functional, the exchange-correlation functional $E_{xc}[n]$, is the most intricate contribution to the total electronic energy. The electronic exchange and correlation effects are lumped together and basically define this functional as the remainder between the exact energy and its Kohn-Sham decomposition in terms of the three previous contributions.

The minimum of the Kohn-Sham functional is obtained by varying the energy functional Eq. B-1) for a fixed number of electrons with respect to the density Eq. B-2) or with respect to the orbitals subject to the orthonormality constraint. This leads to the Kohn-Sham equations

$$\left\{ -\frac{1}{2}\nabla^2 + V_{ext}(\boldsymbol{r}) + V_H(\boldsymbol{r}) + \frac{\delta E_{xc}[n]}{\delta n(r)} \right\} \phi_i(\boldsymbol{r}) = \sum_j \Lambda_{ij} \phi_j(\boldsymbol{r}) \qquad \text{(Eq. B-8)}$$

$$\left\{-\frac{1}{2}\nabla^2 + V_{eff}(\boldsymbol{r})\right\}\phi_i(\boldsymbol{r}) = \sum_j \Lambda_{ij}\phi_j(\boldsymbol{r}) \tag{Eq. B-9}$$

$$H_e^{KS}\phi_i(\boldsymbol{r}) = \sum_j \Lambda_{ij}\phi_j(\boldsymbol{r}) \tag{Eq. B-10}$$

which are one-electron equations involving an effective *one-particle* Hamiltonian H_e^{KS} with the effectif potential V_{eff}. Note that H_e^{KS} nevertheless embodies the electronic *many-body* effects by virtue of the exchange-correlation potential

$$\frac{\delta E_{xc}[n]}{\delta n(\boldsymbol{r})} = V_{xc}(\boldsymbol{r}) \tag{Eq. B-11}$$

A unitary transformation within the space of the occupied orbitals leads to the canonical form

$$H_e^{KS}\phi_i = \epsilon_i\phi_i \tag{Eq. B-12}$$

of the Kohn-Sham equations, where $\{\epsilon_i\}$ are the eigenvalues. In conventional static density functional or "band structure" calculations this set of equations has to be solved self-consistently in order to yield the density, the orbitals and the Kohn-Sham potential for the electronic ground state [3]. The corresponding total energy (Eq. B-2) can be written as

$$E^{KS} = \sum_i \epsilon_i - \frac{1}{2}\int d\boldsymbol{r}\, V_H(\boldsymbol{r})n(\boldsymbol{r}) + E_{xc}[n] - \int d\boldsymbol{r}\frac{\delta E_{xc}[n]}{\delta n(\boldsymbol{r})}\, n(\boldsymbol{r}) \tag{Eq. B-13}$$

where the sum over Kohn-Sham eigenvalues is the so-called "band-structure energy".

Thus, Eqs. (B-8)-(B-10) together with Eqs. (A-33)-(A-34) define Born-Oppenheimer molecular dynamics within Kohn-Sham density functional theory. The functional derivative of the Kohn-Sham functional with respect to the orbitals, the Kohn-Sham force acting on the orbitals, can be expressed as

$$\frac{\delta E^{KS}}{\delta \phi_i^*} = f_i H_e^{KS}\phi_i \tag{Eq. B-14}$$

Which makes clear the connection to Car-Parrinello molecular dynamics, see Eq. A-39.

II. 3. Energy functionals

Crucial to any application of density functional theory is the approximation of the unknown exchange and correlation functional. Those exchange-correlation functionals that will be

considered in the implementation part, belong to the class of the "Generalized Gradient Approximation" [4]

$$E_{xc}^{GGA}[n] = \int d\boldsymbol{r}\, n(\boldsymbol{r})\varepsilon_{xc}^{GGA}\big(n(\boldsymbol{r}); \nabla n(\boldsymbol{r})\big) \qquad \text{(Eq. B-15)}$$

where the unknown functional is approximated by an integral over a function that depends only on the density and its gradient at a given point in space The combined exchange-correlation function is typically split up into two additive terms ε_x and ε_c for exchange and correlation, respectively.

In the simplest case it is the exchange and correlation energy density $\varepsilon_{xc}^{LDA}(n)$ of an interacting but homogeneous electron gas at the density given by the "local" density *n(r)* at space-point *r* in the inhomogeneous system. This simple but astonishingly powerful approximation [5] is the famous local density approximation LDA [6] (or local spin density LSD in the spin-polarized case [7]). The self-interaction correction [8] SIC as applied to LDA was critically assessed for molecules in Ref. [9] with a disappointing outcome. A significant improvement of the accuracy was achieved by introducing the gradient of the density as indicated in Eq. B-14) beyond the well-known straightforward gradient expansions. These so-called GGAs (also denoted as "gradient corrected" or "semilocal" functionals) extended the applicability of density functional calculation to the realm of chemistry.

Another considerable advance was the successful introduction of "hybrid functional" [10, 11] that includes to some extent "exact exchange" [12] in addition to a standard GGA. Although such functional can certainly be implemented within a plane wave approach [13], they are prohibitively time-consuming. A more promising route in this respect are those functional that include higher-order powers of the gradient (or the local kinetic energy density) in the sense of a generalized gradient expansion beyond the first term. Promising results could be achieved by including Laplacian or local kinetic energy terms [14], but at this stage a sound judgment concerning their "prize/performance ratio" has to await further scrutinizing tests. The "optimized potential method" (OPM) or "optimized effective potentials" (OEP) are another route to include "exact exchange" within density functional theory. Here, the exchange-correlation functional $E_{xc}^{OPM} = E_{xc}[\{\phi_i\}]$ depends on the individual orbitals instead of only on the density or its derivatives.

II. 4. The plane wave pseudopotential method

The Kohn Sham equation, (Eq. B-12), can be solved in practice by expanding the Kohn Sham orbitals in a finite set of basis functions. The Schrodinger equation then transforms into an algebraic equation for the expansion coefficient which may be solved by various well–established numerical methods. Among these methods, we limit our discussion to the Plane Wave (PW) basis set. Plane waves are the exact eigenfunctions of the homogeneous electron gas. Therefore, plane waves are the natural choice for a basis expansion of the electron wave functions for simple metals where the ionic cores can be viewed as rather small perturbations to the homogeneous electron gas ("nearly free electron" metals). Plane waves are orthonormal and energy–independent. Hence, upon a basis set expansion the Schrodinger equation transforms into a simple matrix eigenvalue problem for the expansion coefficients. A further advantage of plane waves is that they are not biased to any particular atom. Any region in space is treated on an equal footing so that calculations do not have to be corrected for a basis set superposition error. Since plane waves do not depend on the positions of the atoms, the Hellmann–Feynman theorem can be applied directly to calculate atomic forces. Even for a non-complete basis set the Pulay terms are identical zero.

In practical calculations only plane waves up to a certain cutoff wave vector are included in the basis set. The convergence of the calculations with respect to the basis set size is therefore controlled by a single parameter and can be checked simply by increasing the length of the cutoff wave vector. However, due to the nodal structure of the valence wave functions in the core region of the atoms a prohibitively large number of plane waves would be needed for a good representation of these fast oscillations. For plane wave approaches to be of practical use we have to replace the Coulomb potential of the electron–nucleus interaction by pseudopotentials. By introducing pseudopotentials we are able to achieve two goals: First, we can remove the core electrons from our calculations. The contribution of the core electrons to the chemical bonding is negligible but they contribute most to the total energy of the system (typically a thousand times more than the valence electrons). Hence, the removal of the core electrons from the calculation means that total energy differences between ionic configurations can be taken between much smaller numbers so that the required accuracy for the total energy calculations will be much less demanding than in an all–electron calculation. Second, by introducing pseudopotentials we replace the true valence wave functions by so-called pseudo wave functions which match exactly the true valence wave functions outside the ionic core region but are nodeless inside. These pseudo wave functions can be expanded using a much smaller number of plane wave basis

states. A further advantage of pseudopotentials is that relativistic effects can be incorporated easily into the potential while further treating the valence electrons non–relativistically.

In spite of introducing pseudopotentials, the number of basis functions N_{pw} needed for an accurate calculation is still an order of magnitude larger than for approaches using localized orbitals. This disadvantage, however, is more than compensated by the possibility to evaluate many expressions with the help of the Fast Fourier Transform (FFT) algorithm. The most time consuming step in solving the single–particle Schrodinger equations is to apply the Hamilton operator to the valence wave functions. In a traditional matrix representation of the Hamilton operator this step scales quadratically with the number of basis functions. With plane waves and the FFT algorithm this operation reduces to a $N_{pw}ln(N_{pw})$ scaling. Hence, for large systems the use of plane wave basis functions will become much more efficient than localized basis sets. Furthermore, the total charge density and the Hartree potential are easily calculated in a plane wave representation.

II.4.1. Plane waves

II.4.1.1. Supercell

Although we have simplified the complicated many–body problem of interacting electrons in the Coulomb potentials of fixed nuclei to a set of single–particle equations, the calculation of the one–electron wave functions for an extended (or even infinite) system is still a formidable task. To make the problem tractable we assume that our system of interest can be represented by a box of atoms which is repeated periodically in all three special directions. The box shall be described by three vectors $\mathbf{a}_1$, $\mathbf{a}_2$, and $\mathbf{a}_3$. The volume of the box is given by

$$\Omega_c = \boldsymbol{a}_1.(\boldsymbol{a}_2 x \boldsymbol{a}_3) \qquad \text{(Eq. B-16)}$$

The three vectors define a lattice in real space. General lattice vectors $\mathbf{T}$ are multiples of the primitive lattice vectors:

$$\boldsymbol{T} = N_1\boldsymbol{a}_1 + N_2\boldsymbol{a}_2 + N_3\boldsymbol{a}_3 \qquad \text{(Eq. B-17)}$$

Where N_1, N_2, N_3 can be any integer number. The box can be, for example, either the primitive unit cell of a crystal or a large supercell containing a sufficient number of independent atoms to mimic locally an amorphous solid or a liquid phase. By using supercells also atomic point defects, surfaces or isolated molecules can be modeled as illustrated schematically in Fig. II-1. It is essential to make the supercells large enough to prevent the defects, surfaces or molecules in

neighboring cells from interacting appreciably with each other. The independence of the configurations can be checked systematically by increasing the volume of the supercell until the computed quantity of interest has converged.
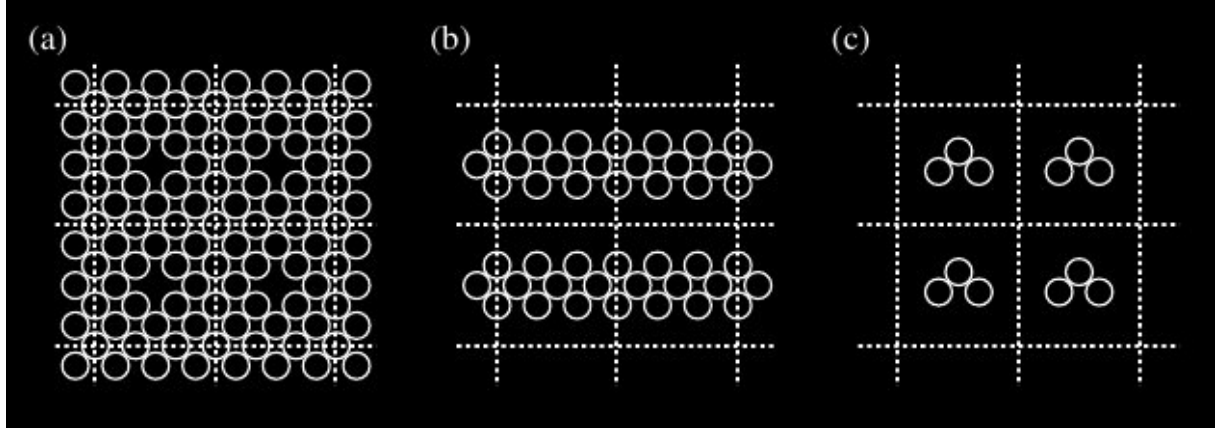
Figure. II-2. Schematic illustration of a supercell geometry (a) for a vacancy in a bulk crystalline solid, (b) surface, and (c) for a isolated molecule. The boundaries of the supercells are shown by dashed lines.

II.4.1.2. Fourier representations

The translational symmetry of the atomic arrangements can now be exploited to reduce the computational cost for solving the Kohn–Sham equations. The effective potential (as well as the electron density) is a periodic function with the periodicity of the lattice, i.e.

$$V_{eff}(\boldsymbol{r} + \boldsymbol{T}) = V_{eff}(\boldsymbol{r}) \tag{Eq. B-18}$$

for any lattice vector **T** of the form of (Eq. B-17). Therefore V_{eff} can be expanded into a Fourier series

$$V_{eff}(\boldsymbol{r}) = \sum_{\boldsymbol{G}} V_{eff}(\boldsymbol{G})e^{i\boldsymbol{Gr}}, \quad V_{eff}(\boldsymbol{G}) = \frac{1}{\Omega_c}\int_{\Omega_c} V_{eff}(\boldsymbol{r})e^{-i\boldsymbol{Gr}}d^3\boldsymbol{r} \tag{Eq. B-19}$$

The sum runs over all vectors **G** which fulfill the condition **G.T**= 2π M for all lattice vectors **T** with M being an integer number. The vectors **G** form a lattice, the so-called reciprocal lattice, which is generated by the three primitive vectors $\boldsymbol{b}_1$, $\boldsymbol{b}_2$, $\boldsymbol{b}_3$ defined by [15]

$$\boldsymbol{a}_i.\boldsymbol{b}_j = 2\pi\delta_{ij} \quad, \quad i,j = 1,2,3 \tag{Eq. B-20}$$

The volume of the unit cell of the reciprocal lattice is given by

$$\boldsymbol{b}_1.(\boldsymbol{b}_2 x \boldsymbol{b}_3) = \frac{(2\pi)^3}{\Omega_c} \tag{Eq. B-21}$$

II.4.1.3. Bloch's Theorem

The solutions of a single–particle Schrödinger equation with a periodic potential are by no means themselves necessarily periodic. However, the eigenstates can be chosen in such a way that associated with each wave function ϕ is a wave vector **k** to hold

$$\phi(\boldsymbol{r} + \boldsymbol{T}) = e^{ik\boldsymbol{T}}\phi(\boldsymbol{r}) \qquad \text{(Eq. B-22)}$$

for every lattice vectors T (Bloch's theorem). From now on all eigenstates of the single– particle Schrödinger equation will be labeled with its corresponding vector k. From the form of the exponential factor in (Eq. B-22) it is obvious that the values of k can be restricted to within one unit cell of the reciprocal lattice. By convention this unit cell is usually taken to be the first Brillouin Zone (BZ) [15]. Different solutions to the same vector k will be labeled with the band index j.

Bloch's theorem is often stated in an alternative form. The property in (Eq. B-22) is equivalent to the statement that all eigenfunctions ϕ_{kj} of a single–particle Schrödinger equation with a periodic potential can be written as a periodic function u_{kj} modulated by a plane wave with wave vector k [15]:

$$\phi_{kj}(\boldsymbol{r}) = e^{ik\boldsymbol{r}}u_{kj}(\boldsymbol{r}) \qquad \text{(Eq. B-23)}$$

This allows us to restrict the calculation of the eigenfunctions to within one unit cell. The form of the eigenfunctions in all other unit cells is determined by applying (Eq. B-22). From now on we will assume that the eigenfunctions are normalized with respect to a single unit cell:

$$\int_{\Omega_c} |\phi(\boldsymbol{r})|^2 d^3\boldsymbol{r} = 1 \qquad \text{(Eq. B-24)}$$

Since the functions u_{kj} are periodic they can be expanded in a set of plane waves. Together with the exponential prefactor we get

$$\phi_{kj}(\boldsymbol{r}) = \sum_{\boldsymbol{G}} c_{\boldsymbol{G}}^{kj} e^{i(\boldsymbol{k}+\boldsymbol{G})\boldsymbol{r}} \qquad \text{(Eq. B-25)}$$

Before we make use of the plane wave expansion of the wave functions we write the Kohn–Sham equations of density functional theory in the notation of Bloch–states:

$$\left(-\frac{h^2}{2m}\Delta + V_{eff}(\boldsymbol{r})\right)\phi_{kj}(\boldsymbol{r}) = \epsilon_{kj}\phi_{kj}(\boldsymbol{r}) \qquad \text{(Eq. B-26)}$$

with

$$V_{eff}(\boldsymbol{r}) = V_{ext}(\boldsymbol{r}) + V_H[n(\boldsymbol{r})] + V_{xc}[n(\boldsymbol{r})]$$ (Eq. B-27)

and

$$n(\boldsymbol{r}) = 2\frac{\Omega_c}{(2\pi)^3}\sum_j \int_{BZ} \left|\phi_{kj}(\boldsymbol{r})\right|^2 \Theta(E_F - \epsilon_{kj})d^3\boldsymbol{k}$$ (Eq. B-28)

V_{ext}, V_H and V_{xc} are the external potential of the nuclei, the Hartree and the exchange– correlation potential, respectively. By the factor of 2 in (Eq. B-28) we take the electron spin into account. Θ is a step function which is one for positive and zero for negative arguments. E_F is the Fermi energy up to which single–particle states have to be occupied. The Fermi energy is defined by the number of electrons N_e in the unit cell:

$$\int_{\Omega_c} n(\boldsymbol{r})d^3\boldsymbol{r} = N_e$$ (Eq. B-29)

For an insulator the Fermi energy lies in a band gap. Hence, at each k–point exactly $N_e/2$ bands will be occupied. For metals one or more bands cross the Fermi energy so that the number of occupied states will change between k–points.

II.4.1.4. k–Point Sampling

By making use of Bloch's theorem we have transformed the problem of calculating an infinite number of electronic states extended infinitely in space to one of calculating a finite number of eigenstates at an infinite number of k–points which are extended over a single unit cell. At first glance this seems to be only a minor improvement since still an infinite number of calculations are needed for the different k–points. However, the electronic wave functions at k–points which are close together will be very similar. Hence it is possible to represent the wave functions of a region of k–space by the wave function at a single k–point. We thus define a regular mesh of N_{kpt} k–points and replace the integral over the Brillouin zone by a discrete sum over the chosen k–point mesh:

$$\frac{\Omega_c}{(2\pi)^3}\int_{BZ} \dots \Theta(E_F - \epsilon_{kj})d^3\boldsymbol{k} \rightarrow \frac{1}{N_{kpt}}\sum_k f_{kj}$$ (Eq. B-30)

The f_{kj} are occupation numbers which are either one or zero. Several schemes to construct such k–point meshes have been proposed in the literature [16-17]. Within this approximation the electronic states at only a finite number of k–points are needed to calculate the charge density and hence the total energy of the solid. The error induced by this approximation can be reduced systematically by increasing the density of the k–point mesh. For insulators it turns out that

usually only a small number of k–points is required to get good converged results. For increasing size of the supercell the volume of the Brillouin zone becomes smaller and smaller (see Eq. B-22). Therefore, with increasing supercell size less and less k–points are needed. From a certain supercell size on it is often justified to use just a single k–point, which is usually taken to be k=0 (k–point approximation). For metallic systems, on the other hand, much denser k–point meshes are required in order to get a precise sampling of the Fermi surface. In these cases the convergence with respect to the k–point density can often be accelerated by introducing fractional occupation numbers [18-19].

II.4.1.5. Fourier representation of the Kohn-Sham equations

In a plane wave representation of the wave functions the Kohn–Sham equations assume a particular simple form. If we insert (Eq. B-25) into (Eq. B-26), multiply from left with $\exp(-i(\boldsymbol{k} + \boldsymbol{G}')r)$ and integrate over r we get the matrix eigenvalue equation

$$\sum_{\boldsymbol{G}} \left(\frac{h^2}{2m}\right) \|\boldsymbol{k} + \boldsymbol{G}\|^2 \delta_{\boldsymbol{G}'\boldsymbol{G}} + V_{eff}(\boldsymbol{G}' - \boldsymbol{G}) c_{\boldsymbol{G}}^{kj} = \epsilon_{kj} c_{\boldsymbol{G}'}^{kj} \qquad \text{(Eq. B-31)}$$

In practical calculations the Fourier expansion (Eq. B-25) of the wave functions is truncated by keeping only those plane wave vectors (**k+G**) with a kinetic energy lower than a given cutoff value E_{pw}:

$$\left(\frac{h^2}{2m}\right) \|\boldsymbol{k} + \boldsymbol{G}\|^2 \le E_{pw} \qquad \text{(Eq. B-32)}$$

The convergence of all calculations with respect to the basis set size can be tested simply by increasing step by step the plane wave cutoff energy.

The electron density in Fourier representation is given by

$$n(\boldsymbol{r}) = \frac{2}{N_{kpt}} \sum_{kj} f_{kj} \sum_{\boldsymbol{G}'} \left(c_{\boldsymbol{G}'-\boldsymbol{G}}^{kj}\right)^* c_{\boldsymbol{G}'}^{kj} \qquad \text{(Eq. B-33)}$$

Since we have truncated the wave functions at a maximum wave vector it is obvious from Eq. B-34 that the electron density has only non-vanishing Fourier components up to twice the length of this cutoff wave vector. In Fourier space the calculation of the Hartree potential is particularly simple. It is given by

$$V_H(\boldsymbol{G}) = 4\pi e^2 \frac{n(\boldsymbol{G})}{\|\boldsymbol{G}\|^2} \qquad \text{(Eq. B-34)}$$

As the electron density, the Hartree potential has a finite Fourier expansion. To calculate the exchange–correlation potential we have to Fourier transform the electron density to real–space, evaluate the given functional and Fourier transform back the result.

II.4.1.6. Fast Fourier Transformation (FFT)

The main advantage of working with plane waves is that the evaluation of various expres- sions can be speeded up significantly by using FFTs. In particular, since the wave functions and the electron density have a finite Fourier representation this can be done without any loss in accuracy, as long as we use in our real–space Fourier grid twice as many grid points in each spacial direction than the number of points in the Fourier space grid [20]. For example, the calculation of the electron density according to Eq. B-34 scales quadratically with the number N_{pw} of plane waves. However, if we Fourier transform the wave functions to real–space (which scales with $N_{pw}ln(N_{pw})$), calculate $\left|\phi_{kj}\left(r\right)\right|^2$ on the real–space Fourier grid (N_{pw} scaling) and then Fourier transform back the result we significantly reduce the computational cost. Along the same arguments we can also reduce the number of calculations for the evaluation of the term $\sum_G V_{eff}(G' - G)c_G^{kj}$ in Eq. B-32 from a N_{pw}^2 to a $N_{pw}ln(N_{pw})$ scaling.

II.4.2. Pseudopotentials

II.4.2.1. Norm conserving Pseudopotentials

The norm–conserving pseudopotential approach provides an effective and reliable means for performing calculations on complex molecular, liquid and solid state systems using plane wave basis sets. In this approach only the chemically active valence electrons are dealt with explicitly. The inert core electrons are eliminated within the frozen–core approximation, being considered together with the nuclei as rigid non–polarizable ion cores. In turn, all electrostatic and quantum–mechanical interactions of the valence electrons with the cores, as the nuclear Coulomb attraction screened by the core electrons, Pauli repulsion and exchange and correlation between core and valence electrons, are accounted for by angular momentum dependent pseudopotentials. These reproduce the true potential and valence orbitals outside a chosen core region but remain much weaker and smoother inside.

The valence electrons are described by smooth pseudo orbitals which play the same role as the true orbitals, but avoid the nodal structure near the nuclei that keeps the core and valence states orthogonal in an all–electron framework. The respective Pauli repulsion largely cancels the

attractive parts of the true potential in the core region, and is built into the therefore rather weak pseudopotential.

This pseudoization of the valence wavefunctions along with the removal of the core states eminently facilitates a numerically accurate solution of the Kohn–Sham equations and the Poisson equation, and enables the use of plane waves as an expedient basis set in electronic structure calculations. By virtue of the norm–conservation property and when constructed carefully pseudopotentials present a rather marginal approximation, and indeed allow for an adequate description of the valence electrons over the entire chemically relevant range of systems.

- Pseudopotentials should be additive and transferable. Additivity can most easily be achieved by building pseudopotentials for atoms in reference states. Transferability means that one and the same pseudopotential should be adequate for an atom in all possible chemical environments. This is especially important when a change of the environment is expected during a simulation, like in chemical reactions or for phase transitions.

- Pseudopotentials replace electronic degrees of freedom in the Hamiltonian by an effective potential. They lead to a reduction of the number of electrons in the system and thereby allow for faster calculation or the treatment of bigger systems.

- Pseudopotentials allow for a considerable reduction of the basis set size. Valence states are smoother than core states and need therefore less basis functions for an accurate description. The pseudized valence wavefunctions are nodeless (in the here considered type of pseudopotentials) functions and allow for an additional reduction of the basis. This is especially important for plane waves. Consider the 1s function of an atom

$$\varphi_{1s}(\mathbf{r}) \sim e^{\wedge}(-Z^* r) \qquad \text{(Eq. B-35)}$$

with $Z^* \approx Z$, the nuclear charge. The Fourier transform of the orbital is

$$\varphi_{1s}(\mathbf{G}) \sim 16\pi \frac{Z^{5/2}}{G^2 + Z^2} \qquad \text{(Eq. B-36)}$$

From this formula we can estimate the relative cutoffs needed for different elements in the periodic table.

- Most relativistic effects are connected to core electrons. These effects can be incorporated in the pseudopotentials without complicating the calculations of the final system.

II.4.2.1.1. Hamann–Schluter–Chiang conditions

Norm–conserving pseudopotentials are derived from atomic reference states, calculated from the atomic Kohn-Sham equation (Eq. B-4). This equation is replaced by a valence electron only equation of the same form

$$(-\nabla^2 + V_{val})|\phi_l^{ps}\rangle = \hat{\epsilon}_l|\phi_l^{ps}\rangle \qquad \text{(Eq. B-37)}$$

Hamann, Schluter, and Chiang [21] proposed a set of requirements for the pseudo wave-function and pseudopotential.

The pseudopotential should have the following properties

1. Real and pseudo valence eigenvalues agree for a chosen prototype atomic configuration. $\epsilon_l = \hat{\epsilon}_l$

2. Real and pseudo atomic wave functions agree beyond a chosen core radius r_c.

$\phi_l(r) = \phi_l^{ps}(r) \, for \, r \geq r_c$

3. The integrals from 0 to R of the real and pseudo charge densities agree for $R \geq r_c$ for each valence state (norm conservation).

$\langle\phi_l^{ps}|\phi_l^{ps}\rangle_R = \langle\phi_l|\phi_l\rangle_R \, for \, R \geq r_c$

where

$$\langle\phi_l^{ps}|\phi_l^{ps}\rangle_R = \int_0^R r^2 |\phi_l^{ps}(r)|^2 dr \qquad \text{(Eq. B-38)}$$

4. The logarithmic derivatives of the real and pseudo wave function and their first energy derivatives agree for $r \geq r_c$.

Property **3)** and **4)** are related through the identity

$$-\frac{1}{2}\left[(r\phi_l^{ps})^2 \frac{d}{d\epsilon}\frac{d}{dr}\ln\phi_l^{ps}\right]_R = \int_0^R r^2 |\phi_l^{ps}|^2 dr \qquad \text{(Eq. B-39)}$$

They also gave a recipe that allows to generate pseudopotentials with the above properties:

1.

$$V_l^{(1)}(r) = V_{AE}(r)\left[1 - f_1\left(\frac{r}{r_{cl}}\right)\right] \qquad \text{(Eq. B-40)}$$

r_{cl} : core radius $\approx 0.4 - 0.6 \, R_{max}$, where R_{max} is the outermost maximum of the real wave function.

2.

$$V_l^{(2)}(r) = V_l^{(1)}(r) + c_1 f_2\left(\frac{r}{r_{cl}}\right) \qquad \text{(Eq. B-41)}$$

determine c_1 so that $\epsilon_l = \hat{\epsilon}_l$ in

$$\left(-\nabla^2 + V_l^{(2)}(r)\right)w_l^{(2)}(r) = \hat{\epsilon}_l w_l^{(2)}(r) \qquad \text{(Eq. B-42)}$$

3.

$$\phi_l^{ps}(r) = \gamma_l \left[w_l^{(2)}(r) + \delta_l r^{l+1} f_3\left(\frac{r}{r_{cl}}\right) \right] \qquad \text{(Eq. B-43)}$$

where γ_l and δ_l are chosen such that

$$\phi_l^{ps}(r) \rightarrow \phi_l(r) \text{ for } r \geq r_{cl}$$

and

$$\gamma_l^2 \int \left| w_l^{(2)}(r) + \delta_l r^{l+1} f_3\left(\frac{r}{r_{cl}}\right) \right|^2 dr = 1 \qquad \text{(Eq. B-44)}$$

4. Invert the Schrodinger equation for $\hat{\epsilon}_l \, \phi_l^{ps}(r)$ to get $V_{val}^l(r)$

5. Unscreen $V_{val}^l(r)$ to get $V_{ps}^l(r)$

$$V_{ps}^l(r) = V_{val}^l(r) - V_H(n_v) - V_{xc}(n_v) \qquad \text{(Eq. B-45)}$$

where $V_H(\rho_v)$ and $V_{xc}(\rho_v)$ are the Hartree and exchange and correlation potentials of the pseudo valence density.

Hamann, Schluter and Chiang chose the following cutoff functions $f_1(x) = f_2(x) = f_3(x) = \exp(-x^4)$.

These pseudopotentials are angular momentum dependent. Each angular momentum state has its own potential that can be determined independently from the other potentials. It is therefore possible to have a different reference configuration for each angular momentum. This allows it for example to use excited or ionic states to construct the pseudopotential for l states that are not occupied in the atomic ground state.

The total pseudopotential in a solid state calculation then takes the form

$$V_{ps}(r) = \sum_L V_{ps}^L(r) P_L \qquad \text{(Eq. B-46)}$$

where L is a combined index *{l,m}* and P_L is the projector on the angular momentum state *{l,m}*.

II.4.2.1.2 Bachelet-Hamann-Schluter (BHS) form

Bachelet et al. [22] proposed an analytic fit to the pseudopotentials generated by the HSC recipe of the following form

$$V_{ps}(r) = V_{core}(r) + \sum_L \Delta V_L^{ion}(r) \qquad \text{(Eq. B-47)}$$

$$V_{core}(r) = -\frac{Z_v}{r} \left[\sum_{i=1}^2 c_i^{core} \text{erf}\left(\sqrt{\alpha_i^{core}} r\right) \right] \qquad \text{(Eq. B-48)}$$

$$\Delta V_L^{ion}(r) = \sum_{i=1}^3 (A_i + r^2 A_{i+3}) \exp(-\alpha_i r^2) \qquad \text{(Eq. B-49)}$$

The cutoff functions were slightly modified to be $f_1(x) = f_2(x) = f_3(x) = \exp(-x^{3.5})$.

They generated pseudopotentials for almost the entire periodic table (for the local density approximation), where generalizations of the original scheme to include spin–orbit effects for heavy atoms were made. Useful is also their list of atomic reference states.

BHS did not tabulate the A_i coefficients as they are often very big numbers but another set of numbers C_i, where

$$C_i = -\sum_{l=1}^{6} A_l Q_{il} \qquad \text{(Eq. B-50)}$$

and

$$A_i = -\sum_{l=1}^{6} C_l Q_{il}^{-1} \qquad \text{(Eq. B-51)}$$

with

$$Q_{il} = \begin{cases} 0 & i > l \\ \left[S_{il} - \sum_{k=1}^{i-1} Q_{ki}^2\right]^{1/2} & i = l \\ \frac{1}{Q_{ii}}\left[S_{il} - \sum_{k=1}^{i-1} Q_{ki}Q_{kl}\right]^{1/2} & i < l \end{cases} \qquad \text{(Eq. B-52)}$$

Where $S_{il} = \int_0^{\infty} r^2 \varphi_i(r)\varphi_l(r)\, dr$ and

$$\varphi_i(r) = \begin{cases} e^{-\alpha_i r^2}, & i = 1,2,3 \\ r^2\, e^{-\alpha_i r^2}, & i = 4,5,6 \end{cases} \qquad \text{(Eq. B-53)}$$

II.4.2.1.3. Kerker Pseudopotetials

Also in this approach [23] pseudopotentials with the HSC properties are constructed. But instead of using cutoff functions (f_1, f_2, f_3) the pseudo wavefunctions are directly constructed from the all–electron wavefunctions by replacing the all–electron wavefunction inside some cutoff radius by a smooth analytic function that is matched to the all– electron wavefunction at the cutoff radius. The HSC properties then translate into a set of equations for the parameters of the analytic form. After having determined the pseudo wavefunction the Schrdinger equation is inverted and the resulting potential unscreened. Note that the cutoff radius of this type of pseudopotential construction scheme is considerably larger than the one used in the HSC scheme. Typically the cutoff radius is chosen slightly smaller than R_{max} , the outermost maximum of the all–electron wavefunction. The analytic form proposed by Kerker is

$$\phi_l^{ps}(r) = r^{l+1}e^{p(r)} \qquad \text{(Eq. B-54)}$$

with

$$p(r) = \alpha r^4 + \beta r^3 + \gamma r^2 + \delta \qquad \text{(Eq. B-55)}$$

The term linear in r is missing to avoid a singularity of the potential at $r = 0$. The HSC conditions can be translated into a set of equations for the parameters α, β, γ, δ.

II.4.2.1.4. Trouiller–Martins Pseudopotentials

The Kerker method was generalized by Trouiller and Martins [24] to polynomials of higher order. The rational behind this was to use the additional parameters (the coefficients of the

higher terms in the polynomial) to construct smoother pseudopotentials. The Trouiller–Martins wavefunctions has the following form

$$\phi_l^{ps}(r) = r^{l+1} e^{p(r)} \qquad \text{(Eq. B-56)}$$

with

$$p(r) = c_0 + c_2 r^2 + c_4 r^4 + c_6 r^6 + c_8 r^8 + c_{10} r^{10} + c_{12} r^{12} \qquad \text{(Eq. B-57)}$$

and the coefficients c_n are determined from

- norm–conservation
- For n=0…4

$$\left.\frac{d^n \phi^{ps}}{dr^n}\right|_{r=r_c} = \left.\frac{d^n \phi}{dr^n}\right|_{r=r_c} \qquad \text{(Eq. B-58)}$$

-

$$\left.\frac{d\phi^{ps}}{dr}\right|_{r=0} = 0 \qquad \text{(Eq. B-59)}$$

II.4.2.1.5. Kinetic Energy Optimized Pseudopotentials

This scheme is based on the observation that the total energy and the kinetic energy have similar convergence properties when expanded in plane waves. Therefore, the kinetic energy expansion is used as an optimization criteria in the construction of the pseudopotentials. Also this type [25] uses an analytic representation of the pseudo wavefunction within r_c

$$\phi_l^{ps}(r) = \sum_{i=1}^{n} a_i j_l(q_i r) \qquad \text{(Eq. B-60)}$$

where $j_l(qr)$ are spherical Bessel functions with i-1 zeros at positions smaller than r_c. The values of q_i are fixed such that

$$\frac{j'(q_i r_c)}{j(q_i r_c)} = \frac{\phi'_l(r_c)}{\phi_l(r_c)} \qquad \text{(Eq. B-61)}$$

The conditions that are used to determine the values of a_i are:

- ϕ_l^{ps} is normalized
- First and second derivatives of ϕ_l are continuous at r_c
- $\Delta E_K (\{a_i\}, q_c)$ is minimal

$$\Delta E_k = - \int d^3 r \phi_l^{ps*} \nabla^2 \Psi_l^{ps} - \int_0^{q_c} d q q^2 |\phi_l^{ps}(q)|^2 \qquad \text{(Eq. B-62)}$$

ΔE_K is the kinetic energy contribution above a target cutoff value q_c. The value of q_c is an additional parameter (as for example r_c) that has to be chosen at a reasonable value. In practice q_c is changed until it is possible to minimize ΔE_K to a small enough value.

II.4.2.2. Pseudopotentials in the Plane Wave Basis

With the methods described in the last section we are able to construct pseudopotentials for states $l = s, p, d, f$ by using reference configurations that are either the ground state of the atom or of an ion, or excited states. In principle higher angular momentum states could also be generated but there physical significance is questionable. In a solid or molecular environment there will be wavefunction components of all angular momentum character at each atom. The general form of a pseudopotential is

$$V_{pp}(\boldsymbol{r},\boldsymbol{r}') = \sum_{l=0}^{\infty}\sum_{m=-1}^{l} V^l(r)P^{lm}(\omega) \tag{Eq. B-63}$$

where $P^{lm}(\omega)$ is a projector on angular momentum functions. A good approximation is to use

$$V^l(\boldsymbol{r}) = V^c(\boldsymbol{r}) \text{ for } l > l_{max} \tag{Eq. B-64}$$

With this approximation one can rewrite

$$V_{pp}(\boldsymbol{r},\boldsymbol{r}') = \sum_{L}^{\infty} V^c(\boldsymbol{r})P^{lm}(\omega) + \sum_{L}^{\infty}[V^l(\boldsymbol{r}) - V^c(\boldsymbol{r})]P^{lm}(\omega)$$

$$= V^c(\boldsymbol{r})\sum_{L}^{\infty} P^{lm}(\omega) + \sum_{L}^{\infty} \delta V^l(\boldsymbol{r})\, P^{lm}(\omega)$$

$$= V^c(\boldsymbol{r}) + \sum_{L}^{\infty} \delta V^l(\boldsymbol{r})P^{lm}(\omega) \tag{Eq. B-65}$$

where the combined index $L = \{l, m\}$ has been used. The pseudopotential is now separated into two parts; the local or core pseudopotential $V^c(r)$ and the non–local pseudopotentials $\delta V^l(r)P^{lm}(\omega)$. The pseudopotentials of this type are also called semilocal, as they are local in the radial coordinate and the nonlocality is restricted to the angular part.

The contribution of the local pseudopotential to the total energy in a Kohn–Sham calculation is of the form

$$E_{local=}\int V^c(\boldsymbol{r})n(\boldsymbol{r})d\boldsymbol{r} \tag{Eq. B-66}$$

It can easily be calculated together with the other local potentials. The non–local part needs special consideration as the operator in the plane wave basis has no simple structure in real or reciprocal space. There are two approximations that can be used to calculate this contribution to the energy. One is based on numerical integration and the other on a projection on a local basis set.

II.4.2.2.1. Gauss–Hermit Integration

The matrix element of the non–local pseudopotential

$$V^{nl}(\boldsymbol{G},\boldsymbol{G}') = \sum_L \frac{1}{\Omega} \int d\boldsymbol{r}\, e^{-i\boldsymbol{Gr}} \Delta V^L(\boldsymbol{r}) e^{i\boldsymbol{G'r}}$$

$$= \sum_L \int_0^\infty dr\, \langle \boldsymbol{G}|Y_L\rangle_\omega\, r^2 \Delta V^L(\boldsymbol{r}) \langle Y_L|\boldsymbol{G}'\rangle_\omega \qquad \text{(Eq. B-67)}$$

where $\langle .|.\rangle_\omega$ stands for an integration over the unit sphere. These integrals still depend on r. The integration over the radial coordinate is replaced by a numerical approximation

$$\int_0^\infty r^2 f(r) dr \approx \sum_i w_i f(\boldsymbol{r}_i) \qquad \text{(Eq. B-68)}$$

The integration weights w_i and integration points $\boldsymbol{r}_i$ are calculated using the Gauss– Hermit scheme. The non–local pseudopotential is in this approximation

$$V^{nl}(\boldsymbol{G},\boldsymbol{G}') = \sum_L \frac{1}{\Omega} \sum_i w_i \Delta V^L(\boldsymbol{r}_i) \langle \boldsymbol{G}|Y_L\rangle_\omega^{r_i} \langle Y_L|\boldsymbol{G}'\rangle_\omega^{r_i}$$

$$= \sum_L \frac{1}{\Omega} \sum_i w_i \Delta V^L(\boldsymbol{r}_i) P_i^{L*}(\boldsymbol{G}) P_i^L(\boldsymbol{G}') \qquad \text{(Eq. B-69)}$$

Where the definition for the projectors P

$$P_i^L(\boldsymbol{G}) = \langle Y_L|\boldsymbol{G}\rangle_\omega^{r_i} \qquad \text{(Eq. B-70)}$$

has been introduced. The number of projectors per atom is the number of integration points (5 -20 for low to high accuracy) multiplied by the number of angular momenta. For the case of s and p non–local components and 15 integration points this accounts to 60 projectors per atom.

The integration of the projectors can be done analytically

$$P_i^L(\boldsymbol{G}) = \int_\omega Y_L^*(w) e^{i\boldsymbol{Gr}_i} d\omega$$

$$= \int_\omega Y_L^*(w) 4\pi \sum_{i=0}^\infty i^l j_l(\boldsymbol{Gr}_i) \sum_{m'=-1}^l Y_{lm'}^*(w) Y_{lm'}(\boldsymbol{G}) d\omega$$

$$= 4\pi i^l j_l(\boldsymbol{Gr}_i) Y_L(\hat{G}) \qquad \text{(Eq. B-71)}$$

where the expansion of a plane wave in spherical harmonics has been used. j_l are the spherical Bessel functions and $\hat{G}$ the angular components of the Fourier vector $\boldsymbol{G}$.

II.4.2.2.2. Kleinman–Bylander Scheme

The other method is based on the resolution of the identity in a local basis set

$$\sum_\alpha |\chi_\alpha\rangle\langle\chi_\alpha| = 1, \qquad \text{(Eq. B-72)}$$

where $\{\chi_\alpha\}$ are orthonormal functions. This identity can now be introduced in the

integrals for the non–local part

$$V^{nl}(\boldsymbol{G}, \boldsymbol{G}') = \sum_L \int_0^\infty d\boldsymbol{r} \langle \boldsymbol{G}|Y_L\rangle_\omega r^2 \, \Delta \, V^L(\boldsymbol{r})\langle Y_L|\boldsymbol{G}'\rangle_\omega$$

$$= \sum_{\alpha,\beta} \sum_L \int_0^\infty d\boldsymbol{r} \, \langle \boldsymbol{G}|\chi_\alpha\rangle\langle\chi_\alpha|Y_L\rangle_\omega r^2 \Delta V^L(r)\langle Y_L|\chi_\beta\rangle_\omega \langle\chi_\beta|\boldsymbol{G}'\rangle \quad \text{(Eq. B-73)}$$

and the angular integrations are easily performed using the decomposition of the basis in spherical harmonics

$$\chi_\alpha(\boldsymbol{r}) = \chi_\alpha^{lm}(\boldsymbol{r})Y_{lm}(\omega) \qquad \text{(Eq. B-74)}$$

This leads to

$$V^{nl}(\boldsymbol{G}, \boldsymbol{G}') = \sum_{\alpha,\beta} \sum_L \langle \boldsymbol{G}|X_\alpha\rangle \int_0^\infty d\boldsymbol{r}\chi_\alpha^{lm}(r)r^2\Delta V^L(r)X_\beta^{lm}(r)\langle\chi_\beta|\boldsymbol{G}'\rangle$$

$$= \sum_{\alpha,\beta} \sum_L \langle \boldsymbol{G}|\chi_\alpha\rangle \, \Delta V_{\alpha\beta}^l \langle\chi_\beta|\boldsymbol{G}'\rangle \qquad \text{(Eq. B-75)}$$

which is the non–local pseudopotential in fully separable form. The coupling elements of the pseudopotential

$$\Delta V_{\alpha\beta}^l = \int_0^\infty d\boldsymbol{r}\chi_\alpha^{lm}(r) \, r^2\Delta V^L(r)\chi_\beta^{lm}(r) \qquad \text{(Eq. B-76)}$$

are independent of the plane wave basis and can be calculated for each type of pseudopotential once the expansion functions χ are known.

The final question is now what is an optimal set of basis function χ. Kleinman and Bylander [26] proposed to use the eigenfunctions of the pseudo atom, i.e. the solutions to the calculations of the atomic reference state using the pseudopotential Hamiltonian. This choice of a single reference function per angular momenta guarantees nevertheless the correct result for the reference state. Now assuming that in the molecular environment only small perturbations of the wavefunctions close to the atoms occur, this minimal basis should still be adequate. The Kleinman–Bylander form of the projectors is

$$\sum_L \frac{|\chi_L\rangle\langle\Delta V^L\chi_L|}{\langle\chi_L\Delta V^L\chi_L\rangle} = 1, \qquad \text{(Eq. B-77)}$$

where χ_L are the atomic pseudo wavefunctions. The plane wave matrix elements of the non–local pseudopotential in Kleinman–Bylander form is

$$V^{KB}(\boldsymbol{G}, \boldsymbol{G}') = \frac{\langle \boldsymbol{G}|\Delta V^L\chi_L\rangle\langle\Delta V^L\chi_L|\boldsymbol{G}'\rangle}{\langle\chi_L\Delta V^L\chi_L\rangle} \qquad \text{(Eq. B-79)}$$

Generalizations of the Kleinman–Bylander scheme to more than one reference function were introduced by Blöchl [27] and Vanderbilt [28]. They make use of several reference functions, calculated at a set of reference energies.

In transforming a semilocal to the corresponding Kleinman–Bylander (KB) pseudopotential one needs to make sure that the KB–form does not lead to unphysical "ghost" states at energies

below or near those of the physical valence states as these would undermine its transferability. Such spurious states can occur for specific (unfavorable) choices of the underlying semilocal and local pseudopotentials. They are an artefact of the KB–form nonlocality by which the nodeless reference pseudo wavefunctions need to be the lowest eigenstate, unlike for the semilocal form [29]. Ghost states can be avoided by using more than one reference state or by a proper choice of the local component and the cutoff radii in the basic semilocal pseudopotentials. The appearance of ghost states can be analyzed by investigating the following properties:

- Deviations of the logarithmic derivatives of the energy of the KB–pseudopotential from those of the respective semilocal pseudopotential or all–electron potential.
- Comparison of the atomic bound state spectra for the semilocal and KB–pseudopotentials.
- Ghost states below the valence states are identified by a rigorous criteria by Gonze et al. [29].

II.4.2.3. Non-linear Core Correction

The success of pseudopotentials in density functional calculations relies on two assumptions: the transferability of the core electrons to different environments and the linearization of the exchange and correlation energy. The second assumption is only valid if the frozen core electrons and the valence state do not overlap. However, if there is significant overlap between core and valence densities, the linearization will lead to reduced transferability and systematic errors. The most straightforward remedy is to include "semi–core states" in addition to the valence shell, i.e. one more inner shell (which is from a chemical viewpoint an inert "core level") is treated explicitely. This approach, however, leads to quite hard pseudopotentials which call for high plane wave cutoffs. Alternatively, it was proposed to treat the non–linear parts of the exchange and correlation energy E_{xc} explicitly [30]. This idea does not lead to an increase of the cutoff but ameliorates the above–mentioned problems quite a bit.

The method of the non-linear core correction dramatically improves results on systems with alkali and transition metal atoms. For practical applications, one should keep in mind that the non-linear core correction should only be applied together with pseudopotentials that were generated using the same energy expression.

II.4.2.4. Ultrasoft Pseudopotentials Method

For norm–conserving pseudopotentials the all-electron wavefunction is inside some core radius replaced by a soft nodeless pseudo wavefunction, with the crucial restriction that the PS wavefunction must have the same norm as the all-electron wavefunction within the chosen core radius; outside the core radius the pseudo and all-electron wavefunction are identical. It is well established that good transferability requires a core radius around the outermost maximum of the all-electron wavefunction, because only then the charge distribution and moments of the all-electron wavefunction are well reproduced by the pseudo wavefunctions. Therefore, for elements with strongly localized orbitals (like first-row, 3d, and rare-earth elements) the resulting pseudopotentials require large plane wave basis sets. To work around this problem, compromises are often made by increasing the core radius significantly beyond the outermost maximum of the all-electron wavefunction. But this is usually not a satisfactory solution because the transferability is always adversely affected when the core radius is increased, and for any new chemical environment, additional tests are required to establish the reliability of such soft pseudopotentials.

An elegant solution to this problem was proposed by Vanderbilt [31]. In his method, the norm–conservation constraint is relaxed and to make up for the resulting charge deficit, lo- calized atom–centered augmentation charges are introduced. These augmentation charges are defined as the charge difference between the all-electron and pseudo wavefunctions, but for convenience they are pseudized to allow an efficient treatment of the augmentation charges on a regular grid. The core radius of the pseudopotential can now be chosen around the nearest neighbor distance; independent of the position of the maximum of the all-electron wavefunction. Only for the augmentation charges a small cutoff radius must be used to restore the moments and the charge distribution of the all-electron wavefunction accurately. The pseudized augmentation charges are usually treated on a regular grid in real space, which is not necessarily the same as the one used for the representation of the wavefunctions. The relation between the ultrasoft pseudopotential method and other plane wave based methods was discussed by Singh [32].

References

[1] P. Hohenberg and W. Kohn. Phys. Rev. B **136**, 864 (1964).

[2] W. Kohn and L. J. Sham. Phys. Rev. A **140**, 1133 (1965).

[3] W. E. Pickett, Comput. Phys. Rep. **9**, 115 (1989).

[4] J. P. Perdew and Y. Wang. Phys Rev. B **45**, 13244 (1992).

[5] R. O. Jones and O. Gunnarsson, Rev. Mod. Phys. **61**, 689 (1989).

[6] W. Kohn and L. J. Sham, Phys. Rev. **140**, A1133 (1965).

[7] U. von Barth and L. Hedin, J. Phys. C **5**, 1629 (1972).

[8] J. P. Perdew and A. Zunger, Phys. Rev. B **23**, 5048 (1981).

[9] S. Goedecker and C. J. Umrigar, Phys. Rev. A **55**, 1765 (1997).

[10] A. D. Becke, J. Chem. Phys. **98**, 1372 (1993).

[11] A. D. Becke, J. Chem. Phys. **98**, 5648 (1993).

[12] A. Görling, Phys. Rev. B **53**, 7024 (1996).

[13] F. Gygi and A. Baldereschi, Phys. Rev. B **34**, 4405 (1986).

[14] E. I. Proynov, S. Sirois, and D. R. Salahub, Int. J. Quantum Chem. **64**, 427 (1997).

[15] N.W Ashcroft and N.D. Mermin, *Solid State Physics*, (Saunders College Publishing, Philadelphia, 1976).

[16] D.J. Chadi and M.L. Cohen, Phys. Rev. B **8**, 5747 (1973).

[17] J. Moreno and J.M. Soler, Phys. Rev. B **45**, 13891 (1992).

[18] C.-L. Fu and K.-M. Ho, Phys. Rev. B **28**, 5480 (1983).

[19] P.E. Blochl, O. Jepsen, and O.K. Andersen, Phys. Rev. B **49**, 16223 (1994).

[20] W.H. Press, S.A. Teukolsky, W.T. Vetterling, and B.P Flannery, *Numerical Recipes*, (Cambridge University Press, 1992).

[21] D.R. Hamann, M. Schl¨uter, and C. Chiang, Phys. Rev. Lett. **43**, 1494 (1979).

[22] G.B. Bachelet, D.R. Hamann, and M. Schluter, Phys. Rev. B **26**, 4199 (1982).

[23] G.P. Kerker, J. Phys. C: Solid State Phys. **13**, L189 (1980).

[24] N. Troullier and J.L. Martins, Phys. Rev. B **43**, 1993 (1991).

[25] A.M. Rappe, K.M. Rabe, E. Kaxiras, and J.D. Joannopoulos, Phys. Rev. B **41**, 1227 (1990).

[26] L. Kleinman and D.M. Bylander, Phys. Rev. Lett. **48**, 1425 (1982).

[27] P.E. Blochl, Phys. Rev. B **41**, 5414 (1990).

[28] D. Vanderbilt, Phys. Rev. B **41**, 7892 (1990).

[29] X. Gonze, R. Stumpf, and M. Scheffler, Phys. Rev. B **44**, 8503 (1991).

[30] S. G. Louie, S. Froyen, and M. L. Cohen, Phys. Rev. B **26**, 1738 (1982).

[31] D. Vanderbilt, Phys. Rev. B **41**, 7892 (1990).

[32] D. J. Singh, Plane waves, Pseudopotentials and the LAPW Method (Kluwer, Dordrecht, 1994).

Tools

The most important factors determining the level of theory of a quantum-mechanical computer experiment are the choice of an exchange–correlation functional, the choice of a basis-set for the expansion of the Kohn–Sham orbitals, charge- and spin densities and potentials, and the algorithm adopted for solving the Kohn–Sham equations and for calculating energies, forces and stresses. The degree to which the chosen functional accounts for many-electron correlations and the completeness of the basis-set determine the accuracy of the calculation, the numerical algorithms are decisive for its efficiency.

Our calculations, both static and ab initio molecular dynamics, were performed using the Generalized Gradient Approximation formulated by Perdew-Wang functional (GGA-PW91) and the UltraSoft PseudoPotential (USPP) method and plane wave basis set. These calculations were carried out using the Vienna Ab initio Simulation Package (VASP). The VASP code is developed at the Institute fur Materialphysik at the University of Wien by Kresse, Furthmüller and Hafner. More details about the calculation methods will be given in the beginning of the two following chapters.

Chapter III

Static ab initio calculations (0K)

In this chapter, the results of the static calculations of the substitutions of Ti and Zr transition metals in the bulk as well as at the $\sum 5$ (310)[001] grain boundary are presented. To this end, the chapter is divided into three sections. In section I, the computational details of our static calculations are given. Section II gives the results of the energetic of the point defects in the bulk of the $D0_3$-Fe_3Al structure. Emphasis is also given on the importance of using relaxation when determining formation energy of calculation for site preference configurations. In the last section, the behaviour of the two transition metals Ti and Zr in the $\sum 5$ (310) grain boundary are discussed. The formation energies, the interface energies and the electronic charge density transfer associated with the presence of the impurity has been investigated.

I. Computational details

I.1. Computational method

Our calculations were performed within the Vanderbilt-type UltraSoft PseudoPotential (USPP) [1] and the formalism of Density Functional Theory as implemented in the Vienna Ab initio Simulation Package (VASP) [2, 3]. The electronic wave functions were expanded in plane waves with a kinetic energy cutoff of 240 eV. The USPPs employed in this work explicitly treated eight valence electrons for Fe ($4s^23d^6$), three valence electrons for Al ($3s^23p^1$) and four valence electrons for both Ti ($4s^23d^2$) and Zr ($5s^24d^2$). The spin polarization was taken into account for all calculations.

The Generalized Gradient Approximation (GGA-PW91) was employed for evaluation of the exchange – correlation energy with the Perdew and Wang version [4, 5].

The Brillouin zone integrations were performed using Γ centered Monkhorst-Pack [6] k-point meshes, and the Methfessel- Paxton [7] technique with a 0.3 smearing of the electrons levels. Tests were carried out for Fe_3Al unit cell (four atoms by cell) using different k-point meshes to ensure the absolute convergence of the total energy to a precision of 10^{-3} eV/atom. As a result, the k-mesh for the Fe_3Al unit cell was adapted using (16x16x16) k-points. Depending on the structure and the size of the cell, the number of k-points changes as a consequence of the resultant modification of the Brillouin zone size. For total energy calculations of the Fe_3Al supercells with 32 atoms (2x2x2 unit cell) and 108 atoms (3x3x3 the unit cell), the (8x8x8) and (4x4x4) k-points mesh were chosen, respectively. In the case of grain boundary configurations, the Monkhorst- Pack grid was adapted to the supercell parameters using (4x2x5) k-points.

The ground state atomic geometries were obtained by the minimizing the Hellman-Feyman forces using a conjugate –gradient algorithm until force on each atom reaches a convergence level of 0.1 Å/atom and for an external pressure lower than 0.3 GPa.

I.2. Structural properties

All the results presented below were obtained employing the computational settings described in the previous paragraph. However, for the *Fe₃Al-D0₃* unit cell additional calculations were also conducted with alternative settings to gauge the overall accuracy of the reported results. Specifically, test calculations were performed employing the Local-Density Approximation (LDA) as well as the GGA, in order to compare the two approximations and determine the influence of the analytical representation of the exchange-correlation functional.

Fig. III-1 shows the total energy plotted, as function of the volume of the unit cell, for the GGA and LDA functionals. The solid lines are the result of fit to Birch-Murnaghan equation of state [8]. The equilibrium lattice constants and bulk modulli were determined from these fitted curves. The values are given in Table. III-1 along with the available theoretical and experimental data for $D0_3$-Fe_3Al.
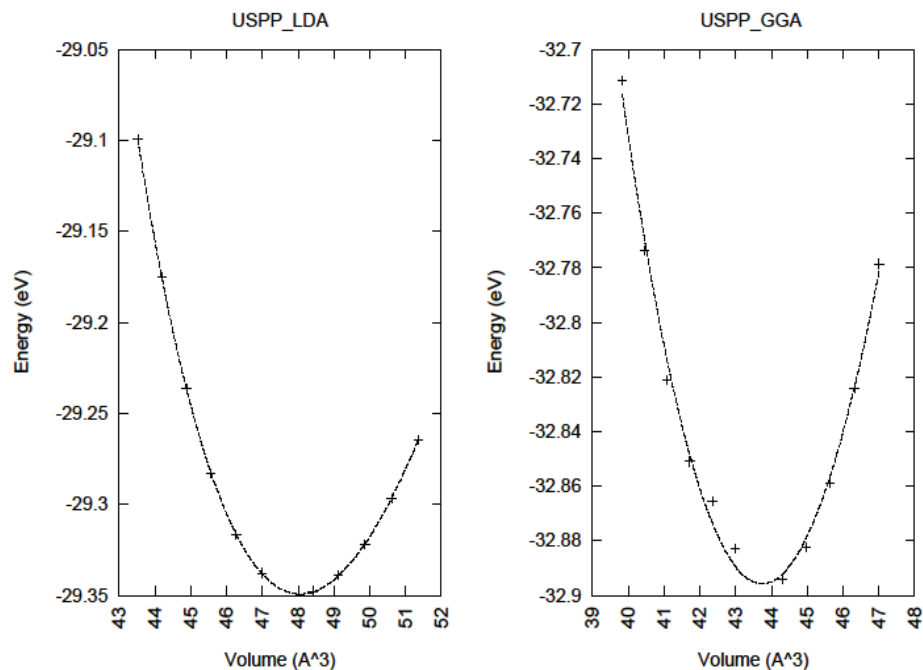
Figure. III- 1 The total energy within LDA and GGA according to the pseudopotential calculations.

Not surprisingly, the GGA functional gives a larger value for the equilibrium lattice constant compared to the LDA functional, as it is well known that in most cases the frequent over binding for transition metals and their compounds in LDA is corrected with GGA. Furthermore, a fairly good agreement is found for the lattice parameter and the bulk modulus, which are calculated with the USPP-GGA, when compared with the values from experiment [13]. The present value of lattice parameter 5.76Å is also comparable to the other theoretical values obtained with GGA exchange-correlation functional [13-14, 15]. In summary, the results show that the used ultarsoft pseudopotential and the GGA exchange-correlation approximation reproduce successfully the structural properties of the $D0_3$-Fe_3Al structure.

Table. III-1. Lattice parameters and the bulk modulus for Fe_3Al- $D0_3$.

	a(Å)	B(Gpa)
Present Work		
USPP-GGA	5.76	143
USPP-LDA	5.59	157
Theory		
FPLAPW-GGA-sp [Gonzales et al. 2002][1]	5.77	–
USPP-PBE [Connétable et al. 2008][2]	5.76	159
MBPP-PBE-sp [Lechermann et al. 2002][3]	5.78	151
MBPP-CAPZ-sp [Lechermann et al. 2002]	5.60	192
PWSCF-PBE [Kellou et al. 2010][4]	5.78	139
Experiment	5.79 [Nishino et al. 1997][5]	144 [Leamy et al. 1967][6]

I.3. Energetics

In this section, we first define the energies used in our calculations.

To examine the preferential site occupations of the transition metal atoms both in the bulk and at the grain boundary, their formation energies E_f were evaluated in different sites by:

$$E_f = E_{solid}\ (Fe_3AlX) + E_{Fe\ or\ Al} - E_{solid}\ (Fe_3Al) - E_X \qquad \text{(Eq.III-1)}$$

for substitutional impurities and by

$$E_f = E_{solid}\ (Fe_3AlX) - E_{solid}\ (Fe_3Al) - E_X \qquad \text{(Eq.III-2)}$$

for interstitial impurities.

The formation energy, for the case of vacancies, was evaluated using the following equation [16]

$$E_f = E_{solid}\ (Fe_3Alv) + E_{Fe\ or\ Al} - E_{solid}\ (Fe_3Al) \qquad \text{(Eq.III-3)}$$

In these equations, X and v represent the T.M. atoms and vacancies, respectively. $E_{solid}(Fe_3AlX)$ (*solid* referring to bulk as well as G.B.) is the energy of the supercell containing one substitutional or interstitial impurity and $E_{solid}\ (Fe_3Al)$ is the energy of the pure supercell without defect. $E_{Fe\ or\ Al}$ (Fe or Al being the atom which is substituted) and E_X are the calculated total energies for pure metals in their equilibrium lattices -*bcc* Fe, *fcc* Al, *hcp* Ti and *hcp* Zr. Note

[1] Ref. [10]
[2] Ref. [11]
[3] Ref. [12]
[4] Ref. [13]
[5] Ref. [14]
[6] Ref. [15]

that, as it is very unlikely that Ti and Zr reside on interstitial sites in the bulk, Eq. III-2 will only be used for the analysis of Ti and Zr interstitials within the G.B.

The grain boundary energy γ_{GB} for the undoped system is defined as:

$$\gamma_{GB} = (E_{GB} - E_{bulk}) / 2A \qquad \text{(Eq.III-5)}$$

E_{GB} and E_{bulk} are the total energies of the grain boundary and bulk supercells, respectively, and A is the area of the interface (the factor of ½ is needed to account for the presence of two symmetrically equivalent grain boundaries per simulation cell). In our computer simulations, the energies E_{GB} and E_{bulk} are calculated for simulations blocks consisting of an equal number of atoms of each species.

For the impurity doped system, the G.B. energy is evaluated from:

$$\gamma_{GB} = (E_{GBX} - E_{Fe3AlX}) / 2A \qquad \text{(Eq.III-6)}$$

In this formulation, as presented in [17, 18], E_{GBX} and E_{Fe3AlX} are the total energies of the supercells with impurity- doped G.B. and bulk Fe₃Al, respectively.

II. Point defects in bulk Fe$_3$Al

We first investigate the properties of point defects in the bulk of the D0$_3$ Fe$_3$Al structure. Because of their atomic size, Ti and Zr must occupy substitutional sites rather than interstitial ones within the bulk Fe$_3$Al. The three types of possible point defects- i.e substitution impurity or vacancy formation on Al, FeI, FeII sites (see Fig. III-2)- were modeled within a supercells containing 32 and 108 atoms. It must be noted that, when substituting an impurity atom (Ti or Zr) on a site of the 32 atoms supercell, the corresponding impurity concentration is about 3 at.%. For the case of 108 atoms supercell, the impurity concentration is about 1 at. %.
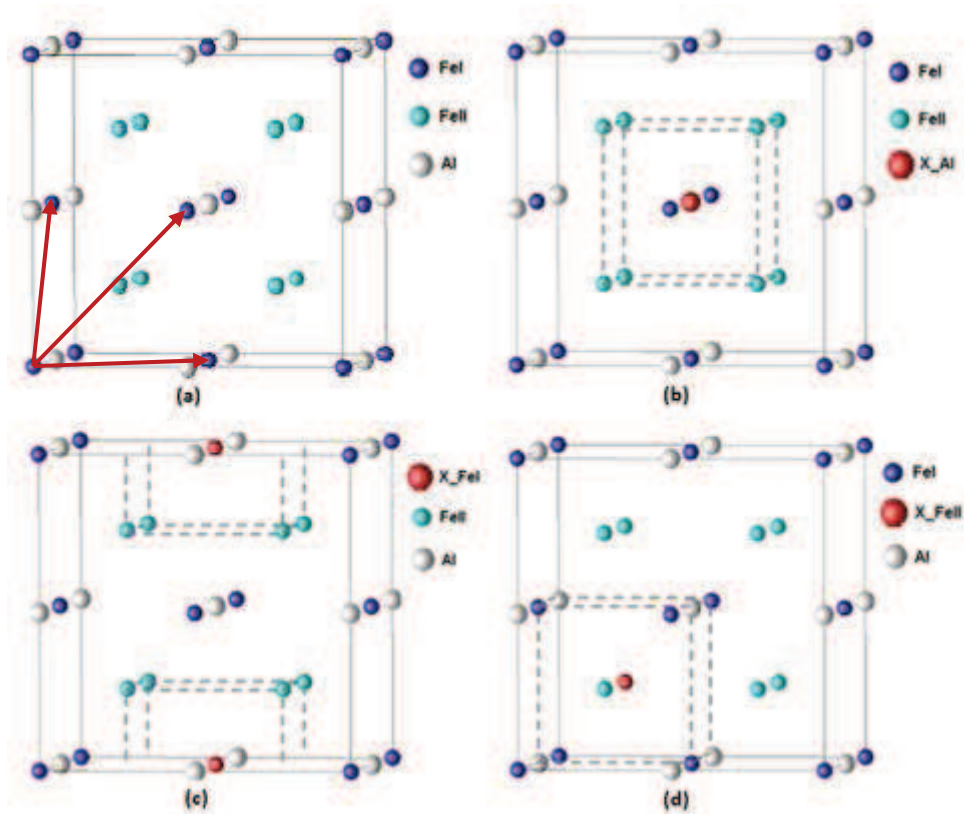
Figure. III- 2 (a) The un-doped structure of the bulk Fe_3Al and the three point defects substitutions as well as vacancies on (b) the Al site (c) the FeI site and (d) the FeII site.

II.1. Importance of relaxation

In order to have some insight in the effect of relaxation and underline the importance of this relaxation for the calculation of intermetallics, Fig. III-3 compares the formation energy of the substitution defects calculated by using unrelaxed and relaxed supercells (with 32 atoms). It is clear that the relaxation leads to an overall reduction in the formation energies. Additionally, though the curves have the same profile, it appears clearly that the differences in formation energies determined using the unrelaxed and relaxed supercells are lower for substitutions of Ti than for Zr. On a first approach, this difference may be attributed to the differences in size between the Ti and Zr atoms (the Ti atom is smaller than the Zr one). What is important to stress here is essentially the magnitude of the differences. While the overall differences under the relaxed and unrelaxed modes are in the range 15 to 50 % for the various Ti substitutions, the relaxation decreases the formation energy by more than 140 % in the case of the substitution of a Zr atom on a Fe^{II} site. For the case of vacancies, the relaxation is more pronounced when the vacancy is created in the Al site. This can also be related to the difference in size between the Fe and Al atoms. Knowing that the Al atom is greater than the Fe one, the void created when the

vacancy is produced in the Al site is larger and, consequently, the relaxation is also more important. Thus, in the following, only data obtained from relaxed configurations are treated.
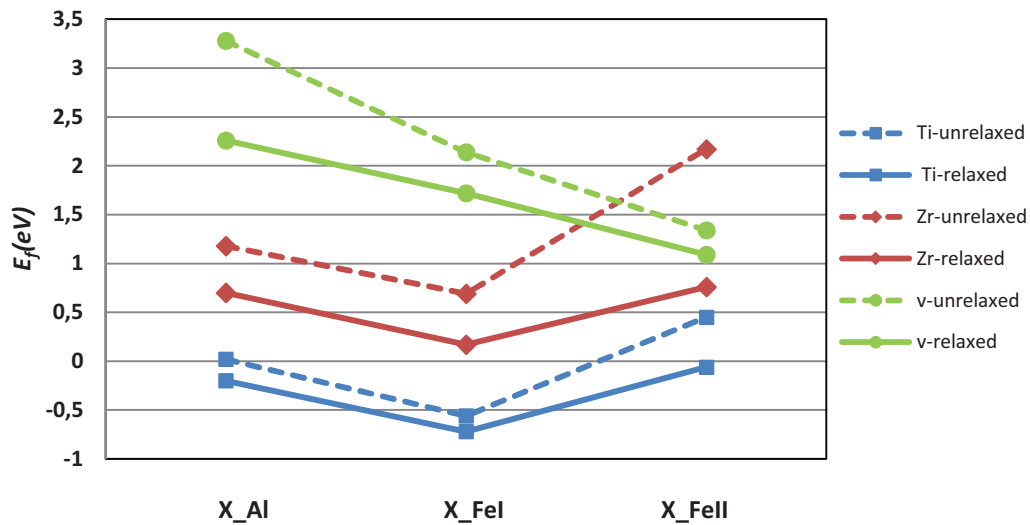
Figure. III- 3 Energy profile of point defects formation energies for unrelaxed and relaxed D0$_3$-Fe$_3$Al supercells.

II.2. The site preference of point defects in the bulk D0$_3$-Fe$_3$Al

The values of formation energies for substitutions and vacancies in relaxed supercells are given in Table III-2. The results obtained by Mayer et al. for 32 atoms [19] are also listed in Table III-2 for comparison.

Table. III-2 The calculated effective formation energies (in eV) for point defects in D0$_3$-ordered bulk Fe$_3$Al.

	E_f^{Ti}			E_f^{Zr}			E_f^{v}		
	Al	FeI	FeII	Al	FeI	FeII	Al	FeI	FeII
Present work									
Relaxed (108 atoms)	-0.46	-1.01	-0.39	0.45	-0.14	0.39	0.94	0.34	0.31
Relaxed (32 atoms)	-0.20	-0.72	-0.06	0.70	0.17	0.76	2.26	1.72	1.09
Theory [19]									
Unrelaxed (32 atoms)							1.97	2.44	1.71

From Table III-2, it can be seen that, though the vacancies occur with positive formation energies in the three different configurations, the lower formation energy correspond to the substitution on the FeII site. This tend agrees well with the conclusion of Mayer et al. [19] obtained by ab-initio pseudopotential method. Our value of the formation energy of a vacancy in

FeII sublattice (1.09 eV) is also comparable to (1.18±0.04 eV) obtained by Schaefer et al. [20] from positron annihilation experiments. Comparatively, Jiraskova et al. [21], who investigated the Mössbauer spectra of a $Fe_{72}Al_{28}$ compound, found that the Fe vacancies appear on the FeI sublattice which is in conflict with our result and that obtained by Mayer et al [19]. Since the results of Jiraskova were obtained at ambient temperature, unlike our calculations and those of Mayer et al. [19] which were carried out at 0K, the difference in site occupation of vacancies can be related to the effect of temperature.

To check this possibility, we have calculated the defect energies of the vacancies on the FeI and FeII sites at 300K, using the Ab Initio Molecular Dynamics. The defect energies are defined as a change in energy of the pure cluster when an impurity replaces the FeI or the FeII sites, namely,

$$E_d = E(d) - E_0 \qquad\qquad \text{(Eq. III-7)}$$

$E(d)$ and E_0 are the energies of the supercell with and without transition metal impurities, respectively. The preferential site then corresponds to the case where the energy is gained by replacing the FeI/FeII sites.

More details about the calculations of the temperature dependence of the defect energies will be presented in Chapter IV. However, some results are presented here in Table. III- 3 together with the results of the defects energies calculated at 0K. The values of the defect energies are more important than that of the formation energies. This is because the value of the total energy of pure iron in its equilibrium lattices (*bcc* Fe) has not been subtracted as defined in Eq. III-2.

As seen from Table. III-3, the FeII site remains the favoured site occupation of vacancies even at 300K. This means that the temperature changes in the range 0→300K does not modify the stability of vacancies in the bulk D0$_3$-Fe$_3$Al intermetallic compound. Here, both the static ab initio and molecular dynamics at 300K results are in conflict with the Mossbauer conclusions. This indicates that the disagreement with the experimental results does not be related to the effect of temperature but is certainly related to the high sensitivity of these alloys to the vacancies. This is because the difference between the formation energies of 3% and 1% of vacancies calculated in supercells with 32 and 108 atoms is important. From Table. III-2, one can see that the formation energies at different sites are reduced by ~60% when the concentration of vacancies is reduced. From 1% (at 108 atoms) to 3% (at 32 atoms), additionally, the difference between the formation energies of vacancies on the FeI and FeII sites is also reduced with the concentration of the vacancies. The difference between the formation energies is about

0.6 eV for the 3% of vacancies while for the case of the concentration of 1%, the difference is only about 0.03 eV.

Table. III-3. The defect energies of vacancies on the FeI and FeII sites. $E(d)$ and E_0 are the energies of the supercell with and without transition metal impurities, respectively.

	$E_d = E(d) - E_0$ (eV)	
	FeI	FeII
0K		
Supercell with 32 atoms (3 at.%)	10.59	9.78
Supercell with 108 atoms (1 at.%)	7.85	7.55
300K		
Supercell with 108 atoms (1 at.%)	9.55	8.89

The calculated formation energies for the substitutions in the relaxed scheme are also shown in Table III-2. For the three configurations of Ti substitution, negative formation energies are obtained. This means that these defects are stable and, in other words, that 1 at% as well as 3 at% of Ti impurities are miscible in Fe_3Al. This is consistent with the solubility data obtained experimentally [22] and from phase diagram calculations available in the literature [23]. The calculation also shows that the most stable configuration for Ti is to reside on the FeI site, with the lower effective formation energies for both types of calculation (i.e. concentration). This is the correct prediction of the experimentally observed behavior [24]. For the case of Zr, the most favoured configuration is also the substitution on a FeI site. However, contrary to Ti, at 3% concentration all the formation energies are positive, indicating a cost in energy to introduce Zr on a substitution site in the bulk. It is interesting to notice that these values tend to diminish when the calculation is carried out with 108 atoms and that the concentration of defects decreases. This is consistent with experimental observation indicating that the solubility of Zr is below 0.1% and that precipitation of a second phases such as Laves phase $Zr(Fe,Al)_2$ and the τ_1 phase $Zr(Fe,Al)_{12}$ by adding small amounts of Zr [25].

III. Impurity segregation at grain boundaries

III.1. Crystal structures and location of structural defects

The atomic structure of the $\sum 5$ (310)[001] symmetric tilt grain boundary in Fe_3Al was obtained using geometrical rules of the Coincidence Site Lattice model (CSL). An overview about the CSL theory is given in *Appendix A*. Fig. III-4 gives a view of the resultant cell showing the symmetry of the $\sum 5$ (310) [001] grain boundary. Along the [001] direction, the supercell contains in fact four alternating (001) layers separated by the fourth lattice constant, a_0. The four

layers consist of two pure FeII layers and two mixed FeI/Al layers as shown in Fig. III-4 (b). The cell size was chosen in order to preserve a large amount of bulk crystal between the two interfaces visible in Fig. III-4 (a), and, thereby, reasonable energy convergence. Several calculations were made preliminarily in order to estimate the sufficient number of planes. Following these energy convergence calculations, it was estimated that 20 planes parallel to the grain boundary plane were required. This configuration leads to a total of 80 atoms per calculation cell. It must also be noted that, considering a grain boundary region having a thickness of five atomic planes, the local concentration of impurities at the grain boundary when substituting one atom is about 1.25 at.%.
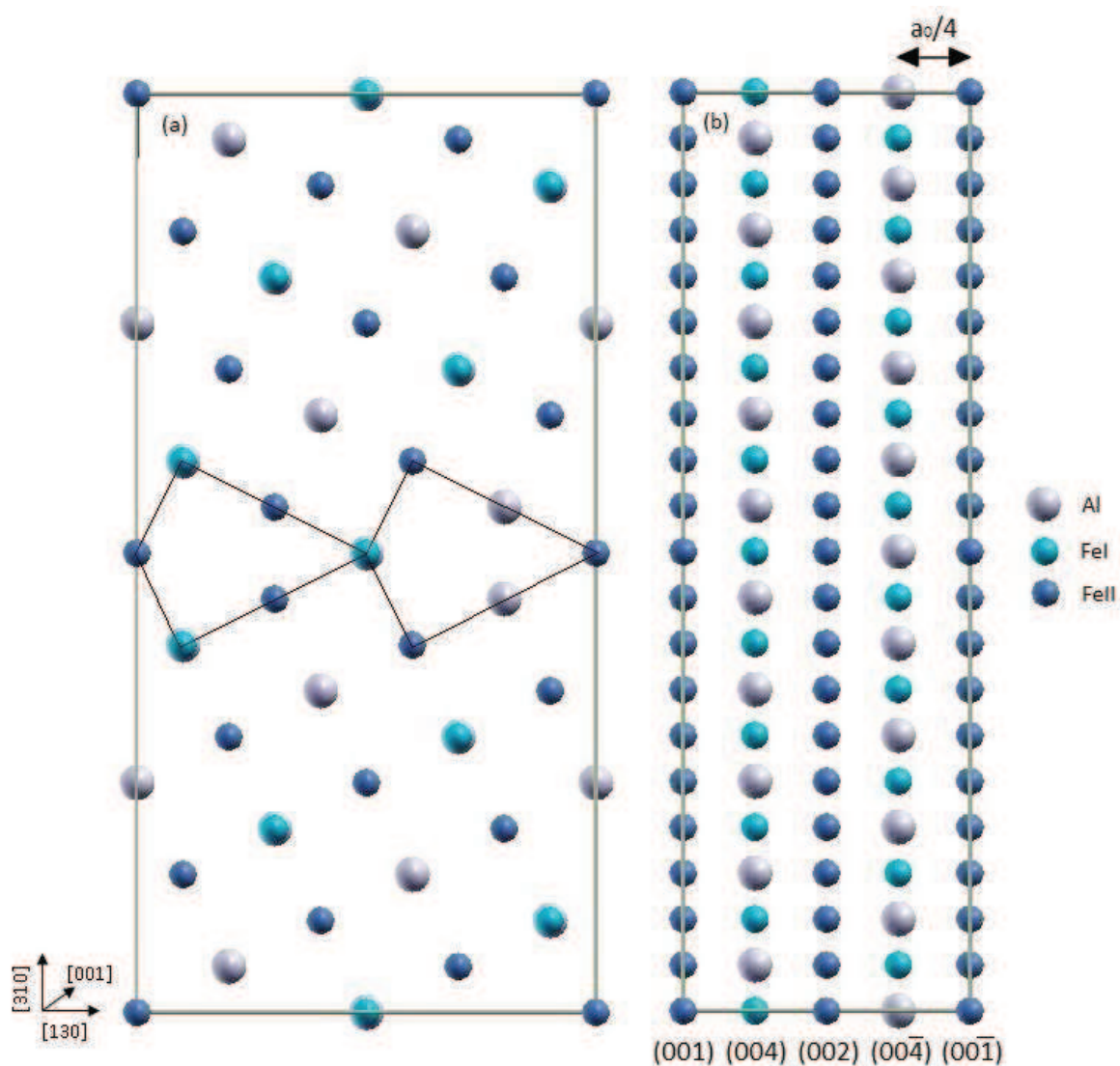
Figure. III- 4 Atomic structure of the Fe_3Al $\sum 5$ (310) [001] grain boundary (a) viewed along the [001] direction (b) viewed along the (130) direction.

The $D0_3$ structure being more complex than the B2 one [26], the number of G.B. defects to be taken into account is significantly larger. The location of the G.B. defects is given in Fig.III-5.

From Fig. III-5 (a), it can be seen that nine typical substitutional sites are present within the $\sum 5$ (310) grain boundary. They are grouped in three categories depending on their distance from the interface: (i) three sites within the G.B. interface *0Al*, *0FeI* and *0FeII* (ii) three sites in the first plane from the G.B. *1Al*, *1FeI* and *1FeII*, and (iii) three sites in the second plane from the GB, *2Al 2FeI* and *2FeII*. In Fig.III-5 (b) are presented the two sites corresponding to the possible insertion of an interstitial atom within the empty space generated at the grain boundary interface. They correspond to the site *(1)* with only *FeII* atoms as first neighbours and the site *(2)* with both *Al* and *FeI* as neighbour atoms.
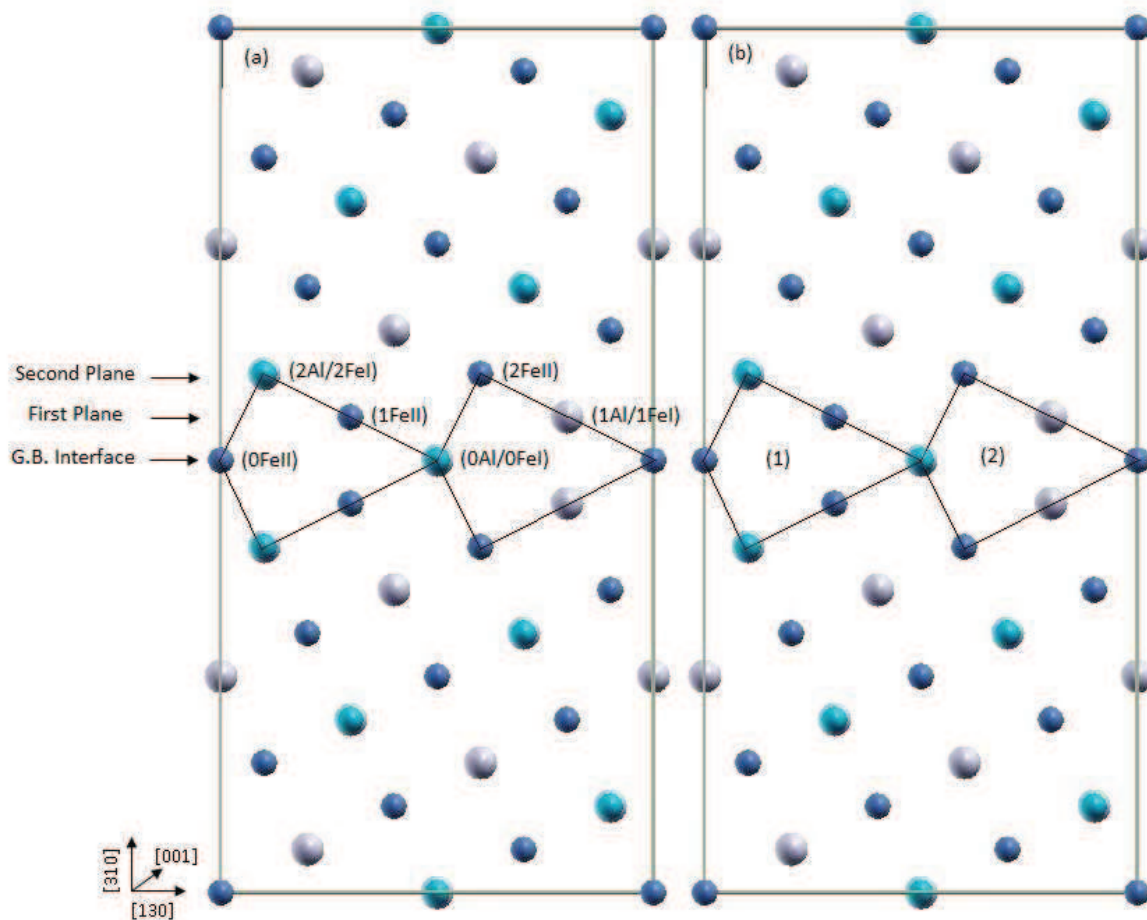
Figure. III- 5 Typical (a) substitutional sites and (b) the interstitial sites within the G.B. interface.

III.2. Site preference and effect of Ti and Zr on the grain boundary cohesion

The calculated impurity formation energies of the two transition metals in the grain boundary are given in Table III-4 for each type of defect.

Table. III-4 The calculated effective formation energies (in eV) for relaxed grain boundary supercells.

				E_f *(in eV)*							
	Insertions		*Substitutions*								
			G.B. Interface			*First plane from G.B.*			*Second plane form G.B.*		
	(1)	**(2)**	0Al	0FeI	0FeII	1Al	1FeI	1FeII	2Al	2FeI	2FeII
Ti- doped GB	0.31	0.90	0.05	-0.86	-0.63	-0.44	-1.32	-1.21	0.31	-0.98	-0.93
Zr- doped GB	-0.18	2.09	0.49	-0.47	-0.51	-0.04	-0.97	-0.90	0.05	-0.66	-0.78

As seen in Table III-4, between the two types of interstitials (**1** and **2**), the most favorable configuration is the interstitial site **(1)** for both Ti and Zr doped grain boundaries. This may be explained simply as a consequence of surroundings effects: in this configuration the impurities are surrounded only by FeII neighboring atoms. The same behavior was obtained in FeAl for B atoms which preferred to be inserted along a $\sum 5$ (310) grain boundary at locations where they could be surrounded by Fe near neighbors [26]. There is however here a clear difference in the behaviors of the Ti and Zr impurity atoms. The formation energy is positive for both configurations if we consider the presence of Ti interstitial, indicating thereby that it costs more energy to insert Ti at the grain boundary interface. Comparatively, the atomic configuration becomes more stable (-0.18 eV) when Zr is inserted at a **(1)** site (i.e. iron rich configuration). As for B in FeAl [26], the negative values of formation energy (-0.18 eV) obtained here for Zr indicates that this atom is more stable when inserted within Fe neighbors at the grain boundary than in the bulk of the material. It is important to recall that small additions of these two atoms tend to bring some ductility in iron aluminides [27-28, 29].

In the case of substitutions, the results given in Table III-4 are also plotted in Figs. III-6 (a) and III-6 (b) by taking into account the distance from the G.B interface (Fig. III-5). For comparison the formation energies of the transition metals substitutions in the bulk (supercell with 108 atoms) are represented in Figs. III-6 (a) and III-6 (b).

The comparison of the formation energies within the bulk material and within the grain boundary shows that Ti is generally stable with the same order both in the bulk and within grain boundary interface. However, for case of the Zr impurity which is clearly not stable in the bulk, prefers to segregate at the grain boundary with lower formation energies Thus, the effect of Zr at grain boundary has really to be taken into account to understand the overall properties of these ternary iron aluminides. Comparing Al and Fe sites, it is clear that substitution of the transition metals on Al sites are never the favoured configurations. For the Fe substitutions, as for the bulk results,

the Ti impurity always prefers to reside on the FeI sites rather than the FeII ones. The situation is less pronounced for Zr. Indeed while Fe sites are always preferred to Al ones, the FeII are favoured when the substitution of Zr atom is located at the G.B. interface (-0.51 eV) and within the second plane (-0.78 eV). Finally, it is also interesting to note that, for both transition metal substitution, the most stable is obtained for substitution on a FeI site located in the first plane away from the interface (-1.32 eV for Ti/-0.97 for Zr).
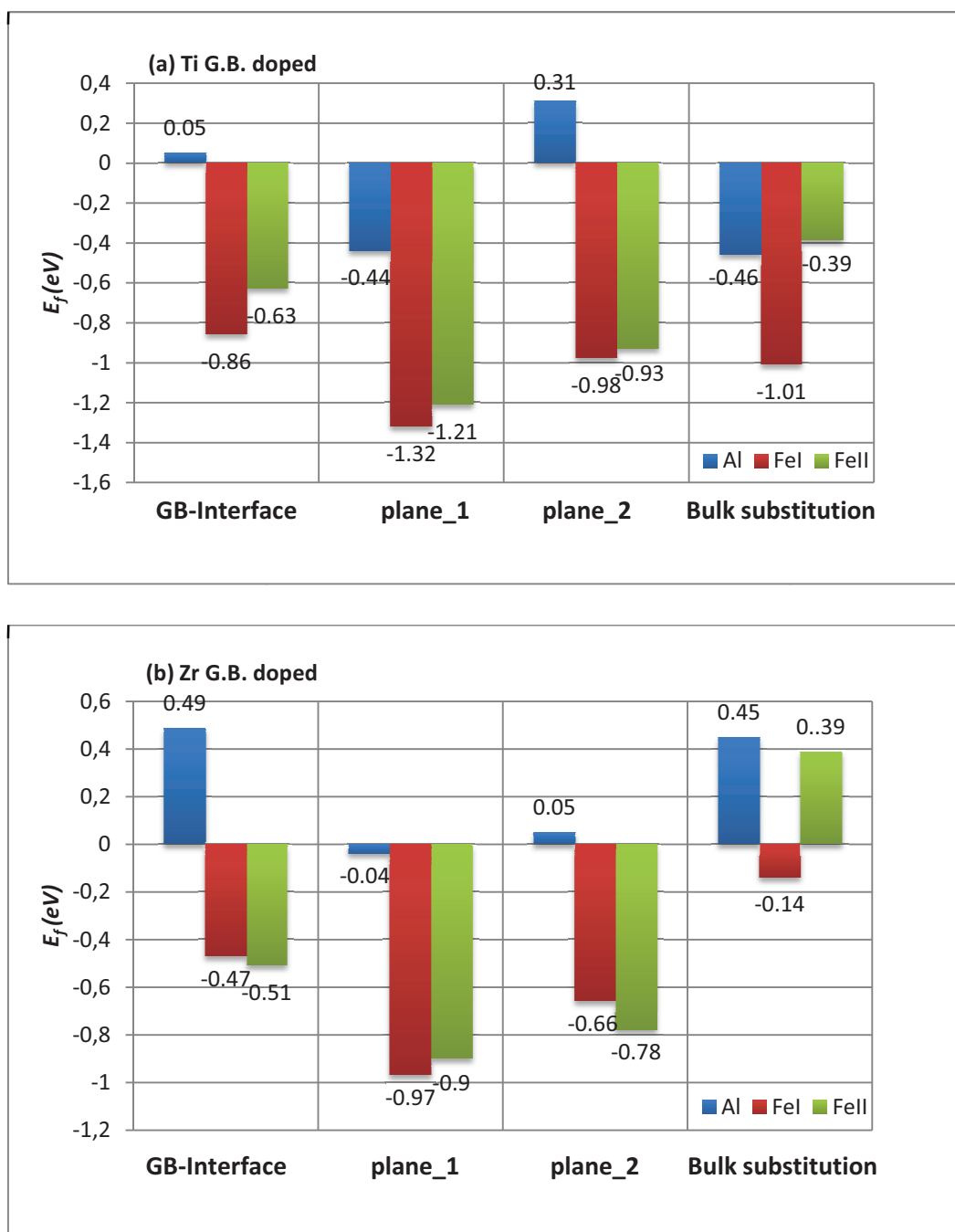
Figure. III- 6 Impurity formation energies (in eV) for different substitution sites in (a) Titanium-doped systems and (b) Zirconium-doped systems.

The influence of the segregated impurities on the interfacial energetic has been calculated for different substitutional configurations using Eq. III-6. Our calculated results are listed in Table III-5 and plotted in Fig. III-7. Our calculation indicates that the values of interface energy for a clean $\sum 5$ (310) [001] D0$_3$-Fe$_3$Al grain boundary is 0,37 J/m^2. Comparatively, this is about three times lower than the values obtained on a $\sum 5$ (310) [001] iron aluminide grain boundary for the FeAl B2 state (1,12 J/m^2) [26]. Except for one case (0Al for Ti/ γ_{GB} =0.38 J/m^2), it can be seen that Ti and Zr impurities lower the interface energy when compared for a clean-grain boundary (0.37 J/m^2). This suggests that the alloying elements Ti and Zr can stabilize the grain boundary in D0$_3$-Fe$_3$Al. The maximum expected reductions are obtained when the transition metals are on a FeII site locate in the first plane away from the exact interface: 14% for Ti (0.32 J/m^2) and 22% for Zr (0.29 J/m^2), respectively. It can be noticed also that the interface energies for the Zr-doped grain boundaries are systematically lower than for the Ti-doped ones [Fig. III-7]. Thus the principal trend that can be drawn here is that zirconium is more cohesion enhancer than titanium for $\sum 5$ (310) Fe$_3$Al-grain boundary. Indeed, the presence of Zr instead of Ti on the various sites systematically decreases further the interface energy by 0.02 / 0.03 J/m^2; this is to say by 5% to 8%.

Table III-5 The calculated interface energies (in J/m^2) for impurities in substitutional sites.

	γ_{GB}	
Clean-GB	0.37	
	Ti doped GB	*Zr doped GB*
	G.B. Interface	
0Al	0.38	0.36
0FeI	0.36	0.34
0FeII	0.34	0.31
	First plane from G.B.	
1Al	0.36	0.33
1FeI	0.34	0.31
1FeII	0.32	0.29
	Second plane from G.B.	
2Al	0.36	0.34
2FeI	0.36	0.33
2FeII	0.33	0.30
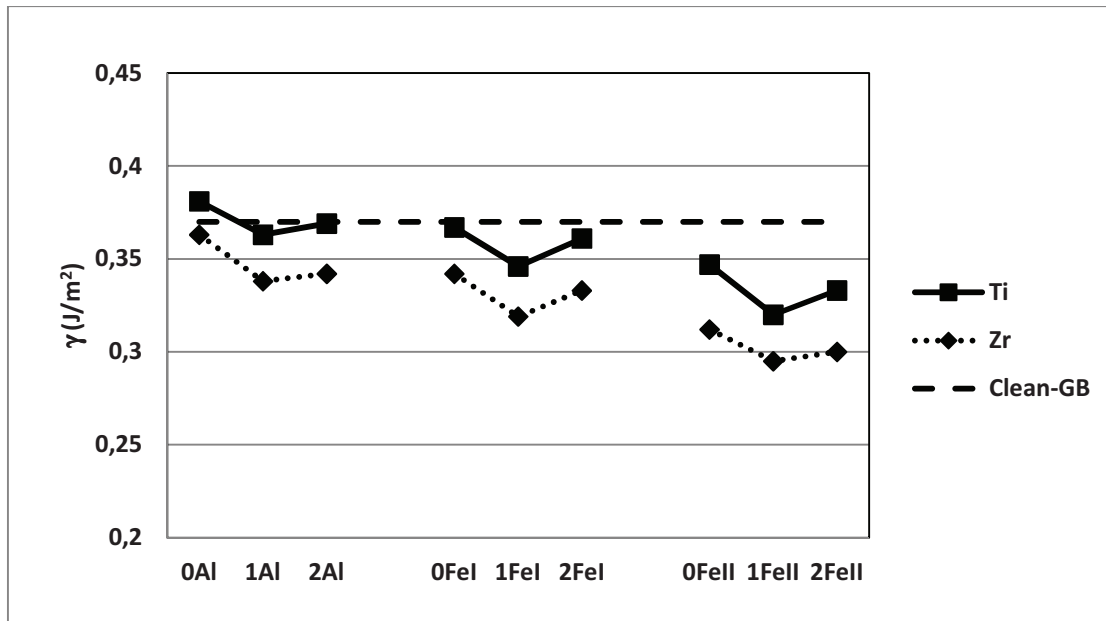
Figure. III- 7 Interface energies (in J/m^2) for impurity-doped grain boundaries and the clean-grain boundary.

In order to investigate the interaction between the impurities and their adjacent atoms, the formation energies are calculated for the first nearest neighbor vacancies to 1FeI substituted by transition metal impurities (i.e. the most stable configuration for the doped grain boundary). For comparison, we have calculated the formation energies for these vacancies in clean-grain boundary. The results of the formation energies are listed in Tables III-6 and III-7 for Ti and Zr impurities. From Table III-6, it can be seen that, for the Ti impurity, the formation energy increased only when the FeII is replaced by a vacancy (1.15 eV) compared to that calculated in the clean grain boundary (1.02 eV). This means that it is more expensive to remove a FeII atom in the presence of Ti impurity which indicates that Ti strengthens the interactions with their FeII first neighbor. This may originate from the antiferromagnetic coupling that forms between Ti and its FeII atoms [30]. However, for the case of Zr impurity (see Table. III-7), the formation energy increases slightly (~+2%) when a vacancy is produced on an Al site.

Table III-6. The calculated formation energies (in eV) for vacancies in clean-grain boundary and Ti doped grain boundary.

	ϑ_{Al}	ϑ_{FeI}	ϑ_{FeII}
$E_f^{\,v}$ (Clean GB)	3.40	1.44	1.02
$E_f^{\,v}$ (Ti doped GB)	3.26	1.08	1.15
Relative difference	-3%	-25%	+13%

Table III-7. The calculated formation energies (in eV) for vacancies in clean-grain boundary and Zr doped grain boundary.

	ϑ_{Al}	ϑ_{FeI}	ϑ_{FeII}
E_f^v (Clean GB)	2.35	1.43	1.11
E_f^v (Zr doped GB)	2.37	0.75	1.01
Relative difference	+2%	-47%	-9%

III.3. Charge density distribution

In order to gain new insight at the microscopic level of the bonding charge density at the grain boundary from that in the bulk, we have calculated the charge density difference both for the bulk system and the grain boundary. The charge density difference is defined as the difference between the total charge density in the solid and the superposition of each charge density placed at lattice sites, namely,

$$\Delta\rho(r) = \rho(Fe_3Al) - \sum\rho(Fe) - \sum\rho(Al)$$ (Eq.III-7)

The bonding charge density represents the net redistribution as atoms are brought together to form the crystal or the grain boundary. The relative redistribution of the bonding normal and parallel to the boundary interface is responsible for the changing in cohesion and the mechanical properties of the grain boundary. Based on this assumption, Lu et al. [31] have explained the detrimental effect of Hydrogen on the cohesion of the $\sum5$ (210) grain boundary in Ni_3Al intermetallics compounds.

The charge density difference for the bulk system on the (004) and (001) planes is shown in Figs. III-8 (a) and III-8 (b), respectively. The (004) plane contains both Al and FeI atoms, while the (001) contains only FeII atoms as in the grain boundary. The positive and negative curves represent contours of increased (accumulation) and decreased (depletion) bonding charge density. Contours start from ±0.25 e/(Å)^3 and increase successively by factor root of 0.008.

a)

b)
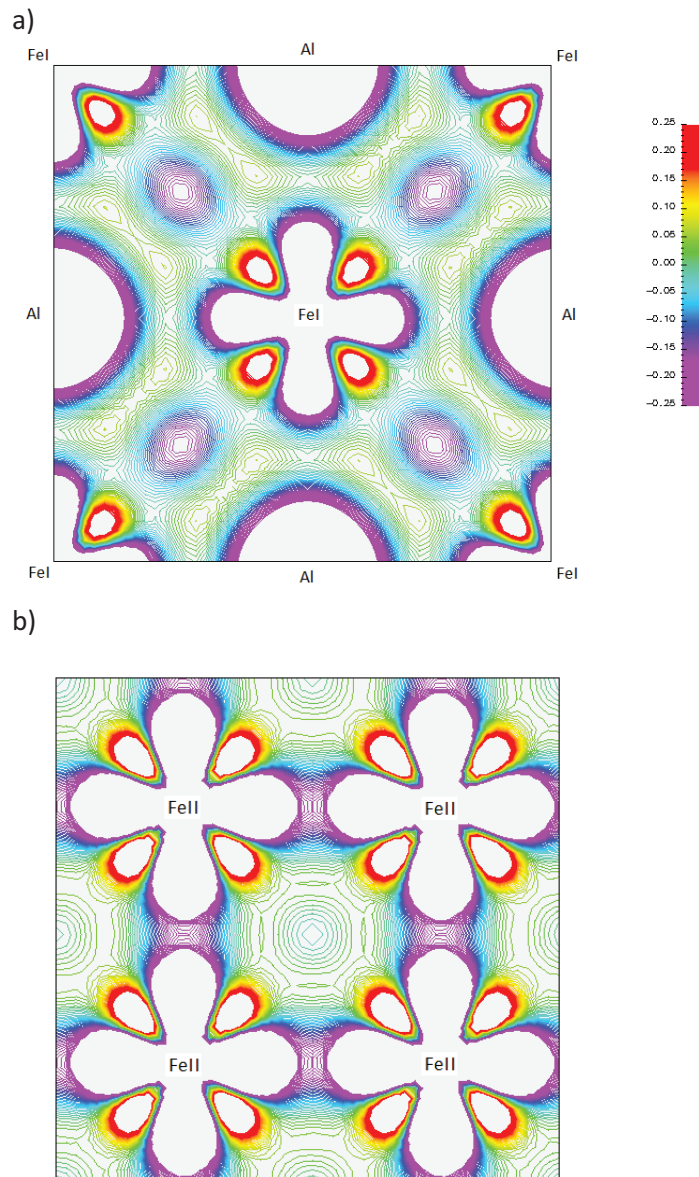
Figure. III- 8 Difference charge density of bulk Fe_3Al on (a) the (004) FeI/Al mixed plane and (b) the (001) pure FeII plane. Positive (negative) contours represent contours of increased (decreased) charge density. Contours start from ± 0.25 $e/(Å)^3$ and increase successively by a factor of root 0.008.

It can be seen that, on (004) plane [Fig. III-8 (a)], there is a charge transfer from Al to Fe atoms. Based on the Bader charge analysis, the results indicate that each Al atom loses three electrons while, comparatively, FeII (with four FeI and four Al atoms as nearest neighbours) atoms each gains 1.45 electrons and a FeI atom gains only 0.08 electrons. This can be compared to the interpretation of Schaefer et al. [20]. Taking the APW electronic band-structure calculations of Ishida et al. [32], and supposing that the electrons outside the muffin-tin spheres may be added proportionally to the electrons inside the muffin-tin spheres, Schaefer et al. have found that the Al atoms lose 1.00 electrons and FeII atoms each gain 0.57 electrons. It also interesting to note

that both on (004) [Fig. III-8 (a)] and (001) [Fig. III-8 (b)] planes the charge density is also transferred from the $dx^2\text{-}y^2/dz^2$ to *dxy, dxz* and *dyz* orbitals in the Fe atoms.

Figs. III-9 (a) and (b) shows the charge density difference for the grain boundary $\sum 5(310)[001]$ on (004) and (001), respectively.
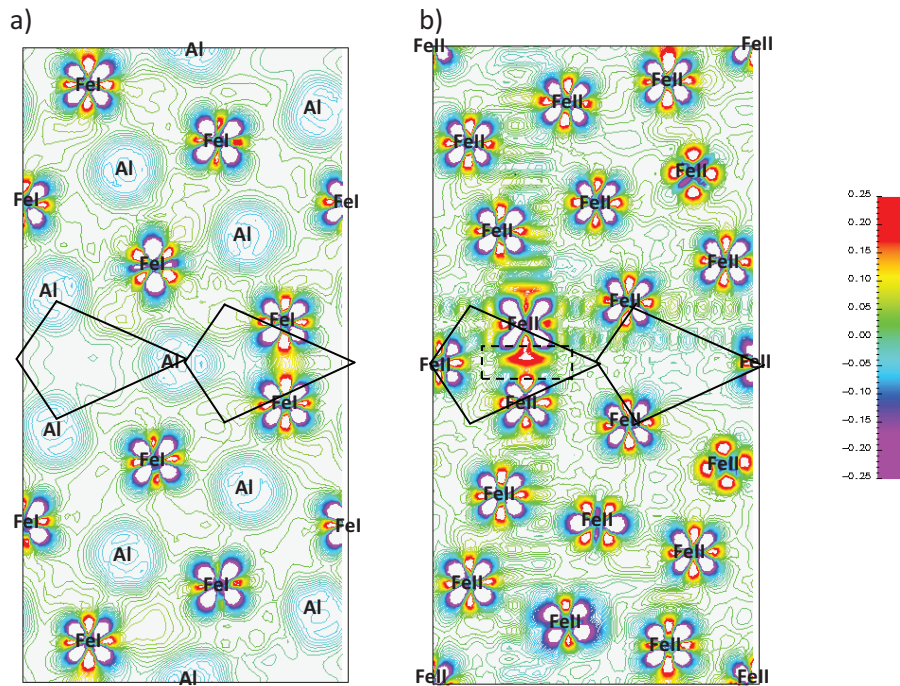
Figure. III- 9 Charge density difference of Fe$_3$Al $\sum 5$ (310) clean grain boundary, on (a) the (004) FeI/Al mixed plane and (b) the (001) pure FeII plane. Positive (negative) contours represent contours of increased (decreased) charge density. Contours start from ±0.25 $e/(\text{Å})^3$ and increase successively by a factor of root 0.008.

As for the case of bulk, it can be seen in Fig. III-9 (a) that in the grain boundary a depletion of electron density at the Al sites is accompanied by a significant build-up of charge density at the Fe sites. Here the orbital directionality in FeI atoms further away from the interface has changed as results of misorientation of the crystals by an angle of 36.8° (the angle of the $\sum 5$ (310) grain boundary), except for one atom in the third plane from the interface who try to create bonding with it next-nearest FeI atom in the first plane from the grain boundary interface.

The bonding charge distribution in the boundary region is different from that in the bulk due to the different atomic rearrangement. The accumulation on the interstitial bonding charge between the two nearest-neighbor FeI-FeI atoms across the boundary plane [Fig. III-9 (a)], increases the covalent bonding normal to the grain boundary. This indicates that the Fe atoms have an important role in holding the grain boundary together.

The charge density difference on the (001) plane in Fig. III-9 (b) shows a different charge distribution between the nearest neighbour FeII-FeII atoms across the grain boundary plane. The bonding parallel to the interface develops between the FeII (refer to rectangle) atoms, which contributes very little, if any, to the grain boundary cohesion. This accumulation is within very thin range and extends only about 0.2 Å away from the grain boundary plane.

In the first plane from the interface, it can be seen that the FeII atoms [Fig. III-9 (b)] have different charge density distributions. This is related (due) to the effect of relaxation as will be demonstrated in the Section III-5. During the relaxation the atoms moves from their initial positions, thus their charge density distribution in the vertical sections to the interface will be different. This is because in the vertical section [Fig. III-9 (b)] only a portion of total charge density are represented.

III.4. Impurities induced bonding charge density

To understand the effect of impurities on the bonding charge properties of the grain boundary we consider the redistribution of bonding charge induced by the impurity atom when placed at the substitutional site (1FeI). This configuration is considered because it is the most stable one between the different tested configurations. The bonding charge properties can be best described by the difference in charge density between the pure and impurity-doped grain boundaries, namely,

$$\Delta\rho(r) = \rho(Fe_3AlX) - \sum\rho(Fe) - \sum\rho(Al) - \rho(X) \qquad \text{(Eq.III-8)}$$

The impurity-induced bonding charge density in (004), (001) planes is shown in Fig. III-10. Figs. III-10(a) and III-10(c) represent the redistribution of bonding charge density for doped Ti-grain boundary and the Figs III-10(b) and III-10(d) are for doped Zr-grain boundary.
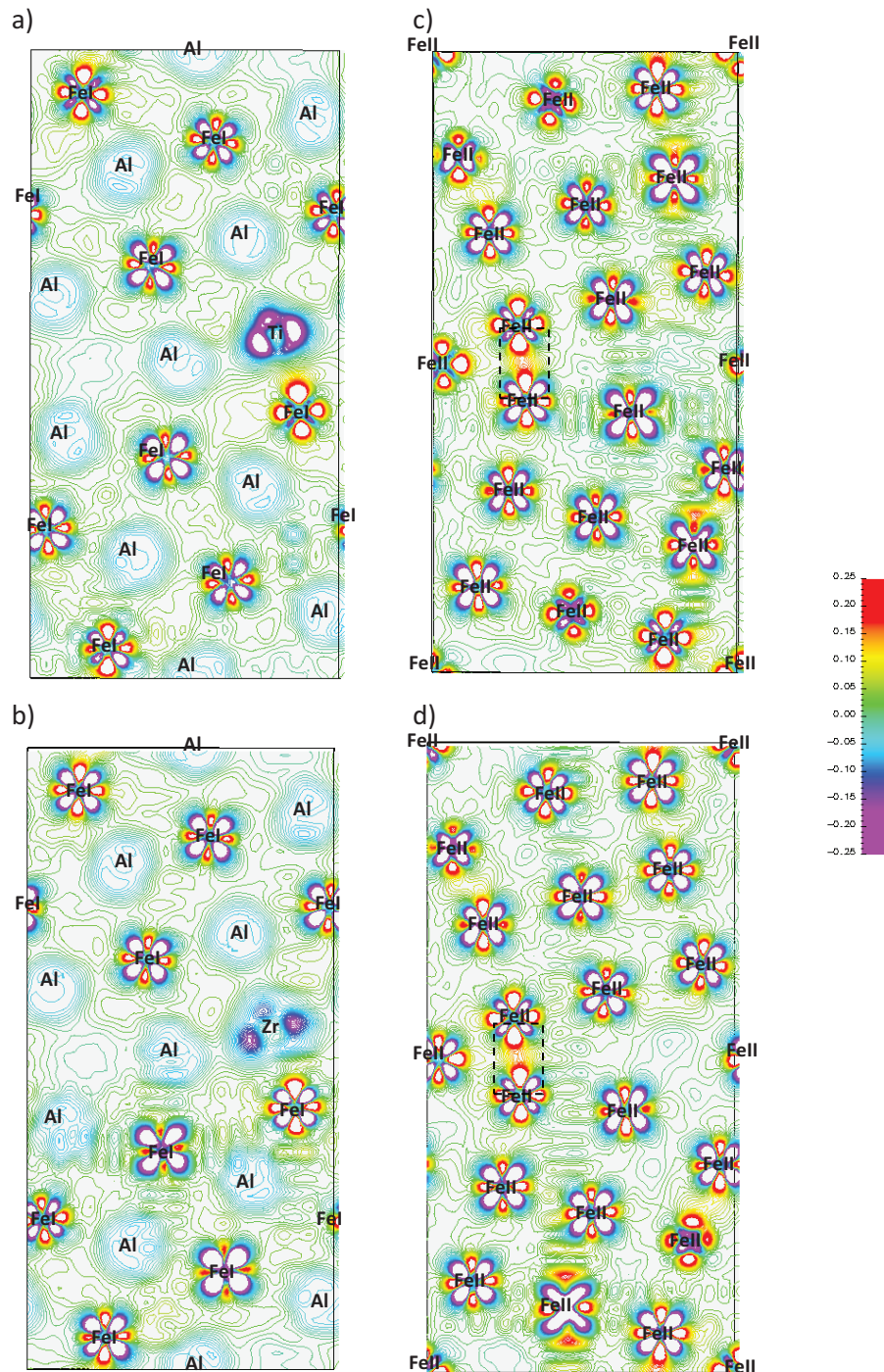
Figure. III- 10 Impurities-induced charge density of $\sum 5$ (310) grain boundary in Fe$_3$Al. The plots (a) and (c) are for Ti-induced charge density in the planes (004) and (001), respectively. The plots (b) and (d) are for Zr-induced charge density in the planes (004) and (001), respectively. The impurities occupy the substitutional site 1FeI on the mixed FeI/Al (004) plane. Positive (negative) contours represent contours of increased (decreased) charge density. Contours start from ± 0.25 e/(Å)^3 and increased successively by a factor of root 0.008.

Comparison of Fig III-9 (a) with Figs. III-10(a) and 10(b), evidences that the substitutinal impurities induce a significant redistribution of bonding charge across the boundary interface. The presence of the impurities results in the reduction of bonding normal to the grain boundary

on the (004) atomic plane. Furthermore, it can be seen that the depletion of charge density for Ti impurity [Fig. III-10(a)] is larger than that of Zr impurity [Fig. III-10(b)]. This indicates that the Ti impurity loses more electrons than the Zr impurity to form bonds with its first neighbour atoms. This is consistent with the results obtained from the calculations of the formations energies of the vacancies created around the Ti and Zr impurities (section III.2.3). It was found that there are more interactions between the Ti impurity and their adjacent atoms (specifically the FeII atoms) than for the case of Zr impurity.

On another hand, on the (001) atomic plane [Figs. III-10(c) and III-10(d)], the bonding charge between the nearest FeII atoms across the grain boundary has been changed when compared to that of the pure G.B. in Fig.III-9 (b) (refer to rectangle). These two atoms develop covalent bonding normal to the interface. Recall that the bonding normal to the boundary plane between the two Fe atoms is the most important contribution to the cohesive force which holds the two grains together; this bonding picture reveals the electronic origin for impurities-induced intergranular cohesion in $Fe_3Al \sum 5$ (310) grain boundary.

As in the clean grain boundary, the closest atoms to the interface have different charge density distributions because they moved from their initial positions by the effect of relaxation. This will be discussed in the following sections.

III. 5. The relaxation of the clean grain boundary

In this section, the effect of relaxation on the structural deformation of the $\sum 5(310)$ grain boundary will be discussed. Fig. III-11 (a) represents the calculated magnitude of displacements of the atoms. The magnitudes of the displacements of the atoms are obtained for each configuration by subtracting the un-relaxed atomic positions from the relaxed ones. The positions of the various atoms (Al, FeI and FeII) are given on the x axes depending on their location (n) away from the exact interface at n=0. Due to the cell symmetry 0 and -/+10 label the two interfaces in the supercell.

From Fig. III-11, it can be seen that the larger values of displacements correspond to atoms located in the vicinity of the interface. This is particularly true for the first and second planes labeled -/+1, -/+2 as well as -/+8 and -/+9. Note also that, the rate of the displacement decay away from the grain boundary interfaces (or towards the bulk). The displacement of each atom from its initial position is also represented by solid arrow in Fig. III-11 (b). The large displacement of the atoms in the first and second planes from the grain boundary interface is clearly visible with the largest arrows. As pointed out in previous study by Wolf et al. [33], the

large atomic displacement seen in the grain boundary interface is mainly due to the strong repulsive forces between the counter atoms in both sides of the mirror plane. This gives rice to a shift of the first and second plane parallel to the interface causing an expansion of the grain boundary. It was found that the grain boundary expansion affects significantly the kinetics of formation and migration of point defects as well as the interaction between lattice dislocations and grain boundaries [34, 35].
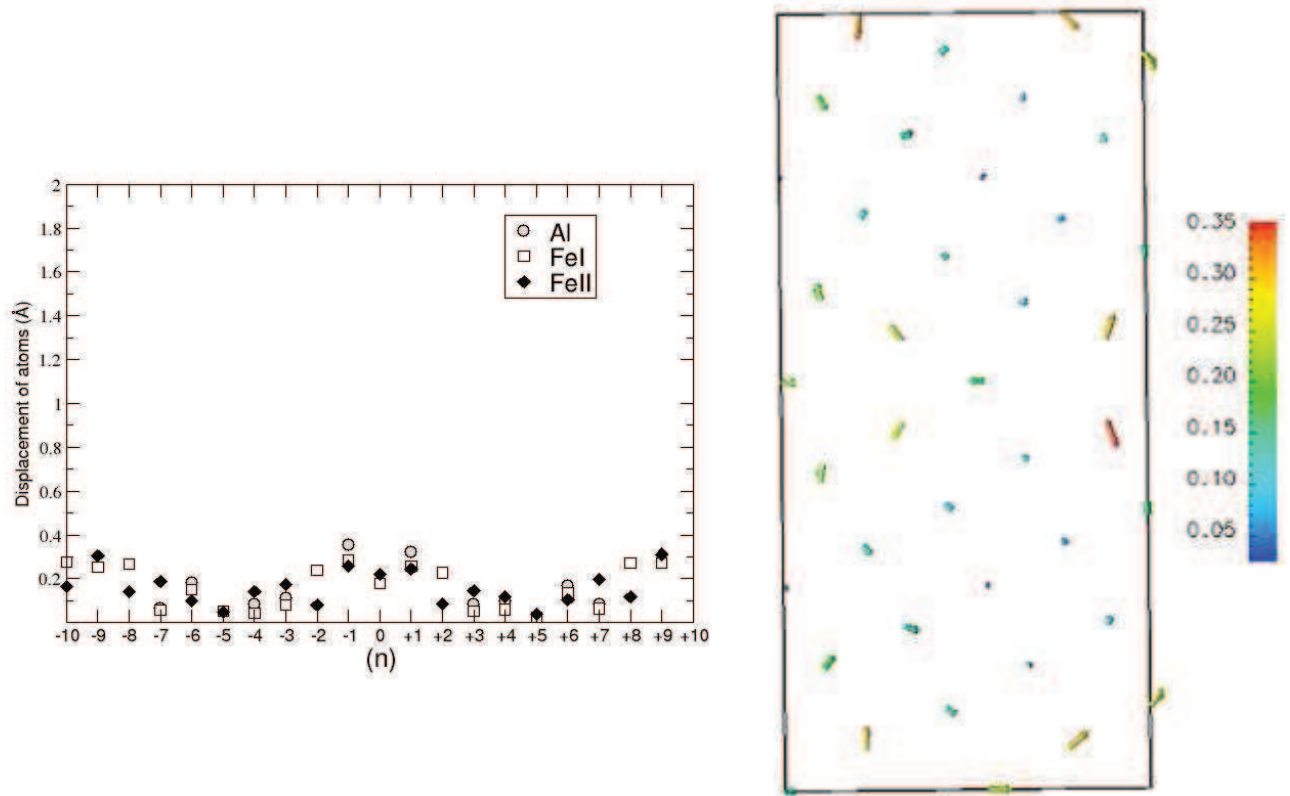
Figure. III- 11 (a) The calculated displacements of the atoms in the relaxed pure-grain boundary as function of distance from (0 and -10 label two interfaces in the supercell). These displacements are represented with solid arrows in (b)

III.5. The relaxation of the doped grain boundary

At first, the displacements of the Ti and Zr impurities in the grain boundary supercell are calculated for different substitutional configurations. The results are represented in Fig. III-12 (a) and (b) for Ti and Zr substitutions, respectively.
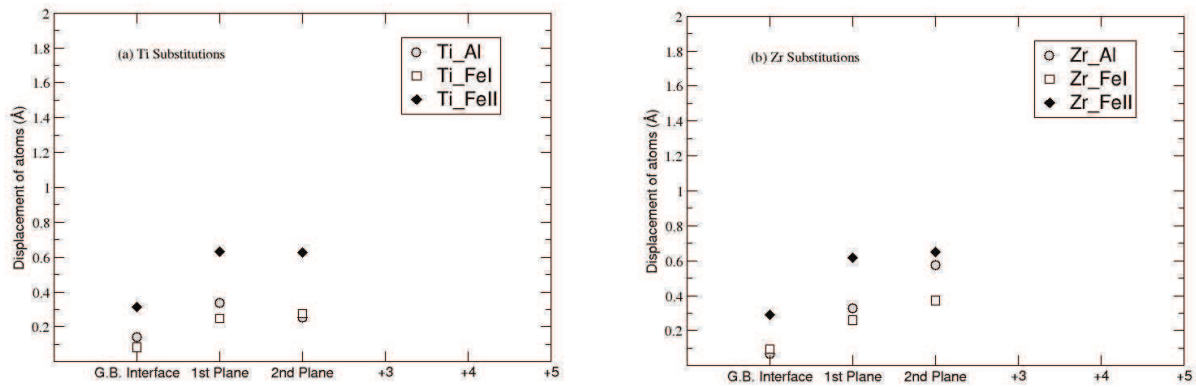
Figure. III- 12 The displacement of the impurities (a) Ti and (b) Zr in different configurations of substitutions.

As seen from Figs. III-12 (a) and (b), for both Ti and Zr impurities the largest displacements correspond to the substitutions on the FeII sites. This may be related to the environment effect. In the FeII substitutions, the impurities are surrounded by four FeI and four Al atoms. Based on the assumption that both Ti and Zr impurities prefer to reside on the FeI site where are surrounded by eight FeII atoms, their large displacements reveals that the impurities tend to relax to an iron rich configuration.

Note also that the displacements of impurities are more important in the first and second planes from the interface. The large displacement is also observed for Zr substitutions on the Al site (~0.6Å) in the second plane from the interface although it is an iron rich configuration. The displacements of the atoms in the grain boundary supercell for this configuration are represented in Fig. III-13 (a) and (b). For comparison, the displacements of the atoms in the case of Ti substitution on the same configuration are represented in Fig.III-14 (a) and (b). It clear that for this configuration, the displacement of Zr is more important when compared to that of Ti impurity. From Fig. III-13 (b), it can be seen also that the Zr impurity tends to relax to the grain boundary interface. This reveals that Zr impurity prefers to segregate at the G.B. interface whatever the nature of the environment, contrary to the Ti impurity which prefers to reside in an iron rich environment.
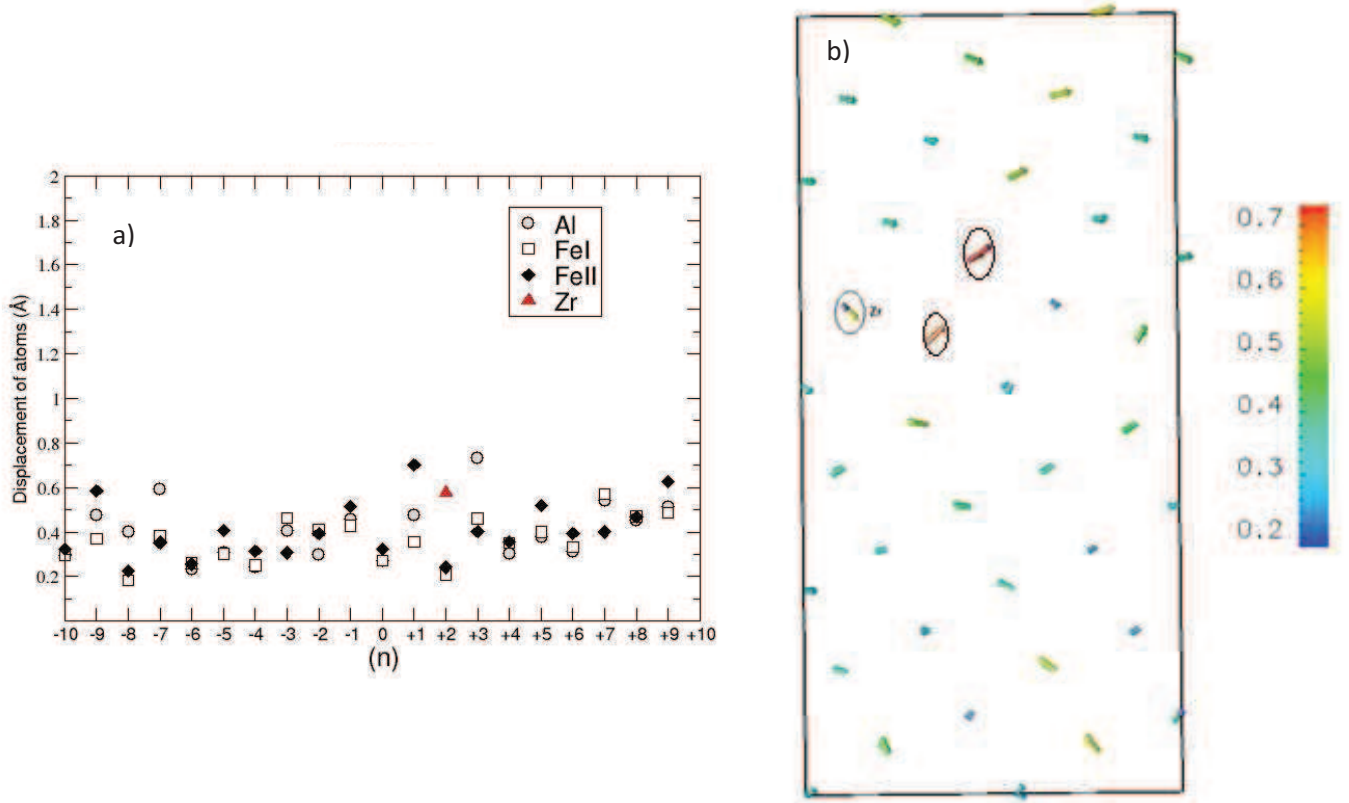
Figure. III- 13 (a) The displacements of the atoms in the relaxed supercell with solid arrows for the case of Zr substitution on the 2Al site. These displacements are represented with solid arrows in (b).
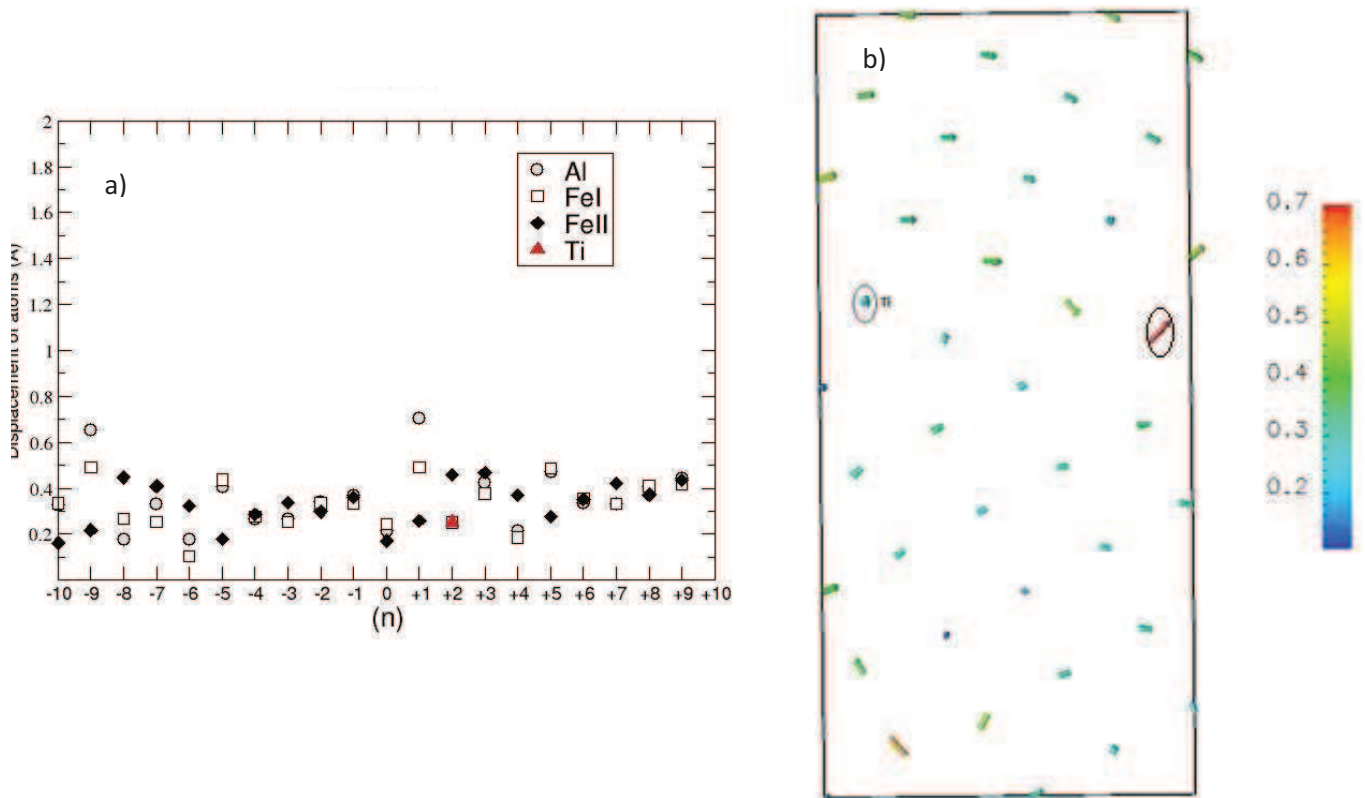
Figure. III- 14 (a) The displacements of the atoms in the relaxed supercell with solid arrows for the case of Ti substitution on the 2Al site. These displacements are represented with solid arrows in (b)

After having examined all the configurations of substitutions, it has been found that the behaviour of impurities can be classified in three different categories according to their distances from the G.B. interface. In this section, three representative configurations will be presented, namely, the impurities substitutions within the G.B. interface, substitutions in the first plane from the interface and substitutions on the second plane from the interface. All the configurations are presented in Appendix B.

For the case of the substitutions with the G.B. interface, we have chosen the configurations for the impurity substitutions on the Al site. Figs .III-15 and III-16 represent the displacement of the atoms in the supercell when the Ti and Zr impurties are placed in the Al site within the interface. From the comparison of Figs. III-15 and III-16 with Fig. III-11, it can be noticed that the presence of impurities does not affect the nature of the relaxation observed for the clean grain boundary supercell. Additionally, in this type of configurations the displacement of the impurities is smaller when compared to that of substitutions on the first and second plane from the interface.

For the case of substitutions on the first plane from the interface, we have chosen to represent the configurations for the impurities substitutions on the FeI site. Figs .III-17 and III-18 represent the displacement of the atoms in the supercell when the Ti and Zr impurties are placed on the FeI in the first plane from the interface. As first point, the displacements of the atoms in the supecell are more important than that for the case of clean grain boundary [Fig.III- 11] and/or substitutions within the G.B interface [Figs.III-15 and III-16]. Furthermore the large displacement correspond to the first nearest neighbours in the opposite plane (n=-1).

For the case of substitutions in the second plane from the interface, we have chosen the configurations of the impurities substitutions on the FeII site. In Figs.III-19 and III-20, the displacement of the atoms in the G.B. supercell with the Ti and Zr impurities on the FeII site in the second plane from the interface are represented, respectively. One can see that both Ti and Zr tend to relax toward the grain boundary interface with an iron rich environment. On other hand, from Figs. III- 19 (a) and III-20 (a), it can be noticed that the displacements of the atoms in the grain boundary supercell are more important than that for the case of the impurities substitutions within the G.B. interface [Figs. III-15 and III-16]. The large displacements of the atoms in the first (n=+1) and third planes (n=+3) correspond to the first nearest neighbours of the impurities. The large displacements of the atoms in the supercell were also observed for the case of substitutions on the FeI site in the first plane from the interface [Figs. III-17 and III-18]. This indicates that the relaxation of the atoms for the case of substitutions further away the interface

(1st and 2nd planes) are more important in the bulk region than that for the configurations when the impurities are placed in the G.B. interface. However the expansion of the interface for these configurations (substitutions in the 1st and 2nd plane) is lower when compared to that produced both in the clean interface and the doped G.B. with impurities substitutions in the G.B. interface. In terms of energy, these configurations correspond to the lower interface energies (listed in Table III-7 and presented in Fig. III-5). This is in agreement with the results of Shiga et al. [36]. These authors show that, the G.B. interface varies depending on the multilayer relaxation of the G.B. interface: the larger the interface expansion, the higher the interface energy.
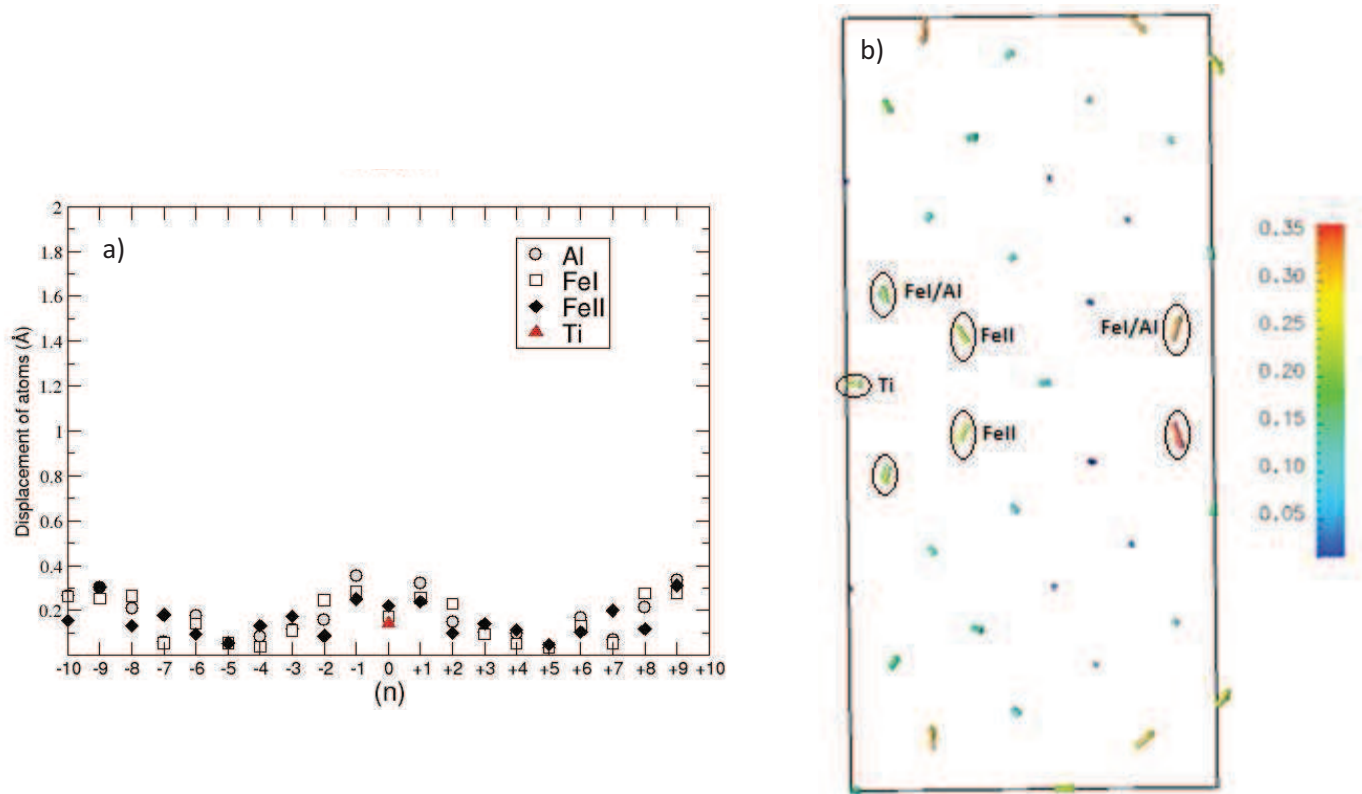
Figure. III- 15 (a) The displacement of the atoms in the relaxed supercell with Ti substitutions on the 0Al site as function of the positions of the planes parallel to the grain boundary interface. These displacements are represented with solid arrows in (b).
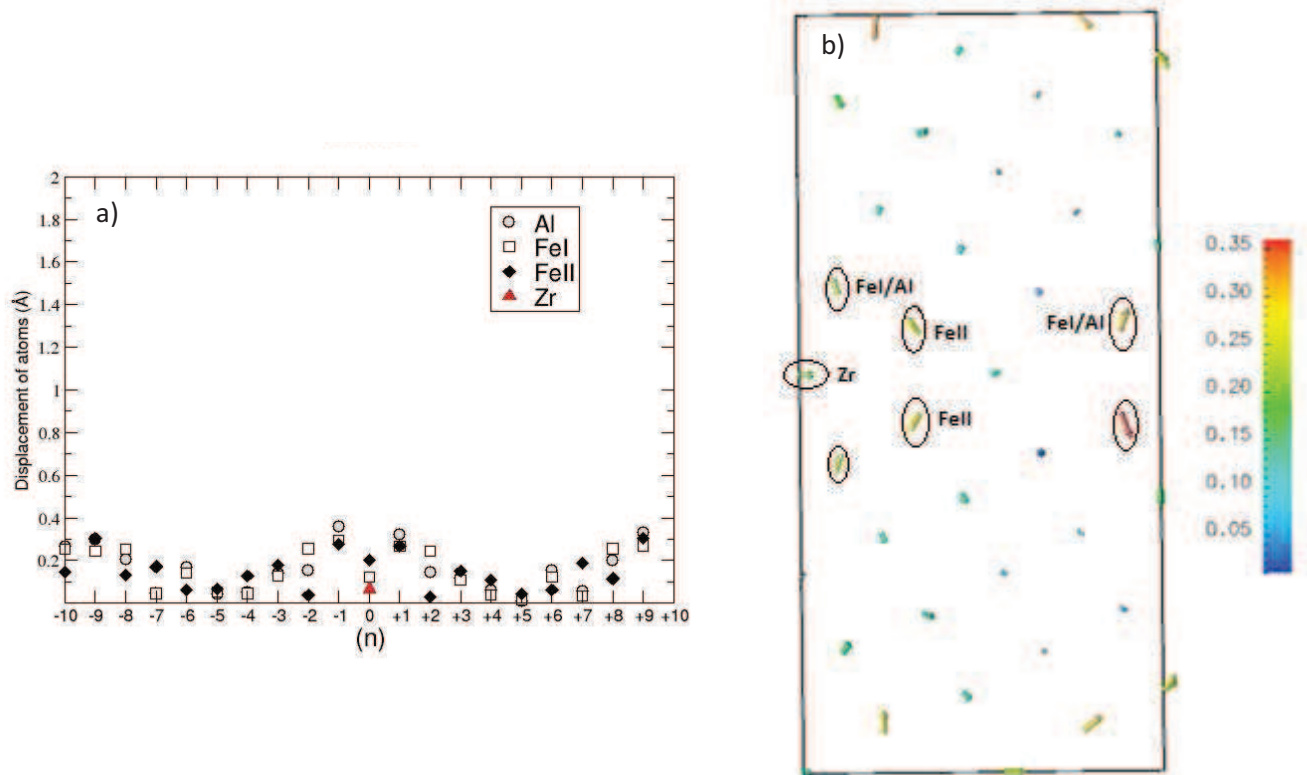
Figure. III- 16 (a) The displacement of the atoms in the relaxed supercell with Zr substitutions on the 0Al site as function of the positions of the planes parallel to the grain boundary interface. These displacements are represented with solid arrows in (b).
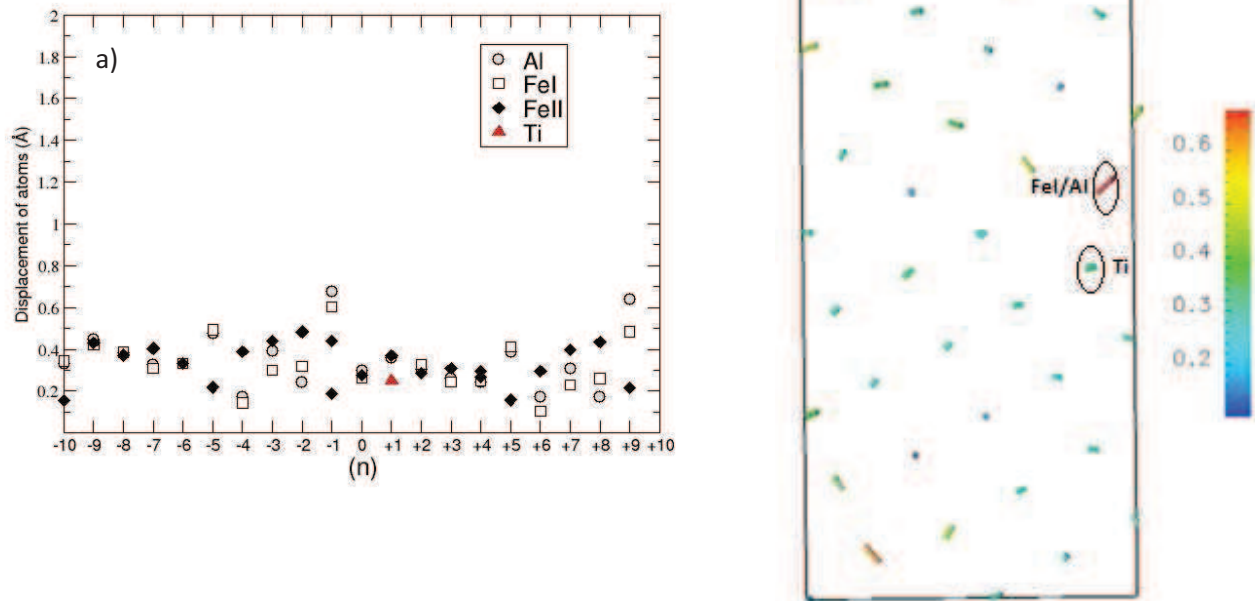
Figure. III- 17 (a) The displacement of the atoms in the relaxed supercell with Ti substitutions on the 1FeI site as function of the positions of the planes parallel to the grain boundary interface. These displacements are represented with solid arrows in (b).
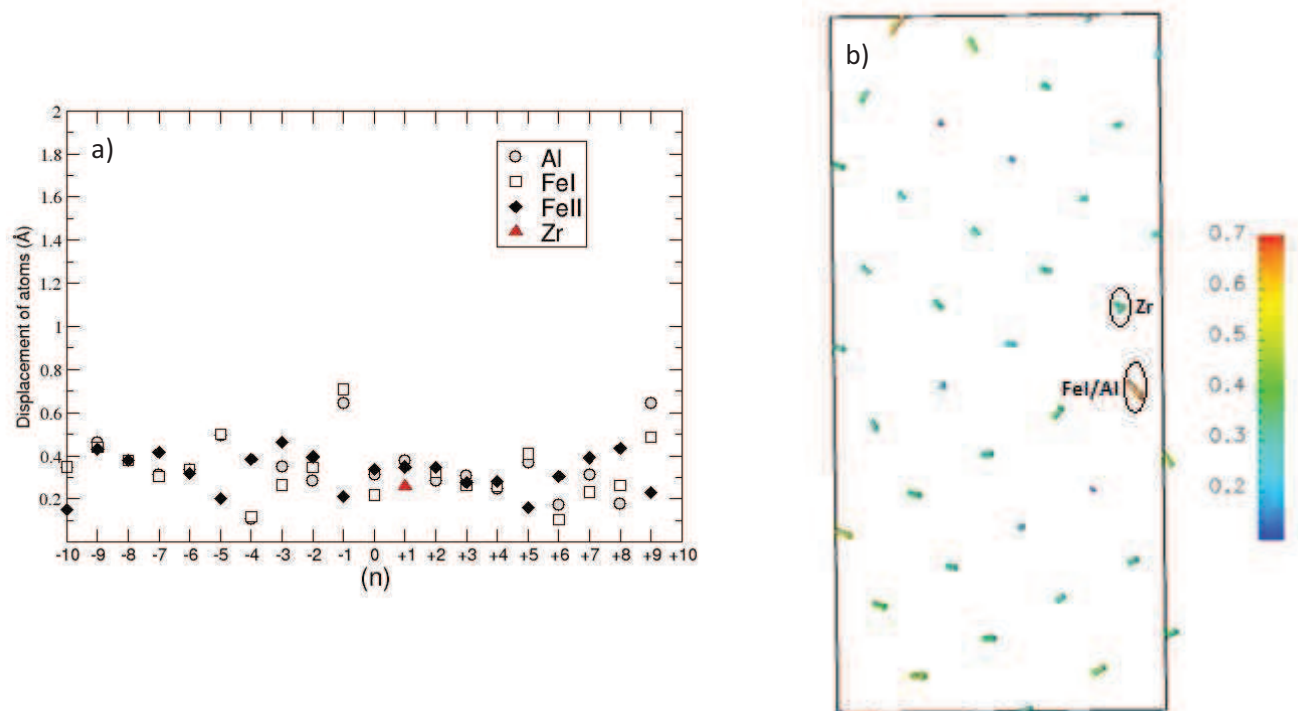
Figure. III- 18 (a) The displacement of the atoms in the relaxed supercell with Zr substitutions on the 1FeI site as function of the positions of the planes parallel to the grain boundary interface. These displacements are represented with solid arrows in (b).
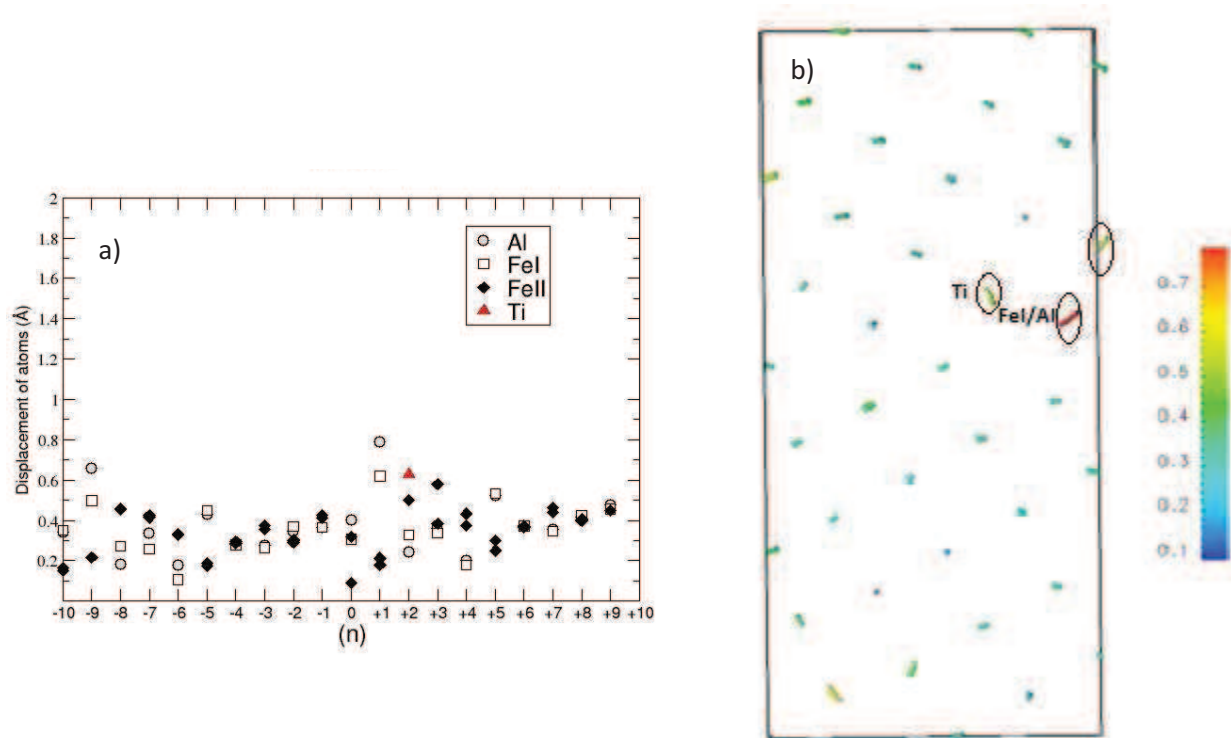
Figure. III- 19 (a) The displacement of the atoms in the relaxed supercell with Ti substitutions on the 2FeII site as function of the positions of the planes parallel to the grain boundary interface. These displacements are represented with solid arrows in (b).
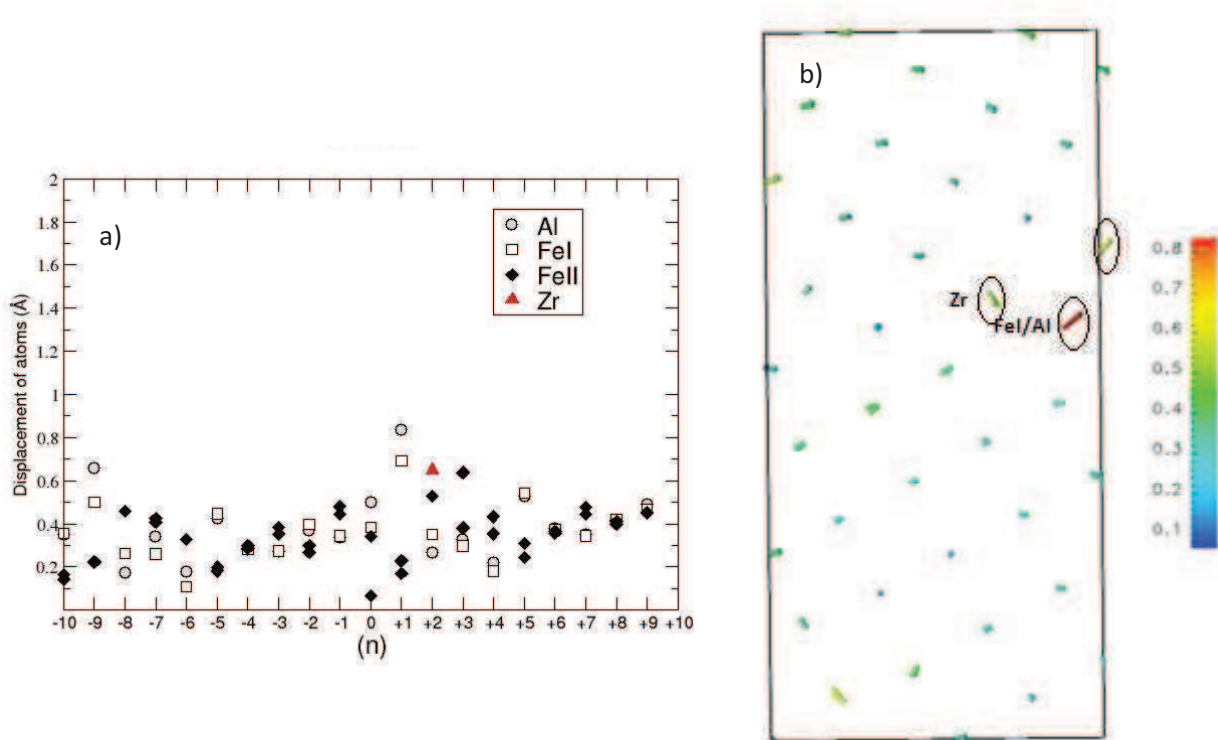
Figure. III- 20 (a) The displacement of the atoms in the relaxed supercell with Zr substitutions on the 2FeII site as function of the positions of the planes parallel to the grain boundary interface. These displacements are represented with solid arrows in (b).

IV. Summary and Conclusion

In this chapter, the effects of Ti and Zr transition metal impurities located in the bulk as well as at the $\sum 5$ (310)[001] tilt grain boundary in the $D0_3$-Fe_3Al intermetallic compound were studied by means of static ab-initio calculations. The main conclusions are as follows:

- Relaxation is extremely important to determine accurate formation energies and determine the stability of the point defects. For example, 140% error in formation energy is obtained when considering a Zr substitution on a FeII site using a cell that is not relaxed.

- In the bulk, the calculated formation energies reveal that the FeII sites are the preferential sites for vacancies while both Ti and Zr prefer to reside on FeI sites.

- The interface energy of a clean $\sum 5$ (310) interface has been found to be (0.36 J/m^2). The lowest formation energies for the T.M. substitutions have always been obtained on FeI sites on the first plane away from the exact grain boundary interface. Ti and Zr impurities are found to reduce the interface energies on various sites of this $\sum 5$ (310) grain boundary by an average of 14% and 22%, respectively. However, significant differences between the behavior of Zr and Ti atoms were revealed. In particular, Ti can reside in bulk and grain boundary configurations with the same order of stability. Comparatively, Zr is stable within the grain boundary both as an insertion and as a substituting element (on FeI and FeII sites). Also, the creation of FeII vacancies in a Ti doped boundary is energetically costly while it favored in a Zr-doped one.

- The expansion of the G.B region occurs as an effect of the relaxation in the pure grain boundary. The presence of the impurities in the G.B interface does not affect the relaxation of the grain boundary. For the case of substitutions in the first and second plane, the important displacements correspond to the first nearest neighbours atoms of the impurities while the G.B. region was not affected. The Ti impurity prefers to reside in iron rich environment while the Zr impurity tends to relax to the grain boundary interface.

References

[1] D. Vanderbilt, Physical Review B **41**, 7892 (1990).

[2] G. Kresse and J. Hafner, Physical Review B **47**, 558 (1993).

[3] G. Kresse and J. Furthmuller, Physical Review B **54**, 11169 (1996).

[4] J.P. Perdew, J.A. Chevary, S.H. Vosko, K.A. Jackson, M.R. Pederson and D.J. Singh et al., Physical Review B **46**, 6671 (1992).

[5] J.P. Perdew, Unified theory of exchange and correlation beyond the local density approximation. In: Ziesche P, Eschrig H, editors. Electronic structure of solids. Berlin: Akademie Verlag; 1991. p. 11–20.

[6] H.J. Monkhorst and J.D. Pack, Physical Review B **13,** 5188 (1976).

[7] M. Methfessel and A.T. Paxton, Physical Review B **40**, 3616 (1989).

[8] F.D. Murnaghan, Proc. Natl. Acad. Sci. U.S.A. **30**, 5390 (1994).

[10] P. G. Gonzales-Ormeňo, H. M. Petrilli & C. G. Schőn. Calphad **26**, No.4, 573 (2002).

[11] D. Connétable, P. Maugis. Intermetallics 16 (2008) 345-352.

[12] F. Lechermann, F. Welsch, C. Elsässer, C. Ederer, M. Fähnle, J.M. Sanchez, B. Meyer, Phys. Rev. B **65**, 132104 (2002).

[13] A. Kellou, J-M. Raulot, T. Grosdidier, Intermetallics **18**, 1293 (2010).

[14] Y. Nishino, C. Kumada and S. Asano. Scripta Materialia **36**, No.4, 461 (1997).

[15] H.J. Leamy, E.D. Gibson and F.X. Kayser. Acta Metallurgica **15**, 1827 (1967).

[16] A. Kellou, H.I. Feraoun, T. Grosdidier, C. Coddet and H. Aourag, Acta Materialia **52**, 3263 (2004).

[17] C. Elsässer and A.G. Marinopoulos, Acta Materiallia **49**, 2951 (2001).

[18] Q.M. Hu, R. Yang, D.S. Xu, Y.L. Hao, D. Li and W.T. Wu, Physical Review B **67** 224203.1 (2003).

[19] J. Mayer, B. Meyer, J.S. Oehrens, G. Bester, N. Börnsen and M. Fähnle, Intermetallics **5**, 597 (1997).

[20] H.E Schaefer, R. Wurschum, M. Sob, T. Zak, W.Z. Yu, W. Physical Review B **41**, 11869 (1990).

[21] Y. Jiraskova, O. Schneeweiss, M. Sob and I. Novotny, Acta Materialia **45**, 2147 (1997).

[22] M. Palm and J. Lacaze, Intermetallics **14**, 1291 (2006).

[23] M. Palm, G. Inden and N. Thomas, Journal of Phase Equilibria **16**, 209 (1995).

[24] G. Athanassiadis, G. Le Caer, J. Foct and L. Rimlinger, Physica Status Solidi (a) **40**, 425 (1977).

[25] F. Stein, G. Sautthof and M. Palm, Zeitschrift für Metallkunde **95**, 469 (2004).

[26] J.M. Raulot, A. Fraczkiewicz, T. Cordonnier, H. Aourag and T. Grosdidier, Journal of Materials Science **43**, 3867 (2008).

[27] D.A. Alven, N.S. Stoloff, Materials Science and Engineering A **239-240**, 362 (1997).

[28] M.A. Crimp and K.M. Vedula, Material Science Engineering **78**, 193 (1986).

[29] C.T. Liu and E.P. George, Scripta Metalllurgica et Materialia **24,** 1285 (1990).

[30] B.V. Reddy, D.H. Satry, S.C. Deevi, S.N. Khanna, Physical Review B **64**, 224419 (2001).

[31] G. Lu, N. Kioussis, R. Wu and M. Ciftan, Physical Review B **59**, 891 (1999).

[32] S. Ishida, J. Ishida, S. Asano and J. Yamashita, Journal of the Physical Society of Japan **41**, 1570 (1976).

[33] D. Wolf, Acta Metall. Mater **38**, 781 (1990)

[34] A.P. Sutton and R.W. Ballhffi. *Interfaces in crystalline materials*. Oxford: Clarendon, 819 (1995).

[35] G. Salishev, S. Mironov, S. Zherebtsov and A. Belyakov, Mater. Charact. **61**, 732 (2010).

[36] M. Shiga, M. Yamaguchi and Hideo Kaburaki, Phys. Review B **68**, 245402 (2003).

Chapter IV

Effect of temperature on the structural stabilities of Ti and Zr in the bulk and the ∑5 grain boundary: Ab Initio Molecular Dynamics study.

In this chapter the results of the AIMD calculations of Ti and Zr substitutions in the bulk and at the ∑5 grain boundary are given. This chapter is divided in three major sections. In the first section (section I), the calculation details together with the preliminary calculations are presented. Section II gives the results of the temperature dependence of the site preference of the two transition metals and their effect on the structural properties of the bulk $D0_3$-Fe_3Al. The pair distribution functions were also calculated in different temperatures to get insight on the phase stability of the $D0_3$ structure with the transition metals additions at higher temperatures. In Section III, the defect energies of Ti and Zr transition metals are calculated in different configurations within the ∑5 grain boundary to compare their stability with the bulk. In a second part of section III, the effects of temperature on the structural relaxation of the grain boundary is given. Finally, the limitations of the CSL model at higher temperature are also discussed.

I. Calculation details

I. 1. Computational methods

In our molecular dynamic simulations, the atomic forces were calculated from Density Functional Theory (DFT) as implemented in the VASP (Vienna Ab initio Simulation Package) code [1, 2]. The calculations are based on the Generalized Gradient Approximation (GGA) [3, 4] and made use of the Ultra Soft Pseudo-Potential approach USPP [5]. The Verlet algorithm was used to integrate the Newton's equations of motion with a time step of Δt=5 fs and each simulation were allowed to turn for a total of 200 steps. To ensure that any memory of the initial configuration is completely erased, the first 100 time steps were reserved for equilibrating the system and were discarded from the subsequent analysis.

We have used a cutoff energy of 250 eV which was found to be required in order to reach convergence in total energy. The valence states used are $4s^2 3d^6$ for Fe, $3s^2 3p^1$ for Al, $4s^2 3d^2$ for Ti and $5s^2 4d^2$ for Zr.

The large dimension of the supercells used in our calculation (108 atoms in bulk supercell and 80 atoms in the $\sum 5$ (310) G.B. supercell) allowed us to limit the sampling of the Brillion zone to the Γ point. The simulation were performed in the canonical ensemble NVT (particle Number, Volume and Temperature are fixed).

I. 2. Preliminary calculations

Preliminary test calculations were performed at each temperature in order to obtain the lattice parameter of the $D0_3$ structure at zero pressure. In a first step, the lattice parameter of the Fe_3Al-$D0_3$ supercell was dilated/compressed to the equilibrium lattice constant at the zero pressure. From this value of lattice parameter, a new calculation was carried out to obtain the new pressure. In the second step, the resulting value of pressure –which is close to zero- was reintroduced in the graph of the evolution of the lattice parameter with the pressure to obtain a more accurate lattice parameter as shown in the Fig. IV-1 from the calculations at 100 K. The deduced lattice parameter at 100K is indicated by red arrow in Fig. IV-1.

The pressure difference was found smaller than 1.5 kBar in the simulated temperature range from 100 to 1100K. Such a small pressure difference in our simulation should not bring significant errors for the comparison of structural properties at different temperatures.
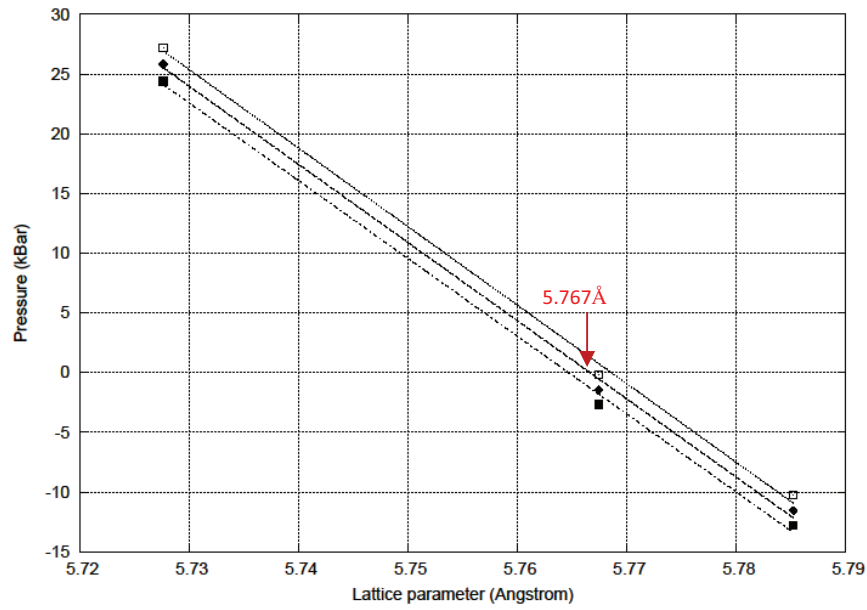
Figure. IV-1. The evolution of pressure as function of expansion/compression of the lattice parameter (at temperature T=100K). The diamond and squares symbols represent the calculated pressure and the statistical uncertainty, respectively.

I.3. Energetic

In order to examine the temperature dependence of the site preference of Ti and Zr transitions metals, their defect energies were calculated both in the bulk and the $\sum 5$ (310)[001] over a wide range of temperatures (100-1100 K). The defect energies are defined as change in energy of the pure supercell when an impurity replaces an atom in the supercell, namely,

$$E_d = E_{solid}(Fe_3AlX) - E_{solid}(Fe_3Al) \qquad \text{(Eq.IV-1)}$$

Where *X* represent the T.M. impurities. $E_{solid}(Fe_3AlX) \ and \ E_{solid}(Fe_3Al)$ (*solid* referring to bulk as well as G.B.) are the energies of the supercell with and without transition metal impurities, respectively. The preferential site then corresponds to the case where the energy is gained by replacing an atom.

Unlike the formula of the formation energy used in the previous chapter (Chapter III, section I-2) the energies of the pure elements (Fe, Al, Ti and Zr) are not introduced in the formula of the defect energy. Thus, the comparisons (i) between the defect energies of the two transition metals and (ii) between substitutions on the Fe and Al sites are not possible.

It is important to recall that the formation energy is defined as

$$E_f = E_{solid}(Fe_3AlX) + E_{Fe\ or\ Al} - E_{solid}(Fe_3Al) - E_X \qquad \text{(Eq. IV-2)}$$

In this equation, $E_{Fe\ or\ Al}$ (Fe or Al being the atom which is substituted) and E_X are the calculated total energies for pure metals in their equilibrium lattices -*bcc* Fe, *fcc* Al, *hcp* Ti and *hcp* Zr.

In the following, we will only examine the replacement of FeI or FeII sites by transition metal impurities. Indeed, the case of substitutions on the Al site was not treated since the comparison is not possible but also as we have found, from the static calculations (at 0K), that the substitutions on the Al sites are not favourable both in the bulk and at the grain boundary $\sum 5$ (310)[001].

II. Transition metal impurities in the bulk D0$_3$-Fe$_3$Al

II.1. Site preference of the Ti and Zr substitutions

The defect energies of the two transition metals were calculated using a system of 108 atoms (81 atoms of Fe and 27 atoms of Al), i.e. 3x3x3 the D0$_3$-Fe$_3$Al unit cell, under periodic boundary conditions. By substituting an impurity in this supercell, the impurity concentration is about 1% (exactly 0.92%). The results of the defect energies are summarized in Table IV-1 for Ti and Zr substitutions. To help and indicate better the trends, the energies differences between the substitution in FeI and FeII sites are also listed and presented in Fig.IV-2.

Table. IV-1. The defect energies (in eV) when the FeI/FeII sites are replaced by the Ti and Zr transition metals.

	Ti			Zr		
T (K)	FeI	FeII	*E$_d$(FeI)-E$_d$(FII)*	*FeI*	*FeII*	*E$_d$(FeI)-E$_d$(FeII)*
100	-1.79	0.05	-1.84	-2.04	-1.29	-0.75
200	-1.62	-0.46	-1.16	-2.34	-1.62	-0.72
300	-2.54	-0.56	-1.98	-2.35	-1.76	-0.59
400	-1.90	-0.65	-1.25	-2.62	-1.93	-0.69
500	-1.77	-0.34	-1.43	-2.30	-1.60	-0.7
600	-2.16	-0.48	-1.68	-2.36	-1.69	-0.67
700	-1.98	-0.55	-1.43	-2.23	-1.71	-0.52
800	-1.99	0.16	-2.15	-2.29	-1.79	-0.5
900	-2.35	-0.08	-2.27	-2.08	-2.55	+0.47
1000	-2.55	-0.70	-1.85	-2.65	-2.28	-0.37
1100	-1.71	-0.31	-1.40	-2.58	-2.14	-0.31
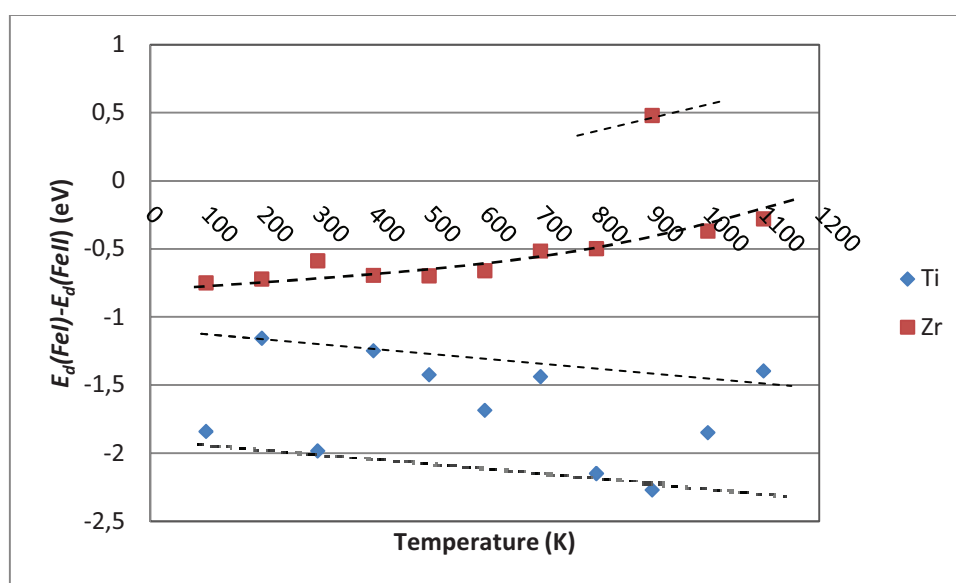
Figure. IV-2. The energies differences (in eV) between the substitutions on FeI and FeII sites.

The replacement of Ti on the FeI site leads to a significant gain in energy (-1.62~-2.55 eV) on the overall temperature range. Comparatively, the replacement on the FeII site is energetically more expensive (+0.05~-0.7 eV). This also indicates that, over the entire tested temperature range, the Ti impurity is always more stable when seated on the FeI site. For the case of the Zr impurity, the gains in energy are even more substantial: (-2.04~-2.65 eV) and (-1.29~-2.55 eV) on a FeI and FeII sites, respectively.

The most interesting point revealed by these data is the evolution with temperature of the relative stability between the different sites for the two transition metals. The difference in behavior between the two elements is more clearly depicted in Fig.IV-2. For Ti, the preference of the FeI site over the FeII site is confirmed with a difference in energy in the range -1.16 to -2.27 eV. In addition, the negative slope depicted by the data points in Fig.IV-2 indicates a clear trend for increasing the stability of the FeI over the FeII sites when the temperature increases. The observed trends for Zr are rather different. First, the magnitude in terms of energy difference between the two sites does not exceed 0.75 eV (-0.75 max at 100K). Second, while FeI is favoured at low temperature, increasing the temperature tends to stabilize more and more the FeII site. Ultimately, with very stable energetic configuration for the FeII site at 900K (-2.55 eV), 1000K (-2.28 eV) and 1100K (-2.14), the site preference for the FeI and FeII sites are very close.

The reason for the large difference in energies, between the two occupancies in the case of Ti substitutions, can be related to the equilibrium bond lengths of Ti-Al that are substantially larger than the corresponding Ti-Fe bond lengths. The insertion of Ti at the FeII site, therefore, leads to a large repulsion between Al and the Ti transition metal atom. The calculated distances between Ti when placed at the FeII site and its first neighbors Fe and Al atoms are represented in Fig. IV-3. The FeII-FeI and the FeII-Al bond lengths in the pure Fe_3Al supercell are also presented for a comparison. From Fig. IV-3, note that the distance of the Al atoms from the central FeII site increased from ~2.5 Å in the pure Fe_3Al supercell to ~ 2.65 Å for the case when the site was occupied by Ti impurities overall range of temperature. However, the distances between the Ti and its FeI neighbours are smaller compared with the FeII-FeI bond lengths. This indicates that there are more interactions between the Ti and its Fe first neighbours.

Fig. IV-4. shows the calculated distances between the Zr atom, when placed in the FeII site, and its first neighbour FeI and Al. As seen in Fig. IV-4, both the Zr-FeI and Zr-Al bond lengths are larger when compared to the FeII-FeI and FeII-Al ones in the pure supercell over the entire temperature range. This may be related to the size effect, knowing that the atomic radius of

zirconium is greater than that of the Fe and Al Atoms. From Fig. IV-4 it can be seen also that up to 500K, the Zr-FeI bond lengths are substantially smaller than that of Zr-Al ones. This indicates the interactions between the Zr and their first neighbours FeI are stronger than that with the Al atoms. However, from about 600K, the distances between Zr and its first neighbours converge and become almost equal. This means that repulsive interactions occurs between the Zr and its first neighbours FeI.
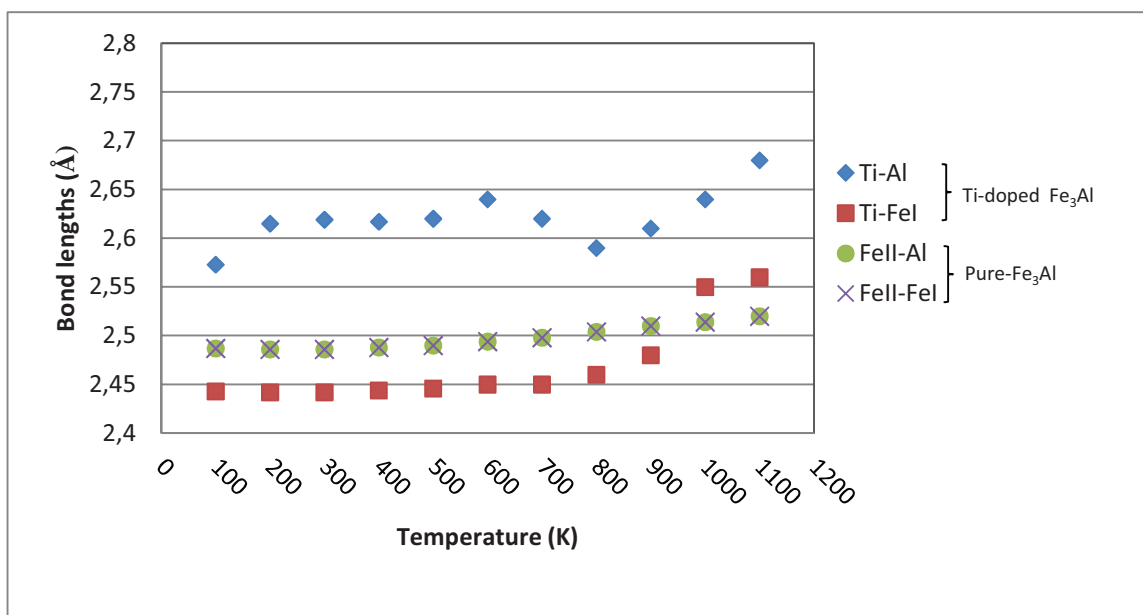
Figure. IV-3. The bond lengths in the relaxed pure and Ti-doped Fe$_3$Al supercells.
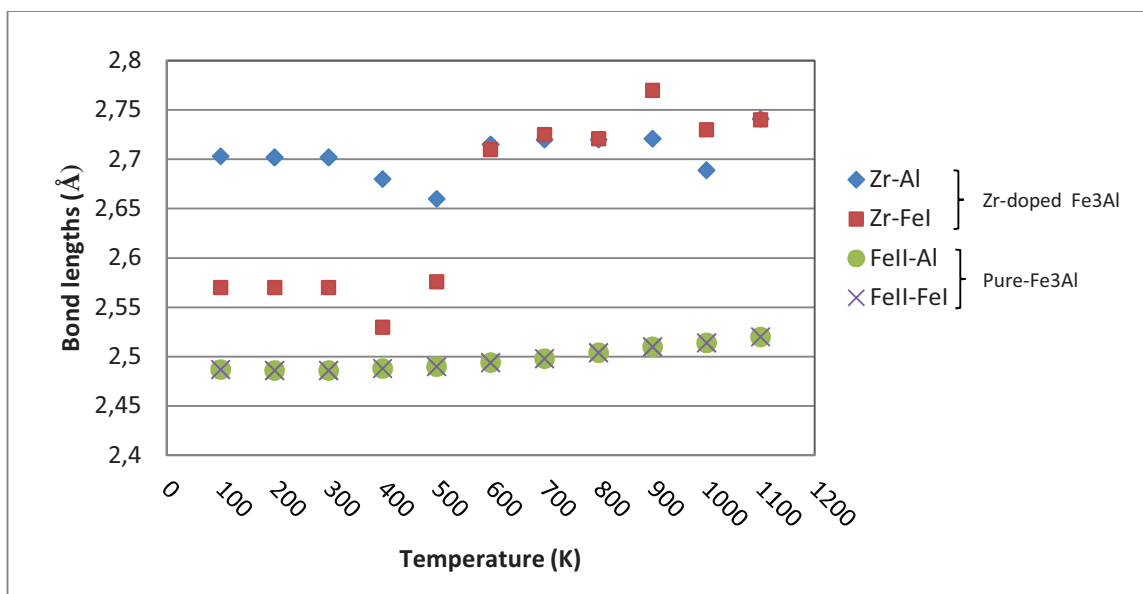
Figure. IV-4. The bond lengths in the relaxed pure and Zr-doped Fe$_3$Al supercells.

To quantify the interactions between the Zr impurity and their adjacent atoms at higher temperatures the defect energies were calculated for the first neighbour vacancies to FeII site substituted by Zr impurity. We have chosen to perform these calculations in the most stable configurations; i.e. substitutions on the FeII site at 900K and 1000K. For comparison, the defect energies for these vacancies were calculated in the pure supercell. This method is more detailed in the previous chapter (Chapter III, Section III-1). The results of defect energies are presented in Table IV-2 together with the relative difference between the defect energies of vacancies in doped and pure Fe_3Al. The defect energies of vacancies in Ti-doped Fe_3Al are also listed.

The results of the defect energies shows that the vacancies are more favoured in the Zr doped Fe_3Al than in the pure supercell. Their defect energies of vacancies decrease by (-39%) and (-66%) when the vacancies are created in the Al and the FeI sites, respectively, at 900K. This suggests that the presence of Zr on a FeII site weakens both the FeAl and the FeFe bonds. Despite the small increase in the defect energy of vacancy at 1000K, it remains low compared to that in the case of Ti additions. One can see from Table IV-2 that it is energetically more expensive (about +60%) to create a vacancy on the FeI site when the FeII is replaced by the Ti impurity. Comparatively, the defect energy of vacancy created on the Al site is (-65%) smaller than that created in the pure-Fe_3Al, at 900K. Further the Ti-Al average bond length is about 2.6 Å compared to Ti-Fe average bond length of 2.45 Å. The occupancy of a FeII site by a Ti, therefore, not only leads to a reduced interactions but also induces strain on the neighbouring Al atoms. Ti atoms, therefore, occupy FeI site even at higher temperatures.

Table. IV-2. The calculated defect energies (in eV) for vacancies in pure Fe_3Al as well as Ti and Zr-doped Fe_3Al. The relative difference between the defect energies of vacancies in the pure and doped Fe_3Al are also presented.

	Pure-Fe_3Al	*Ti-doped Fe_3Al*	*Zr-doped Fe_3Al*
		900K	
Vacancies on Al sites (ϑ_{Al})	-2.64	-7.61 (-65%)	-4.18 (-39%)
Vacancies on FeI sites (ϑ_{FeI})	1.14	2.79 (+59%)	0.38 (-66%)
		1000K	
Vacancies on Al sites (ϑ_{Al})	-8.16	-7.12 (+13%)	-8.08 (+1.2%)
Vacancies on FeI sites (ϑ_{FeI})	-4.61	-1.78 (+61%)	-4.24 (+8%)

The above results reveal that the behaviour of the Zr impurity differs from that of the Ti one. At higher temperature (about ~900K), while Ti impurity remains stable on a FeI site, the Zr impurity can reside on both the FeI and/or the FeII sites with the same order of stability.

II.2. Structural and stability results

II.2.1. Equilibrium lattice parameters

Fig. IV-5 represent the calculated lattice parameters of $D0_3$-Fe_3Al in the temperature interval 100 – 1100 K with the increment $\Delta T=100$ K. The value obtained at 0K from the static ab initio calculations are also ploted (5.76Å).
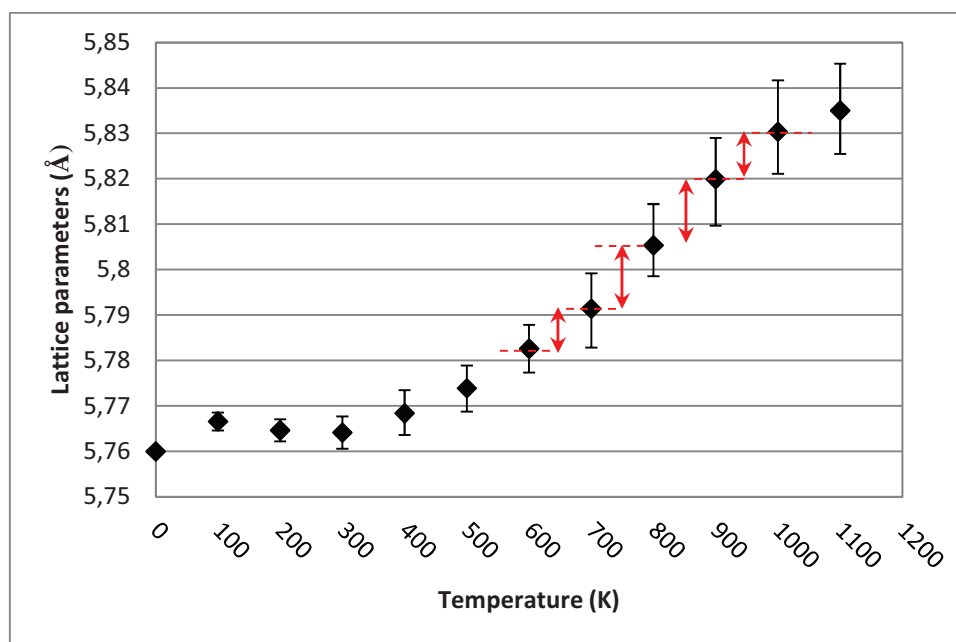
Figure. IV-5. The calculated lattice parameters at different temperatures for pure $D0_3$-Fe_3Al. The error bars represent the statistical uncertainty.

From Fig. IV-5 it can be seen that a small decrease in the lattice parameter takes place between 100 and 300K before the curves level off at 400K. This small decrease may be due to the changes of magnetic moment at these temperatures. According to a theoretical calculation [7], performed by TB-LMTO code, it was found that there is a close relationship between Fe magnetic moment and lattice parameter in the FeAl intermetallic compounds. On other hand, magnetization measurements [8] and neutron diffraction analysis [9] have reported magnetization decrease with temperature below 170 K in $D0_3$-Fe_3Al. Fig. IV-6 shows our calculated magnetic moment of Fe atoms as function of the temperature. In agreement with the experimental results [8, 9] a small decrease in the magnetic moment is observed below 200K. Another interesting point is the increase in the magnetic moment that occurs smoothly from about 600K and increasing sharply at 800K. This is related to the structural disorder that occurs in the $D0_3$ after 830K. This is reflected also on the lattice parameter. From Fig.IV-5, it can be seen that, from about 300K the lattice parameter increases gradually with temperature up to

700K. Between 700 and 900K the rate of increase of the lattice parameter is slightly larger. Thus, in agreement with the experimental result, there is a direct relationship between the magnetic and structural properties in the $D0_3$-Fe_3Al intermatallic compounds.
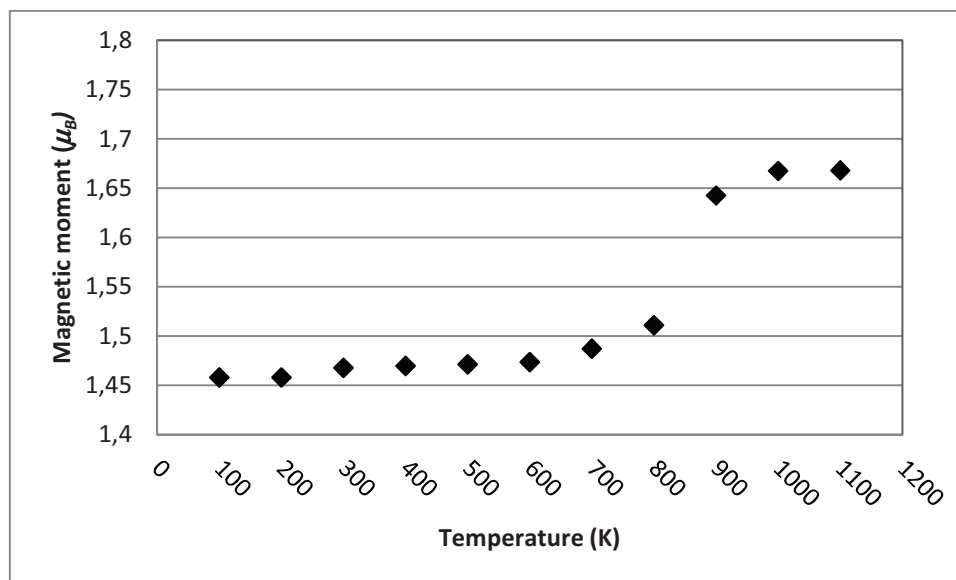
Figure. IV-6. the temperature dependence of the total magnetic moment in the $D0_3$-Fe_3Al.

Fig. IV-7 shows the temperature dependence of the fractional length change $\Delta L/L(T_0) = [L(T) - L(T_0)]/L(T_0)$ where the reference of temperature T=300K, together with the previously experimental [10] and theoretical [11] data.
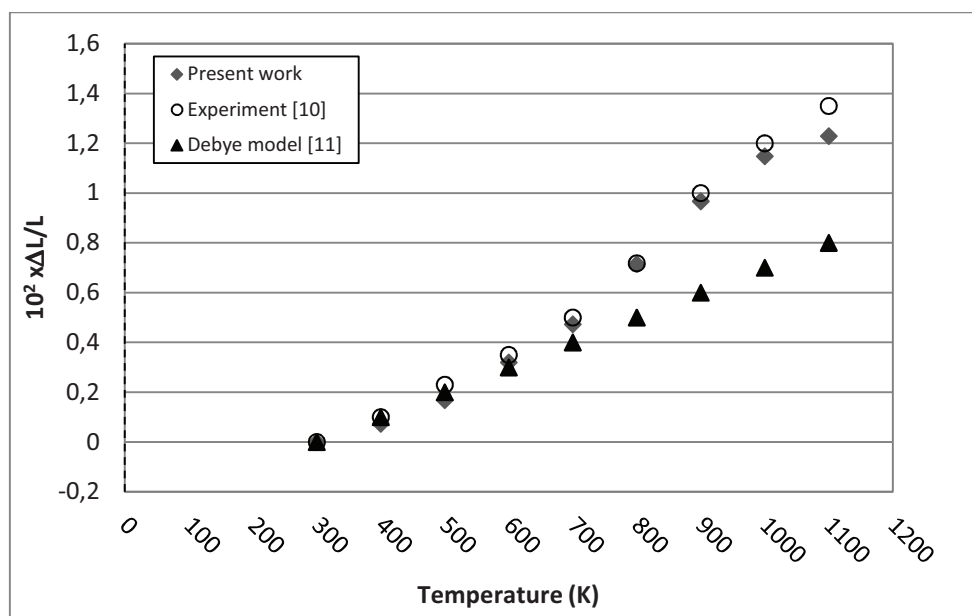
Figure. IV-7. Fractional length change data of $D0_3$-Fe_3Al.

From Fig. IV-7 it can be seen that our results are very close to the experimental data which indicates the validity of the AIMD used method. Our results are also comparable with the pioneer results obtained by Seletskaia et al. [11] using the Debye model to take into account the effect of temperature. At low temperatures, the calculated fractional lengths obtained using the Debye model are consistent with our results as well as the experimental data. However, an increasing divergence is observed when the temperature increases. This is due to the growing contribution of the optical phonons to the thermal expansion, since, the anharmonic effects (the vibrational contributions) are neglected in the Debye model. Considerable effort has lately gone into understanding the role of lattice vibrations in thermodynamics of chemical ordering in binary substitunational alloys [12, 13]. It has been suggested [14, 15] in this connection that the contribution of vibrational entropy to the phase stability in alloys can be quite significant. Nix and Shockley [16] first suggested that the state of order could affect the lattice vibrations through a change in the Debye temperature. Suprisingly enough, the vibrational entropy contribution has remained largely neglected as compared to the configurational entropy for quite some time. Several theoretical calculations [17, 18] followed, emphasizing its significance. This indicates that the approach used in the present work is rather powerful to take into account the effect of the temperature in this kind of material.

Fig. IV-8 shows the temperature dependence of the lattice parameter with Ti and Zr substitutions in FeI sites, respectively. The lattice parameters of the pure Fe_3Al are also represented for comparison.
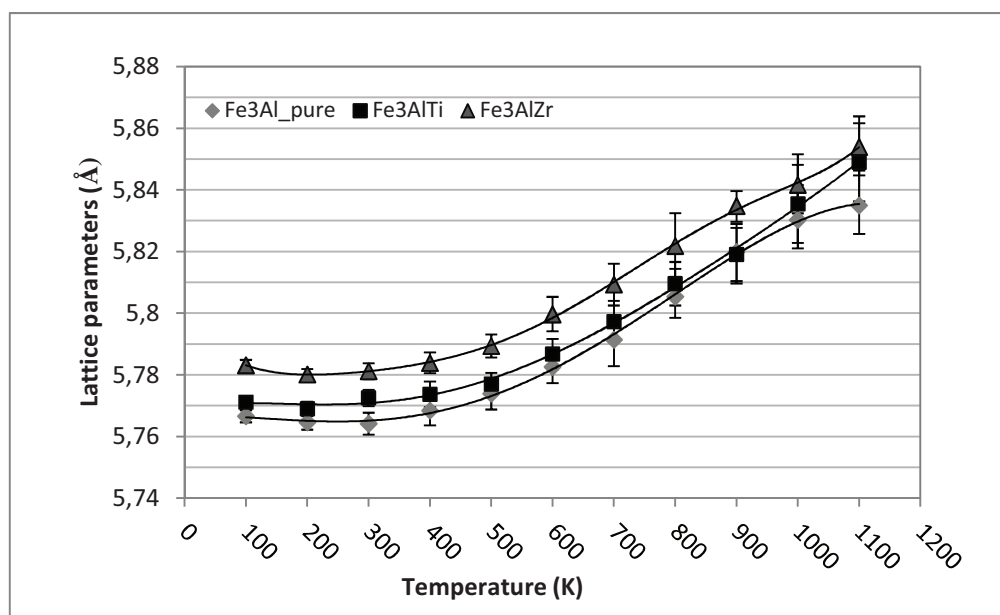
Figure. IV-8. The calculated lattice parameters at different temperatures for pure Fe_3Al, Ti doped-Fe_3Al and the Zr-doped-Fe_3Al. The error bars represent the statistical uncertainty.

It is clear that the addition of Ti and Zr leads to an increase on the lattice parameter. It appears also that the effect of Zr addition on the calculated lattice parameter is more important than that of Ti one. This difference is related to the difference in size between the Zr and Ti atoms (the Ti atom is smaller than the Zr one). What is important to stress here is the profile of the curves above 800K. For the case of Ti substitution, the lattice parameter increases linearly up to higher temperature. Comparatively, the rate of increase becomes lower of the pure Fe_3Al compound and Zr doped compound. This suggests that the Zr impurity does not affect the structural stability of pure Fe_3Al, from about 800K, despite the large increase that it brings to the lattice parameter.

Fig. IV-9 shows the variation of the fractional length $\Delta L/L(T_0)$ as a function of temperature for the pure Fe_3Al, Ti-doped Fe_3Al and Zr-doped Fe_3Al when the transition metals are placed in on a FeI site.
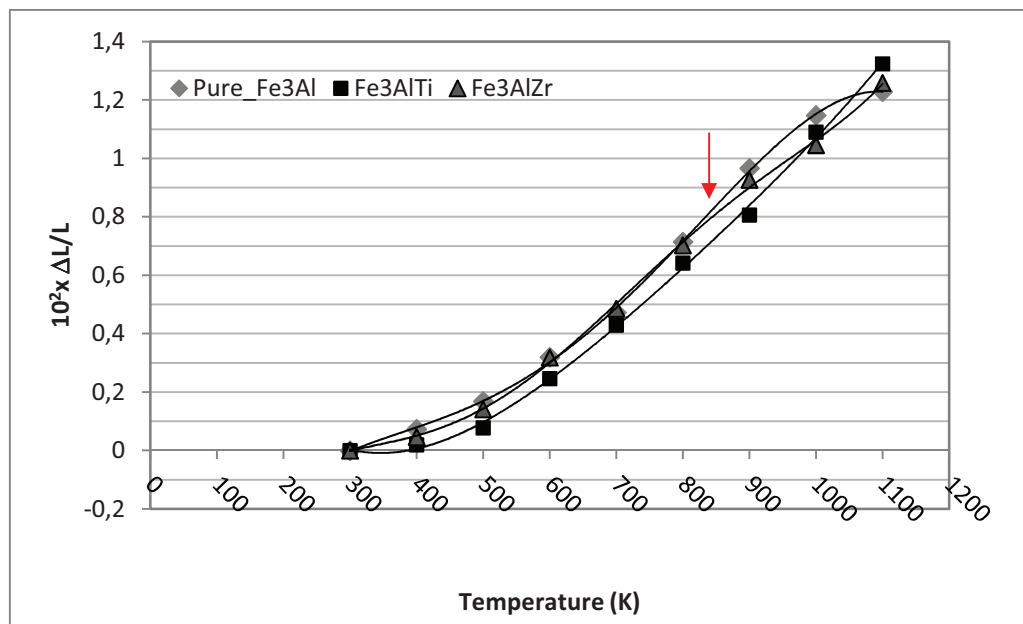
Figure. IV-9. Fractional length change data of $D0_3$-Fe_3Al, Ti-doped Fe_3Al and Zr-doped Fe_3Al (Ti and Zr are placed on the FeI site).

As seen from Fig.IV-9, the values of the fractional length for Ti-doped Fe_3Al are smaller than that of the pure and Zr-doped Fe_3Al. This means that the thermal expansion of Ti-Fe_3Al is lower than that of the pure and Zr-doped Fe_3Al. Interestingly, the variation of the Ti doped compound linear up to the highest temperature of 1100K while a change in slope is visible for the case of pure and Zr-doped-Fe_3Al compounds. It is clearly visible, from Fig. IV-9, that the evolution of the three fractional lengths remain rather close up to 800K. The discontinuity starts to take place for the pure Fe_3Al between 900 and 1000K. There is a cross over between the curves corresponding to the Ti and Zr doped compounds between 1000 and 1100K. This means that the

effects of Ti and Zr on thermal expansion of the Fe_3Al are different reflecting their different effects on the stability of the $D0_3$-Fe_3Al above 800K. These trends are consistent with the results depicted in Fig. IV-8 for the lattice parameters.

In order to explore, in more detail, the effect of these transition metals on the stability of the $D0_3$ structure we will examine, in the following section, the pair distribution functions for the pure Fe_3Al structure and those for Ti and Zr-doped Fe_3Al, repectively.

II.2.2. Pair distribution function

The Pair Distribution Function PDF or pair correlation function, $g(r)$, is a very suitable measure to analyze the structure of material. Its variation with temperature and pressure gives information about the structural phase transition.
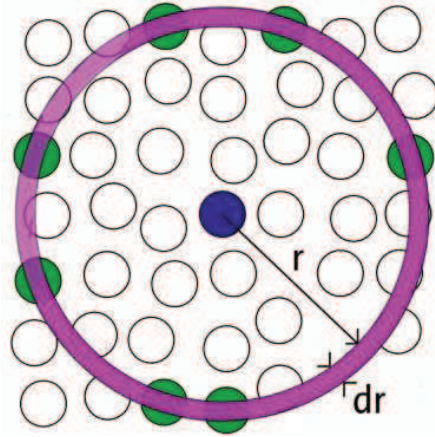
Figure. IV-10. Space discretization for the evaluation of the radial distribution function.

Considering an homogeneous repartition of the particles in space, the $g(r)$ represents the probability to find a particle in the shell dr at the distance r of another particle (Fig. IV-10).

By discretizing the space in intervals dr (Fig. IV-10), it is possible to compute for a given atom the number of atoms $dn(r)$ at a distance between r and $r + dr$ of this atom:

$$dn(r) = \frac{N}{V} g(r) \, 4\pi \, r^2 \, dr \qquad \text{(Eq.IV-4)}$$

where N represents the total number of particles, V the volume and where $g(r)$ is the radial distribution function.

In this notation the volume of the shell of thickness dr is approximated ($V_{shell} = \frac{4}{3}\pi(r + dr)^3 - \frac{4}{3}\pi r^3 \approx 4\pi \, r^2 \, dr$).

By distinguishing the chemical species it is possible to compute the partial radial distribution functions $g_{\alpha\beta}(r)$:

$$g_{\alpha\beta}(r)= \frac{dn_{\alpha\beta}(r)}{4\pi r^2 dr \rho_\alpha} \quad \text{with} \quad \rho_\alpha = \frac{V}{N_\alpha} = \frac{V}{N x c_\alpha} \tag{Eq.IV-5}$$

where c_α represents the concentration of species α. These functions give the density probability for an atom of the α species to have a neighbour of the β species at a given distance r.

In the following, we have computed the $g_{\alpha\beta}(r)$ evolution with temperature (T=100-1000K) in order to investigate the effect of temperature on the structural phase stability of the D0$_3$-Fe$_3$Al structure, the Ti doped D0$_3$-Fe$_3$Al and Zr doped D0$_3$-Fe$_3$Al.

II.2.2.1. Pair distribution functions for D0$_3$-Fe$_3$Al

Fig. IV-11 shows the PDFs g(r) in D0$_3$-Fe$_3$Al for the Fe-Fe [Fig. IV-11(a)], Al-Al [Fig. IV-11(b)] and Fe-Al [Fig. IV-11(c)] pairs.

From the comparison of each profile with the corresponding g(r) at 100K, it can be seen that all the peaks of the g(r) become broader when the temperature increases. This is due to the larger thermal motion of atoms in the supercell.

For the case of the $g_{Fe\text{-}Fe}(r)$, the noticeable feature is that the characteristic double-peak structure in the range 2.5 Å-3 Å disappears as the temperature reaches 800K. The first peak is located at around 2.5 Å ($\frac{\sqrt{3}}{4} a$, the distance between the FeI and its eight first near negibours FeII atoms). This peak decreases and widens gradually with increasing temperature. However, the peak position is almost unchanged meaning that the distance between the first near neighbours Fe atoms remains constant. The second peak is located at around 2.87 Å ($\frac{a}{2}$, the distance between the FeII and its second near neighbours FeII atoms). With the increase of temperature, its position shows a slight shift towards 3 Å and its height decreases obviously.

In the Al-Al PDF curve [Fig. IV-11 (b)], the first peak position is around 4.1 Å ($\frac{\sqrt{2}}{2}a$, the distance between the first near neighbours Al atoms in the D0$_3$-Fe$_3$Al structure). Its height decreases with the increase in temperature. Furthermore, it can be noticed that a new peak appears around 3.9 Å in the profile of $g_{AlAl}(r)$ from about 800 K. The appearance of the new peak in the $g_{Al\text{-}Al}(r)$ indicates that the distances between the first near neighbour atoms decreases as a consequence of the large displacement of the Al atoms in the supercell. This means also that the order of the D0$_3$ superlattice is affected from this temperature. This result is remarkable as it

points to a direct correlation with the experimentally observed transition phase ($D0_3$-B_2) that occurs around 820K in the Fe_3Al compound.

As shown in Fig. IV-11 (c), the disappearance of the second peak from 800K is also noticed in the g $_{FeAl}$(r) pair distribution function.
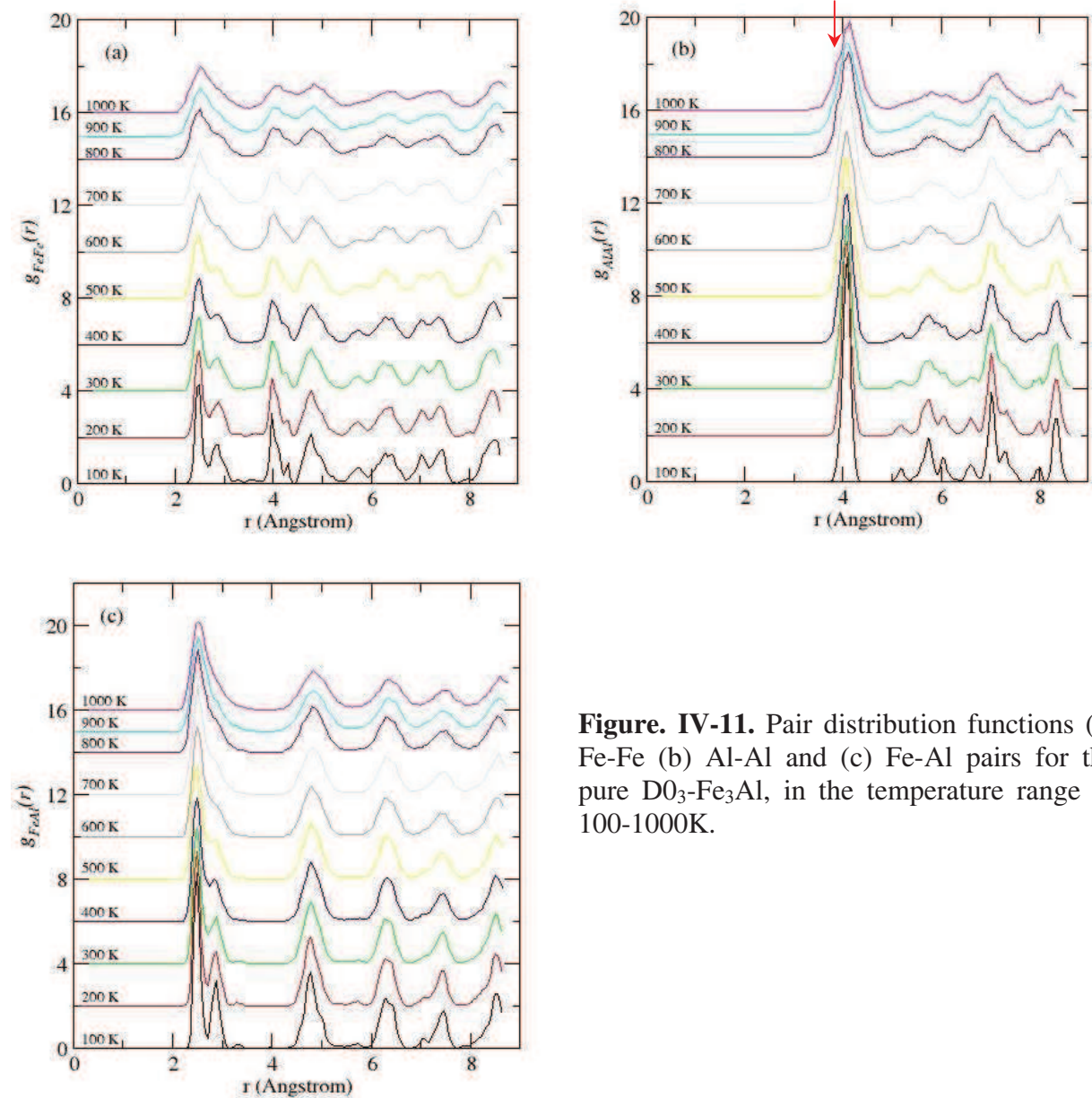
Figure. IV-11. Pair distribution functions (a) Fe-Fe (b) Al-Al and (c) Fe-Al pairs for the pure $D0_3$-Fe_3Al, in the temperature range of 100-1000K.

II.2.2.2. Pair distribution functions for doped Ti and Zr-Fe_3Al

Based on the results obtained from the defect energies calculations, the radial distribution functions were calculated at first time for the Ti and Zr substitutions on the FeI site in the $D0_3$ structure. For the case of Zr, the pair distribution functions were also calculated for the FeII substitutions at higher temperatures for comparison knowing that the stability of Zr on the FeI and FeII becomes equivalent at higher temperatures.

Figs. IV-12 and IV-14 represent the PDFs g(r) in D0$_3$-Fe$_3$Al with Ti and Zr substitutions in the FeI site, respectively, for (a) Al-Al, (b) Fe-Fe and (c) Fe-Al pairs.
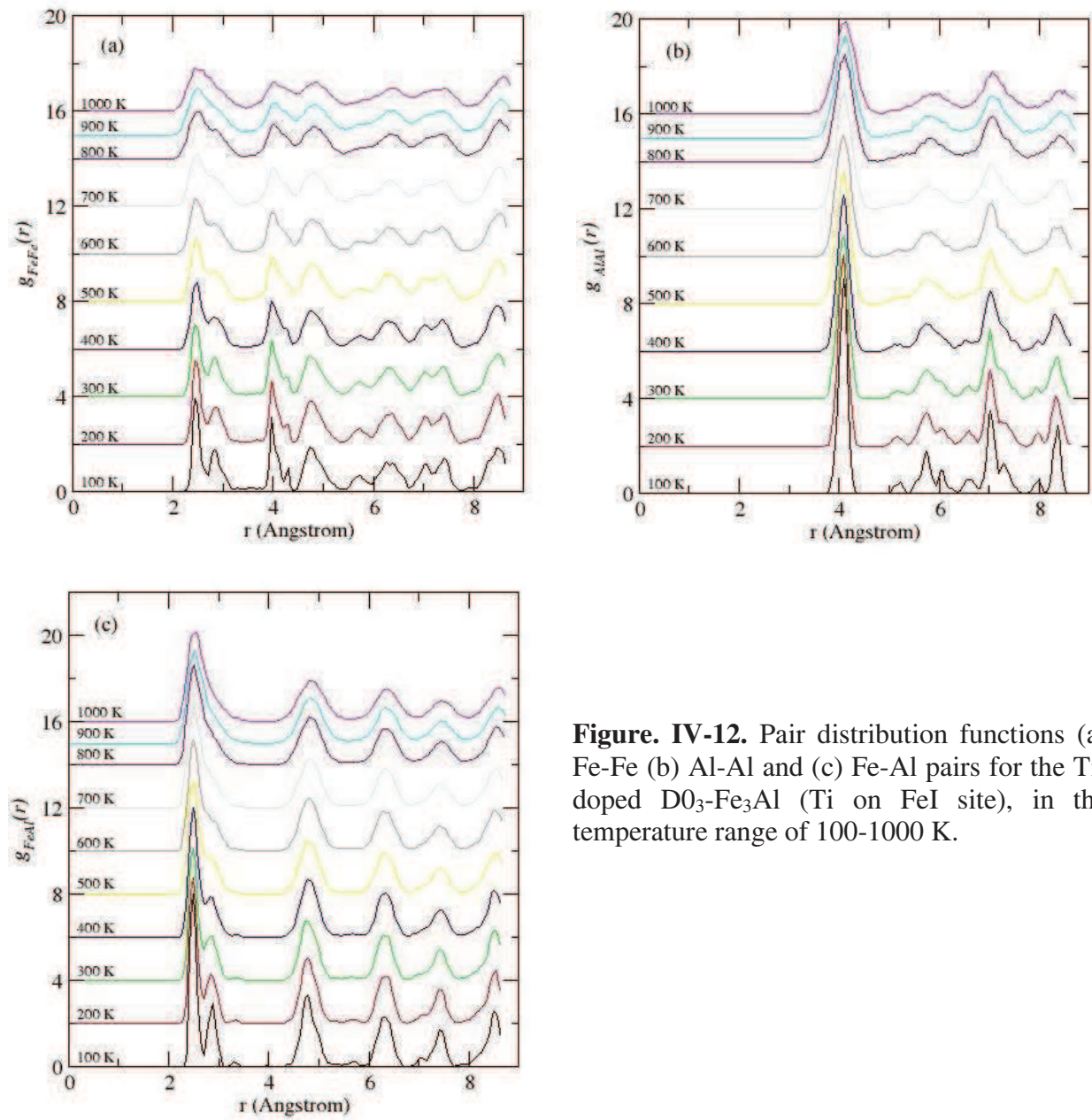
Figure. IV-12. Pair distribution functions (a) Fe-Fe (b) Al-Al and (c) Fe-Al pairs for the Ti-doped D0$_3$-Fe$_3$Al (Ti on FeI site), in the temperature range of 100-1000 K.
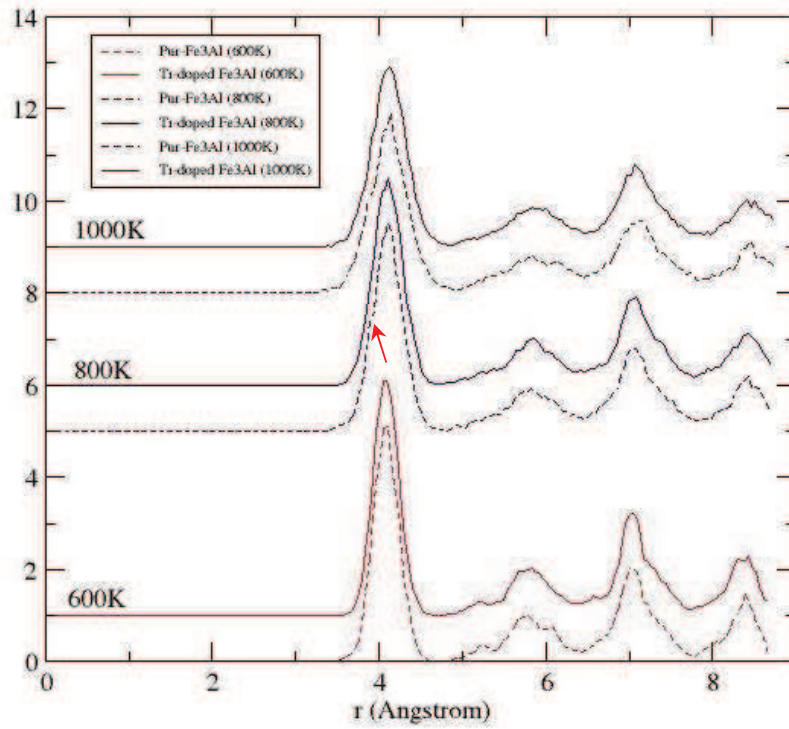
Figure. IV-13. The $g_{AlAl}(r)$ for pure and Ti-doped $D0_3$ Fe_3Al (on the FeI site) at 600K, 800K and 1000K.
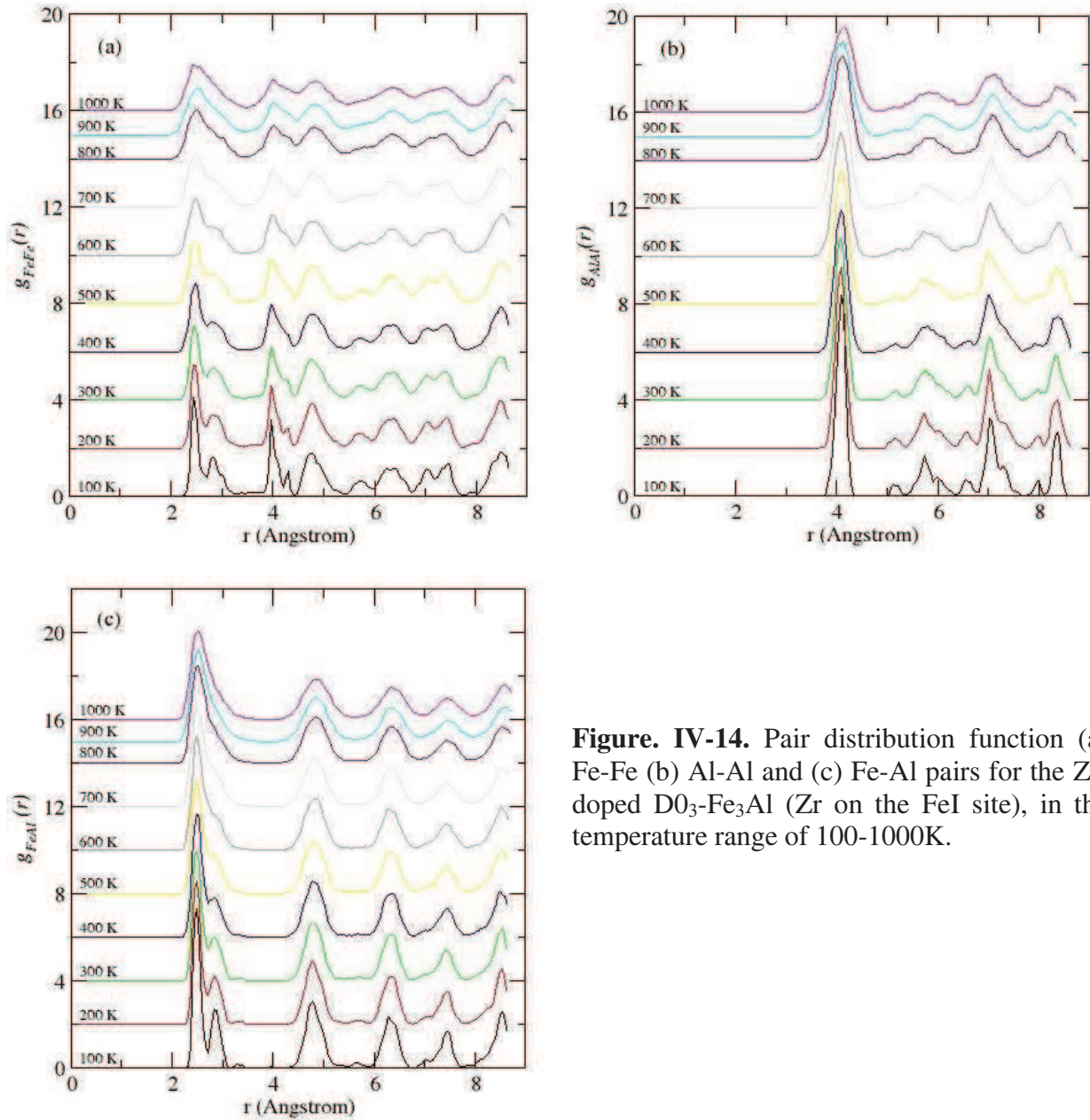
Figure. IV-14. Pair distribution function (a) Fe-Fe (b) Al-Al and (c) Fe-Al pairs for the Zr-doped D0$_3$-Fe$_3$Al (Zr on the FeI site), in the temperature range of 100-1000K.

From Fig. IV-12 (a), the Fe-Fe PDF of Fe$_3$Al doped with Ti impurity, it can be seen that the two peaks (in 2.5-3 Å) remain even 800 K, contrary to the Fe-Fe PDF of pure Fe$_3$Al in which a shift of the second peak from 2.8 Å to 3 Å was observed.

On the other hand, note that the profile curve of g$_{AlAl}$(r) [Fig. IV-12 (b)] remains unchanged, and the peak (around 3.8 Å) which appears at about 800K in the Al-Al PDF curve of pure-Fe$_3$Al is not observed here. This is clearly visible when the Al-Al PDFs for the pure and Ti-doped D0$_3$-Fe$_3$Al are represented together in the Fig. IV-13. The pair distribution functions in Fig. IV-13 are represented selectively for three temperatures 600K, 800K and 1000K to illustrate the difference that occurs above 800K. The absence of the peak around 3.8 Å (at the temperatures 800 and

900K) reveals that the distance between the first nearest neighbours remains constant up to higher temperatures and the Al atoms remain stable in their initial positions. Form Fig. IV-13 it can be seen clearly that the peak appears again at 1000K in the $g_{AlAl}(r)$ curve. This indicates that the order in the $L2_1$ structure (the ternary equivalent of the $D0_3$ structure) is affected only from about this temperature. Thus, the PDFs indicate that the presence of Ti in FeI site maintains the short range order of the L21-Fe$_3$Al intermetallic up the temperature 1000K. This finding is in agreement with the experimental results reported by [18]. Indeed, these authors have shown that the addition of 1% of titanium in the $D0_3$ structure increases the stability of the $D0_3$ structure up to 1000K.

However, in the PDFs for Fe$_3$Al doped with Zr impurity (Fig. IV-14), it can be seen that the peaks are less affected by the presence of Zr impurity in FeI site. In $g_{FeFe}(r)$ [Fig. IV-14(a)], the position of the second peak shows a slight shift with the increase of temperature. The appearance of the peak at around 3.8 Å in the $g_{AlAl}(r)$ [Fig. IV-14(b)] is also observed from about 800 K. This indicates that the stability of the D03 structure is not affected by the presence of Zr on the FeI site.

Knowing that the stability of Zr on the FeII increases site for higher temperatures and tends to be equivalent to that of FeI substitutions, the pair distribution functions were also calculated for the case when the Zr is placed on the FeII site. The the calculated $g_{AlAl}(r)$ for Zr substitutions on the FeI and FeII sites are represented in Fig. IV-15 together for comparison. As can be seen from figure, the profile curves of the two PDFS shows that there is no significant difreneces between the substitutions on the FeI and FeII sites. This indicates that the presence of Zr whether on a FeI site or a FeII site has no effect on the stability of the D0$_3$-structure.
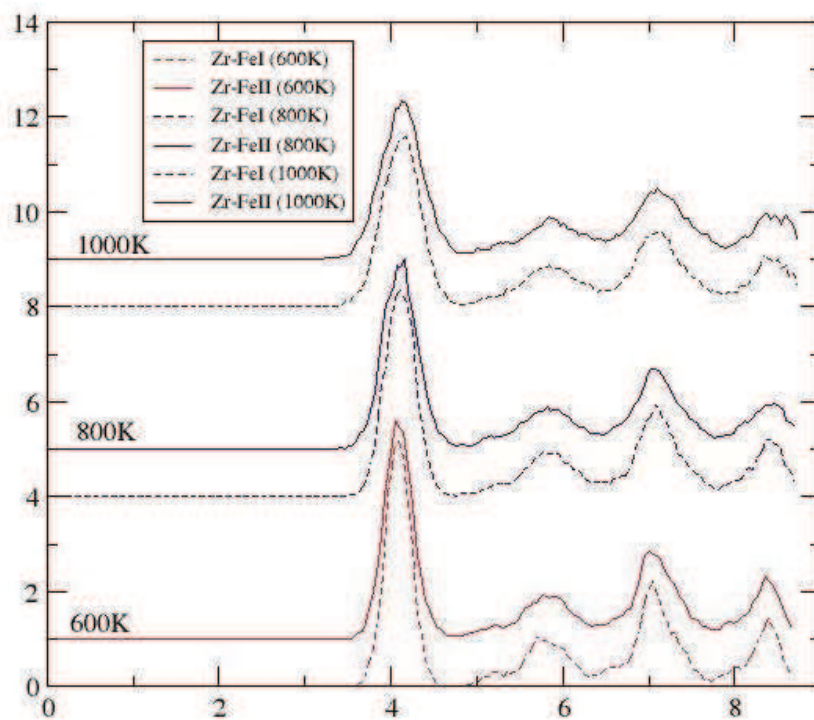
Figure IV-15. the gAlAl(r) for pure and Zr-doped D0$_3$ Fe$_3$Al on the FeI site and FeII sites at 600K, 800K and 1000K.

III. Transition metals segregation in ∑5 (310) [001] grain boundary

After having determined the differences in the behaviour between of the two transition metals (Ti and Zr) in the bulk, in the following, their stabilities in the ∑5 (310) [001] will be treated.

The calculations were performed using a supercell with 80 atoms. More details about the method used for the construction of the grain boundary and the choice of the size of the supercell are described in the previous chapter (Chapter III, Section III-1). The configurations of the transition metals substitutions considered in our calculations are given in the Fig. IV-16. These configurations are grouped in three categories (i) three substitutions in the grain boundary interface (ii) three substitutions in the first plane from the interface and (iii) three substitutions in the second plane from the interface.
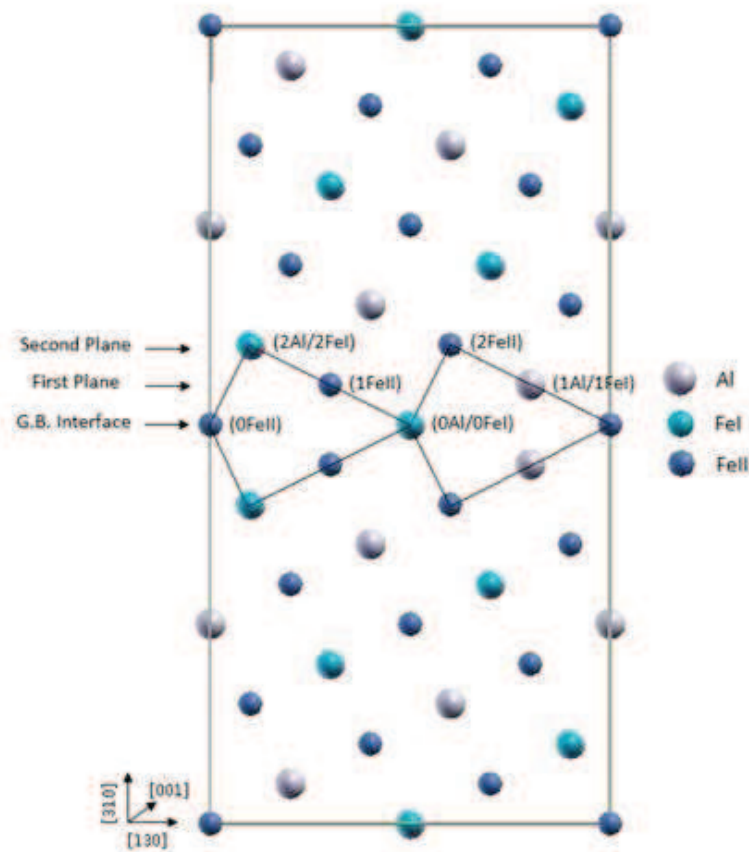
Figure. IV-16. Sketch showing the nine substitutional sites located within three different planes the within ∑5 (310)[001] grain boundary.

Unlike the bulk, each calculation has been turned with 400 dynamic molecular steps in order to gain a compromise between the size of the supercell and the relative running time. The 300 first

steps were reserved for equilibrating the system and were discarded from the subsequent analysis.

III.1. Site preference of Ti and Zr in the $\sum 5(310)[001]$

Because the large number of configurations to be taken into account in the $\sum 5$ (310) [001] grain boundary and the AIMD consuming calculation time, the defect energies of the two transition metal impurities were determined only for three temperatures (300 K, 600 K and 900 K).

The defect energies of the two transition metals in the grain boundary were calculated using the Eq. IV-1. *However, unlike the bulk, the defect energies were also calculated for the transition metals substitutions on the Al site in addition to the substitutions on the FeI and FeII site. These calculations were carried out to determine the site preference of the transition metals between the substitutions on the Al configurations and then to examine the relaxation of the grain boundary. It is important to recall that the comparisons (i) between the defect energies of the two transition metals and (ii) between substitutions on the Fe and Al sites are not possible.* The results are represented in Figs. IV-17 and IV-18 for substitutions on the (a) Al sites (b) FeI sites and (c) FeII sites, by taking into account the distance from the G.B. interface. For comparison, the values obtained from the static calculations at 0K (Chapter III) are also recalled.
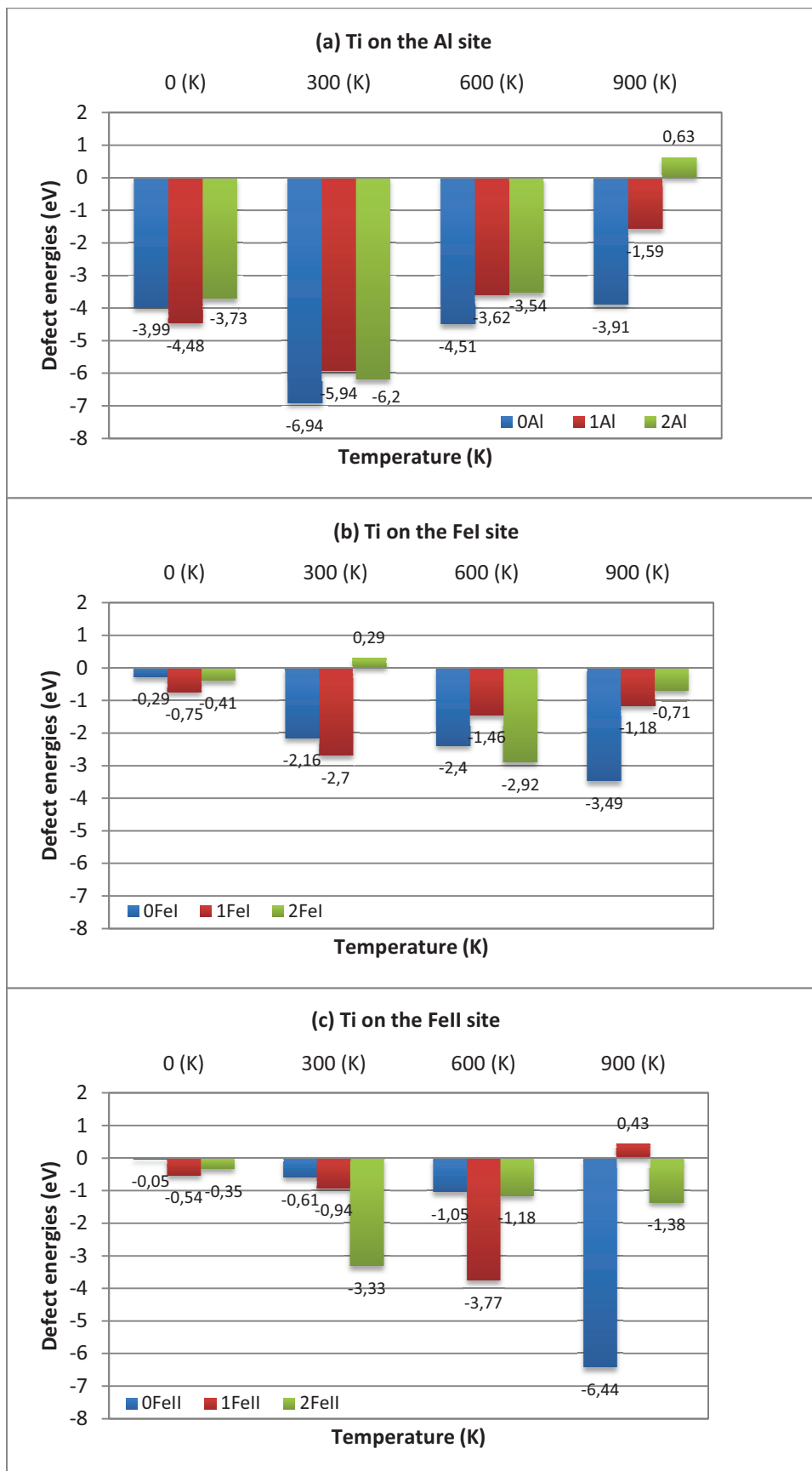
Figure. IV-17. The calculated defect energies of Ti impurity in the $\sum 5$ (310) [001] grain boundary at 300 K, 600 K and 900 K temperatures, for substitutions on (a) Al sites (b) FeI sites and (c) FeII sites, by taking into account the distance from the G.B. interface.
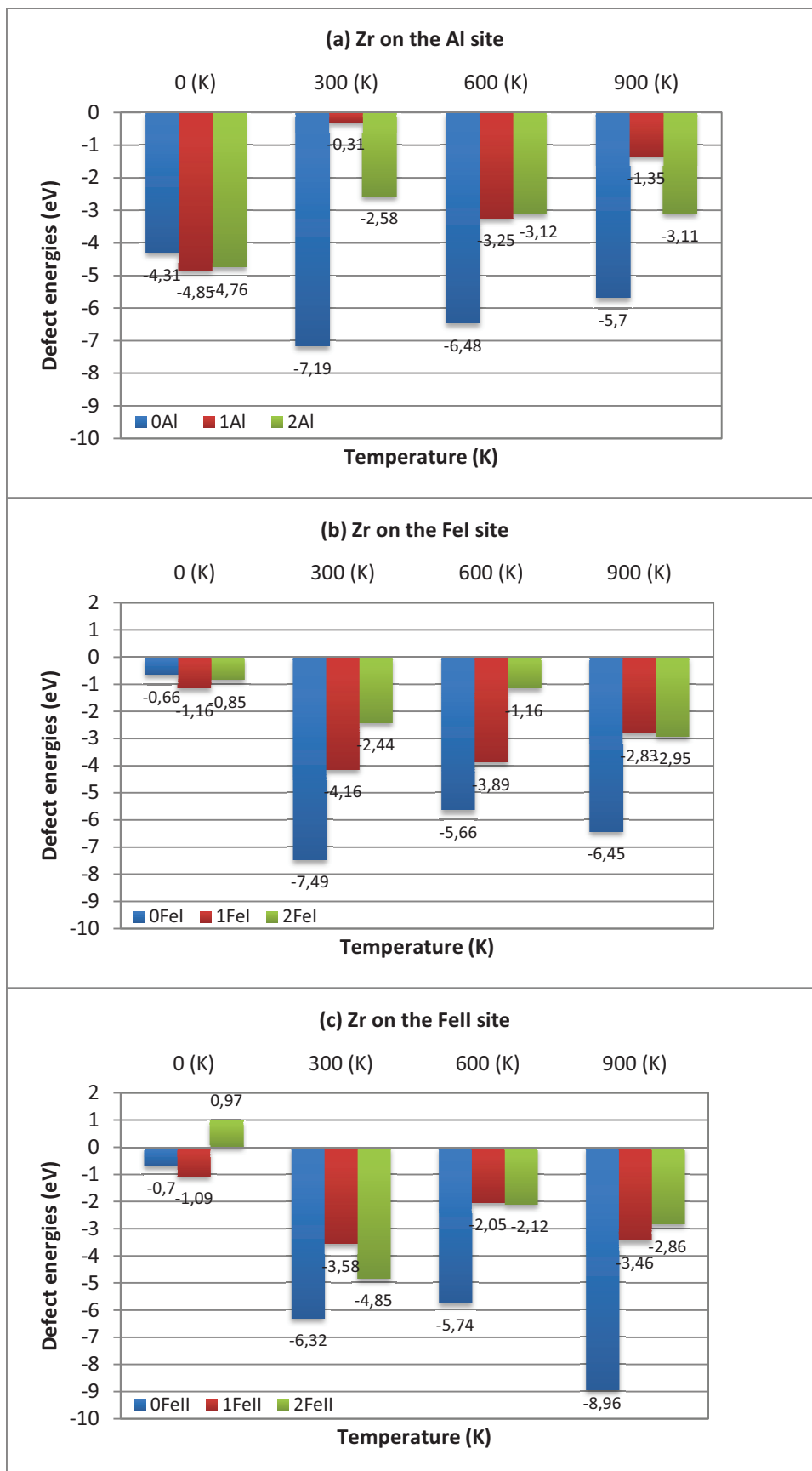
Figure. IV-18. The calculated defect energies of Zr impurity in the ∑5 (310) [001] grain boundary at 300 K, 600 K and 900 K temperatures, for substitutions on (a) Al sites (b) FeI sites and (c) FeII sites, by taking into account the distance from the G.B. interface.

As shown in Fig. IV-17 (a) for Ti on Al configuration, for the three temperatures, the most stable configuration corresponds to substitutions in the G.B. interface. For the case of Fe configurations, a comparison between the substitutions of Ti on the FeI and FeII sites [Figs. IV-17 (b) and (c)] shows that for the three temperatures, the defect energies are generally smaller for the configurations of the FeI substitutions, except for the three configurations 2FeII at 300K (-3.33 eV), 1FeII at 600K (-3.77 eV) and 0FeII at 900K (-6.44 eV) when the Ti impurity occupy the FeII sites with lower defects energies. The fact that the Ti impurity occupy the FeII site near the interface may be related to the effect of the environment knowing that the Ti impurity prefers to occupy the site where is surrounded only by the Fe atoms as first neighbours (i.e. iron rich environment). Note also that, contrary to the bulk, the geometry of the grain boundary has greatly changed as an effect of the temperature which led to changes in the first nearest neighbours of the Ti impurity. The structural environment of the impurities will be discussed below (Section III-2).

On the other hand, The classification of the most favourable configurations for the three temperatures, by taking into account the distance from the interface, is Fe substitution in: the second plane at 300K (2FeII)→ the first plane from the interface at 600K (1FeII)→ the G.B interface at 900K (0FeII). This indicates that the stability of the Ti impurity changes with increasing the temperature. While for intermediate temperatures (300K) is stable within configuration close to the bulk, by increasing temperature Ti impurity tends to occupy configuration in the grain boundary interface. In another words, this means that, it takes more temperature for the Ti impurity to be stable at the G.B. interface.

For the case of Zr substitutions, it can be seen from Fig.IV-18 that the most favorable configurations correspond to the substitutions in the G.B. interface (0Al, 0FeI and 0FeII) for the three temperatures. Contrary to the case of Ti configurations at the grain boundary, the Zr impurity prefers to reside in the G.B. interface even at intermediate temperature. It is important to recall that, from the static calculations at zero temperature [Fig. IV-18], the most favorable configurations were found to be the substitutions in the first plane from the grain boundary interface (1Al, 1FeI and 1FeII) for the two transition metals. Therefore, the small increase in temperature (to the intermediate temperature) leads to the migration of Zr impurity to the G.B. interface. Whereas for the case of Ti substitutions, a higher temperature (~900K) was needed to cause its relaxation to the grain boundary.

Now, the comparison between the defect energies for substitutions in the FeI and the FeII sites [Figs. IV-18(a) and (b)] shows that for intermediate temperature (300K) the Zr impurity prefer to

occupy the FeI sites. However, for higher temperatures, the Zr impurity tends to occupy the FeI and FeII sites with nearly equal energies. This indicates that, like in the bulk, the stability of Zr on the FeII site increases with increasing temperature.

From the calculated defect energies, it is clear that the two transition metals have different behaviours. While Ti is more stable at the bulk and it takes a higher temperature to relax to the grain boundary, the Zr impurity prefers to segregate at the grain boundary with lower defect energies even at intermediate temperature.

III.2. The effect of temperature on the structural relaxation of ∑5 grain boundary

In this section, the influence of temperature on the structural deformations of the Ti and Zr - doped grain boundaries will be treated. Before attempting to model the geometrical relaxation of the grain boundary induced by the impurity segregation, it is important to examine the relaxation of the pure grain boundary structure.

III.2.1. Relaxation of the clean grain boundary

To quantify the relaxation of the atoms we have calculated their displacements in the supercell. The displacements were calculated as difference between the average positions of the last 100 MD steps. We have considered only the last 100 steps after having tested that the movements of the atoms become almost to a stable configuration after relaxation towards the final positions. For example, Fig. IV-19 represents the positions of atoms during the relaxation, at 300K, for (a) 400 molecular dynamic (MD) steps (b) the last 200 MD steps and (c) the last 100 MD steps. It is clear from Fig.IV-19 (b) that the relaxation of atoms is less important when the 200 first steps were removed. The effect of relaxation is even less important when only the last 100 steps are considered [Fig. IV-19 (c)]. This suggests that the atoms have relaxed to their final positions after the 300 first steps of thermalization of the system.

Fig.IV-20 represents the displacements of the atoms calculated from the static calculations at 0K and that from AIMD calculations for the three different temperatures 300K, 600K and 900K. It is important to note before further analysis that the scale indicating the magnitude of the displacement vectors are rather different between 0K and 300K-600K and 900K.

Clearly one can see that the relaxations with temperature of the grain boundary structure are important when compared to that at 0K. For the temperatures 300 and 600K, the displacements of the atoms are in range 0.2-1.6 Å. Comparatively, for the case of relaxation at 0K, the
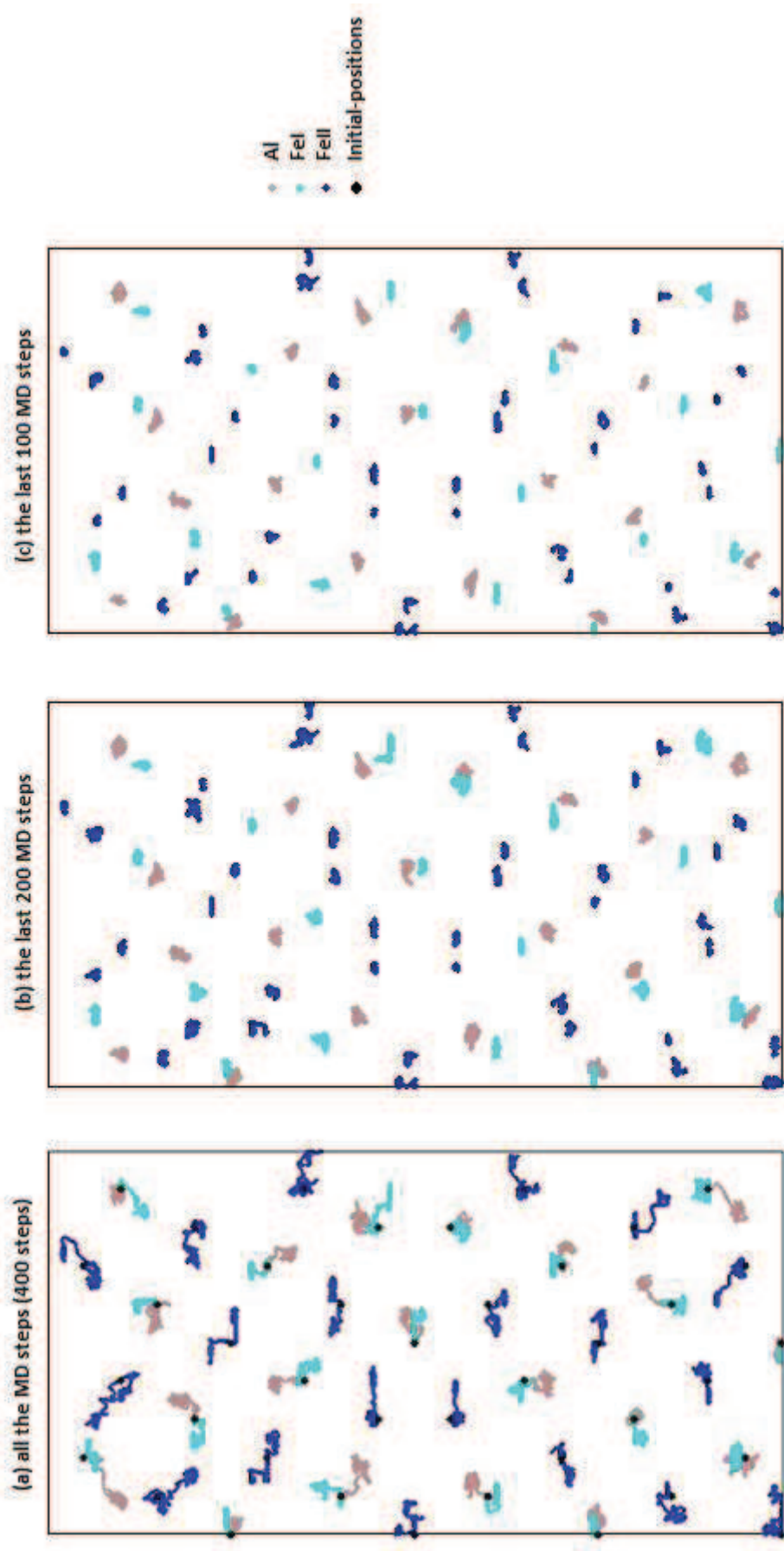
Figure.IV-19. The atomic positions in pure grain boundary $\Sigma5$ (310) for (a) 400 MD steps (b) the last 200 MD steps and (c) the last 100 MD steps.
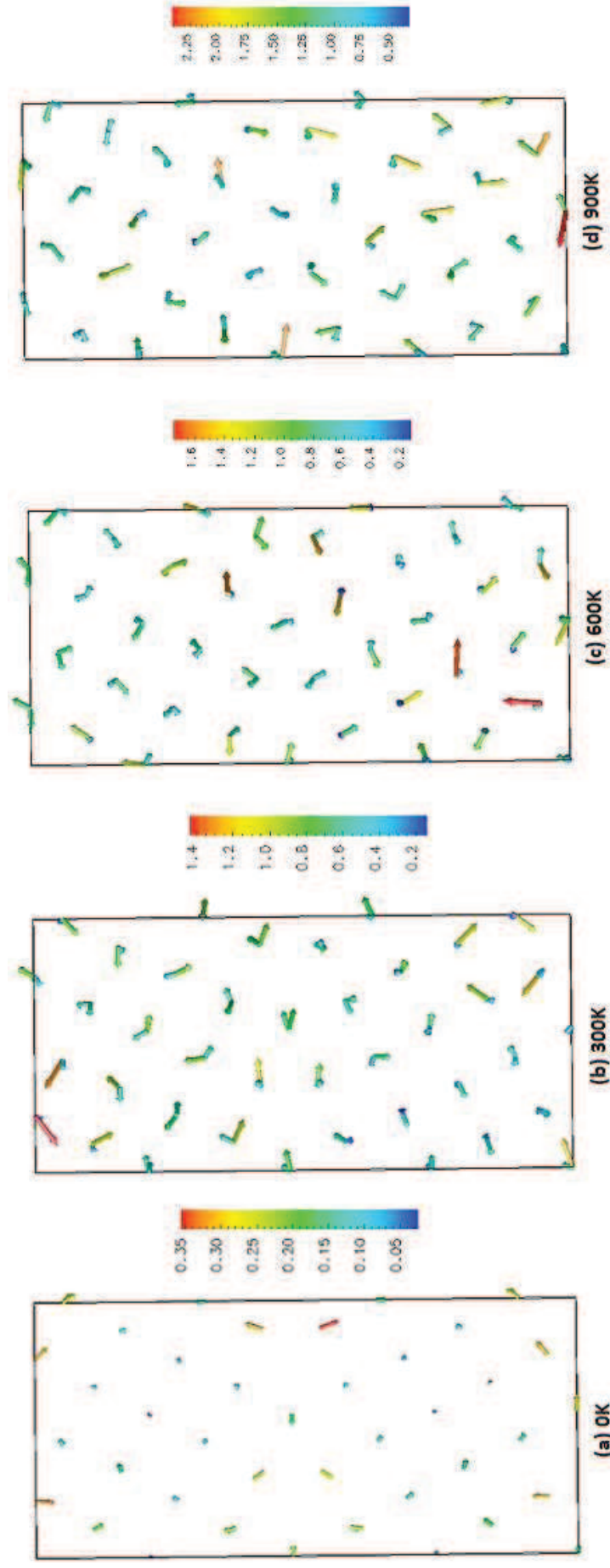
Figure.IV-20. The displacement of the atoms from in the relaxed grain boundary supercell from their initial positions (a) at 0K (b) at 300K (c) at 600K and (d) at 900K.

displacements of the atoms are in between 0 and 0.35Å, i.e. on average 70% smaller than that at 300K. This is due to the large vibrations of atoms as an effect of temperature. Increasing the temperature increases the internal energy and this is reflected in an increase in the average motion of the atoms in the system. For the case of relaxations at 900K, it can be seen that the displacements are more important, and can reach up to 2.5 Å ($\approx$ to the distance between the Fe nearest neighbours atoms in Fe_3Al) in the interface region. Fig. IV-21 gives the relative difference between the average displacements at each temperature and the average positions in the relaxed grain boundary at 0K. On can see that the displacement of atoms at 900K are very important, about ~90%. This indicates that a local disorder occurs in the grain boundary suprecell at this temperature. This trends is consistent with the experimental and theoretical results presented in the literature. Some authors consider indeed, from experimental results of grain boundary relaxation, that pronounced relaxation takes place when the temperature is higher than $T_0 \cong 0.4\ T_m$ or so (T_m is the melting temperature) [19]. Note, that for the case the Fe_3Al intemetallic compounds $T_0 \cong 614K \cong 0.4 \times 1536K$. Thus is consistent with our estimation showing a shop change between 600 and 900K. This also indicates that significant local disordering only occurs above this temperature. Also, according to results of dynamic molecular simulation for bicrystals with CSL structure becomes disordered above this temperature [20, 21]. This signifies that T_0 is the transformation temperature at which the structure of the grain boundary transforms from CSL structure to disordered structure. Thus in the following, the study will be limited to the structural relaxation at the intermediate temperature of 300K.
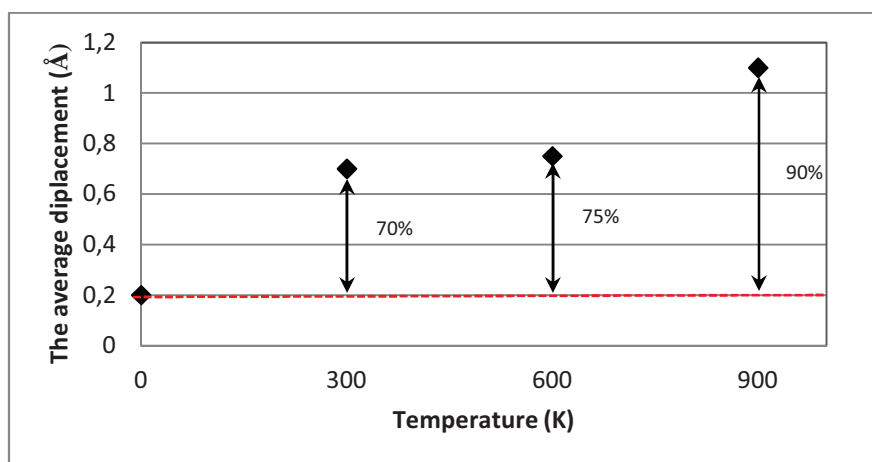
Figure .IV-21 Average displacements of the atoms in the relaxed supercells at 0K, 300K, 600K and 900K. The relative differences are marked in the graph.

Fig. IV-22 gives the relaxed pure grain boundary (a) at 0K and (c) at 300K. The displacements of the atoms from their initial positions are represented in Fig. IV-22 (b). At first sights, the magnitude of the displacement seems such that the center of the simulation box (away from the G.B) has a different aspect. This different aspect is in fact partially related the fact that the image of the grain boundary in Fig. IV-22 (c) correspond to the superposition of four different planes contained in the depth of the simulation box and that even the small displacement of the atom position leads to a higher number of atoms visible in Fig. IV-22 (c). However, comparison between Fig.IV- (a) and (c), shows that despite the apparent important relaxation of the atoms from their initial positions, the global structure of the $\sum 5$ (310) is preserved. In particular, the misorientation angle of the grain boundary is not affected.

As reported by T.S. Ke et al. [22], the coincidence lattice grain boundary constructed on the basis of geometrical considerations can not be stable when the temperature increases, because atomic overlaps or crowding of atoms will be produced in the boundary plane so that atomic readjustment or rigid translations will take place to reduce the energy. Then, although the periodicity of the boundary can be maintained, it is expected that the coincidence sites will no longer coincide with atoms. Especially when the misorientation is large or when there are deviations from coincidence site lattice misorientations, the disordered grain boundary region formed should be complicated.
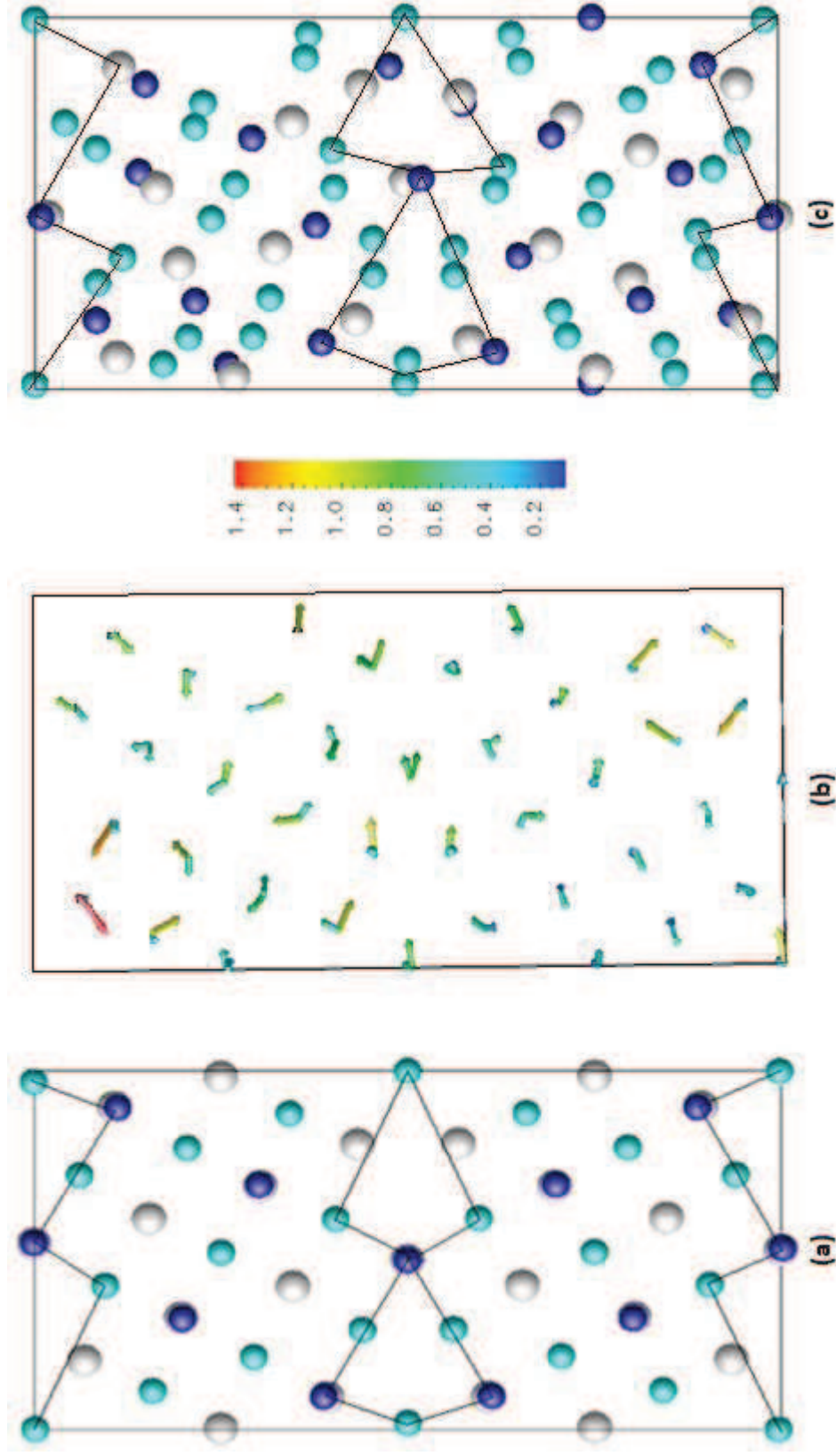
Figure. IV-22. (a) The initial positions of the relaxed grain boundary at 0K (b) the displacement of the atoms from the initial positions in the relaxed grain boundary at 300K and (c) the final positions of the atoms in the relaxed grain boundary at 300K.

III.2.2. Relaxation of the doped grain boundary at 300K

Now we turn to the structures of the doped grain boundaries with the substitutional Ti and Zr transition metal impurities.

First of all, we examine the displacement of the impurities in different substitutional configurations. Fig. V-23 (a) and (b) shows the calculated displacement of the impurities in different substitutional configurations. In Fig. V-23 the configurations are classified based on their positions from the grain boundary interface. For comparison, the calculated displacements of Ti and Zr impurities at 0K are also represented in Fig V-23 (c) and (d) respectively.
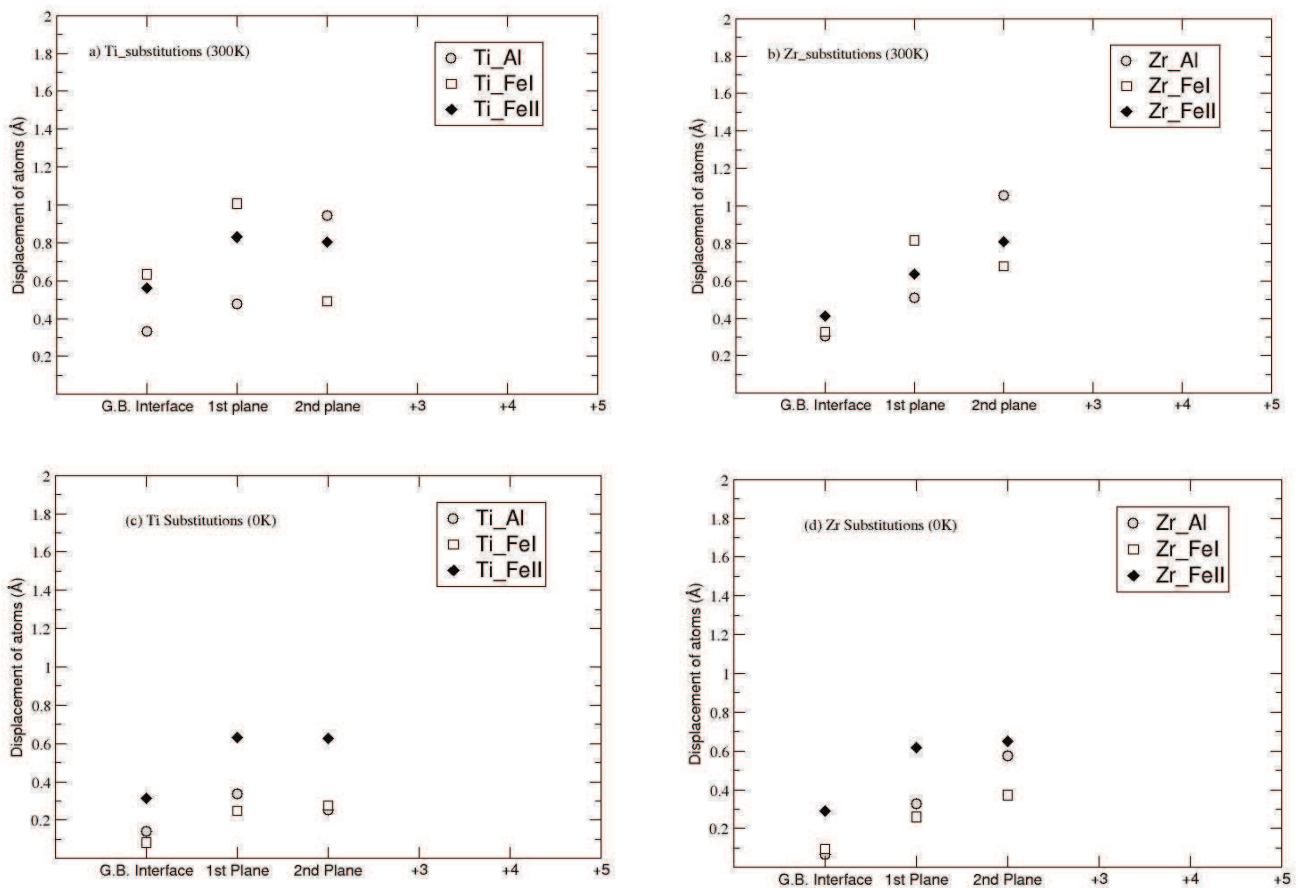
Figure. IV-23. The displacements of the impurities (a) Ti (b) Zr at 300K, (c) Ti and (d) Zr at 0K on different substitutional configurations.

The first point to be made is that the displacements of the impurities at 300K are more important than that at 0K. From Fig.V-23 it can be seen that the displacements of the impurities at 0K are in between 0.1 and 0.6 Å. Comparatively, while for the case of 300K, the amplitudes of displacements is between 0.35 and 1.1 Å. On the other hand, it can be seen that the most significant displacements take place when impurities are incorporated in the first and second planes from the grain boundary interface. These displacements are in between 0.8 and 1.1 Å,

which are closer to the distance between two parallel planes (0.92 Å) in the grain boundary supercell. This suggests that the impurities tend to relax to the grain boundary interface.

It important to recall that, at 0K, it has been found that the largest displacements of the impurities correspond to the configurations of the substitutions on the FeII sites (Figs. IV-23 (c) and (d)). The reason for this is that the impurities, particularly the Ti impurity, in these configurations (poor iron environment, 4FeI+4Al) tend to relax to an iron rich environment. However, at 300K, it can be seen from Figs. IV-23 (a) and (b), that the displacements of the impurities are important for substitutions on the FeII sites as well as for Al and FeI sites. Additionally, in the first and second planes from the interface, the displacements of the impurities on the Al and FeI sites are larger than that on the FeII ones, despite the fact that these configurations are initially richer in iron.
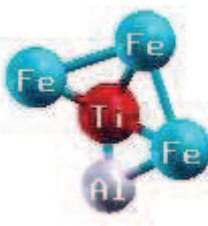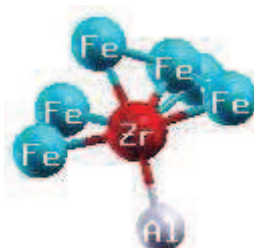
Knowing that the atoms in the grain boundary supercell have moved from their initial positions, it very much possible that the environment around the impurities has changed due to the large displacement of the first nearest neighbours. In this case, it is likely that the impurities also tried to move towards a new iron rich environment. To check this possibility we have analyzed the environment (the first nearest neighbours) corresponding to each configuration after relaxation. Fig. IV-24 represents the structural environment distributions for the different configurations of the Ti and Zr substitutions. For comparison, the structural environments of the impurities in the un-relaxed grain boundary are also represented. In this figure, the calculated defect energies that were obtained in Section III.1 (Chapter IV) are also listed to get more insights about the most stable configurations.
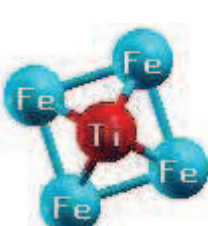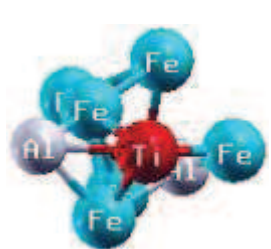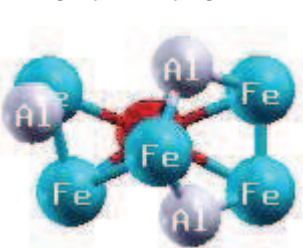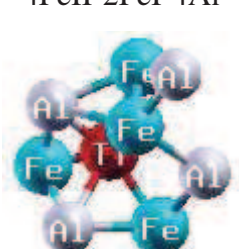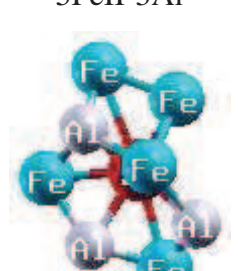
For the un-relaxed configurations, due to the different atomic arrangement in the grain boundary region, one can see that the structural environment of substitutions on the G.B. interface (0Al, 0FeI and 0FeII) and the first plane from the interface (1Al, 1FeI and 1FeII) are different from that of substitutions in the bulk (see Fig.IV-16). Further away from the G.B. interface (2Al, 2FeI and 2FeII), the structural environments becomes similar to that of the bulk.

For the case of Ti substitutions, the comparison between the defect energies of the three configurations (i.e. G.B interface, 1st plane and 2nd plane) for each type of substitutions (i.e. Al, FeI and FeII) shows that the most stable configurations correspond to the substitutions with an iron rich environments. The three most stable configurations are, depending on the nature of substitutions, substitution on the 0Al site within the G.B. interface with (5FeII+3FeI) as first neighbours, substitution on the 1FeI site in the first plane from the interface with (3FeII-2FeI-

2Al) as first neighbours and substitution on the 2FeII site in the second plane from the interface with (3FeII-3FeI-2Al) as first neighbours.

On another hand, comparison between the substitutions on the FeI and FeII sites reveals that the most stable configuration corresponds to substitutions on the FeII site in the second plane from the interface (2FeII) with the lower defect energies. This indicates that the Ti, in addition to the nature of the environment, prefers to occupy a configuration close to the bulk. Comparatively, for the case of Zr substitutions, the most stable configurations correspond to the substitutions on the G.B. interface (0Al, 0FeI and 0FII). Except for the case of substitution on the 0FeI site with (5FeII-3Al), the two other configurations correspond to the substitutions with iron rich environments. This indicates that, contrary to the Ti impurity, the Zr atom prefers to reside in the configurations within the G.B. interface whatever the nature of its environment.

Configurations	Un-relaxed G.B.	Ti-doped G.B.	E_d^{Ti}	Zr-doped G.B.	E_d^{Zr}
0Al	8FeII	5FeII-3FeI	**-6.94**	5FeII-3FeI	**-7.19**
1Al	6FeII-1FeI-1Al	3FeII-3FeI-2Al	**-5.94**	3FeII-4FeI-1Al	**-0.31**
2Al	8FeII	6FeII-2FeI	**-6.20**	6FeII-2FeI	**-2.58**

0FeI	8FeII	4FeII-1FeI-3Al	**-2.16**	5FeII-3Al	**-7.49**
1FeI	6FeII-1Fe1-1Al	3FeII-2FeI-2Al	**-2.7**	6FeII-2Al	**-4.16**
2FeI	8FeII	6FeII-2Al	**0.29**	4FeII-4Al	**-2.44**
0FeII	4FeI-4Al	3FeII-2FeI-3Al	**-0.61**	2FeII-4FeI-2Al	**-6.32**
1FeII	4FeI-2FeII-2Al	4FeII-2FeI-4Al	**-0.94**	5FeII-3Al	**-3.58**

2FeII	4FeI-4Al	2FeII-4FeI-2Al	-3.33	FeII-3FeI-4Al	-4.85
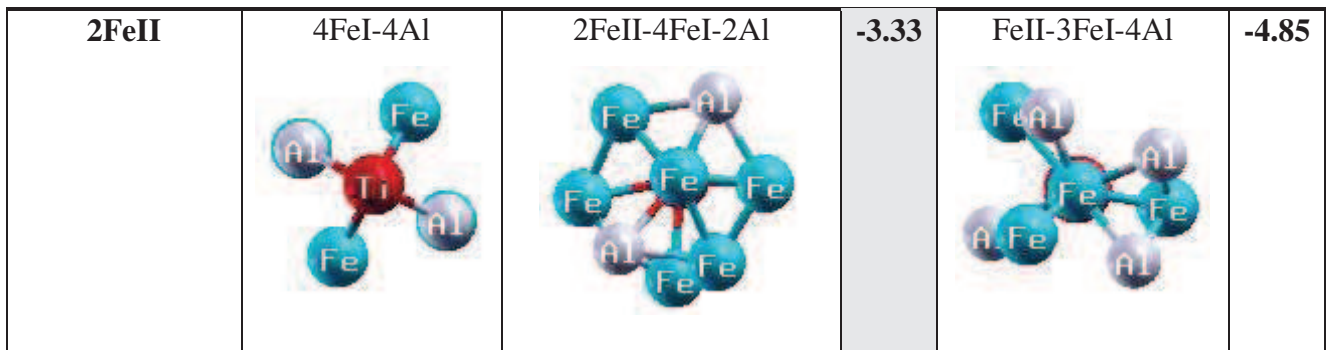
Figure.IV-23. Snapshots of the structural environment of the impurities before and after relaxation in the $\sum 5$ (310)[001] grain boundary.

Figs. V-24 and V-25 show the relaxed grain boundary geometries with the substitutional Ti and Zr transition metal impurities, respectively, for the most stable configurations among the three types of substitutions on (a) Al sites (b) FeI sites and (c) FeII sites at 300 K.

It is important to recall that from the calculated defects energies, it has been found that the 0Al, 1FeI and 2FeII are the most stable configurations for Ti substitutions. For the case of the Zr substitutions, the most stable configurations are 0Al, 0FeI and 0FeII. In order to understand the mechanism which lead to grain boundary deformation, a simplified representation of the same atomic positions shown in Figs. (a), (b) and (c) is given in Figs. (e), (d) and (f), respectively, in which the displacement of each atom from its initial position is shown by solid arrow.

Examination of the doped-grain boundary structures (Fig. IV-24 and 25) indicates that the addition of transition metal impurities affect the relaxation process of the grain boundary in an irregular manner for different configurations and diffusion process can take place in the grain boundary interface. Thus the grain-boundary relaxation becomes pronounced. In general, the segregation of the impurities at the grain boundary induces the deformation of its structure. However, comparison between the Figs. IV-24 and IV-25 shows that, despite the bigger size of Zr impurity, the distortions of the G.B. interface created by Ti additions are more important than that created by Zr additions. The reason for this is that the Ti impurity tends to reinforce the bonds with their first nearest neighbours.
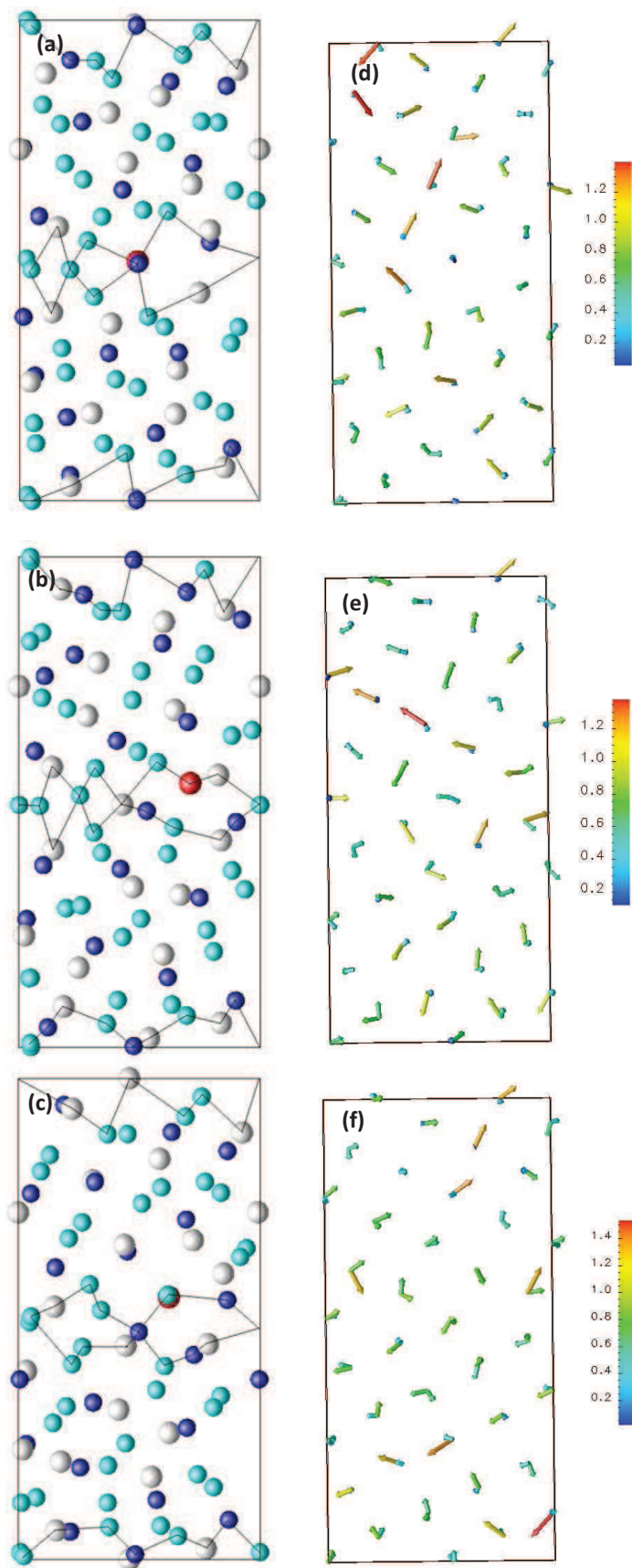
Figure. V-24. The left plots (a), (b) and (c) are the relaxed grain boundary geometries with Ti substitution on the most stable configurations 0Al, 1FeI and 2FeII, respectively. The right plots (d), (e) and (f) the displacement of each atom in the grain boundaries represented in (a), (b) and (c) from its initial positions.
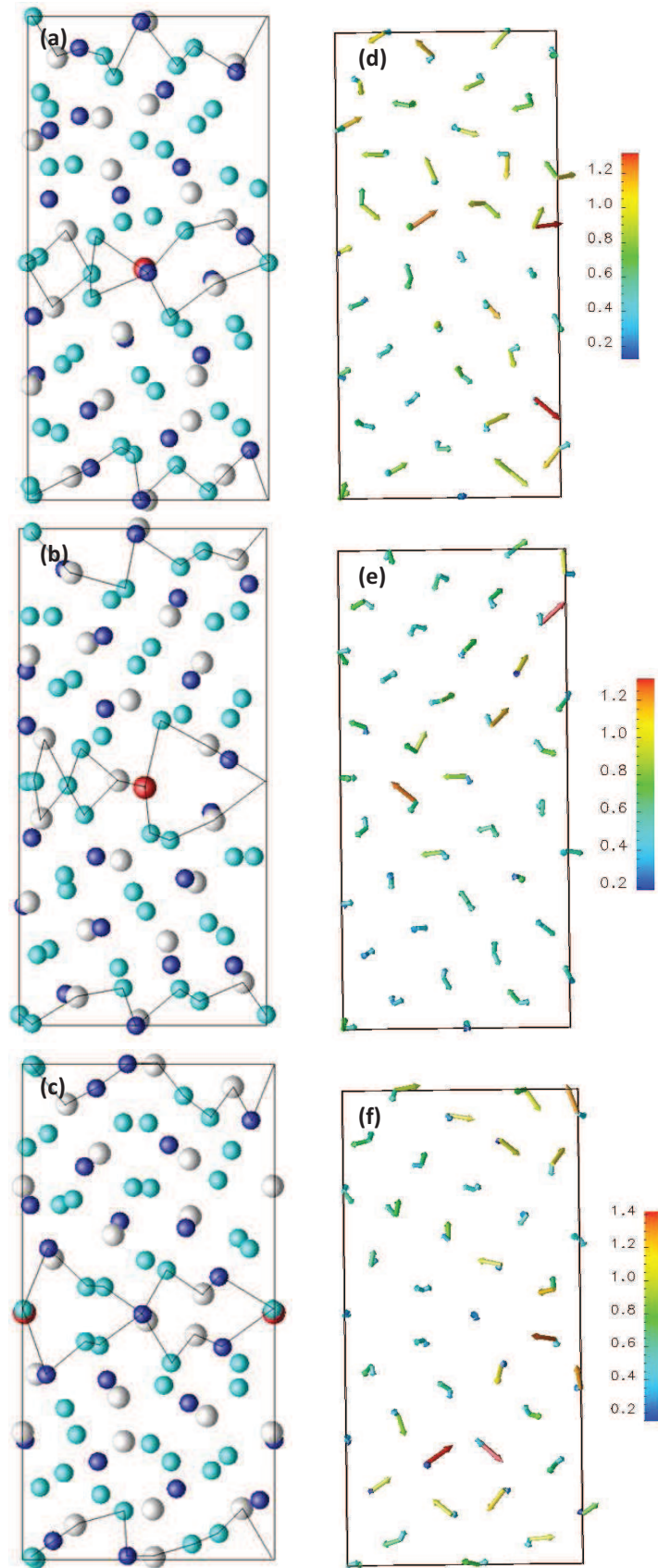
Figure. V-25. The left plots (a), (b) and (c) are the relaxed grain boundary geometries with Zr substitution on the most stable configurations 0Al, 1FeI and 2FeII, respectively. The right plots (d), (e) and (f) the displacement of each atom in the grain boundaries represented in (a), (b) and (c) from its initial positions.

IV. Summary and conclusion

In this chapter Ab Initio Molecular Dynamic study was set to investigate the effect of temperature on the structural stabilities of Ti and Zr impurities in the bulk and $\sum 5$ (310)[001] of the $D0_3$-Fe_3Al intermetallic compound.

The results of defect energies indicate that the stability of Ti on the FeI site increase with temperature. Comparatively, Zr impurities have the tendency to occupy nearly equally the FeI and FeII sites at higher temperatures.

The calculated defect energies of vacancies created in the first nearest neighbours to the impurities allow to draw the conclusion that the Ti impurity strengthens the interaction with their Fe first neighbour atoms. However, the Zr additions reduce the interactions with their first nearest neighbours when compared to Fe-Al and Fe-Fe bonds in the pure Fe_3Al.

The calculated pair distribution functions in the pure Fe_3Al reveal that the structural stability of the $D0_3$ is affected from about 800K. We show also that, in agreement with the experimental results, there is a direct relationship between the magnetic moment and the lattice parameter of the $D0_3$ Fe_3Al intermetallic compounds. The structural disorder of the $D0_3$ starting from about 800K alters the values of magnetic moment of the Fe atoms. In agreement with the the trends observed experimentally, it is found here that the 1% of Ti increases the stability of the $D0_3$ structure up to 1000K. Comparatively, the Zr addition does not affect the stability of the $D0_3$ structure.

The calculated defect energies of the impurities in the $\sum 5(310)$ grain boundary show that the Ti impurity prefers to reside in an iron rich environment further away the interface at intermediate temperature of 300K. It becomes stable at the G.B. interface only at high temperature (900K). The results show also that, contrary to the Ti impurity, the Zr segregate at the G.B. interface with the lower defect energies even at intermediate temperatures.

The relaxation of the $\sum 5$ (310) grain boundary at the temperatures of 300K and 600K is 70% more important than that occurred at 0K. However, the structural geometries of the interface remain unchanged. In agreement with the theoretical assumptions and experimental data for metals, the relaxation of the grain boundary becomes pronounced only above $0.4 \times T_m$ (T_m melting temperature). At the intermediate temperature of 300K, the segregation of impurities in the $\sum 5$ (310) grain boundary affects its relaxation in an irregular manner and a local disorder occurs in the grain boundary interface.

Reference

[1] Kresse G, Hafner J. Physical Review B **47** (1993) 558.

[2] Kresse G, Furthmuller J. Physical Review B **54** (1996)11169.

[3] Perdew JP, Chevary JA, Vosko SH, Jackson KA, Pederson MR, Singh DJ, Fiolhais C. Physical Review B **46** (1992) 6671.

[4] Perdew JP. Unified theory of exchange and correlation beyond the local density approximation. In: Ziesche P, Eschrig H, editors. Electronic structure of solids. Berlin: Akademie Verlag; 1991. p. 11–20.

[5] Vanderbilt D. Physical Review B **41** (1990) 7892.

[6] B.V. Reddy, D.H. Satry, S.C. Deevi, S.N. Khanna, Physical Review B **64** (2001) 224419.

[7] E. Apinaniz, F. Plazaola, J.S. Garitaonandia, J. Magn. And Magn. Mater **272-276** (2004) 794.

[8] D. Martin Rofriguez, F. Plazaola, J.S. Garitaonandia, G.J. Guello, J. Magn. And Magn. Mater **316** (2007) e488.

[9] R.D. Shull, H. Okamoto, P.A. Beck, solid State Commun. **20** (1976) 863.

[10] Y .S.Touloukian, R.K.Kirby, R.E.Taylor and P.D.Desai, Thermodynamical Properties of matter: Thermal Expansion Metallic Elements and Alloys, (IFI/ Plenum, NY 1975).

[11] T. Seletskaia, L. Muratov, B. Cooper, American Physical Society, Annual APS March Meeting, March 18 - 22, 2002.

[12] B.N. Person, Phys. Rev. B **40**. (1980) 7115.

[13] G.D. Garbulsky and G. Ceder, Phys. Rev B **49** (1994) 6327.

[14] L. Anthony, J.K. Okamoto, B. Fultz, Phys. Rev. Lett. **70**, (1994) 1128.

[15] B. Fultz, L.J. Nagel, L. Anthony, and J.K. Okamoto, Phys. Rev. Lett. **73**, (1994) 3034.

[16] C. Booth and J.S. Rowlinson, Trans. Faraday Soc. 51, (1955) 463.

[17] C. Tuijn and H. Bakker, J. Phys. C **19** (1986) 5585.

[18] L. Anthony, B. Fultz, Acta Metall. Mater. **43** (1995) 3885.

[19] T.S. Ke and Duan Yuhua: Acta Metall. Mater.**41** (1993) 1003.

[20] P.S. Ho, T. Kwok, T. Neuyen, C. Nitta, and S.Yip: Scripta Metall **19** (1985) 993.

[21] Chen Zhiying, Duan Yuhua and GE Tingsui: Acta Mech. Sinica **11** (1995) 259.

[22] T. S. Ke , F. Mehl, Metallurgical and Materials Transactions A **30** (1999) 2267.

Conclusion

Combining low density with creep and corrosion resistance, the D0$_3$ ordered iron aluminides are promising materials for a wide variety of medium to high-temperature structural applications. However, their application is still limited because of their room-temperature intergranular brittleness and their low strength and creep resistance at higher temperatures. Efforts to improve the high-temperature mechanical properties have often included ternary additions to Fe$_3$Al in order to extend the temperature range over which the D0$_3$ phase is stable up to higher temperatures. In this work, the effects of Ti and Zr transition metals on the stability of the D0$_3$ structure were studied by means of ab-initio calculations. Knowing that, in these compounds, small additions of transition elements, such as Zr, can strengthen the grain boundary cohesion, comparison of the behaviour of these two transition metals when are placed at the $\sum 5$ (310) [001] has been then investigated. Our study was performed both by using the static and Ab Initio Molecular Dynamics to take into account the effect of temperature.

The results obtained based on the static ab initio calculations can be summarized as follows :

The analysis of site occupancy in the bulk confirms, consistently with the previous literature results, that FeII sites are the preferential sites for vacancies. Comparatively, both Ti and Zr prefer to reside on FeI sites. The positive formation energies calculated for all Zr substitutions suggest however that Zr has very little miscibility in the bulk D0$_3$-Fe$_3$Al while the 3% of Ti impurities are miscible in Fe$_3$Al.

The interface energy of a clean $\sum 5$ (310) interface has been found to be (0.36 J/m^2). The presence of transition metal impurities on various sites is found to reduce the interface energies by about 14% and 22% for Ti and Zr, respectively. The maximum expected reductions are obtained when the transition metals are located on a FeII site in the first plane away from the exact interface. This suggests that both Ti and Zr doped grains boundaries are more stable than the parent 'clean' grain boundary. The interface energies for the Zr-doped grain boundaries are systematically lower than for the Ti-doped boundary. So that the stability induced with Zr is more important than that of Ti. The interface energy depends also on the relaxation of the

multilayers of the G.B interface: the larger the interface expansion, the higher the interface energy.

At the grain boundary, the analysis of interstitial configurations indicates that the most favorable sites for Zr and Ti is the one for which this transition metal impurity interacts with only Fe atoms as first neighbors. Interestingly, the negative values of formation energy (-0.18 eV) obtained for Zr indicates that this atom is more stable when inserted on such a site at a $\sum 5$ (310) grain boundary than in the bulk of the material. Comparatively, Ti is clearly more stable within the bulk than inserted at the grain boundary.

Contrary to Ti which is not stable as an insertion, the results indicates that Zr is stable within the grain boundary both as an insertion and as a substituting element (on FeI and FeII sites). This brings a high potential for introducing Zr at the grain boundary with a large domain of stability in terms of the exact location within a relaxed grain boundary.

The bonding charge distribution in the boundary region is different from that in the bulk due to the different atomic rearrangement. For the clean grain boundary, the bonding normal to the grain boundary develops between the FeI atoms in the (001) planes. Whereas, in the (002) plane, the accumulation of interstitial bonding charge across the neighbours FeII pair is parallel to the grain boundary. The T.M. impurities (when substituted) in the most stable configuration are found to reduce the general bonding with their first neighbor FeI atoms in the (004) plane and enhance the bonding charge normal to the interface between the FeII atoms in the pure FeII plane. Therefore the beneficial effect of the impurities on the cohesion of the $\sum 5$ (310)[001] grain boundary may originate from the FeII-FeII covalent bonding normal to the interface in the pure FeII planes which holds the two grains together.

Selected results from the ab initio molecular dynamics are summarized below:

The analysis with temperatures (100-1100 K) of the site preference for substitutions of Ti and Zr impurities on FeI and FeII sites of the Fe_3Al has revealed interesting differences between the two transition metal elements. Ti is more stable on a FeI site and the stability of this site increases with temperature. Comparatively, Zr impurities have the tendency to occupy nearly equally the FeI and FeII sites at high temperature.

The calculated bond lengths between the impurities and their first nearest neighbours show that the Ti impurity induces a strain on their neighbouring Al atoms when it is placed on the FeII site. Complementary, it was found that it is rather more expensive to create a vacancy on the Fe site

first nearest neighbour to the Ti impurity than on the Al one. This indicates that the Ti impurities strengthen the interactions with their first Fe nearest neighbours atoms. However, for the case of Zr additions, the vacancies are favoured both on the Fe and Al sites. Therefore, the Zr impurities reduce the interactions with their first nearest neighbours in the Fe_3Al structure.

The appearance of new peaks in the Al-Al pair distributions function, calculated for the pure Fe_3Al, from about 800K indicates that the stability of the $D0_3$-Fe_3Al structure is affected from this temperature and local disorder occurs. For the case of Ti substitutions, the pair distributions function $g_{Al-Al}(r)$ maintains unchanged up to 1000K. This indicates that, in agreement with the experimental observations, the 1% of Ti increases the stability of the $D0_3$ structure up 1000K. However, for the case of Zr substitutions, the analysis of the pair distribution function shows that the Zr additions have no effect on the stability of the $D0_3$ both when are placed on the FeI and FeII sites.

The calculated defect energies of the impurities in the $\sum 5(310)[001]$ grain boundary shows that the Ti impurity prefers to occupy the iron rich configurations further away the interface at intermediate temperature of 300K. The relaxation of Ti impurity to the G.B. interface occurs only at high temperature (at 900K). Comparatively, the Zr impurities occupy the configurations at the G.B interface with the lower defect energies even at intermediate temperatures.

The relaxation of the grain boundary becomes significant as an effect of temperature. It was found that the relaxation at intermediate temperatures is 70% more important than that occurred at 0K. However, although the large displacement of the atoms, the structural stability of the $\sum 5$ (310)[001] grain boundary maintains unchanged. From about 600K the relaxation becomes pronounced, 90% more important than that at 0K, and the disorder occurs in the grain boundary supercell. Based on the theoretical and experimental assumptions this temperature corresponds to the temperature transformation $T_0 \cong 0.4xT_m$ (T_m, melting temperature) of the CSL grain boundary structure to a disordered structure.

Thus, in our study, the analysis of the structural geometries induced by the segregated impurities has been limited to the intermediate temperature of 300K. It has been found that the segregated impurities (Ti and Zr) affect the relaxation process of the grain boundary. The relaxation of both Ti and Zr doped-grain boundaries occurs in irregular manners. However, despite the bigger size of the Zr impurity, it has been found that, the distortions created by Ti addition are more important than that produced in the case of Zr segregation. The reason is because the Ti impurity tends to strengthen the interactions with their first neighbours Fe atoms.
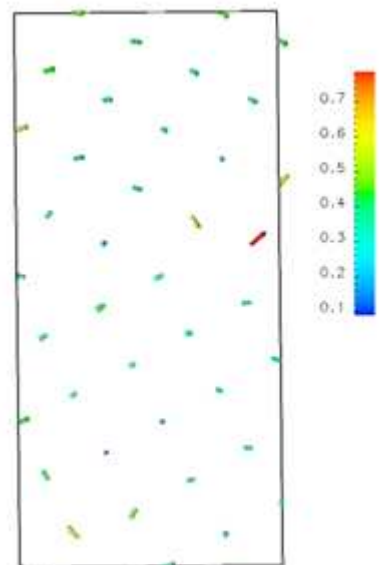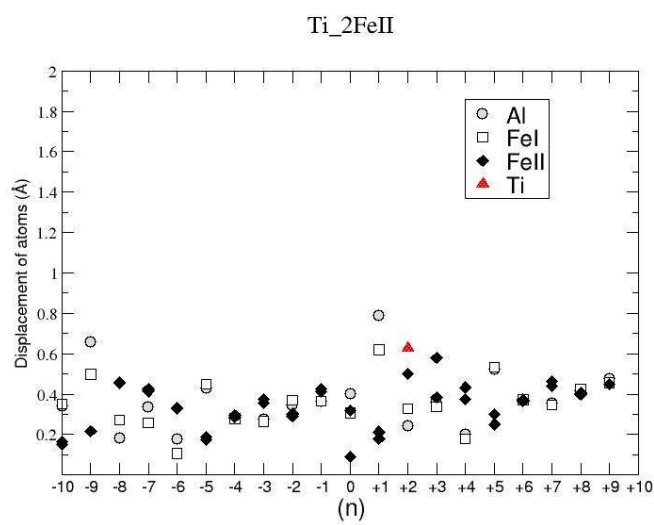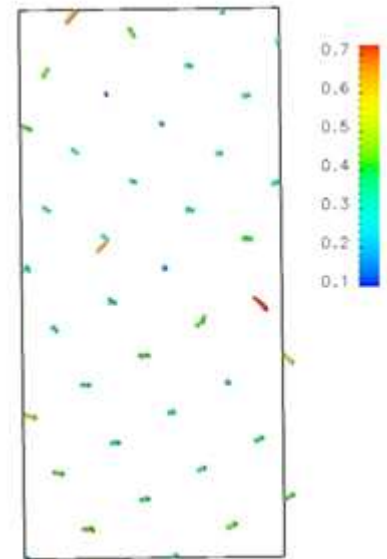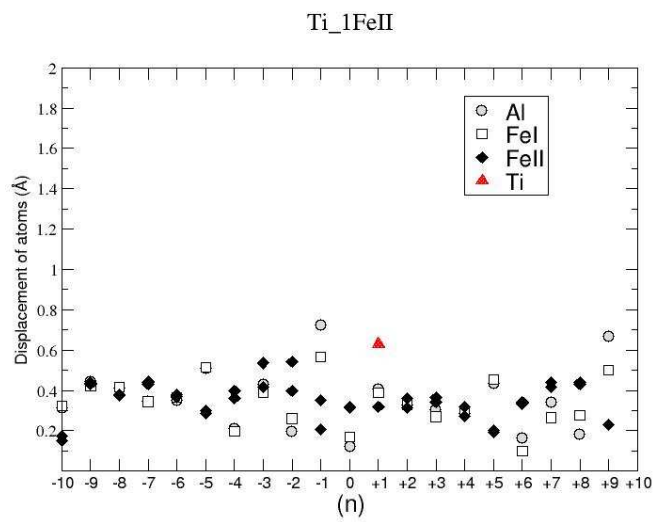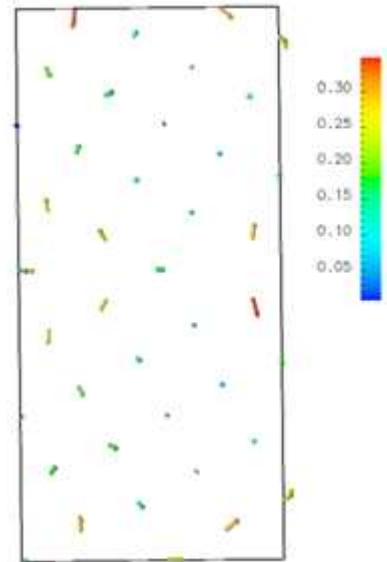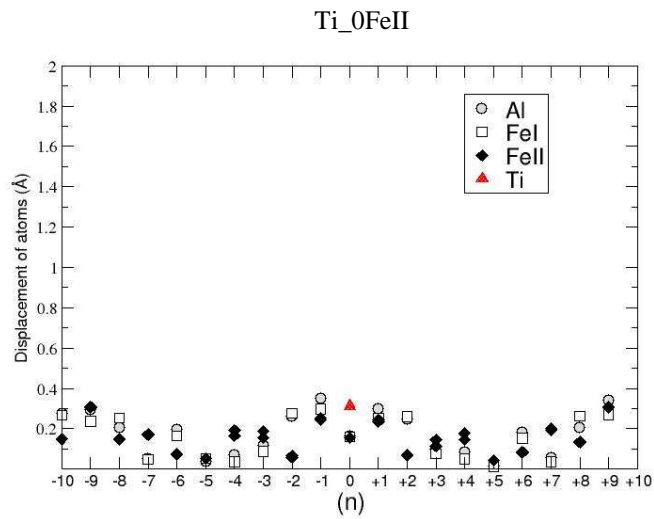
On a more general basis, the work carried out in this PhD brings additional information on the complex field dealing with the understanding of the effect of transition metal additions in intermetallic coumpounds. Indeed, it is worth remembering that the iron aluminide based intermetallic compounds still presents several open questions, despite the numerous experimental and theoretical studies in the literature. For example, it is well known that their ductility and fracture toughness can be modified by addition of ternary elements and that the associated grain boundary segregation can change the fracture mode in several compounds of the FeAl systems. However, little is known from the microscopical point of view on dislocation nucleation, mobility or pile-up at grain boundaries and the influence of interstitial and substitution solutes. A lot of work is still required before mastering the modeling of crack tip plasticity or the atomistics of brittle fracture in the presence of ductilizing additives. The type of work carried out in this thesis is just one of the numerous stages to be done to understand, in the future with the combination of the experimental investigation, the effect of segregated elements on the ductility/hardening of the FeAl intermetallic compounds. Our work, using first principal density functional theory calculation, has shown that Ti and Zr are two transition metals having significantly different effects in Fe_3Al. Their site preferences with temperature have been determined in the bulk and for a specific $\sum 5$ grain boundary. Such information on the location of site defects and the way different transition metals relax a grain boundary is the type of important information that will be required by mechanical engineers and metallurgists dealing with dislocation interactions to understand plasticity (or lack of plasticity) in these alloys.
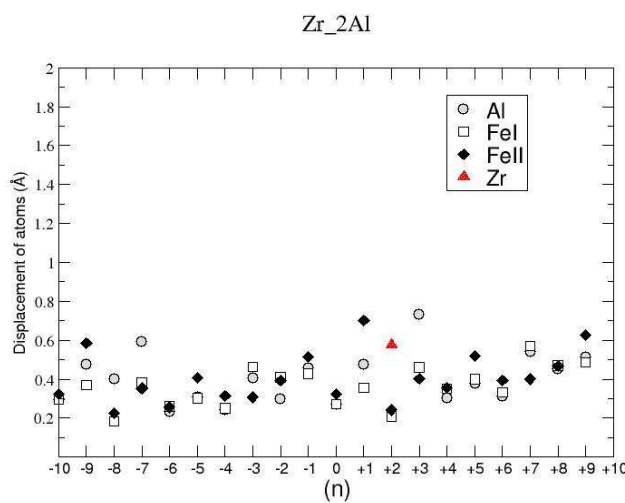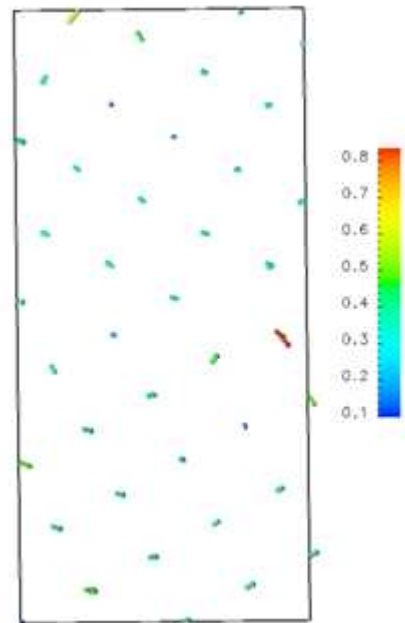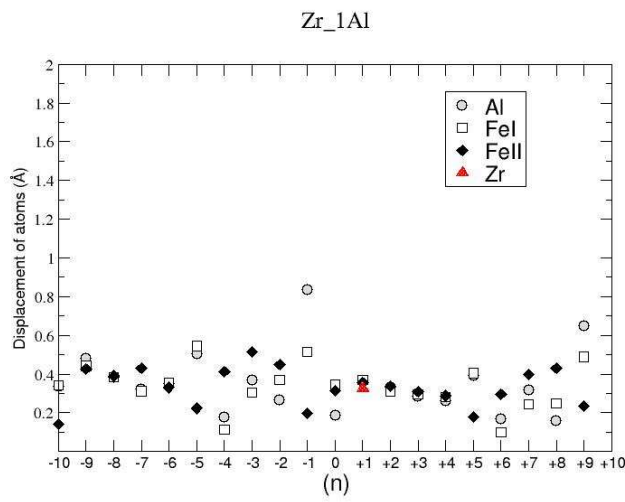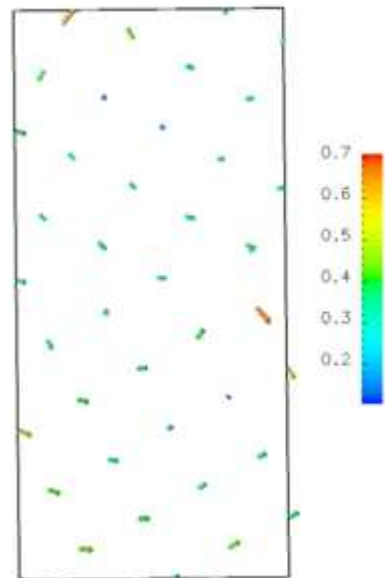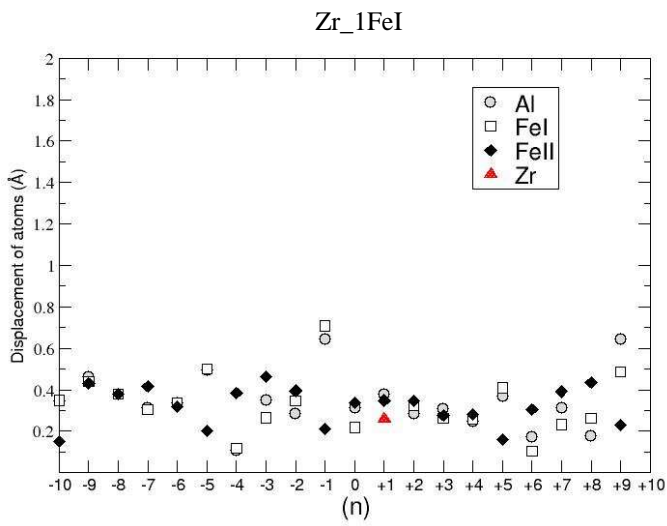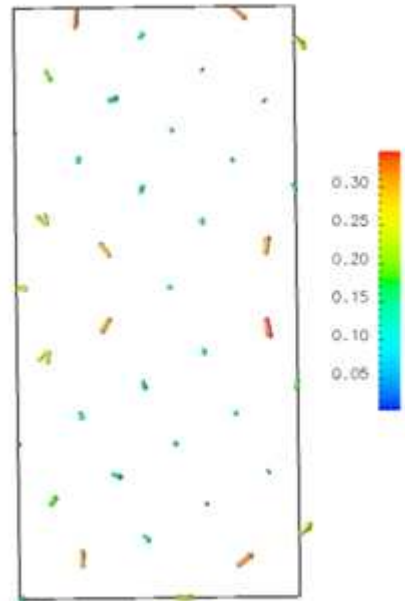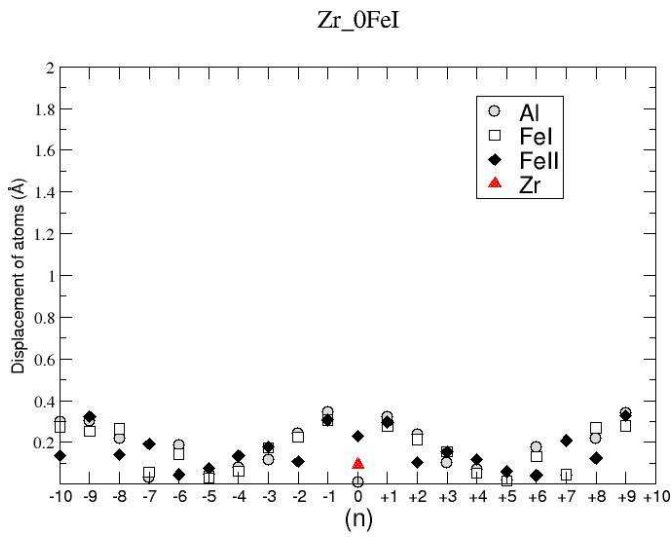
Appendix A

In this Appendix, the calculated displacements of the atoms in the doeped-grain boundary supercell will be presented. It is important to recall that the displacement of the atoms is calculated as difference between the final positions of the atoms in the relaxed supercell and the initial positions in the un-relxed supercell. The following left plots represent the calculated displacements of the atoms. The positions of the various atoms (Al, FeI and FeII) are given on the x axes depending on their location (n) away from the exact interface at n=0. Due to the cell symmetry 0 and -/+10 label the two interfaces in the supercell. In the right plots, the displacements are represented by solid arrows.
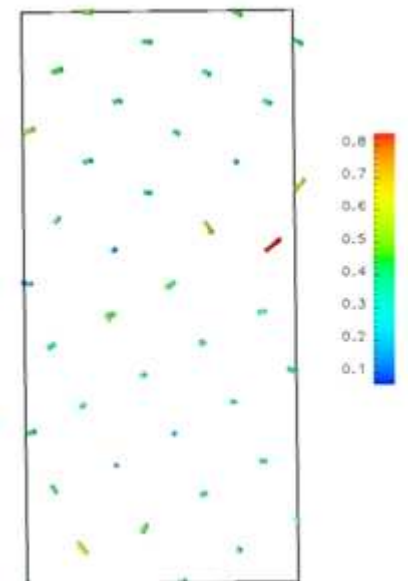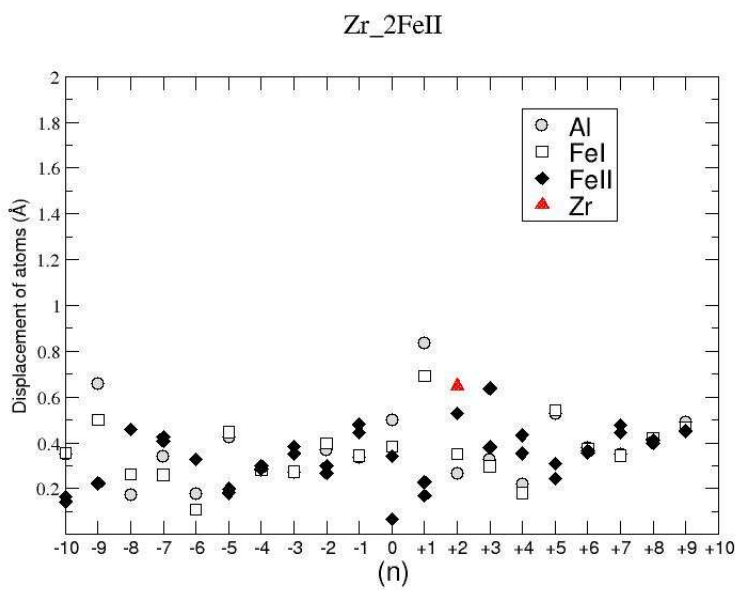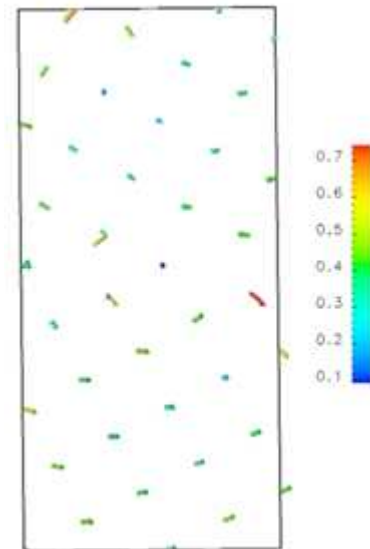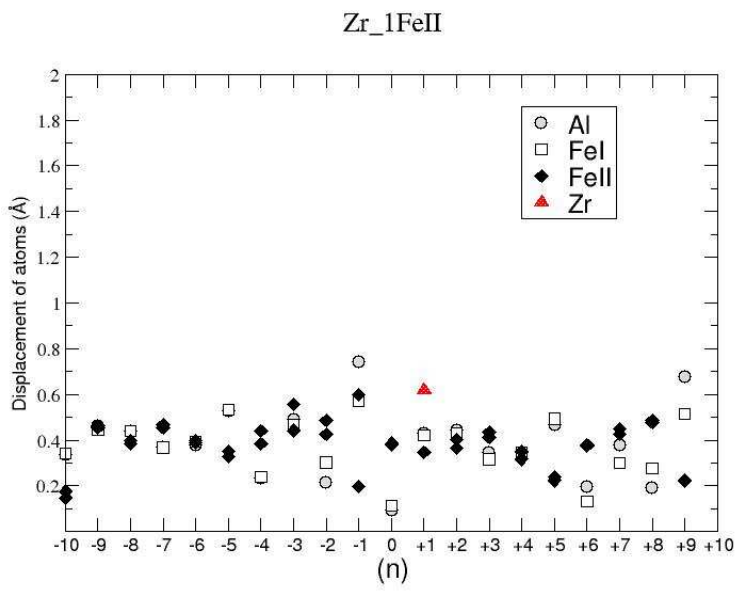
Ti_0Al

Ti_1Al

Ti_2Al

Ti_0FeI

Ti_1FeI

Ti_2FeI

Ti_0FeII

Ti_1FeII

Ti_2FeII

Zr_0Al

Zr_1Al

Zr_2Al

Zr_0FeI

Zr_1FeI

Zr_2FeI

Zr_0FeII
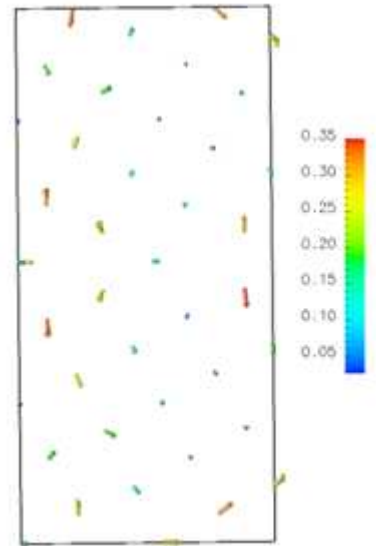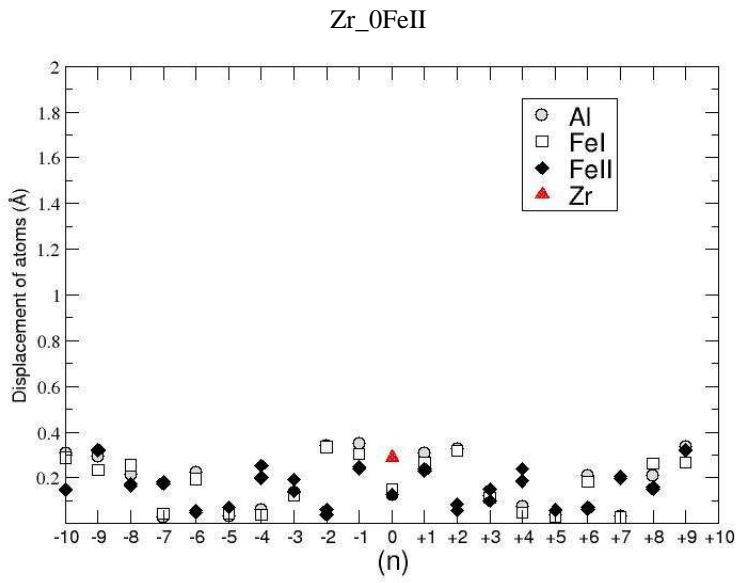

Zr_1FeII

Zr_2FeII
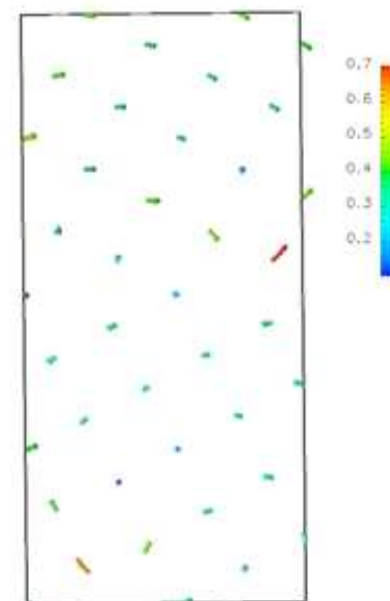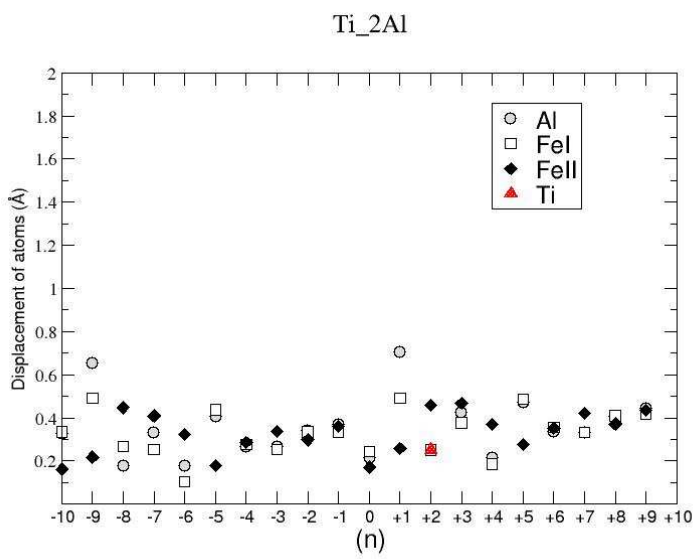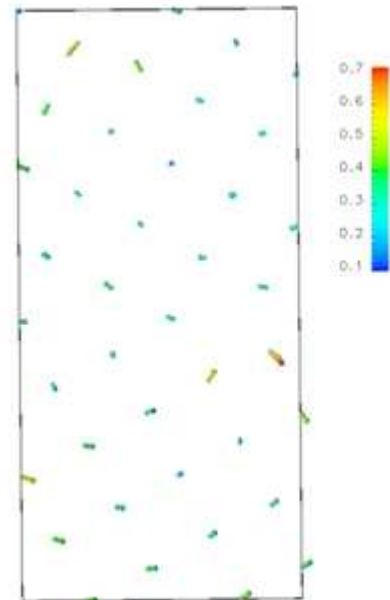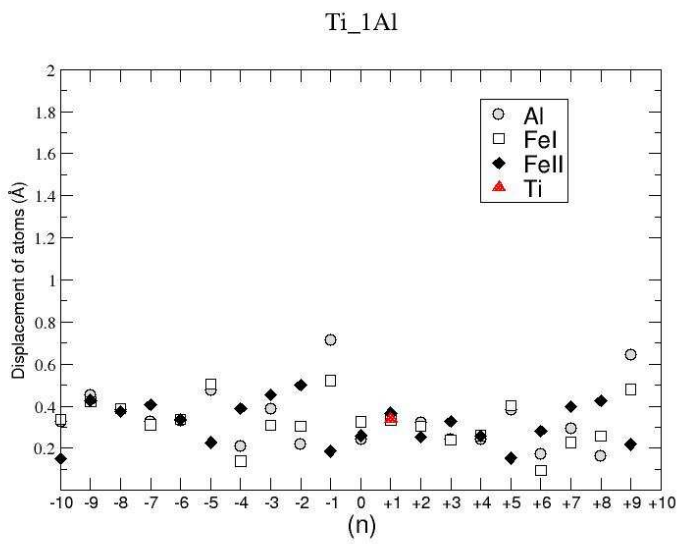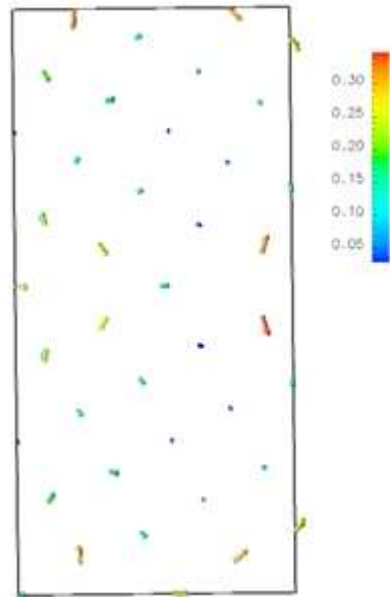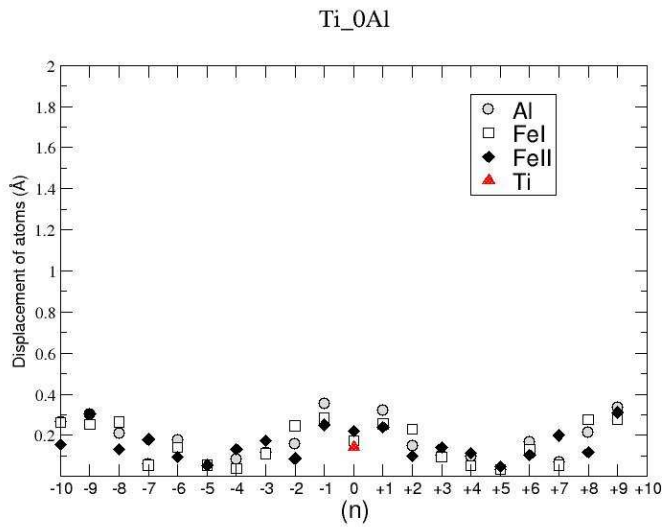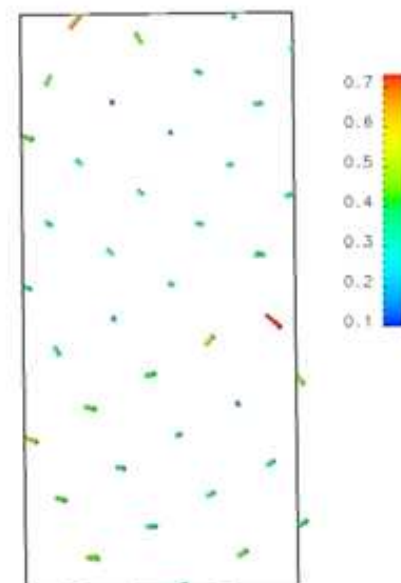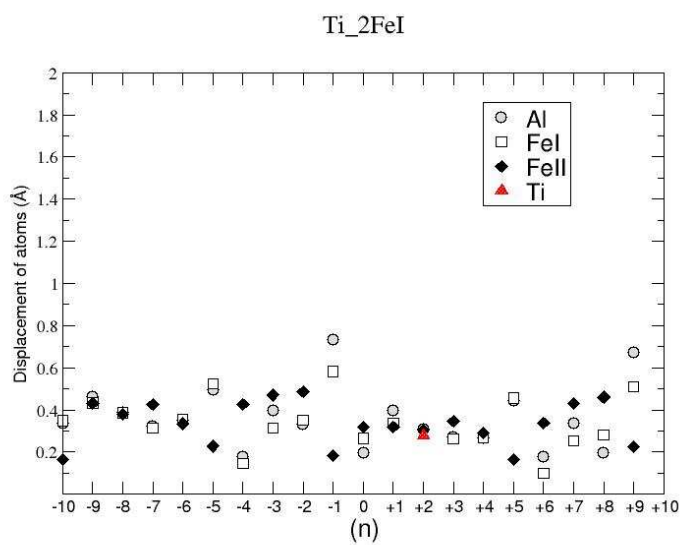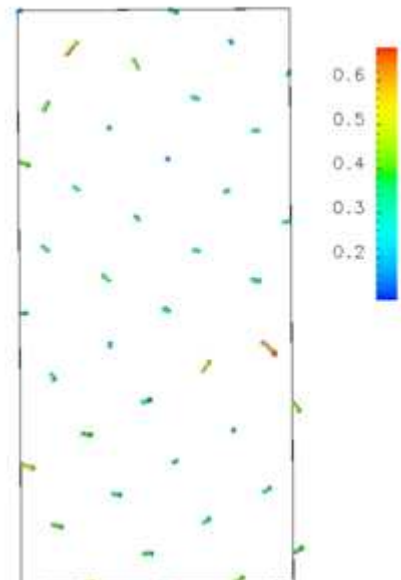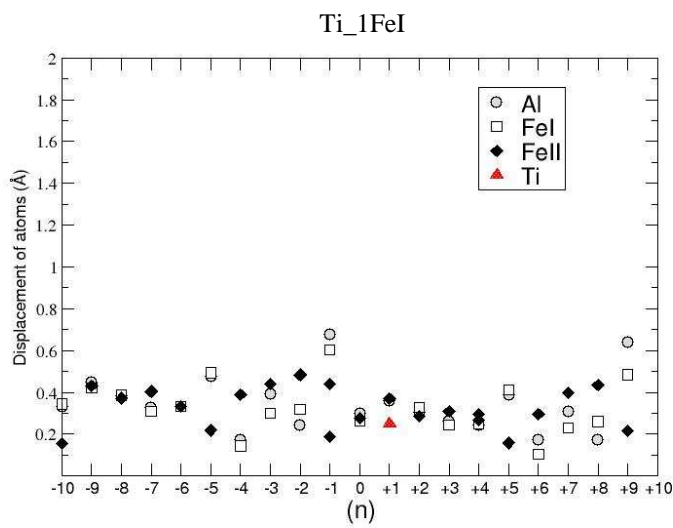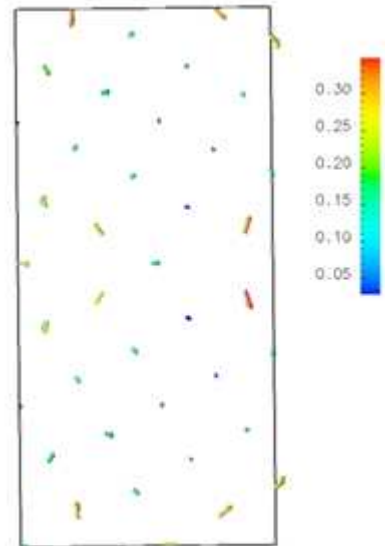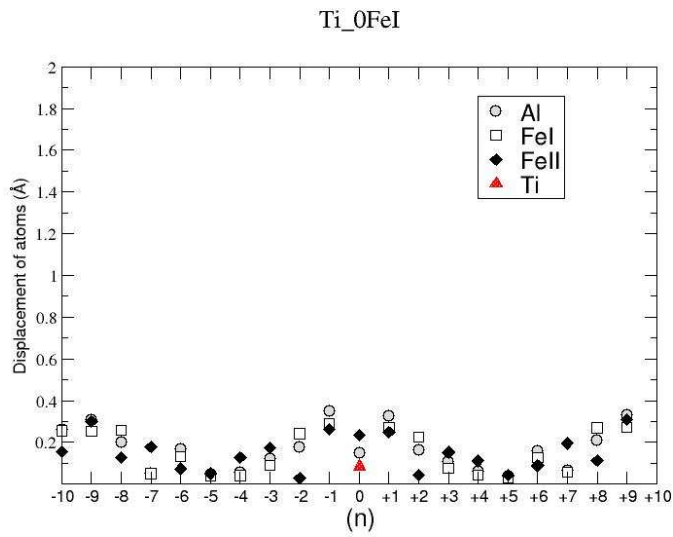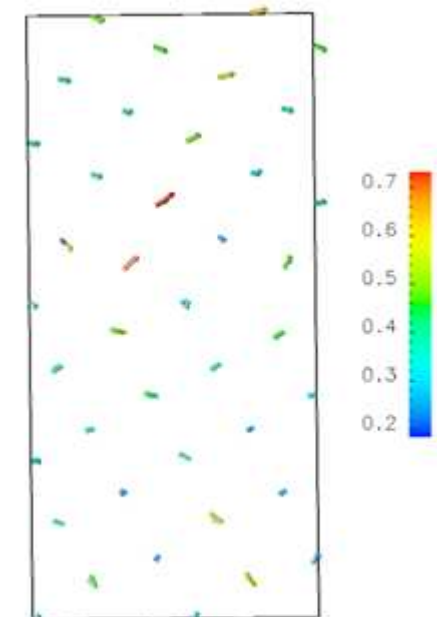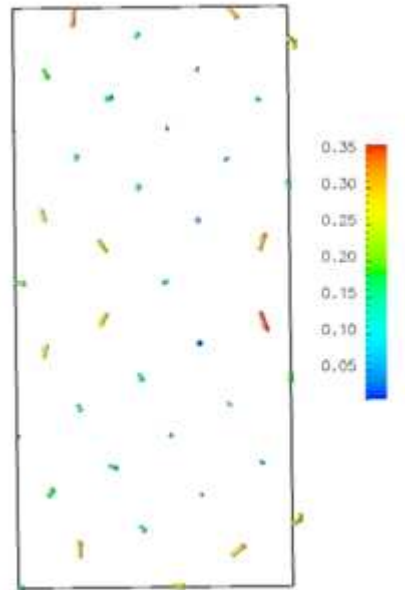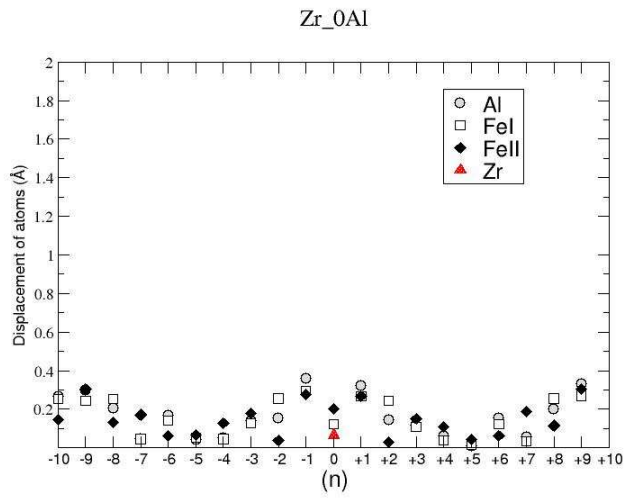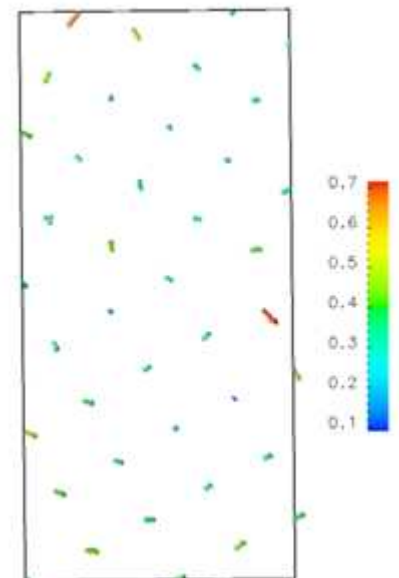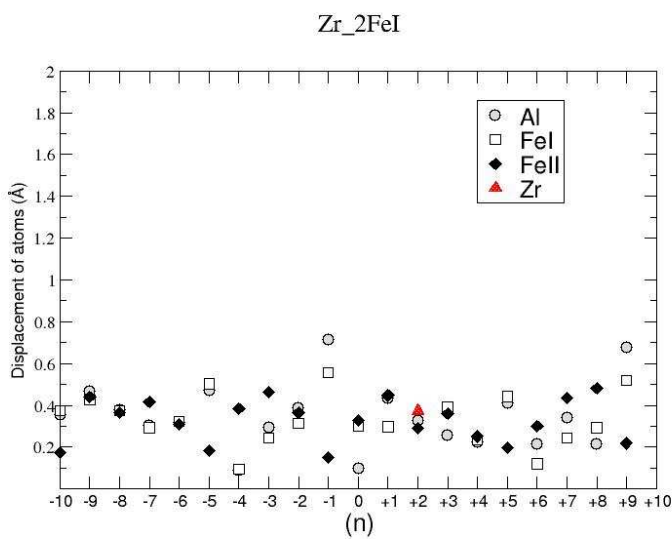
Appendix B

This appendix will give a brief general introduction into the field of two-dimensional defects in materials and the Coincidence Site Lattice theory.

Generally one speaks of an interface being present in a system if the physical properties discontinuously change across that interface. Phase boundaries i.e. exist between phases of different state of order. For example this is true for liquid-solid or liquid-gaseous interfaces. Limiting the discussion to internal interfaces in solid state materials one differentiates between either phase or grain boundaries. Phase boundaries separate grains of different phases. This i.e. could be grains having different lattice structure. Grain boundaries (GBs) separate almost stress free grains having the same lattice structure but different orientation. Throughout history the structure of GBs was seen quite differently. First models by Rosenhain [1] understood a GB as being an amorphous disordered region separating grains. A succeeding model by Mott [2] assumed that GBs are two-dimensional defects where zones of good lattice match and zones of bad lattice match exist.

A different approach is to discuss GBs in the framework of dislocations. The Read-Shockley model [3] tried to explain GBs on the basis of dislocations. Such an approach is well suited for low-angle GBs. Here it is well known that low-angle GBs can form by arrays of lattice dislocations. Although discrete lattice dislocations are having long-range stress fields, dislocation theory is able to show that by linear superposition of GB dislocation stress fields, GBs can be formed that only exhibit a short range stress field. For instance Fig. 1 demonstrates how stable almost stress free GBs can be formed. One of the major drawbacks of this model is the non-inclusion of any rigid body translations between crystals [9].
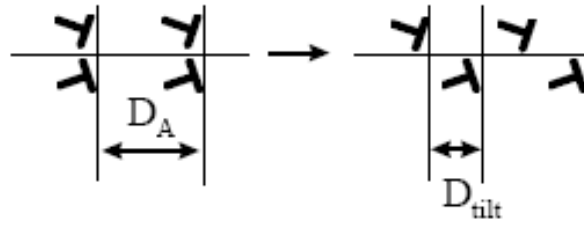
***Fig. 1** The description of tilt GBs in the framework of edge dislocations.*

A model which has received much success in the interpretation of experimental data is the coincidence site lattice (CSL) model [4, 5]. This is the model upon which the present work is based. Thus it seems necessary to explain in more detail the basic idea of the CSL.

The coincidence site lattice

In general the CSL represents lattice points of two discrete lattices that coincide if one imagines that the two lattices interpenetrate each other. If both crystals have the same crystal structure and are aligned without any misorientation or translation then the CSL would be the underlying lattice of the material. Introducing a misorientation between the two lattices described by a rotation matrix *R* will only give CSLs for certain misorientation angles and axes. For a better understanding of the underlying mathematics let us recall here that the position of an atom *i* can only be found in real space if its coordinates (x_i, y_i, z_i) as well as the unit vectors, e_x, e_y and e_z, spanning out the actual coordinate system are known. Here $r_i = (x_i, y_i, z_i)$ only gives the coordinates of atom i with respect to a certain coordinate system and its real space vector would be given by $r_i = x_i \, e_x + y_i \, e_y + z_i \, e_z$. The same is true for two misoriented crystals that do interpenetrate each other. Here this means that for either of the two crystals the internal coordinates (x_i, y_i, z_i) of any atom *i* are exactly the same when bearing in mind that they are defined with respect to each coordinate system. This now offers a simple way of mathematically expressing the basic equation for coincidence, namely writing

$$r^{L2} = R.r^{L1} = r^{L1} + t^{L1} \qquad \text{(Eq. 1)}$$

where r^{L1} represents the internal coordinates of a certain lattice point with respect to coordinate system No.1, r^{L2} the internal coordinates of that lattice point with respect to coordinate system No.2 and finally t^{L1} the coordinates of a translation vector of lattice No.1

with respect to coordinate system No.1. Thus any lattice point r^{L1} of lattice No.1 that satisfies Eq. III-4 is a lattice point of lattice No.1 and No.2 and therefore represents a coincident point. Here one should note that the CSL is confined to descrite lattice points.

In order to find the vectors that span out the CSL, Eq. 1 needs to be rewritten and thus one obtains Eq. 2. Inserting the translation vectors of lattice No.1 in Eq. 1 would then give the CSL vectors.

$$R \cdot r^{L1} - r^{L1} = (R - 1)\, r^{L1} = t^{L1} \quad \Leftrightarrow \quad r^{L1} = (R^{-1} - 1)\, t^{L1} \tag{Eq. 2}$$

Extending the discussion to any point r^{L1} and r^{L2} within the lattices leads to the concept of the O-lattice [6]. It is a more general concept than the CSL and the CSL is a sub-lattice of the O-lattice.

There are several different approaches to describe a misorientation relationship between two coordinate system. In this work the misorientation relationship is expressed by a rotation axis $[H, K, L]$ and a rotation angle θ. For certain misorientation relationships between two crystals depending on the rotation axis and angle well-defined CSL lattices exist that are characterized by a single parameter namely their $\sum$ values. Since this work only deals with cubic materials, the further discussion is restricted to cubic materials. Well-defined misorientations between both crystals can for instance be expressed by a rational Rodrigues vector $\rho = \frac{m}{n}[H, K, L]$, where *m, n, H, K* and *L* are integers [6]. Here the misorientation angle is not explicitly set but rather defined through the distinct set of *m, n, H, K* and *L*.

In terms of rotation axis and angle the Rodrigues vector represents a rotation about an axis $[H, K, L]$ by θ where θ is given by

$$tan\left(\frac{\theta}{2}\right) = \frac{m}{n}\sqrt{H^2 + K^2 + L^2} \tag{Eq. 3}$$

Furthermore the ratio of the volume of the primitive CSL with respect to the atomic volume of the material is characterized by $\sum$ and formally given by

$$\sum = n^2 + m^2 \cdot (H^2 + K^2 + L^2) \tag{Eq. 4}$$

Eq. 3 and 4 can be used as master equations to calculate the misorientation angle θ and $\sum$ for a chosen rotation axis $[H, K, L]$ and *m* and *n*. If $\sum$ as given by Eq. 4 is an even number, $\sum$ is

then to be divided by 2β with β being the smallest integer to find the largest odd ∑ number. The CSL scheme itself is not unique concerning the misorientation path. Theoretically a given CSL can be generated by 24 different misorientation paths for cubic materials due to the symmetry operations possible for cubic materials [7]. For instance one obtains a ∑5 CSL by a 36.87° [001] rotation (see Fig. 2) as well as by a 53.13° [001] rotation. These two representations are linked by the 270° [001] symmetry operation of the cubic lattice. So far a GB has yet not appeared in the discusssion of the CSL scheme and thus the plain CSL scheme is therefore only associated with misorienting two crystals. Utilizing the CSL concept to misorient two crystals, the final step to geometrically generate symmetrical CSL twist GBs, symmetrical CSL tilt GBs as well as asymmetrical CSL tilt GBs is to define the GB plane that will separate the two crystals from each other. This means that either one of the crystals only exists on one side of the GB, thus here the discussion of interpenetrating crystals comes to an end. Obviously the scheme itself is rather theoretical since for instance in sample preparation of experiments such a working sequence of misorienting interpenetrating crystals can only be regarded as imaginary.
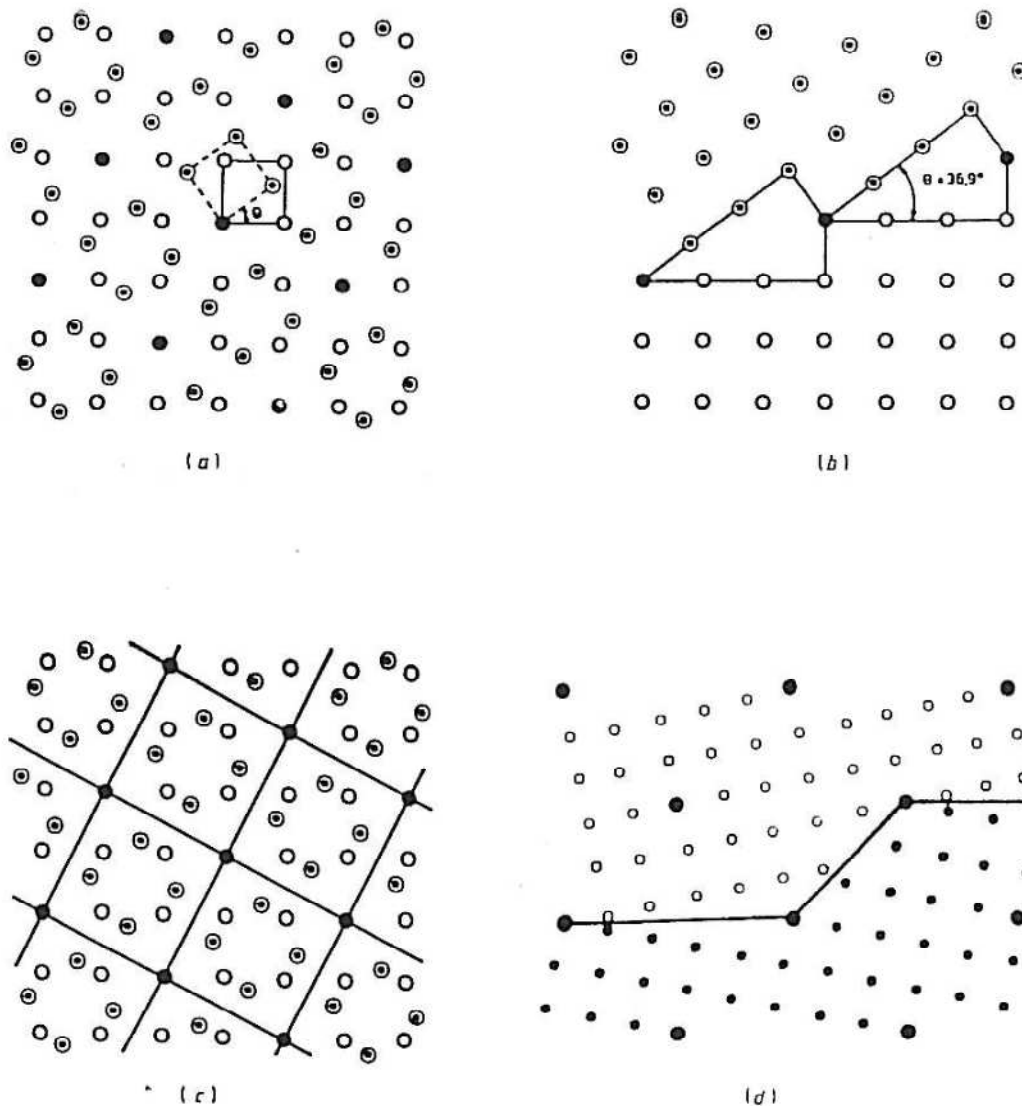
Fig. 2 *(a) Two interpenetrating lattices, misoriented by 36.87° /001 forming a dichromatic pattern, viewed down 001. (b) GB generated from the dichromatic pattern in (a). (c) coincidence site lattice, $\sum=5$, generated by the misorientation shown in (a) and (b). (d) GB formed by a misoriented of 22.62°/001, which gives a CSL of $\sum=13$. The coincidence sites are denoted by solid symbols throughout.* [8]

Concerning the nature of GBs some general statements can be made with respect to the CSL procedure if one restricts the discussion to one distinct CSL misorientation representation out of the 24 possible. Generally it can then be stated that a pure twist GB follows the rule that its GB normal and the misorientation axis are parallel. For pure tilt GBs a similar rule exists, namely that the GB normal and the tilt axis are perpendicular to each other. These rules are rather simple and once again illustrated by Fig. 3 (a) and (b) and for any pure twist or tilt GB the rule will apply for at least one of the 24 misorientation representations.
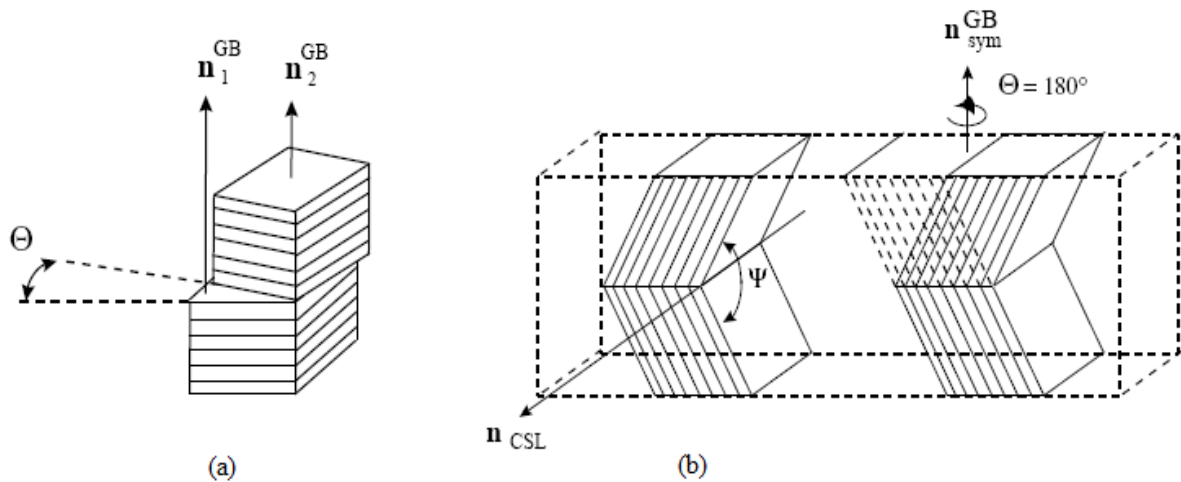
Fig. 3 *Schematic of twist and tilt GB geometries. (a) illustrates the generation scheme of symmetrical twist GBs and (b) illustrates the generation scheme of symmetrical tilt GBs.*

Reference

[1] W.Rosenhain and D.Ewen, J. Inst. Metals **10**, 119 (1913).

[2] N.F.Mott, Proc. Phy. Soc. **60**, 391 (1948),.

[3] W.T.Read and W.Shockley, Phys. Rev. **78**, 275 (1950).

[4] A. Sutton, International Metals Review **29**, 377 (1984).

[5] A. Brokman and R. Balluffi, Acta Metal **29**, 1703 (1981).

[6] J.M.Howe,'Interfaces in Materials', John Wiley & Sons 1997.

[7] Bernd Schönfelder, 'Atomistic Simulations of Grain Boundary Migration in Face-Centred Cubic Metals', Thesis (2002).

[8] V.Randle, The Measurement Of Grain Boundary Geometry, IOP Publishing Ltd (2003).

[9] L. Priester, Les joints de grains de la théorie à l'ingénierie, EDP sciences (2006).

Abstract

Fe₃Al-based intermetallic compounds are promising materials for structural applications at high temperature. Their advantageous properties originate from their low density and their high corrosion resistance in oxidizing and sulfidizing environments. However, because of their limited room temperature ductility and their low strength and creep resistance at higher temperatures (~550℃), it is necessary to im prove their properties to adapt them for structural applications. An interesting aspect of these alloys is their behaviour towards transition metal impurities. Some elements like Ti increase the stability of the D0₃ by increasing the D0₃/B2 transition towards higher temperature. The situation is less clear for Zr addition, indeed, despite the beneficial effect of small Zr addition on the grain boundary cohesion and ductility; there is no experimental data available concerning its effects on the stability of the D0₃-Fe₃Al compounds. In this thesis the effect of the Ti and Zr transition metals on the D0₃-Fe₃Al intermetallic compounds has been investigated by means of ab initio PseudoPotentials numerical simulations based on Density Functional Theory. Two main issues will be addressed *(i)* the understanding of the role of these two transition metals in terms of stability of the bulk at the light of their site preference in the D0₃-Fe₃Al structure *(ii)* the behaviour of Ti and Zr transition metals in the ∑5 (310) [001] grain boundary and their effect on the structural stability of this interface. An important issue when studying these aspects is to take into accounts the effect of temperature. This requires a molecular dynamics treatment of the atoms in the supercell. The technique known as *ab initio* molecular dynamics (AIMD) solves these problems by combining 'on the fly' electronic structure calculations with finite temperature dynamics. Thus, our study was conducted both using the conventional static ab initio calculations (0K) as well as by taking into account the effect of temperature (Ab Initio Molecular Dynamics).

The keywords: The intermetallics alloys Fe3Al-D03, The Density Functional Theory (DFT), The alloying elements Ti and Zr.

Résumé

Les alliages intermétalliques riches en fer du système fer-aluminium, Fe₃Al, ont des caractéristiques très intéressantes pour des applications mécaniques à haute température. Ils possèdent, comme la plupart des composés intermétalliques, une résistance mécanique élevée, une bonne résistance à l'oxydation ainsi qu'une faible densité. Cependant, les principales raisons qui limitent leurs applications sont leur fragilité à température ambiante et une forte diminution de leur résistance pour des températures supérieures à 550℃. Un aspect intéres sant de ces alliages est leur comportement envers les métaux de transition. Certains éléments, comme Ti, peuvent augmenter la stabilité de la phase D0₃, en augmentant la transition D0₃/B2 vers des températures plus élevées. La situation est moins claire dans le cas du Zr. En effet, malgré l'effet bénéfique du dopage en Zr sur la cohésion des joints de grains et la ductilité, il n'existe pas de données expérimentales concernant son effet sur la stabilité de la structure D0₃ du composé Fe₃Al. Ce travail de thèse vise à étudier l'effet de ces deux métaux de transitions Ti et Zr sur les propriétés du composé intermétallique D0₃-Fe₃Al en utilisant des calculs pseudopotentiels ab initio basées sur la théorie de la fonctionnelle de la densité (DFT). Deux principaux thèmes ont été abordées: *(i)* la compréhension du rôle de ces deux métaux de transition en termes de stabilité de la phase D0₃ à la lumière de leur site préférentiel dans la structure D0₃-Fe₃Al *(ii)* le comportement du Ti et Zr dans le joint de grains Σ5 (310) [001] ainsi que leur effet sur la stabilité structurale de cette interface. Un élément important pour étudier ces aspects est de prendre en compte l'effet de la température. Cela nécessite un traitement de type dynamique moléculaire des atomes dans la supercellule. La technique dynamique moléculaire ab initio (AIMD) résout ces problèmes en combinant des calculs de structure électronique avec la dynamique à une température finie. Ainsi, notre étude a été menée à la fois en utilisant des calculs ab initio statiques à 0K ainsi que par la prise en compte de l'effet de la température jusqu'à 1100K (Dynamique Moléculaire Ab Initio).

Les mots clés : Les alliages intermétalliques Fe3Al-D03, La théorie de la fonctionnelle de la densité (DFT), les additions Ti et Zr.

الملخص

المركبات Fe₃Al-D0₃ تمتلك عدة خصوصيات تجعلهم قابلة للاستعمالات الهيكلية في درجات الحرارة المرتفعة. خصوصياتهم تكمن في الكثافة المنخفضة و المقاومة ضد الصدأ في البيئات المؤكسدة. مع ذلك بسبب محدودية الليونة في درجات الحرارة المنخفضة و الانخفاض في القوة في درجات الحرارة المرتفعة المقاربة ل C° 550 ، لابد من تحسين هذه الخواص للتكيف مع هذه التطبيقات الهيكلية. من الجوانب المثيرة للاهتمام في هذه المركبات، سلوكهم نحو الشوائب. بعض العناصر مثل Ti يزيد من الارتفاع في استقرار D0₃ بزيادة درجة الانتقال D0₃/B2 الى درجات حرارة عالية. الحالة اقل وضوحا بالنسبة لتأثير Zr على درجة الانتقال D0₃/B2 رغم ان الزيادات الصغيرة ل Zr تحسن تماسك GB (Grain boundary)اذ لا يوجد بيانات تجريبية توضح اثار هذه الزيادات على D0₃/B2 في المركب Fe₃Al . في هذه الرسالة سيتم دراسة تأثير هذه الشوائب Ti و Zr على المركبات Fe₃Al و ذلك باستعمال الطريقة ab initio Pseudopotentiels المؤسسة عن نظرية DFT . سيتم تناول قضيتين رئيسين *(1)*سيتم فهم دور هذه المعادن (الشوائب) على درجة الحرارة الانتقالية D0₃/B2 واستقرار المرحلة D0₃ و ذلك في ضوء مواقعهم المفضلة في البنية*(2)*سلوكTi و Zr على استقرار The grain boundary Σ5 (310)[001] . قضية هامة يجب تاخد بعين الاعتبار عند دراسة هذه الجوانب هي تأثير درجة الحرارة و هذا يتطلب معالجة ديناميكية. تعرف هذه التقنية ب التي تجمع بين الحسابات الالكترونية و الديناميكية. لهذا اجرينا الدراسة على حد السواء باستخدام الحسابات عند و كذلك مع الاخد بعين الاعتبار تأثير درجة الحرارة.

المفاتيح :المركب Fe₃Al-D0₃، نظرية DFT ، اظافات Tiو Zr.